Ring polymer molecular dynamics

Ian R. Craig

Jesus College, University of Oxford

A thesis submitted for the degree of Doctor of Philosophy

Hilary Term, 2006

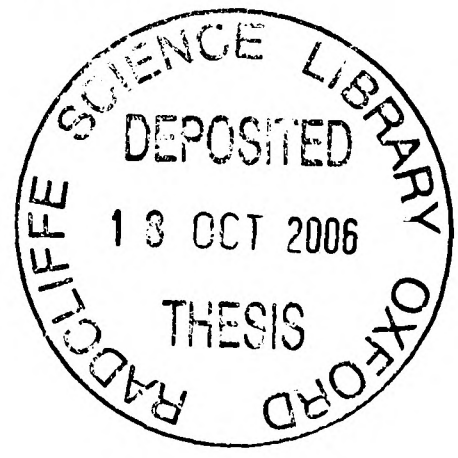

Ring polymer molecular dynamics

Ian R. Craig, Jesus College

A thesis submitted in partial fulfilment of the requirements
for the degree of Doctor of Philosophy of the University of Oxford

Hilary Term, 2006

Abstract

This thesis presents the ring polymer molecular dynamics (RPMD) approximation to the Kubo-transformed time correlation function and shows how it may be used as the basis of an approximate quantum-mechanical method for determining the dynamical properties of condensed-phase molecular systems.

The performance of the RPMD method is initially investigated by calculating the position ($\hat{q}$), and position-cubed ($\hat{q}^3$), autocorrelation functions of a series of one-dimensional potential wells of varying anharmonicity. It is then applied to the evaluation of the incoherent dynamic structure factors of liquid para-hydrogen at 14 K. Finally, the RPMD method is used to determine canonical rate coefficients for two one-dimensional models of bimolecular chemical reactions and a multidimensional model of a solution-phase proton transfer reaction. For each application, the accuracy of the RPMD method is established by comparison with exact quantum-mechanical results and/or with experiment. Throughout this work, an emphasis is placed upon identifying the situations in which the RPMD approximation breaks down.

It is found that the RPMD method is capable of providing an accurate approximation to the time correlation functions of a variety of condensed-phase molecular systems. Situations for which it is inaccurate include correlation functions which correlate highly nonlinear operators and those involving significant quantum interference effects in the real-time dynamics.

Acknowledgements

I will always consider the limitless insight, advice, and encouragement given to me by Professor David Manolopoulos as being supervision above and beyond all reasonable expectations. His enthusiasm and friendship have, in addition, made the past few years a hugely enjoyable experience and for this I am sincerely grateful.

I have had the benefit of working alongside a sequence of intelligent, good-humoured and good-natured people. In different ways Tomas, Ed, Rob Heaton, Martin, Tommy and Rob Arbon all made me look forward to getting into the lab in the morning. I am also grateful to Rosana, Scott, Alex, Xinhui and Tom for making the lab such a productive place in which to write-up.

I close by thanking my parents, my brother and my girlfriend. I can't begin to acknowledge the ways in which they have assisted and guided me – I can only express my deepest gratitude.

Contents

Introduction

Molecular simulation techniques are used in many areas of physical and biological science to investigate condensed-phase systems such as liquids, solutions, surfaces, and (bio)polymers [1, 2]. In some areas of research these simulations are primarily used as aids to the design and interpretation of experimental work. In others it is found that the information provided by molecular simulation is complementary to that which can be obtained through experiment [1].

Theoretical studies can also benefit from the availability of results from a relevant simulation. It is frequently simpler to test theoretical predictions against simulation rather than experiment since the former is often capable of providing the 'exact' results for a given model [3]. Furthermore, an examination of the data from a simulation may lead to insight that inspires new directions for theoretical research. For these reasons and others, molecular simulation can be a useful tool for studying condensed-phase systems.

Perhaps the most important questions that can be answered by molecular simulation concern the (time-independent) equilibrium characteristics of complex, condensed-phase systems. Examples of such characteristics include the radial distribution function of a liquid, the solvation structure of the solvent surrounding a solute, and the magnitude of the average molecular electric dipole moment in a polar liquid. In certain molecular systems, some of these static equilibrium properties can be simulated

accurately within the framework of classical statistical mechanics (see Section 1.1). However, many of the systems of interest to chemistry involve light atoms (e.g. hydrogen) and so their statistical mechanics can be distinctly nonclassical. The path-integral formulation of quantum statistical mechanics [4–6] is an indispensible tool with which to simulate the static equilibrium properties of such systems (see Section 1.2). Whether quantum-mechanical or classical in nature, static equilibrium properties obtained through simulation can provide insight into the nature of condensed-phase molecular systems which is difficult to obtain in other ways.

Of course, many of the most interesting characteristics of complex molecular systems relate to their motion rather than just their equilibrium structure. Examples of the kind of dynamical properties that are frequently important in understanding condensed-phase systems are diffusion rates, viscosities, thermal conductivities, and chemical reaction rates. Since there is no net motion of a system at equilibrium the dynamical properties of a system are nonequilibrium properties, and so at first it would seem that the equilibrium techniques referred to in the previous paragraph could not be applied. However, within linear response theory [7, 8], *nonequilibrium* dynamical properties are given in terms of time correlation functions of the *equilibrium* system. These correlation functions quantify the dissipation of spontaneous fluctuations in the relevant properties, as they occur at equilibrium.

As for static properties, it may or may not be possible to accurately evaluate a particular correlation function by classical simulation techniques. However, whereas the path-integral formalism has led to feasible, general and exact quantum-mechanical methods for calculating the quantum static properties of condensed-phase systems, there exists no widely-applicable extension for calculating quantum dynamical properties. Furthermore, no methodology of *any* sort is able to evaluate the exact quantum dynamical properties of a condensed-phase molecular system, unless it is the simplest

of models [9–11]. The exact quantum-mechanical basis-set techniques that have been so successful for studying the dynamics of small-molecule gas-phase systems are inapplicable due the exponential scaling of the required computational workload with system size [12].

The absence of a method that is capable of calculating the exact quantum dynamical properties of condensed-phase molecular systems has resulted in a great effort being invested in the search for approximate but computationally efficient alternatives [13–20]. For reasons discussed in Chapter 1, none of the resulting approximate schemes has emerged as the 'method of choice' in the manner of the path-integral approach for quantum static equilibrium properties. The scope for developing a method that complements or improves upon the existing approximate approaches has motivated the work presented here.

This thesis develops a novel and conceptually simple approximation to a particular type of quantum-mechanical time correlation function and therefore establishes a new method for calculating the quantum dynamical properties of condensed-phase molecular systems. The Ring Polymer Molecular Dynamics (RPMD) method is applied to the calculation of dynamical properties for a number of different systems and the accuracy of the approximation is established by comparison to exact quantum-mechanical results (when available) and/or experiment. In order to guide and inform any future studies using the new approach, a particular emphasis is placed upon identifying the situations in which the RPMD approximation breaks down.

An outline of the thesis

Chapter 1 begins this thesis with a survey of some of the methods already devised for the purpose of calculating approximate quantum dynamical properties of condensed-

phase systems. With this background established, the developments that result in the RPMD approximation are presented in Chapter 2. In order to justify the use of the new method, the chapter goes on to show that the approximate RPMD correlation function shares a number of symmetries with the exact quantum-mechanical correlation function and that it also equals the exact analogue in three different limits. The chapter closes by applying the RPMD method to three simple one-dimensional test problems and uses the results of these calculations to give an initial assessment of its accuracy.

The remainder of the thesis is then concerned with examining the performance of the new method for problems which involve the quantum dynamics of multidimensional molecular systems. In Chapter 3 the RPMD method is applied to the calculation of the incoherent dynamic structure factors of liquid para-hydrogen at 14 K. At this temperature the static equilibrium properties of liquid para-hydrogen are poorly described by classical statistical mechanics [21], and one would expect that quantum-mechanical effects are also important in determining the dynamical properties of the system. However, the quantum dynamics of this realistic model of a many-particle system cannot be calculated exactly by any currently-available technique. Thus, the liquid para-hydrogen system is representative of the type of multidimensional *and* significantly quantum-mechanical molecular system for which the RPMD approximation is likely to be of most use. The accuracy of this RPMD evaluation of the incoherent dynamic structure factors of liquid para-hydrogen is established using purely theoretical moment (sum rule) constraints and also by comparison with the results of recent neutron-scattering experiments [22].

In the field of chemical physics, the calculation of chemical reaction rates in condensed-phase systems is an extremely challenging, but important, problem [23]. For the reasons mentioned above, the methodologies that are able to produce exact quantum-

mechanical rate coefficients for small-molecule gas-phase reactions quickly become inapplicable as more atoms are added to the reactive system [24]. Therefore, condensed-phase chemical reaction rates are another type of dynamical process which must almost always be studied by approximate methods. Chapter 4 develops a new approach for calculating these quantities by combining the RPMD approximation with the time correlation function formulation of chemical reaction rates [25]. It is shown that the resulting method possesses theoretically appealing short- and long-time limits; as $t \to 0$ it tends to a well-defined quantum transition-state theory and as $t \to \infty$ it gives a rate coefficient that is independent of the choice of dividing surface. For these reasons the method should be comparatively practical for the calculation of the rate coefficients of complex reactive systems. However, Chapter 4 only goes as far as applying the RPMD approach to a couple of one-dimensional models of bimolecular chemical reactions.

In Chapter 5, the RPMD reaction rate theory is applied to the well-studied system-bath model for a solution-phase proton transfer. This model is composed of a symmetric double-well bilinearly coupled to a representative bath of harmonic oscillators and is a rare example of a multidimensional reactive system for which the quantum-mechanical rate coefficients can be calculated exactly [26]. It therefore presents an excellent opportunity to gauge the accuracy of the new method for the rate coefficients of condensed-phase systems. Comparison is also made with the results of a number of other approximate approaches that have been applied to this model. The chapter closes with a discussion of the importance of classical and quantum-mechanical dividing-surface recrossing effects in condensed-phase chemical reactions.

Chapter 6 summarizes what has been accomplished in this thesis and leaves two appendices to expand on some technical details.

Chapter 1

Alternative methods

This chapter briefly reviews a number of techniques for simulating the static and dynamic properties of condensed-phase molecular systems. This survey of existing methods provides a context for the developments presented in later chapters, and also serves to introduce many of the concepts and quantities that are needed there. All expressions are formulated for a generic one-dimensional system since this allows the important points to be made most simply. The extensions to systems with more degrees of freedom are straightforward.

1.1 Classical molecular dynamics

Classical molecular dynamics simulations are a well-established tool for predicting the static and dynamic properties of large assemblies of atoms and/or molecules [1, 2]. Within the classical approximation, the static properties of systems at canonical equilibrium (e.g. radial distribution functions or average kinetic energies) are calculated as phase-space integrals of the form:

$$\langle A \rangle_{\rm cl} = \frac{1}{(2\pi\hbar) Z_{\rm cl}} \int dp \int dq \; e^{-\beta H(p,q)} A(p,q). \tag{1.1}$$

In this expression, p and q are respectively the momentum and position variables of the one-dimensional system, $\beta = 1/k_B T$ where k_B is the Boltzmann constant and T is the temperature, and $A(p,q)$ is a function representing the quantity of interest. The classical approximation to the canonical partition function is

$$Z_{\rm cl} = \frac{1}{(2\pi\hbar)} \int dp \int dq \; e^{-\beta H(p,q)}, \tag{1.2}$$

where $H(p,q)$ is the classical Hamiltonian of the system. In a molecular dynamics simulation $\langle A \rangle_{\rm cl}$ is evaluated as the average of the function $A(p,q)$ over the phase-space points (p,q) visited by trajectories that are based upon the classical equations of motion

$$\dot{q} = \frac{\partial H(p,q)}{\partial p} \quad ; \quad \dot{p} = -\frac{\partial H(p,q)}{\partial q}. \tag{1.3}$$

These equations generate constant-energy trajectories and therefore sample a micro-canonical (fixed-energy) distribution of points in phase space. The next chapter (Section 2.1) discusses schemes that augment these equations of motion so that they produce constant-temperature trajectories. Since the static quantity is calculated from time-independent information these modified trajectories are just a convenient mechanism for sampling the canonical (fixed-temperature) phase-space distribution.

Linear-response theory relates dynamic properties (e.g. diffusion constants or rotational relaxation times) to time correlation functions [7, 8, 27]. The classical expressions for these correlation functions are also phase-space integrals, i.e.,

$$c_{\rm AB}^{\rm cl}(t) = \frac{1}{(2\pi\hbar) Z_{\rm cl}} \int dp_0 \int dq_0 \; e^{-\beta H(p_0,q_0)} A(p_0,q_0) B(p_t,q_t), \tag{1.4}$$

where the subscripts on p and q indicate time. The correlation functions quantify the dissipation of spontaneous fluctations in the quantities of interest, as they occur at canonical equilibrium. According to Onsager's regression hypothesis [8], it is this

which is directly related to the relaxation of nonequilibrium states and thus the dynamical characteristics of the system. The integral in Eq. (1.4) can also be evaluated using molecular dynamics, although the trajectories are now more than just tools for sampling the phase space. Since the dynamics determines the sequence in which the phase-space points are visited it also governs the extent of any (average) correlation between $A(p_0, q_0)$ at some initial time and $B(p_t, q_t)$ at a later time t.

Classical molecular dynamics techiques are widely applied both academically and commerically [1, 2, 28]. However, in many systems the dynamic processes have significiant quantum-mechanical character and are therefore poorly described by the classical equations of motion (Eq. (1.3)). In particular, classical simulations are inaccurate when the particle mass and/or the temperature is low, i.e. when the available thermal energy ($\sim k_B T$) is much less than the spacing of the energy levels relevant to the property of interest. Important examples are dynamical quantities that are governed by the motion of hydrogen nuclei. In such situations the classical time correlation function in Eq. (1.4) will be a poor approximation to its exact quantum-mechanical analogue and will lead to an unreliable description of the dynamical process.

Some scope for optimizing the classical description arises from the fact that Eq. (1.4) is the classical limit of not one but a number of quantum-mechanical correlation functions [29]. The operator noncommutation that causes these quantum analogues to differ collapses in the classical limit and one can therefore conceive of using $c^{\mathrm{cl}}_{\mathrm{AB}}(t)$ as an approximation to any of them. The important question is then: to which quantum correlation function is $c^{\mathrm{cl}}_{\mathrm{AB}}(t)$ the most accurate approximation? Put another way: having calculated $c^{\mathrm{cl}}_{\mathrm{AB}}(t)$, what is the best way to use it?

The 'standard' quantum-mechanical analogue of $c^{\mathrm{cl}}_{\mathrm{AB}}(t)$ is

$$c^{0}_{\mathrm{AB}}(t) = \frac{1}{Z}\mathrm{tr}\left[e^{-\beta\hat{H}}\,\hat{A}\,e^{i\hat{H}t/\hbar}\,\hat{B}\,e^{-i\hat{H}t/\hbar}\right], \tag{1.5}$$

where Z is the quantum-mechanical canonical partition function, 'tr' indicates a trace and $\hat{A}$ and $\hat{B}$ are operators representing the quantities whose time correlation is of interest. Now, certain properties of the exact quantum $c^0_{\rm AB}(t)$ are not shared by $c^{\rm cl}_{\rm AB}(t)$. Firstly, for position-dependent operators ($\hat{A} = A(\hat{q})$ and $\hat{B} = B(\hat{q})$), $c^0_{\rm AB}(t)$ is a complex-valued function of time whereas the equivalent classical $c^{\rm cl}_{\rm AB}(t)$, with real position-dependent functions $A(q)$ and $B(q)$, is a real (and even) function of time (see Section 2.3). Secondly, $c^{\rm cl}_{\rm AB}(t)$ does not share the *detailed-balance* symmetry of $c^0_{\rm AB}(t)$, i.e. if the spectral representation of the latter is

$$C^0_{\rm AB}(\omega) = \frac{1}{2\pi}\int_{-\infty}^{\infty} dt\, e^{-i\omega t}\, c^0_{\rm AB}(t), \tag{1.6}$$

then

$$C^0_{\rm AB}(-\omega) = e^{-\beta\hbar\omega} C^0_{\rm AB}(\omega). \tag{1.7}$$

The equivalent *classical* symmetry is

$$C^{\rm cl}_{\rm AB}(-\omega) = C^{\rm cl}_{\rm AB}(\omega), \tag{1.8}$$

where $C^{\rm cl}_{\rm AB}(\omega)$ is the spectral representation of $c^{\rm cl}_{\rm AB}(t)$ and is defined by analogy to Eq. (1.6). This classical symmetry is only equal to Eq. (1.7) at high temperatures and/or low frequencies (ω), suggesting that $c^{\rm cl}_{\rm AB}(t)$ is not a good approximation to $c^0_{\rm AB}(t)$ away from the classical limit.

However, $c^0_{\rm AB}(t)$ is just one member of an entire class of quantum-mechanical correlation functions which have $c^{\rm cl}_{\rm AB}(t)$ as the classical limit. These 'lambda' correlation functions take the form

$$c^{\lambda}_{\rm AB}(t) = \frac{1}{Z}{\rm tr}\left[e^{-(\beta-\lambda)\hat{H}}\,\hat{A}\,e^{-\lambda\hat{H}}\,e^{i\hat{H}t/\hbar}\,\hat{B}\,e^{-i\hat{H}t/\hbar}\right], \tag{1.9}$$

for $0 \leq \lambda \leq \beta$, and so $\lambda = 0$ gives the standard quantum correlation function in Eq. (1.5). The symmetry properties discussed above are now useful for identifying which of these $c_{\mathrm{AB}}^{\lambda}(t)$ are promising candidates for approximation by $c_{\mathrm{AB}}^{\mathrm{cl}}(t)$. It turns out that if $\hat{A} = A(\hat{q})$ and $\hat{B} = B(\hat{q})$ then only the lambda correlation function with $\lambda = \beta/2$ is a real and even function of time. It can also be shown that this symmetry is sufficient to ensure that

$$C_{\mathrm{AB}}^{\beta/2}(-\omega) = C_{\mathrm{AB}}^{\beta/2}(\omega), \tag{1.10}$$

in agreement with Eq. (1.8). The classical correlation function therefore shares crucial symmetries with $c_{\mathrm{AB}}^{\beta/2}(t)$, which is reason to suppose that it might be more appropriate to associate $c_{\mathrm{AB}}^{\mathrm{cl}}(t)$ with $c_{\mathrm{AB}}^{\beta/2}(t)$ rather than with $c_{\mathrm{AB}}^{0}(t)$. Having done this, an approximation to the standard quantum correlation function can still be recovered using the exact frequency-domain relationship:

$$C_{\mathrm{AB}}^{0}(\omega) = e^{\beta\hbar\omega/2}\, C_{\mathrm{AB}}^{\beta/2}(\omega), \tag{1.11}$$

and the inverse of Eq. (1.6), i.e.,

$$c_{\mathrm{AB}}^{0}(t) = \int_{-\infty}^{\infty} d\omega\, e^{i\omega t}\, C_{\mathrm{AB}}^{0}(\omega). \tag{1.12}$$

The former expression (Eq. (1.11)) is obtained by evaluating the traces in $c_{\mathrm{AB}}^{0}(t)$ (Eq. (1.5)) and $c_{\mathrm{AB}}^{\beta/2}(t)$ (Eq. (1.9)) using the basis of energy eigenstates. If $c_{\mathrm{AB}}^{\mathrm{cl}}(t)$ is used as an approximation to $c_{\mathrm{AB}}^{\beta/2}(t)$ then Eq. (1.11) motivates going to the frequency domain and multiplying $C_{\mathrm{AB}}^{\mathrm{cl}}(\omega)$ by $D_{\mathrm{s}}(\omega) = e^{-\beta\hbar\omega/2}$ to produce a second classical approximation to $C_{\mathrm{AB}}^{0}(\omega)$ and thus, by Eq. (1.12), to $c_{\mathrm{AB}}^{0}(t)$. Unlike the direct classical approximation discussed above, the correlation function produced in this way satifies

the detailed-balance symmetry in Eq. (1.7) because

$$D_{\rm s}(-\omega) = e^{-\beta\hbar\omega}\, D_{\rm s}(\omega). \tag{1.13}$$

Thus, $D_{\rm s}(\omega)$ is one of the (many) 'detailed-balance correction factors' that are used to obtain an improved classical approximation to the standard quantum correlation function [30].

Yet another quantum-mechanical analogue of the classical correlation function is the 'Kubo' correlation function [31],

$$\tilde{c}_{\rm AB}(t) = \frac{1}{\beta}\int_0^\beta d\lambda\, c_{\rm AB}^{\lambda}(t), \tag{1.14}$$

which is just the average of the lambda correlation functions over the range $0 \leq \lambda \leq \beta$. This Kubo correlation function also shares symmetries with the classical correlation function, i.e. for position-dependent hermitian operators it is a real and even function of time [32] and its spectral representation ($\tilde{C}_{\rm AB}(\omega)$) is therefore a real and even function of frequency. As above, $\tilde{C}_{\rm AB}(\omega)$ can be related to $C^0_{\rm AB}(\omega)$ by evaluating the relevant correlation functions using the basis of energy eigenstates. The result is

$$C^0_{\rm AB}(\omega) = \frac{\beta\hbar\omega}{1 - e^{-\beta\hbar\omega}}\tilde{C}_{\rm AB}(\omega), \tag{1.15}$$

and therefore, if the classical correlation function is associated with the Kubo correlation function then the detailed-balance correction factor

$$D_{\rm ho}(\omega) = \frac{\beta\hbar\omega}{1 - e^{-\beta\hbar\omega}}, \tag{1.16}$$

gives a classical approximation to $C^0_{\rm AB}(\omega)$ (and thus $c^0_{\rm AB}(t)$) that satisfies the detailed-balance symmetry in Eq. (1.7) (because $D_{\rm ho}(-\omega) = e^{-\beta\hbar\omega}\, D_{\rm ho}(\omega)$). It should be

stressed that $D_{\mathrm{ho}}(\omega)$ is the exact conversion factor between the spectral representation of the Kubo correlation function ($\tilde{c}_{\mathrm{AB}}(t)$) and that of the standard quantum correlation function ($c^{0}_{\mathrm{AB}}(t)$), and thus the only approximation in this approach is that involved with using $c^{\mathrm{cl}}_{\mathrm{AB}}(t)$ in place of $\tilde{c}_{\mathrm{AB}}(t)$.

A serious limitation of the detailed-balance correction factor approach is that the absence of a unique $D(\omega)$ limits its predictive power. It is, in other words, difficult to know which correction factor is most accurate for a given application without having exact results (or experimental data) to compare to. However, strong support for associating $c^{\mathrm{cl}}_{\mathrm{AB}}(t)$ with the Kubo correlation function is drawn from observations that suggest that, of all the quantum-mechanical correlation functions, $\tilde{c}_{\mathrm{AB}}(t)$ is the closest relation of $c^{\mathrm{cl}}_{\mathrm{AB}}(t)$. Firstly, if the operators $\hat{A} = \hat{B} = \hat{q}$ are linear position operators, then the Kubo and classical correlation functions are identical for a harmonic potential [32]. Secondly, it is $\tilde{c}_{\mathrm{AB}}(t)$ that appears naturally in the quantum-mechanical version of linear-response theory and, furthermore, the expressions involving $\tilde{c}_{\mathrm{AB}}(t)$ are isomorphic with the classical expressions involving $c^{\mathrm{cl}}_{\mathrm{AB}}(t)$ [29]. It has been suggested that these are good enough reasons to stop searching for a better correction factor than $D_{\mathrm{ho}}(\omega)$ and to start looking for a better approximation to the Kubo correlation function than $c^{\mathrm{cl}}_{\mathrm{AB}}(t)$ [29]. That is exactly the aim of this thesis.

1.2 Path integral methods

Perhaps the most successful means of improving upon the description provided by classical molecular dynamics is the path-integral formulation of quantum statistical mechanics [4, 5]. This can be used to perform numerically exact calculations of the quantum *static* equilibrium properties of systems composed of up to 10^3 atoms [33]. Early path-integral simulations included a study of an electron solvated in liquid KCl [34] and an investigation of the difference in structure between liquid H_2O and D_2O [35]

– a quantity which vanishes within classical statistical mechanics. A derivation of the relevant path integral expressions will now be given since they are the foundations of the approximate *dynamical* method that is the subject of this thesis.

The starting point is the quantum-mechanical expression for a static property at canonical equilibrium

$$\langle A \rangle = \frac{1}{Z} \mathrm{tr}\left[e^{-\beta \hat{H}} \hat{A} \right], \tag{1.17}$$

where 'tr' indicates a trace,

$$Z = \mathrm{tr}\left[e^{-\beta \hat{H}} \right], \tag{1.18}$$

and $\hat{A}$ is an operator representing the quantity of interest. The Boltzmann operator $e^{-\beta \hat{H}}$ involves the Hamiltonian $\hat{H}$ where

$$\hat{H} = T(\hat{p}) + V(\hat{q}) = \frac{\hat{p}^2}{2m} + V(\hat{q}). \tag{1.19}$$

The symbol m, as usual, denotes the mass of the one-dimensional system. The key step involves recognising that one may split the Boltzmann operator into an arbitary number of identical factors and without approximation write

$$\langle A \rangle = \frac{1}{Z} \mathrm{tr}\left[(e^{-\beta_n \hat{H}})^n \hat{A} \right] = \frac{1}{Z} \mathrm{tr}\left[(e^{-\beta_n (\hat{T}+\hat{V})})^n \hat{A} \right], \tag{1.20}$$

in which $\beta_n = \beta/n$. The Trotter splitting

$$e^{-\beta_n (\hat{T}+\hat{V})} \approx e^{-\beta_n \hat{V}/2} e^{-\beta_n \hat{T}} e^{-\beta_n \hat{V}/2}, \tag{1.21}$$

becomes exact in the limit $n \to \infty$ ($\beta_n \to 0$) [36] and so an exact reformulation of Eq. (1.17) is

$$\langle A \rangle = \lim_{n \to \infty} \frac{1}{Z} \mathrm{tr}\left[(e^{-\beta_n \hat{V}/2} e^{-\beta_n \hat{T}} e^{-\beta_n \hat{V}/2})^n \hat{A} \right]. \tag{1.22}$$

In the case that the operator $\hat{A}$ is a function of only the position operator $\hat{q}$, an evaluation of the trace in the basis of position eigenstates gives

$$\langle A \rangle = \lim_{n\to\infty} \frac{1}{Z} \int dq_1 \, \langle q_1 | \, (e^{-\beta_n \hat{V}/2} e^{-\beta_n \hat{T}} e^{-\beta_n \hat{V}/2})^n | q_1 \rangle \, A(q_1). \tag{1.23}$$

The n Boltzmann factors are then separated by inserting between them $(n-1)$ complete sets of position eigenstates, i.e.,

$$\langle A \rangle = \lim_{n\to\infty} \frac{1}{Z} \int dq_1 \, dq_2 \, \ldots dq_n \, A(q_1) \left(\prod_{j=1}^{n} \left\langle q_j \left| e^{-\beta_n \hat{T}} \right| q_{j+1} \right\rangle e^{-\beta_n V(q_{j+1})} \right)_{q_{n+1}=q_1}, \tag{1.24}$$

where $\hat{V}|q\rangle = V(q)|q\rangle$ has been used. Note the cyclic path condition $q_{n+1} = q_1$; it is a consequence of the trace operation and will be implicit for expressions throughout this thesis. The matrix element in Eq. (1.24) is evaluated by inserting a complete set of momentum (and therefore kinetic energy) eigenstates to give

$$\left\langle q_j \left| e^{-\beta_n \hat{T}} \right| q_{j+1} \right\rangle = \int dp \, \langle q_j | p \rangle \, e^{-\beta_n p^2/2m} \, \langle p | q_{j+1} \rangle \, . \tag{1.25}$$

Since [37]

$$\langle q | p \rangle = \frac{1}{\sqrt{2\pi\hbar}} e^{+iqp/\hbar}, \tag{1.26}$$

Eq. (1.25) is just a Gaussian integral, and it can be done by completing the square to leave

$$\left\langle q_j \left| e^{-\beta_n \hat{T}} \right| q_{j+1} \right\rangle = \left(\frac{\beta_n m \omega_n^2}{2\pi} \right)^{1/2} e^{-\frac{1}{2}\beta_n \omega_n^2 (q_j - q_{j+1})^2}, \tag{1.27}$$

where $\omega_n = 1/\beta_n\hbar$. With this result, Eq. (1.24) is

$$\langle A \rangle = \lim_{n\to\infty} \frac{1}{Z} \left(\frac{\beta_n m \omega_n^2}{2\pi} \right)^{n/2} \int d\mathbf{q} \, e^{-\beta_n \phi_n(\mathbf{q})} A_n(\mathbf{q}), \tag{1.28}$$

where $\mathbf{q}$ is shorthand for the n-vector $(q_1, \ldots, q_n)^T$ and the effective potential energy

function is

$$\phi_n(\mathbf{q}) = \sum_{j=1}^{n} \left(\frac{1}{2} m\omega_n^2 (q_j - q_{j+1})^2 + V(q_j) \right). \tag{1.29}$$

Furthermore, the invariance of Eq. (1.24) to a cyclic relabelling of the position coordinates has been used to introduce the average

$$A_n(\mathbf{q}) = \frac{1}{n} \sum_{j=1}^{n} A(q_j). \tag{1.30}$$

The remarkable result is that the discretized path-integral expression for a quantum static property involves a *classical* configurational integral (Eq. (1.28)), albeit one involving an extended position space and an effective potential $\phi_n(\mathbf{q})$. This correspondence between the quantum statistical mechanics of a system and the classical statistical mechanics of an extended analogue is known as the 'classical isomorphism' [38].

The extended system is defined by the $2n$ terms that compose the effective potential $\phi_n(\mathbf{q})$ in Eq. (1.29). Each of the n 'slices' of the Boltzmann operator is connected to its immediate neighbours by the harmonic spring terms that arise from the factorized kinetic energy operators (see Eq. (1.27)). This results in a cyclic structure that can be thought of as a 'necklace' or 'ring polymer' composed of n linked 'beads'. The force constant of the kinetic spring terms ($m\omega_n^2$) is proportional to the mass and the square of the temperature, and so the kinetic springs become stiffer, and the n beads start to coincide, as the particle mass or the temperature is increased. In this way, the spatial delocalization of the ring polymer decreases until, in the classical limit, the necklace becomes the point particle of classical mechanics. In addition to the n 'kinetic spring' terms, each bead contributes an external potential term given by the value of the classical potential energy at its position.

As mentioned above, the cyclic structures occur because the trace in the expression

for static quantities leads to a sum over diagonal matrix elements, e.g. if $\hat{A} = A(\hat{q})$ in Eq. (1.17) then

$$\langle A \rangle = \frac{1}{Z} \mathrm{tr}\left[e^{-\beta \hat{H}} \hat{A} \right] = \frac{1}{Z} \int dq_1 \left\langle q_1 \left| e^{-\beta \hat{H}} \right| q_1 \right\rangle A(q_1). \tag{1.31}$$

The operator connecting the bra and ket of these matrix elements is the Boltzmann operator, and this is equivalent to the time-evolution operator $e^{-i\hat{H}t/\hbar}$ for an imaginary time $t = -i\beta\hbar$. The ring polymers are therefore discrete representations of paths which are cyclic in an imaginary time $\beta\hbar$. Moreover, the discretized expressions such as Eq. (1.28) are thermally-weighted sums over all such paths – hence the term 'path integral'.

These conceptual points aside, a few practical points about the path integral expression in Eq. (1.28) are now made:

(i) as derived above it is only valid for position-dependent operators (i.e. $A(\hat{q})$), although analogous expressions for momentum-dependent operators can also be developed,

(ii) it is only exact in the limit $n \to \infty$, although in practical applications it is generally found that the static property will converge at a finite n that is mass- and temperature-dependent,

(iii) it reduces to a purely classical configurational integral as $n \to 1$, and so the path-integral formalism provides a connection between exact quantum statistical mechanics and its classical limit.

Path-integral methods, based on expressions like Eq. (1.28), are routinely used to evaluate the static equilibrium properties of quantum systems. But what of the quantum *dynamical* properties of such systems? Linear-response theory relates them to

the quantum time correlation functions that were introduced in the previous section. The definitions of these correlation functions contain multiple operators of the form $e^{-\alpha\hat{H}}$, i.e. exponential functions of the Hamiltonian multiplied by some constant α. Some of these operators have a real α and are therefore imaginary-time evolution operators like the Boltzmann operator in the trace expression for quantum static properties Eq. (1.17). Others have an imaginary α and are therefore real-time evolution operators. In every case, a discretization procedure like the one presented above can be employed to produce a discrete path-integral expression for the quantum-mechanical correlation function [39]. For example, a path-integral discretization of $c^0_{\mathrm{AB}}(t)$ (Eq. (1.5)) leads to

$$c^0_{\mathrm{AB}}(t) = \lim_{n\to\infty} \frac{1}{Z} R_n(t) \int d\mathbf{q}\, e^{\frac{i}{\hbar} S_n(\mathbf{q},t)} \left[AB\right]_n(\mathbf{q},t), \tag{1.32}$$

where $R_n(t)$ is a complex normalization constant, $S_n(\mathbf{q},t)$ is a complex function of the position coordinates, and $\left[AB\right]_n(\mathbf{q},t)$ depends on the eigenvalues of $\hat{A}=A(\hat{q})$ and $\hat{B}=B(\hat{q})$ at the n bead positions. As for a static property (Eq. (1.28)), this is an integral over an n-dimensional position space but, in contrast, the integrand is now a complex function of the position vector $\mathbf{q}$.

The principal difficulty with expressions such as Eq. (1.32) is the fact that the integrands are oscillatory and become more so as the time t increases [11]. Many-dimensional integrals over oscillatory integrands are notoriously difficult to evaluate numerically and this has prevented any extensive use of real-time path integral techniques for calculating the time correlation functions of condensed-phase systems. Much effort has been invested in solving this 'dynamical sign problem' [40], and in certain model systems the calculations do become tractable because most of the integration can be done analytically [26]. Nevertheless, much work remains to be done before these methods can be applied more generally. The problematic nature of the real-time

path integral has lent emphasis to the search for approximate quantum-dynamical methods that are suitable for large and complex molecular systems. Some of these are summarized in the remaining sections of this chapter.

1.3 Semiclassical methods

A 'potentially practical' [41] way of dealing with the difficulties of the real-time path integral is to apply the stationary phase approximation [42, 43]. Indeed, this step leads to a family of approximate quantum-dynamical methods which become exact in the limit $\hbar \rightarrow 0$ and are therefore termed 'semiclassical'. A brief outline of these methods follows, for more detail see recent reviews and the references within [41, 42, 44]. In addition to the anticipated relief from the dynamical sign problem, the use of the stationary phase approximation has another favourable consequence. In the path-integral sum over all paths, it is the classical ones which have stationary phases and so these semiclassical methods are based upon nothing more complicated than classical trajectories. This has both practical and conceptual advantages: (a) the effort required to compute a classical trajectory can be made to scale linearly with system size, (b) highly efficient techniques for propagating classical trajectories (developed for use in molecular dynamics simulations) already exist, and (c) classical trajectories give an intuitive picture of the dynamical process.

The initial result of applying the stationary phase approximation to real-time path integrals are expressions which involve a sum over all classical trajectories which satisfy a set of double-ended boundary conditions [42, 45, 46]. Some of these boundary conditions are constraints on the initial phase-space coordinates of the trajectories and the rest relate to the final coordinates. Finding every qualifying trajectory is an extremely challenging task in large systems, but the problem can be transformed so that all the boundary conditions are applied at the initial time [41, 47]. The resulting expressions

are examples of semiclassical initial-value representations (SC-IVRs), a class of semiclassical methods which involve integration over an entire initial phase-space rather than the original but equivalent sum over a restricted set of trajectories.

A practical evaluation of a SC-IVR requires propagation of classical trajectories from initial phase-space coordinates. Of course, a purely classical trajectory contains no information about quantum-dynamical effects but these semiclassical methods dress the classical trajectory with a phase factor $e^{iS/\hbar}$ in which S is the classical action [41]. It is the interference between the phase factors arising from different trajectories that provides the approximate description of quantum-mechanical effects such as tunneling and zero-point energy. However, this interference is also responsible for causing the phase-space integrands in SC-IVR correlation functions to be oscillatory. Thus a version of the dynamical sign problem remains in these semiclassical methods and has prevented their wide-spread adoption.

A great deal of work has been directed towards taming the semiclassical sign problem [41, 42]. The result is a set of time-dependent semiclassical methods whose members capture quantum interference effects to a greater or lesser extent. In this context, the interference effects are both a blessing and a curse – employing additional approximations in order to suppress the sign problem invariably results in a poorer description of the quantum-mechanical effects. One strategy involves a spatially-local 'pre-averaging' of the integrand so as to remove the rapid oscillations [48–50]. The costs associated with this approach are the introduction of adjustable parameters into the calculation and a certain loss of accuracy. Furthermore, it is not yet entirely clear that this procedure leads to feasible calculations for large and realistic molecular systems.

In the SC-IVR picture, the forward ($e^{-i\hat{H}t/\hbar}$) and backward ($e^{+i\hat{H}t/\hbar}$) evolution operators in the quantum correlation functions of Section 1.1 result in classical trajectories

with sections that are propagated forwards and backwards in time. A second strategy for suppressing the semiclassical sign problem involves combining these forward and backward sections so that the associated phase factors approximately cancel each other out. The straightforward implementation of this approach results in the 'forward-backward' semiclassical methods [51], which can also be obtained by the application of a further stationary phase approximation to a full SC-IVR [23]. However, remnants of the sign problem persist and further applications to realistic systems will be required to establish the true utility of these forward-backward methods.

A physically-motivated approach for smoothing the double phase-space integrand exploits the fact that an SC-IVR integral is dominated by forward-backward trajectory pairs that are very close to each other [42]. One may focus on these pairs by changing the integration variables from the initial values of the forward and backward paths, (p_f,q_f) and (p_b,q_b), to the corresponding sum and difference coordinates ($\bar{p} = \frac{1}{2}(p_f+p_b)$, $\Delta p = p_b - p_f$ and $\bar{q} = \frac{1}{2}(q_f + q_b)$, $\Delta q = q_b - q_f$). Expanding the terms in the integrand to first order in the difference variables leads to the classical Wigner model (CWM) [14, 52] for a time correlation function

$$c_{\mathrm{AB}}^{\mathrm{cw}}(t) = \frac{1}{(2\pi\hbar)Z}\int dp_0 \int dq_0 \;\; [e^{-\beta\hat{H}}\hat{A}]_{\mathrm{w}}(p_0,q_0)\,[B]_{\mathrm{w}}(p_t,q_t), \tag{1.33}$$

in which the Wigner transform [53] of an operator is defined as

$$[\hat{\Omega}]_{\mathrm{w}}(p,q) = \int dy\, e^{-ipy/\hbar} \left\langle q + y/2 \left| \hat{\Omega} \right| q - y/2 \right\rangle, \tag{1.34}$$

and the time-evolved phase-space coordinates (p_t, q_t) are obtained using the classical equations of motion (Eq. (1.3)). This expression, which is also known as the linearised SC-IVR or LSC-IVR, can also be obtained by other routes [15, 52, 54].

The neglect of interference arising from trajectories with distinct forward and back-

ward paths means that the CWM is incapable of describing coherent quantum dynamical effects [55]. This is not a serious shortcoming if one is interested in the many condensed-phase dynamical processes for which coherent quantum motion is 'washed-out' of the relevant quantum correlation function by the thermal averaging over the states of the environment. The resulting rapid regression behaviour of condensed-phase correlation functions is therefore key to the accuracy of the CWM, as it is to many other approximate approaches to calculating the quantum-dynamical properties of large molecular systems. It will be an important consideration later in this thesis.

The CWM in Eq. (1.33) has the same form as a classical time correlation function (Eq. (1.4)), and in fact the only difference is the presence of a Wigner distribution for the initial coordinates of the classical trajectories. The evaluation of the Wigner distribution is a demanding part of the CWM calculation because it has to be calculated via Eq. (1.34). This Fourier integral has an oscillatory integrand and therefore even the drastic linearization procedure used to derive the CWM does not fully eradicate the semiclassical sign problem.

In real systems Eq. (1.34) must be evaluated numerically – a task which requires an effort that grows exponentially with the size of the system. In order to avoid this prohibitive scaling, some authors have adopted harmonic approximations to the potential energy surface of the system so that the Wigner transform can be evaluated analytically [14, 16, 56]. For points on the potential energy surface which have imaginary harmonic frequencies (i.e. potential energy barriers), this approach fails below a (frequency-dependent) critical temperature because the momentum distribution becomes undefined [14, 16]. Despite this, the CWM has been successfully applied to a series of problems that involve no long-time quantum coherence effects [14, 16, 57], and it represents one of the more practical schemes with which to go beyond a purely classical description of condensed-phase dynamical processes.

1.4 Centroid molecular dynamics

The semiclassical methods of the previous section are derived by making approximations to the path-integral expressions for *dynamical* quantities. Conversely, the alternative approach outlined in this section has its foundations in the path-integral treatment of quantum *static* properties [19].

It has long been realised that the framework of classical statistical mechanics can be used to provide an exact formulation of quantum static properties if the classical potential is replaced by the following effective quantum potential [4, 58]:

$$V_c(q_c) = -\frac{1}{\beta} \ln \rho_c(q_c). \tag{1.35}$$

In this expression, $\rho_c(q_c)$ is given by an imaginary-time path-integral sum over all cyclic paths ($q(\tau)$) with a mean position equal to q_c. This mean position is called the centroid and is defined as

$$q_0 = \frac{1}{\hbar\beta} \int_0^{\hbar\beta} d\tau \, q(\tau). \tag{1.36}$$

The continuous path-integral form of $\rho_c(q_c)$ is therefore

$$\rho_c(q_c) = \sqrt{\frac{2\pi\hbar^2\beta}{m}} \oint Dq(\tau) \, \delta(q_c - q_0) e^{-S[q(\tau)]/\hbar}, \tag{1.37}$$

where $\delta(q_c - q_0)$ is a Dirac delta function and $S[q(\tau)]$ is the imaginary-time action along the cyclic path [39]. In this formulation of quantum statistical mechanics the coordinate q_c that takes on a role analogous to the position of the point particle in classical statistical mechanics.

In terms of $\rho_c(q_c)$, the exact quantum-mechanical partition function is

$$Z = \left(\frac{m}{2\pi\hbar^2\beta}\right)^{1/2} \int dq \, \rho_c(q), \tag{1.38}$$

and therefore $\rho_c(q_c)$ is a classical-like distribution function for the centroid position. In principle, the exact quantum dynamics associated with this centroid distribution function can be evolved using the quantum Liouville equation. In practice, evaluating such dynamics requires a prohibitive computational effort in more than a few dimensions [20] and so they do not form the basis of a feasible scheme for the calculation of condensed-phase correlation functions.

However, the 'centroid' formalism can be used to develop an approximate approach to the calculation of dynamic quantities. Instead of evaluating the true quantum dynamics of the centroid density, the centroid molecular dynamics (CMD) method evolves the classical equations of motion for the centroid on the effective quantum potential $V_c(q)$ [17, 19, 20]. The resulting dynamical information can then be used to construct an approximation to the Kubo-transformed correlation function (Eq. (1.14)) as long as one of the operators involved is a linear function of position (or momentum) [20]. This CMD approximation to the (linear-operator) correlation function is exact at $t=0$, for all times in a harmonic potential, and in the classical limit.

The CMD equations of motion involve the force exerted on the centroid by the effective quantum potential, i.e.,

$$F_c(q_c) = -\frac{dV_c(q_c)}{dq_c} = -\frac{1}{\beta\rho_c(q_c)}\frac{d\rho_c(q_c)}{dq_c}. \tag{1.39}$$

The force is thus given in terms of an imaginary-time path integral – the fact that it is needed at each time step of the centroid trajectory means that CMD calculations require significantly more effort than classical molecular dynamics simulations. One of the most efficient ways of obtaining the path-integral sum over paths required in Eq. (1.39) is to propagate the higher normal-modes of the ring polymer along with the centroid (which is the zero-frequency normal mode) [18]. The trick is to choose the

mass of the non-centroid normal modes to be so small that their dynamics occur on a far shorter timescale than that of the centroid. An adiabatic separation then ensures that the relevant (centroid-constrained) cyclic paths are explored at each (pseudo-stationary) centroid position and therefore that the effective quantum potential is accurately reproduced. The cost is that the timestep used to calculate the dynamics must now be matched to the fast normal modes rather than to the slower (physical) timescale of the centroid dynamics. This is a key difference between this 'adiabatic CMD' approach [18] and the new approximate dynamical method that is introduced in the next chapter.

Chapter 2

Ring polymer molecular dynamics

The previous chapter outlined a number of existing methods that can be used to study the (approximate) quantum dynamics of condensed-phase molecular systems. This chapter introduces a recently-developed alternative that is based upon an approximate model for the Kubo correlation function in Eq. (1.14). The chapter begins with a discussion of the foundations of the new method, which lie in the molecular dynamics approach to evaluating the discretized path-integral expressions of Section 1.2. It then presents the approximate model and certain arguments in justification of it. The resulting method is then applied to some one-dimensional test problems, allowing an initial assessment of its performance to be made. Much of this work appears in Ref. [32].

2.1 Path integral molecular dynamics

The previous chapter derived a path-integral expression for the static properties of a system at canonical equilibrium (Eq. (1.28)). A restatement of this result is

$$\langle A \rangle = \lim_{n\to\infty} \langle A \rangle_n \,, \tag{2.1}$$

where

$$\langle A \rangle_n = \frac{1}{Z_n} \left(\frac{\beta_n m \omega_n^2}{2\pi} \right)^{n/2} \int d\mathbf{q}\, e^{-\beta_n \phi_n(\mathbf{q})}\, A_n(\mathbf{q}). \tag{2.2}$$

The notation is retained from the earlier chapter, i.e. $\phi_n(\mathbf{q})$ is the ring-polymer potential energy of Eq. (1.29), $\omega_n = 1/\beta_n\hbar$ where $\beta_n = \beta/n$, and

$$Z_n = \left(\frac{\beta_n m \omega_n^2}{2\pi} \right)^{n/2} \int d\mathbf{q}\, e^{-\beta_n \phi_n(\mathbf{q})} \tag{2.3}$$

is the n-bead ring-polymer approximation to the canonical partition function.

As written, Eq. (2.2) could be evaluated using path-integral Monte Carlo (PIMC) sampling [59–62]. An expression suitable for evaluation by path-integral molecular dynamics (PIMD) techniques would require a momentum to be associated with each ring-polymer bead so that some form of dynamics could be used to sample the position space $\mathbf{q}$. To achieve this, the identity

$$1 = \left(\frac{\beta_n}{2\pi m'} \right)^{n/2} \int d\mathbf{p} \exp \left[-\beta_n \sum_{j=1}^{n} p_j^2 / 2m' \right] \tag{2.4}$$

is inserted into Eq. (2.2) to obtain [34]

$$\langle A \rangle_n = \frac{1}{(2\pi\hbar)^n Z_n} \left(\frac{m}{m'} \right)^{n/2} \int d\mathbf{p} \int d\mathbf{q}\, e^{-\beta_n H_n'(\mathbf{p},\mathbf{q})} A_n(\mathbf{q}), \tag{2.5}$$

where the ring-polymer Hamiltonian is

$$H_n'(\mathbf{p},\mathbf{q}) = \sum_{j=1}^{n} \left(\frac{p_j^2}{2m'} + \frac{1}{2} m \omega_n^2 (q_j - q_{j+1})^2 + V(q_j) \right), \tag{2.6}$$

and, as always, $q_{n+1} = q_1$. The PIMD technique uses the classical dynamics of the

ring-polymer Hamiltonian, i.e.,

$$\dot{q}_j = +\frac{\partial H'_n}{\partial p_j} = \frac{p_j}{m'}, \tag{2.7}$$

$$\dot{p}_j = -\frac{\partial H'_n}{\partial q_j} = -m\omega_n^2 \left[2q_j - q_{j+1} - q_{j-1}\right] - \frac{dV(q_j)}{dq_j}, \tag{2.8}$$

to move trajectories through, and thus sample, the ring-polymer phase-space [34, 39]. Averaging the property $A_n(\mathbf{q})$ (Eq. (1.30)) over all the phase-space points visited by these PIMD trajectories then leads to the ensemble-averaged static quantity $\langle A \rangle_n$. In this context, the 'classical isomorphism' is the observation that (in the limit $n \to \infty$) Eq. (2.5) gives the exact quantum static property in terms of a standard average over a classical (albeit extended) phase-space. The remainder of this section discusses some practical matters involved in evaluating this average.

First, a problem: the PIMD equations of motion generate trajectories which can only explore the regions of phase-space that are consistent with their fixed energy, and they therefore fail to sample the entire canonical distribution. These fixed-energy (micro-canonical) trajectories must be modified if they are to produce a fixed-temperature (canonical) distribution. A popular strategy for achieving this involves linking additional vibrational modes onto the physical degrees of freedom of the system [63–65]. The ficticious 'thermostat' modes are coupled to the momenta of the physical degrees of freedom and regulate the kinetic energy fluctuations to produce constant-temperature trajectories.

It turns out that degrees of freedom which are dominated by harmonic motion require the use of not one but a chain of thermostat modes [65]. Since the harmonic kinetic spring terms play an important part in the ring-polymer dynamics, a separate thermostat chain would be required for each physical degree of freedom. This approach to constant-temperature ring-polymer trajectories would therefore require solving the

equations of motion for a significantly extended system. Furthermore, although the canonical distribution is rigorously reproduced with thermostat chains of sufficient length [66], the relationship between the dynamics of the thermostatted system and the unthermostatted system is not clear. This last point is of limited relevance to the calculation of static properties but it will be of importance if, as in the next section, dynamical information is to be extracted from the trajectories.

An alternative technique for generating a canonical distribution from microcanonical trajectories involves periodically resampling their momenta from the Maxwell distribution contained in $e^{-\beta_n H'_n}$ [67, 68]. The physical basis of this approach is that it mimics inelastic collisions with an external heat bath of fixed temperature. In addition to generating constant-temperature trajectories this approach also alleviates a problem which was identified in some of the earliest work on applying molecular dynamics techniques to the evaluation of the discretized path integral expressions [34, 68]. Specifically, as the number of beads in the ring-polymer is increased the harmonic spring terms become increasingly stiff and start to dominate the dynamics. It is well-known that microcanonical trajectories in such systems may not even explore all of the *fixed-energy* subspace, i.e. on the timescale accessible to a computer simulation they can be 'nonergodic' [68]. Thus,

$$\lim_{M\to\infty} \frac{1}{M} \sum_{j=1}^{M} A_n(\mathbf{q}\,; t_j) \;\neq\; \frac{1}{\Omega(E)} \int d\mathbf{p} \int d\mathbf{q}\; \delta(E - H_n(\mathbf{p},\mathbf{q}))\, A_n(\mathbf{q}), \qquad (2.9)$$

where $t_j = j\Delta t$ for some time interval Δt along a microcanonical trajectory with fixed energy E and where $\Omega(E)$ is the microcanonical partition function at that energy. The momenta resampling scheme not only allows the trajectory to access regions of phase-space with different energies but also disrupts this nonergodic behaviour [69].

The last consideration to be discussed here is the choice of the PIMD mass parameter

m'. The left-hand side of Eq. (2.5) is formally independent of this mass since for any m' the momentum integral can be performed analytically to yield the position-space path integral expression of Eq. (2.2). However, the choice of the mass parameter will affect the efficiency of the molecular dynamics sampling since it governs the rate at which the trajectory moves through the phase-space. A high-mass trajectory will move relatively slowly and will take a long time to sample the whole phase-space. Conversely, a low-mass trajectory will require short, and thus many, time-steps to converge the sampling. In early work, Parrinello and Rahman made the arbitrary choice $m' = 1\,\mathrm{u}$, which is intermediate between the physical masses in their application ($m_e \approx 0.0005\,\mathrm{u}$ $m_{\mathrm{K^+/Cl^-}} \approx 40\,\mathrm{u}$) [34].

In the two decades since its conception, developments that tackle the nonergodicity problem [70] and new multiple-time-step integrators capable of efficiently treating the many timescales in the ring-polymer dynamics [71] have made PIMD methods competitive with modern PIMC techniques. Along with PIMC, it is one of the few exact approaches for studying the quantum mechanics of large molecular systems [23]. It is of course restricted to calculating the *static* properties of such systems, and uses the dynamics only as a tool to sample the phase-space. Early studies stressed the fact that the classical dynamics of the Hamiltonian H'_n (involving the arbitrary mass m') are not the true quantum dynamics of the system:

> "Strictly speaking, the time trajectories thus obtained have no real meaning and are a mere computational device for exploring the properties of $[\phi_n]$ at various temperature and density conditions."
>
> *Parrinello and Rahman, 1984* [34]

This statement is of course correct. However, the next section will show that careful use of the dynamical information generated by ring-polymer trajectories may indeed allow

the construction of an approximate model for quantum time correlation functions, thus permitting the study of quantum dynamical processes in complex molecular systems.

2.2 Ring polymer molecular dynamics

The ring polymer molecular dynamics (RPMD) method generalizes the PIMD approach so that, in addition to exact quantum static properties, one can also calculate approximate quantum dynamical properties of large and complex molecular systems [32].

The basis of this new approach is the concept that ring-polymer trajectories *can* be made to yield meaningful, but approximate, dynamical information if certain steps are taken. First, a particular choice of the PIMD mass parameter

$$m' = m, \tag{2.10}$$

is made so as to ensure that the motion of each individual ring-polymer bead over the potential energy surface would be a genuine classical trajectory for the system were it not for the kinetic spring terms. Note that this choice of mass causes the prefactor in Eq. (2.5) to simplify, and so the n-bead PIMD expression for a static property is now just the classical phase-space average for the n-bead ring polymer system

$$\langle A \rangle_n = \frac{1}{(2\pi\hbar)^n Z_n} \int d\mathbf{p} \int d\mathbf{q}\, e^{-\beta_n H_n(\mathbf{p},\mathbf{q})} A_n(\mathbf{q}), \tag{2.11}$$

where the ring-polymer Hamiltonian has become

$$H_n(\mathbf{p},\mathbf{q}) = \sum_{j=1}^{n} \left(\frac{p_j^2}{2m} + \frac{1}{2} m\omega_n^2 (q_j - q_{j+1})^2 + V(q_j) \right). \tag{2.12}$$

After this choice of mass has been made, a second step involves using the ring-polymer trajectories to obtain approximate dynamical information in an optimal way. Now, the discussion thus far has involved only static properties, but a connection to dynamical properties can be made by recognising that at t=0 the correlation functions are themselves just static ensemble averages, albeit ones involving two operators. The following are just two of the possible double-operator generalizations of the PIMD expression above (Eq. (2.11)):

$$\frac{1}{(2\pi\hbar)^n Z_n} \int d\mathbf{p} \int d\mathbf{q}\, e^{-\beta_n H_n(\mathbf{p},\mathbf{q})} (AB)_n(\mathbf{q}), \tag{2.13}$$

and

$$\frac{1}{(2\pi\hbar)^n Z_n} \int d\mathbf{p} \int d\mathbf{q}\, e^{-\beta_n H_n(\mathbf{p},\mathbf{q})} A_n(\mathbf{q}) B_n(\mathbf{q}). \tag{2.14}$$

Every term here has been defined previously, but for clarity note that

$$(AB)_n(\mathbf{q}) = \frac{1}{n} \sum_{j=1}^{n} A(q_j) B(q_j). \tag{2.15}$$

The first construct (Eq. (2.13)) is easily recognised as the n-bead approximation to the standard correlation function at t=0 since

$$c_{\mathrm{AB}}^0(0) = \langle AB \rangle = \lim_{n\to\infty} \langle AB \rangle_n\,, \tag{2.16}$$

and using Eq. (2.11) for $\langle AB \rangle_n$ gives Eq. (2.13).

Less obviously, the second construct (Eq. (2.14)) is the n-bead approximation to the Kubo-transformed correlation function at t=0. To see this, begin by rewriting the double sum in Eq. (2.14):

$$A_n(\mathbf{q}) B_n(\mathbf{q}) = \frac{1}{n^2} \sum_{j,k=1}^{n} A(q_j) B(q_k) = \frac{1}{n^2} \sum_{j,k=1}^{n} A(q_{k+j-1}) B(q_k). \tag{2.17}$$

Since the n beads are equivalent (in the sense that a cyclic relabelling leaves the phase-space integral of Eq. (2.14) unchanged) the average over k may be removed. Setting k=1 leaves

$$\frac{1}{(2\pi\hbar)^n Z_n} \int d\mathbf{p} \int d\mathbf{q}\, e^{-\beta_n H_n(\mathbf{p},\mathbf{q})} \left(\frac{1}{n} \sum_{j=1}^{n} A(q_j) \right) B(q_1), \tag{2.18}$$

then taking the sum over j outside the integral gives

$$\frac{1}{n} \sum_{j=1}^{n} \left(\frac{1}{(2\pi\hbar)^n Z_n} \int d\mathbf{p} \int d\mathbf{q}\, e^{-\beta_n H_n(\mathbf{p},\mathbf{q})} A(q_j)\, B(q_1) \right). \tag{2.19}$$

The summand can be recognised as an n-bead discretization of the t=0 value of the lambda correlation function ($c_{\mathrm{AB}}^{\lambda}(0)$ in Eq. (1.9)) where $\lambda = (j-1)\beta_n$. Thus, the sum is just a discretization of the Kubo-transformed correlation function. To see this, consider the $n \to \infty$ limit of Eq. (2.19) – the variable $\lambda = (j-1)\beta_n$ takes on the continuous range of values $0 \leq \lambda \leq \beta$ and so the sum can be replaced by an integral. The previous expression is then

$$\frac{1}{\beta} \int_0^{\beta} d\lambda\, c_{\mathrm{AB}}^{\lambda}(0), \tag{2.20}$$

which is the $t \to 0$ limit of the Kubo-transformed correlation function $\tilde{c}_{\mathrm{AB}}(t)$ defined in Eq. (1.14).

Now, the RPMD strategy for extending either of these double-operator constructs to nonzero times would involve using the classical dynamics of the ring-polymer Hamiltonian $H_n(\mathbf{p},\mathbf{q})$ to make an evaluation of the function $B(\mathbf{q})$ at the desired time t. The underlying classical dynamics would give the resulting correlation functions certain similarities with the purely classical correlation function (Eq. (1.4)). This suggests that the RPMD strategy is best used to generalize Eq. (2.14), rather than Eq. (2.13), to $t \neq 0$ since, as discussed previously, the Kubo correlation function has more classical-like

properties than the other quantum correlation functions. Specifically, it shares time symmetries with $c_{\mathrm{AB}}^{\mathrm{cl}}(t)$ and it is the Kubo correlation function that arises naturally in the quantum generalisation of linear response theory [29].

These considerations lead to the following definition of the RPMD approximation to the Kubo-transformed quantum correlation function [32]:

$$\tilde{c}_{\mathrm{AB}}(t) \approx \lim_{n\to\infty} \langle A(0)B(t)\rangle_n^{\mathrm{rp}}\,, \tag{2.21}$$

where the n-bead ring-polymer correlation function is

$$\langle A(0)B(t)\rangle_n^{\mathrm{rp}} = \frac{1}{(2\pi\hbar)^n Z_n} \int d\mathbf{p}_0 \int d\mathbf{q}_0\, e^{-\beta_n H_n(\mathbf{p}_0,\mathbf{q}_0)} A_n(\mathbf{q}_0) B_n(\mathbf{q}_t). \tag{2.22}$$

This expression is exact for t=0, and for all other times the position coordinates $\mathbf{q}_t$ are obtained by integration of the ring-polymer equations of motion

$$\dot{q}_j = \frac{p_j}{m} \quad ; \quad \dot{p}_j = -m\omega_n^2\,[2q_j - q_{j+1} - q_{j-1}] - \frac{dV(q_j)}{dq_j}. \tag{2.23}$$

This time evolution and the phase-space integral of Eq. (2.22) can be evaluated simultaneously using the PIMD techniques that were introduced in the previous section. Since the RPMD model is developed from the discretized path-integral expression in Eq. (1.28) it inherits the formal limitation to position-dependent operators ($\hat{A}=A(\hat{q})$ and $\hat{B}=B(\hat{q})$). However, it will become clear that many correlation functions which involve momentum-dependent operators (e.g. velocity autocorrelation functions) can be expressed as time derivatives of position-dependent correlation functions, and are thus accessible to RPMD [21].

The difference between PIMD and RPMD is that in the latter method information from distinct times along the ring-polymer trajectory is correlated (and averaged) to

characterise the regression of spontaneous fluctuations in, and thus the linear-response dynamic properties of, the system. Of course it must be stressed that the classical dynamics of the ring-polymer trajectories have no general equivalence to the true quantum dynamics of the system. An obvious deficiency is the lack of any phase information and the associated inability to describe quantum interference phenomena [41]. Despite this, the next section analyses various properties of the RPMD model and finds reason to believe that it may be a justifiable approximation in some circumstances.

2.3 Properties of the RPMD model

The development presented in the previous section does not constitute a derivation of the RPMD model. It is instead a heuristic argument and as a result the precise nature of the approximation remains undefined. This makes the analysis of the properties of the model an important step in understanding when the method is (and is not) applicable.

2.3.1 Limits

The RPMD approximation is equal to the Kubo-transformed quantum correlation function in three important limits.

A. The time-zero limit.

At t=0 there is no need to invoke the dynamical approximation. The RPMD model reduces to a PIMD expression (Eq. (2.14)) which, in the limit $n \rightarrow \infty$, is the exact time-zero value of $\tilde{c}_{\mathrm{AB}}(t)$. A consequence of this, which will be illustrated later in this chapter, is that numerically-converged RPMD correlation functions 'start off' at the correct value. The same cannot always be said of the correlation functions of other approximate quantum dynamical methods, e.g. the classical Wigner model (CWM)

is not exact at t=0 if a harmonic approximation to the potential is used [14], nor is centroid molecular dynamics (CMD) if both operators $\hat{A}$ and $\hat{B}$ are nonlinear functions of the position [20].

B. The classical limit.

In the classical limit all quantum-mechanical effects vanish and the exact $\tilde{c}_{\mathrm{AB}}(t)$ tends to $c_{\mathrm{AB}}^{\mathrm{cl}}(t)$. In the RPMD model the kinetic springs stiffen (ω_n=$1/\beta_n\hbar \to \infty$) and the ring polymers collapse to point particles. As a result, a single ring-polymer bead (n=1) is sufficient to converge the path-integral statistical mechanics. It is not difficult to see that for n=1 the RPMD correlation function (Eq. (2.22)) also tends to $c_{\mathrm{AB}}^{\mathrm{cl}}(t)$, and is therefore exact in this limit.

C. The 'harmonic system plus linear operator' limit.

If the potential energy function is harmonic and the correlated operators are linear functions of $\hat{q}$, i.e. if

$$V(\hat{q}) = \frac{1}{2}m\omega^2\hat{q}^2, \tag{2.24}$$

and

$$A(\hat{q}) \text{ and/or } B(\hat{q}) = a\hat{q} + b, \tag{2.25}$$

where a and b are arbitrary constants, then the RPMD model gives the exact quantum Kubo-transformed correlation function. A proof of this concludes the current subsection.

First consider the exact result for the case $\hat{A}$=$\hat{B}$=$\hat{q}$. The trace in $\tilde{c}_{\mathrm{qq}}(t)$ (see Eq. (1.14))

can be evaluated in the basis of the energy eigenstates ($\hat{H}|j\rangle=E_j|j\rangle$) to give

$$\begin{aligned}\tilde{c}_{\mathrm{qq}}(t) &= \frac{1}{Z}\sum_j e^{-\beta E_j}\,|\langle j\,|\hat{q}|\,j\rangle|^2 \\ &+ \frac{1}{Z}\sum_{j\neq k} e^{-\beta E_j}\,|\langle j\,|\hat{q}|\,k\rangle|^2\, e^{-i(E_j-E_k)t/\hbar}\left(\frac{e^{\beta(E_j-E_k)}-1}{\beta(E_j-E_k)}\right),\end{aligned} \tag{2.26}$$

after taking the integral over λ. In a harmonic oscillator

$$\langle j\,|\hat{q}|\,k\rangle = \frac{1}{\sqrt{2m\omega^2}}\left[\delta_{j,k+1}\sqrt{(k+1)\hbar\omega}+\delta_{j,k-1}\sqrt{k\hbar\omega}\right], \tag{2.27}$$

which shows that $\hat{q}$ only connects adjacent energy eigenstates in this system. The first term in Eq. (2.26) is therefore zero. On substituting Eq. (2.27) into the second, the sum over j is reduced to the two terms with $E_j = E_k \pm \hbar\omega$. Some manipulation then leads to

$$\begin{aligned}\tilde{c}_{\mathrm{qq}}(t) &= \left(\frac{1}{Z}\sum_k e^{-\beta E_k}\left[\frac{\hbar(k+1)}{2m\omega}+e^{\beta\hbar\omega}\frac{\hbar k}{2m\omega}\right]\frac{1-e^{-\beta\hbar\omega}}{\beta\hbar\omega}\right)\cos(\omega t), \\ &= \tilde{c}_{\mathrm{qq}}(0)\cos(\omega t).\end{aligned} \tag{2.28}$$

This result shows that the exact Kubo-transformed correlation function $\tilde{c}_{\mathrm{qq}}(t)$ contains just a single frequency component at the natural frequency of the harmonic oscillator.

Now consider the n-bead RPMD approximation to the position-position correlation function,

$$\langle q(0)q(t)\rangle_n^{\mathrm{rp}} = \frac{1}{(2\pi\hbar)^n Z_n}\int d\mathbf{p}_0\int d\mathbf{q}_0\, e^{-\beta_n H_n(\mathbf{p}_0,\mathbf{q}_0)} q_c(\mathbf{q}_0)q_c(\mathbf{q}_t), \tag{2.29}$$

in which q_c is the centroid of the ring-polymer position coordinates,

$$q_c = \frac{1}{n}\sum_{j=1}^{n} q_j. \tag{2.30}$$

An evaluation of this correlation function requires the time-evolved centroid $q_c(\mathbf{q}_t)$, which is obtained by integrating the equations of motion

$$\dot{q}_c = \frac{1}{n}\sum_{j=1}^{n}\dot{q}_j = \frac{1}{n}\sum_{j=1}^{n}\frac{p_j}{m} = \frac{p_c}{m}, \tag{2.31}$$

$$\dot{p}_c = \frac{1}{n}\sum_{j=1}^{n}\dot{p}_j = -\frac{1}{n}\sum_{j=1}^{n}\frac{\partial\phi_n(\mathbf{q})}{\partial q_j} = -\frac{1}{n}\sum_{j=1}^{n}m\omega^2 q_j = -m\omega^2 q_c, \tag{2.32}$$

where p_c is the centroid momentum, $\phi_n(\mathbf{q})$ is the ring-polymer potential energy function and the harmonicity of the external potential has been used. Note that in the third equality of the last equation all forces arising from the kinetic spring terms have cancelled out. This cancellation, which will occur whether the potential is harmonic or not, means that the time evolution of the centroid coordinates is less oscillatory than that of the individual ring-polymer beads. The closed-form solution of Eq. (2.31) and Eq. (2.32) is

$$q_c(\mathbf{q}_t) = q_c(\mathbf{q}_0)\cos(\omega t) + \frac{p_c(\mathbf{p}_0)}{m\omega}\sin(\omega t). \tag{2.33}$$

On substitution of this expression into the ring-polymer phase-space average of Eq. (2.29) the integral over the $\sin(\omega t)$ term vanishes because that integrand is antisymmetric in $p_c(\mathbf{p}_0)$. Therefore

$$\langle q(0)q(t)\rangle_n^{\mathrm{rp}} = \left(\frac{1}{(2\pi\hbar)^n Z_n}\int d\mathbf{p}_0\int d\mathbf{q}_0\, e^{-\beta_n H_n(\mathbf{p}_0,\mathbf{q}_0)}q_c(\mathbf{q}_0)q_c(\mathbf{q}_0)\right)\cos(\omega t). \tag{2.34}$$

The integral inside the bracket is just the t=0 RPMD correlation function. It has already been established that the RPMD model is exact at time-zero if the number of ring-polymer beads is sufficiently large. Thus, in the limit $n\to\infty$ the bracket becomes exactly $\tilde{c}_{\mathrm{qq}}(0)$ and (as was to be proved) the RPMD model generates the exact Kubo-transformed correlation function (Eq. (2.28)) in the case of a harmonic potential and linear operators. In fact, the RPMD model is exact for all times in a harmonic system

even if one of the operators ($\hat{A}$,$\hat{B}$) is nonlinear [32].

2.3.2 Symmetries

As well as sharing certain limits with the exact $\tilde{c}_{\rm AB}(t)$, the RPMD model will now be shown to have a number of the same symmetries. The exact $\tilde{c}_{\rm AB}(t)$ is restated here as

$$\tilde{c}_{\rm AB}(t) = \frac{1}{\beta Z}\int_0^\beta d\lambda\, {\rm tr}\Big[e^{-(\beta-\lambda)\hat{H}}\,\hat{A}\,e^{-\lambda\hat{H}}\,e^{+i\hat{H}t/\hbar}\,\hat{B}\,e^{-i\hat{H}t/\hbar}\Big]. \tag{2.35}$$

Because the trace operation is invariant to a cyclic permutation of the operators within it (i.e. ${\rm tr}[\hat{X}\hat{Y}\hat{Z}] = {\rm tr}[\hat{Z}\hat{X}\hat{Y}]$ [72]), and since some of the operators commute, this expression can be rearranged to

$$\tilde{c}_{\rm AB}(t) = \frac{1}{\beta Z}\int_0^\beta d\lambda\, {\rm tr}\Big[e^{-\lambda\hat{H}}\,\hat{B}\,e^{-(\beta-\lambda)\hat{H}}\,e^{-i\hat{H}t/\hbar}\,\hat{A}\,e^{+i\hat{H}t/\hbar}\Big]. \tag{2.36}$$

A change of integration variable to $\lambda' = \beta - \lambda$ gives the first time symmetry

$$\tilde{c}_{\rm AB}(t) = \frac{1}{\beta Z}\int_0^\beta d\lambda'\, {\rm tr}\Big[e^{-(\beta-\lambda')\hat{H}}\,\hat{B}\,e^{-\lambda'\hat{H}}\,e^{-i\hat{H}t/\hbar}\,\hat{A}\,e^{+i\hat{H}t/\hbar}\Big] \tag{2.37}$$

or

$$\boxed{\tilde{c}_{\rm AB}(t) = \tilde{c}_{\rm BA}(-t).} \tag{2.38}$$

The remaining symmetries can be obtained by evaluating the trace in the basis of the eigenstates of $\hat{H}$ ($\hat{H}|j\rangle$=$E_j|j\rangle$), i.e.,

$$\tilde{c}_{\rm AB}(t) = \frac{1}{\beta Z}\int_0^\beta d\lambda \sum_{j,k}\left[e^{-(\beta-\lambda)E_j}A_{jk}e^{-\lambda E_k}e^{+iE_kt/\hbar}B_{kj}e^{-iE_jt/\hbar}\right], \tag{2.39}$$

in which, for example, $A_{jk} = \langle j|\hat{A}|k\rangle$. Noting the reality of the energy eigenvalues, the

complex conjugate of the correlation function is

$$\tilde{c}_{\mathrm{AB}}(t)^* = \frac{1}{\beta Z}\int_0^\beta d\lambda \sum_{j,k}\left[e^{-(\beta-\lambda)E_j}A^*_{jk}e^{-\lambda E_k}e^{-iE_kt/\hbar}B^*_{kj}e^{+iE_jt/\hbar}\right], \tag{2.40}$$

and if $\hat{A}$ and $\hat{B}$ are hermitian then

$$\tilde{c}_{\mathrm{AB}}(t)^* = \frac{1}{\beta Z}\int_0^\beta d\lambda \sum_{j,k}\left[e^{-(\beta-\lambda)E_j}A_{kj}e^{-\lambda E_k}e^{-iE_kt/\hbar}B_{jk}e^{+iE_jt/\hbar}\right]. \tag{2.41}$$

Employing the same change of integration variable that was used to obtain the previous symmetry gives

$$\tilde{c}_{\mathrm{AB}}(t)^* = \frac{1}{\beta Z}\int_0^\beta d\lambda \sum_{k,j}\left[e^{-(\beta-\lambda)E_k}A_{kj}e^{-\lambda E_j}e^{+iE_jt/\hbar}B_{jk}e^{-iE_kt/\hbar}\right], \tag{2.42}$$

after some rearrangement. Removing the sums over eigenstates leads to the second symmetry

$$\boxed{\tilde{c}_{\mathrm{AB}}(t)^* = \tilde{c}_{\mathrm{AB}}(t).} \tag{2.43}$$

For the third and final time symmetry, return to Eq. (2.40). Since the matrix elements of position-dependent operators can be chosen to be real in the basis of energy eigenstates, i.e.,

$$A^*_{jk} = A_{jk} \text{ and } B^*_{kj} = B_{kj}, \tag{2.44}$$

the complex-conjugated correlation function is

$$\tilde{c}_{\mathrm{AB}}(t)^* = \frac{1}{\beta Z}\int_0^\beta d\lambda \sum_{j,k}\left[e^{-(\beta-\lambda)E_j}A_{jk}e^{-\lambda E_k}e^{-iE_kt/\hbar}B_{kj}e^{+iE_jt/\hbar}\right], \tag{2.45}$$

giving

$$\boxed{\tilde{c}_{\mathrm{AB}}(t)^* = \tilde{c}_{\mathrm{AB}}(-t).} \tag{2.46}$$

The second and third symmetries are sufficient to show that $\tilde{c}_{\rm AB}(t)$ is a real and even function of time for hermitian $\hat{A}$ and $\hat{B}$ that depend only on position. Combining all three symmetries then leads to $\tilde{c}_{\rm AB}(t)$=$\tilde{c}_{\rm BA}(t)$.

Having established three time symmetries of the exact Kubo-transformed correlation function, it is now shown that they are shared by the RPMD model. The n-bead RPMD approximation to the right-hand side of the first symmetry (Eq. (2.38)) is

$$\langle B(0)A(-t)\rangle_n^{\rm rp} = \frac{1}{(2\pi\hbar)^n Z_n}\int d\mathbf{p}_0 \int d\mathbf{q}_0\, e^{-\beta_n H_n(\mathbf{p}_0,\mathbf{q}_0)} B_n(\mathbf{q}_0) A_n(\mathbf{q}_{-t}). \tag{2.47}$$

A shift in the time-origin produces

$$\langle B(0)A(-t)\rangle_n^{\rm rp} = \frac{1}{(2\pi\hbar)^n Z_n}\int d\mathbf{p}_t \int d\mathbf{q}_t\, e^{-\beta_n H_n(\mathbf{p}_t,\mathbf{q}_t)} B_n(\mathbf{q}_t) A_n(\mathbf{q}_0). \tag{2.48}$$

Because the RPMD model just involves classical dynamics in an extended phase-space the Liouville theorem holds, i.e. $d\mathbf{p}_0\, d\mathbf{q}_0 = d\mathbf{p}_t\, d\mathbf{q}_t$ [27]. Applying this gives

$$\langle B(0)A(-t)\rangle_n^{\rm rp} = \frac{1}{(2\pi\hbar)^n Z_n}\int d\mathbf{p}_0 \int d\mathbf{q}_0\, e^{-\beta_n H_n(\mathbf{p}_t,\mathbf{q}_t)} B_n(\mathbf{q}_t) A_n(\mathbf{q}_0). \tag{2.49}$$

Finally, the equations of motion used to obtain $(\mathbf{p}_t, \mathbf{q}_t)$ conserve the ring-polymer Hamiltonian, and so

$$\langle B(0)A(-t)\rangle_n^{\rm rp} = \frac{1}{(2\pi\hbar)^n Z_n}\int d\mathbf{p}_0 \int d\mathbf{q}_0\, e^{-\beta_n H_n(\mathbf{p}_0,\mathbf{q}_0)} A_n(\mathbf{q}_0) B_n(\mathbf{q}_t), \tag{2.50}$$

which is

$$\boxed{\langle B(0)A(-t)\rangle_n^{\rm rp} = \langle A(0)B(t)\rangle_n^{\rm rp},} \tag{2.51}$$

proving that the first symmetry (Eq. (2.38)) holds for any n in the RPMD approximation. This symmetry is essentially the statement that in an equilibrium system the

ensemble-averaged correlation between spontaneous fluctuations at two points in time $t' \leq t''$ depends only on the difference $t''-t'$ [7, 27].

The second symmetry (Eq. (2.43)) follows directly from the definition of the RPMD model

$$\boxed{(\langle A(0)B(t)\rangle_n^{\rm rp})^* = \langle A(0)B(t)\rangle_n^{\rm rp}\,,} \tag{2.52}$$

if $A(q)$ and $B(q)$ are real. The n-bead RPMD approximation to the right-hand side of the third time symmetry (Eq. (2.46)) is

$$\langle A(0)B(-t)\rangle_n^{\rm rp} = \frac{1}{(2\pi\hbar)^n Z_n}\int d\mathbf{p}_0 \int d\mathbf{q}_0\, e^{-\beta_n H_n(\mathbf{p}_0,\mathbf{q}_0)} A_n(\mathbf{q}_0) B_n(\mathbf{q}_{-t}(\mathbf{p}_0,\mathbf{q}_0)). \tag{2.53}$$

The reversibility of the classical dynamics

$$\mathbf{q}_{-t}(\mathbf{p}_0,\mathbf{q}_0) = \mathbf{q}_t(-\mathbf{p}_0,\mathbf{q}_0), \tag{2.54}$$

can be used in Eq. (2.53) to give

$$\langle A(0)B(-t)\rangle_n^{\rm rp} = \frac{1}{(2\pi\hbar)^n Z_n}\int d\mathbf{p}_0 \int d\mathbf{q}_0\, e^{-\beta_n H_n(\mathbf{p}_0,\mathbf{q}_0)} A_n(\mathbf{q}_0) B_n(\mathbf{q}_t(-\mathbf{p}_0,\mathbf{q}_0)). \tag{2.55}$$

Changing the integration variable $\mathbf{p}_0 \rightarrow -\mathbf{p}_0$ and using the symmetry of the ring-polymer Hamiltonian ($H_n(-\mathbf{p}_0,\mathbf{q}_0) = H_n(\mathbf{p}_0,\mathbf{q}_0)$) leads to

$$\begin{aligned}\langle A(0)B(-t)\rangle_n^{\rm rp} &= \frac{1}{(2\pi\hbar)^n Z_n}\int d\mathbf{p}_0 \int d\mathbf{q}_0\, e^{-\beta_n H_n(\mathbf{p}_0,\mathbf{q}_0)} A_n(\mathbf{q}_0) B_n(\mathbf{q}_t), \\ &= \langle A(0)B(t)\rangle_n^{\rm rp}\,. \end{aligned} \tag{2.56}$$

Together with Eq. (2.52), this proves that the RPMD model posesses the third and

final time symmetry for any n

$$\boxed{(\langle A(0)B(t)\rangle_n^{\rm rp})^* = \langle A(0)B(-t)\rangle_n^{\rm rp}\,.} \tag{2.57}$$

Thus, in addition to being equal to $\tilde{c}_{\rm AB}(t)$ in three special limits, the RPMD approximation shares three time symmetries with the exact Kubo-transformed correlation function.

This section now closes with a discussion about the significance of these shared properties and the applicability of the RPMD model. The first comment is that the standard correlation function $c^0_{\rm AB}(t)$ has only one limit (classical) and one time symmetry ($c^0_{\rm AB}(t)^*$=$c^0_{\rm AB}(-t)$) in common with $\langle A(0)B(t)\rangle_n^{\rm rp}$. In contrast, the three limits and three symmetries shared between the RPMD model and the exact $\tilde{c}_{\rm AB}(t)$ are strong support for associating the former with the latter.

It should be mentioned that the classical correlation function $c^{\rm cl}_{\rm AB}(t)$ (Eq. (1.4)) shares all three time symmetries and only lacks the t=0 limit. This correspondence between $c^{\rm cl}_{\rm AB}(t)$ and $\tilde{c}_{\rm AB}(t)$ is well-known, and was mentioned in the previous chapter as a justification for using $D_{\rm ho}(\omega)$ as the detailed-balance correction factor. Associating the RPMD model with the Kubo correlation function implies that a RPMD approximation to $c^0_{\rm AB}(t)$ can be obtained by using $D_{\rm ho}(\omega)$ in the same way as it is used to generate a purely classical approximation to $c^0_{\rm AB}(t)$ (see Section 1.1). Thus, the hope is that the RPMD approximation might provide a better approximation to $\tilde{c}_{\rm AB}(t)$ than $c^{\rm cl}_{\rm AB}(t)$.

But what is the nature of the RPMD approximation? It is an exact description of the quantum statistical mechanics of a system at canonical equilibrium combined with a *consistent* classical dynamics. This consistency is the source of many of the appealing features of the model – the validity of the Liouville theorem being perhaps the most important. Problems that occur in other methods due to a dynamics that is inconsis-

tent with the quantum statistics (e.g. zero-point energy flow in the classical Wigner model) are avoided. The consistent classical dynamics are of course just approximate dynamics, and correlation functions which show significant quantum-dynamical effects will be poorly described. However, a typical condensed-phase correlation function will decay fairly quickly to zero without any long-time dynamical structures (e.g. coherent oscillations). Physically, this is because long-time correlation between instantaneous fluctuations tends to be lost in the averaging over the dynamics of multiple degrees of freedom [16, 73]. Short-time statistical effects, which are included exactly in the RPMD model, are therefore most important for condensed-phase applications. The remainder of this thesis is an investigation of the utility of the RPMD approximation.

2.4 One-dimensional tests

The RPMD approximation has been introduced and has been shown to be exact in the classical, t=0, and "harmonic potential plus linear operator" limits. In general, however, the types of problems to which one would like to apply it might involve neither harmonic potentials nor linear operators, and it is clearly not just the t=0 regime that is important in determining dynamical properties. Therefore, in order to get a first impression of how well the model performs away from these exact limits this section applies it to three simple one-dimensional test problems.

The three models have Hamiltonians of the form

$$H = \frac{p^2}{2} + V(q), \tag{2.58}$$

and use scaled unit systems where $m = \hbar = k_B = 1$. The first two were introduced by Jang and Voth for the purpose of testing CMD and some related approximations [20]. Both require the calculation of a position autocorrelation function and are therefore in

the linear operator limit – they will not reveal anything about the effects of operator nonlinearity on the accuracy of the new method. Instead, the two tests can be used to explore how well RPMD (or any other approximate dynamical method) works away from the harmonic potential regime. Thus, in the first problem the potential is mildly anharmonic

$$V(q) = \frac{1}{2}q^2 + \frac{1}{10}q^3 + \frac{1}{100}q^4, \tag{2.59}$$

whereas in the second it is that of the strongly anharmonic quartic oscillator

$$V(q) = \frac{1}{4}q^4. \tag{2.60}$$

The calculations were carried-out using the techniques outlined earlier in this chapter. Thus, a large number of ring-polymer trajectories were evolved, each starting from the final position of the previous one with new momenta sampled from the Maxwell distribution contained in $e^{-\beta_n H_n}$. The time-evolution algorithm was based upon alternating free ring-polymer and external force steps. Because the free ring-polymer is a purely harmonic system it can be evolved analytically across any time interval (via the normal mode transformation in Appendix B). The timestep of the RPMD calculation can therefore be matched to the magnitude of the external forces rather than the high-frequency oscillations of the harmonic ring-polymer springs. The position autocorrelation function at time t was obtained as the average of $q_c(\mathbf{q}_0)q_c(\mathbf{q}_t)$ over the ring-polymer trajectories.

The quantum-mechanical, classical and RPMD position autocorrelation functions for the mildly anharmonic potential are shown in Fig. 2.1 at two temperatures. For the higher temperature (β=1), n=4 ring-polymer beads were found to converge the RPMD calculation. At the lower temperature (β=8), which is further from the classical limit, it was found that n=32 beads were required. The classical results were

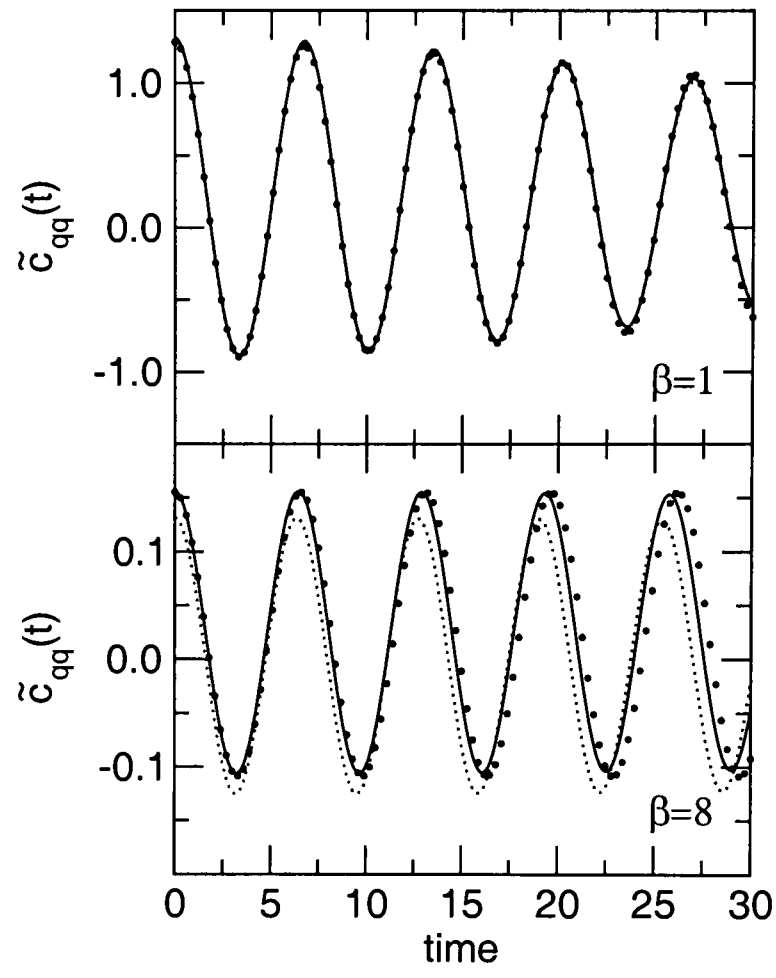

Figure 2.1: Kubo-transformed position autocorrelation functions for the mildly anharmonic potential defined in Eq. (2.59), at two temperatures. The exact quantum-mechanical result is represented as filled circles, the RPMD result as a solid line, and the classical result as a dotted line.

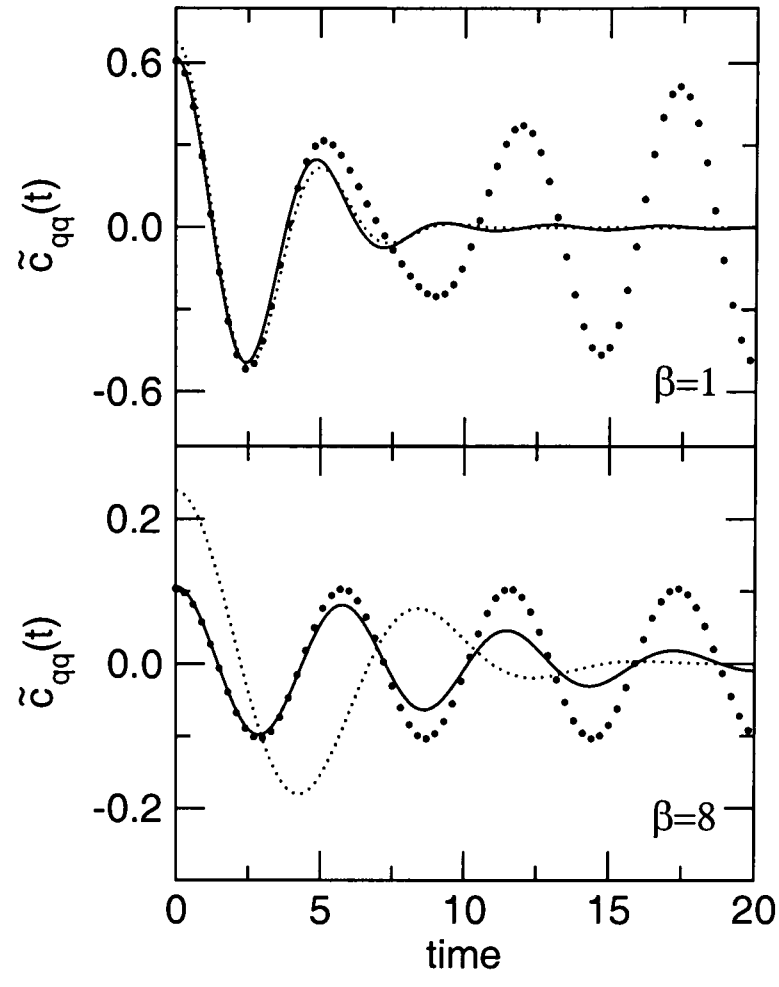

Figure 2.2: Kubo-transformed position autocorrelation functions for the quartic oscillator potential in Eq. (2.60), at two temperatures. Symbols as in Fig. 2.1.

obtained from the same computer code by setting n=1. At the higher temperature the three correlation functions are almost indistinguishable for all times considered – the mild anharmonicity is not sufficient to induce any signicant deviations of $\tilde{c}_{qq}(t)$ (and the RPMD model) from $c_{qq}^{cl}(t)$. At the lower temperature the differences are more marked. In particular, the oscillation of the classical correlation function has the incorrect amplitude and frequency. It can be seen that the RPMD correlation function significantly improves on both of these failings, and that it really only degrades after a few oscillations.

Whilst the results for the mildly anharmonic oscillator are encouraging, it is a system which is not too far from the harmonic limit in which RPMD is exact. The strongly anharmonic quartic oscillator provides a better illustration of the effects of potential anharmonicity on the accuracy of the approximation. The results presented in Fig. 2.2

are for the same temperatures considered previously, and the same numbers of ring-polymer beads were used. The anharmonicity in this system is sufficient to create considerable differences between the correlation functions at high temperatures. The classical result completely fails to reproduce the persistent but irregular oscillations in the exact results, and the RPMD model does little to improve the situation.

So, does this second application already show the new method failing catastrophically? The answer is yes. The long-time structures in the exact Kubo-transformed correlation function at $\beta = 1$ are a result of coherent oscillations in a highly anharmonic well. A description of these coherent dynamical effects would require phase information which is not present in the RPMD approximation. Thus, the new method should not be expected to describe such features. However, it is important to recognise that these coherent effects are likely to be 'averaged-out' of the correlation functions of many condensed-phase systems [16], and are therefore expected to be insignificant in many of the applications for which the RPMD model is intended.

The results for the quartic oscillator at the lower temperature ($\beta = 8$) are shown in the bottom panel of Fig. 2.2. It is clear that the classical results are now in even greater error, failing to reproduce even the first oscillation. It also clear, however, that at this temperature the RPMD model does improve on the classical correlation function. The RPMD correlation function has the correct value at t=0 because it is based upon an exact formulation of quantum statistical mechanics. It then has a reasonable amplitude for a couple of oscillations, and in addition, the frequency of these oscillations is well-matched with that seen in the exact result. A large part of the decay in amplitude is due to the dephasing amongst the higher normal modes of the ring-polymer, which couple to the motion of the centroid ($q_c \propto$ the zero-frequency normal-mode) through the anharmonic potential. The RPMD approximation is more successful in this latter case because at the lower temperature the thermal time $\beta\hbar$ is

longer, and therefore quantum statistical effects, which are described exactly by the new model, are important for longer than they are when $\beta=1$.

For these two problems the accuracy of the RPMD approximation appears to be comparable to that of the CMD method, although a direct comparison of their results is not possible because Ref. [20] studied the real part of $c^0_{\rm AB}(t)$ rather than the Kubo-transformed $\tilde{c}_{\rm AB}(t)$. The only significant difference between the methods occurs for the low temperature quartic oscillator, where the CMD result maintains the correct amplitude for longer times. Bearing in mind the marked contrast in the simplicity and efficiency of the two methods, the performance of the RPMD method for these two test problems is encouraging.

The first two problems allow a cursory examination of the ability of the new method to calculate accurate linear-operator correlation functions in anharmonic systems. Conversely, the third and final test problem considers the effect of operator nonlinearity in systems with harmonic potentials. Thus, the $A(\hat{q})=B(\hat{q})=\hat{q}^3$ autocorrelation function of the $V(\hat{q})=\frac{1}{2}\hat{q}^2$ harmonic oscillator was calculated at the two different temperatures. The numbers of ring-polymer beads used at each temperature is the same as for the previous problems. The exact, classical and converged RPMD results displayed in Fig. 2.3 lead to two important observations. Firstly, the operator nonlinearity is handled exceedingly well in this case – it might be suspected that (in the harmonic potential) the q^3 operator does not represent a particularly severe test. Secondly, the low-temperature results provide a clear demonstration of the ability of the new method to improve upon the classical correlation function for systems away from the classical limit. This improvement is a result of the exact quantum statistical mechanics which form the foundations of the RPMD method. Although the associated (and consistent) dynamics have been shown to fail to describe long-time quantum dynamical effects (Fig. 2.2), it is again stressed that such effects are found to be far from important in

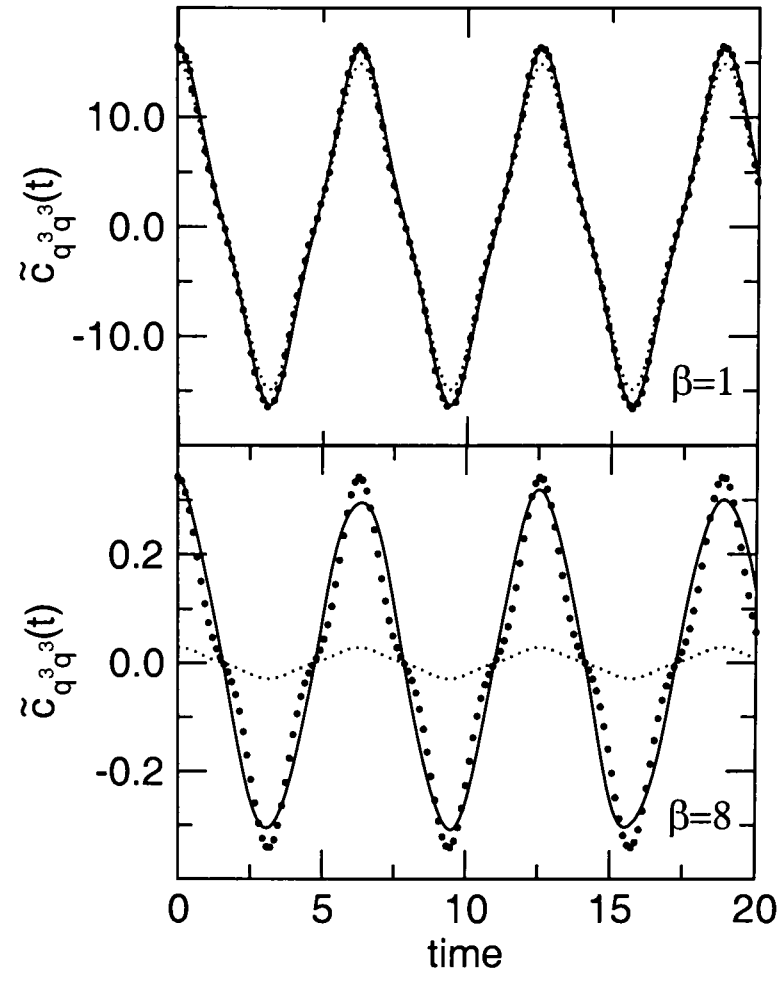

Figure 2.3: Kubo-transformed q^3 autocorrelation functions for the harmonic potential ($V = \frac{1}{2}q^2$), at two temperatures. Symbols as in Fig. 2.1.

many complex molecular systems. The remainder of this thesis, which is concerned with applying the RPMD method to two topics in condensed-phase quantum dynamics, will provide ample evidence for this last assertion.

Chapter 3

Inelastic neutron scattering

Inelastic neutron scattering experiments can provide information about the microscopic structure and dynamics of condensed-phase systems. In this chapter, results from recent neutron scattering experiments on liquid para-hydrogen are used to test the RPMD model in a situation for which classical molecular dynamics is inadequate. In addition to this comparison with experimental data, the time correlation functions relevant to neutron scattering lend themselves to a purely theoretical investigation of the effect of operator nonlinearity on the RPMD approximation in a condensed-phase system. This continues and extends the previous chapter's analysis of the situations in which the RPMD model breaks down. Much of this work appears in Ref. [74].

3.1 Introduction and chapter outline

An inelastic neutron scattering experiment measures the differential cross-section for inelastic collisions between neutrons and a condensed-phase target [27]. This differential cross-section is proportional to the probability that a neutron scatters at a given angle with a particular energy loss. Furthermore, it can be related to a time correlation function which involves the exponential operators $e^{\pm i\boldsymbol{\kappa}\hat{\mathbf{q}}}$, where $\hbar\boldsymbol{\kappa}$ quantifies

the momentum transferred from the neutron to the target by the collision [75, 76]. Since these operators depend only on position ($\hat{\mathbf{q}}$), the RPMD model can be used to approximate the exact quantum-mechanical neutron-scattering correlation functions (see Section 2.2). Crucially, at least for the purposes of this thesis, the exponential operators can be tuned between the linear and highly nonlinear regimes by varying the physical parameter κ. Thus, an analysis of the accuracy of the RPMD correlation functions across a broad range of momentum transfers constitutes a systematic and self-contained test of the effect that nonlinear operators have on the performance of the new method. In addition, the liquid para-hydrogen system is an ideal arena for these tests because it typifies a condensed-phase (multi-dimensional) system with significant quantum-mechanical character.

After a short account of the theory of inelastic neutron scattering in Section 3.2, most of this chapter is concerned with:

(i) the calculation of the approximate neutron-scattering correlation functions,

(ii) the subsequent analysis of their accuracy.

Step (i) is the subject of Section 3.3, in which two RPMD-based approaches are presented. One is a direct application of the RPMD model to the Kubo-transformed neutron-scattering correlation functions. The other involves an additional, but reliable, approximation that requires a velocity autocorrelation function as the dynamical input [77].

Step (ii) requires the assessment of the accuracy of a molecular simulation. In general, the two possibilities for doing this are comparison with experiment and comparison with theoretical results – this chapter will follow both strategies. Thus, Section 3.4 will present exact results for some spectral moments of the neutron-scattering correlation functions. In this context, a spectral moment is a property related to the shape of the

spectral representation (i.e. Fourier transform) of a correlation function, and provides a purely theoretical means of analysing its quality.

The spectral moment tests are applied to the results of the two RPMD-based approximation schemes in the first half of Section 3.5. They clearly demonstrate that the direct application of the RPMD approximation to the Kubo-transformed correlation function is a strategy that breaks down at large momentum transfers where the correlated operators are nonlinear. Furthermore, the results of the tests also show that the alternative RPMD approximation scheme suffers no such degradation in accuracy as $\kappa=|\boldsymbol{\kappa}|$ is increased. This second approach is therefore the one used to generate results that are compared with the experimental data in the other half of Section 3.5. These experimental results provide a particularly attractive test for the following reasons:

(i) at the experimental temperature of 14 K, a typical wavefunction for a liquid-phase para-hydrogen molecule has a spatial extent that is significant in comparison with the molecular dimensions. This indicates that there are likely to be sizeable quantum effects in the nuclear structure and dynamics of the system and that classical molecular dynamics is likely to be inaccurate [21]. Thus, liquid para-hydrogen is exactly the sort of system for which methods like RPMD are required,

(ii) this 'quantum dispersion' effect is not large enough to mean that identical particle exhange must be accounted for. Thus, the quantum statistical mechanics encompassed in the Boltzmann operator (which are treated exactly in the RPMD model) have been shown to give an accurate description of static properties of the system [78],

(iii) the low reduced-mass of the H_2 molecule gives it widely separated rotational energy levels. Therefore, at the temperature considered almost all (>99%) para-

hydrogen molecules are in the ground rotational state. The molecular wavefunction in this state is spherically symmetric, and so the interaction between two molecules depends only on the distance between them,

(iv) there exists an accurate potential energy surface whose static properties have been studied and found to compare well with experimental data [79].

To reiterate a point made in previous chapters: the presence of many degrees of freedom in the liquid para-hydrogen system are expected to limit the importance of long-time quantum-dynamical effects in the calculated neutron-scattering correlation functions. This, and the fact that a realistic anharmonic model of the pair interaction in liquid para-hydrogen can be used (see Section 3.5), make this chapter's test of the effect of operator nonlinearity more relevant and important than the one-dimensional model studied at the end of Chapter 2. Furthermore, the scarcity of exact quantum mechanical results for the dynamics of condensed-phase molecular systems makes the opportunity to compare with reliable experimental data highly valuable.

3.2 Theory of inelastic neutron scattering

The theory of neutron scattering from condensed matter is well-established following decades of rigorous research activity that began in the 1950s [76, 80]. An extensive theoretical framework has been developed and used to support and interpret the neutron scattering experiments that have been undertaken in many areas of modern science [76]. This section contains a selective development of the relevant parts of this framework.

A neutron scattering experiment obtains information on scattering probabilities (i.e. the differential cross-section) by observing a large number of neutron scattering events.

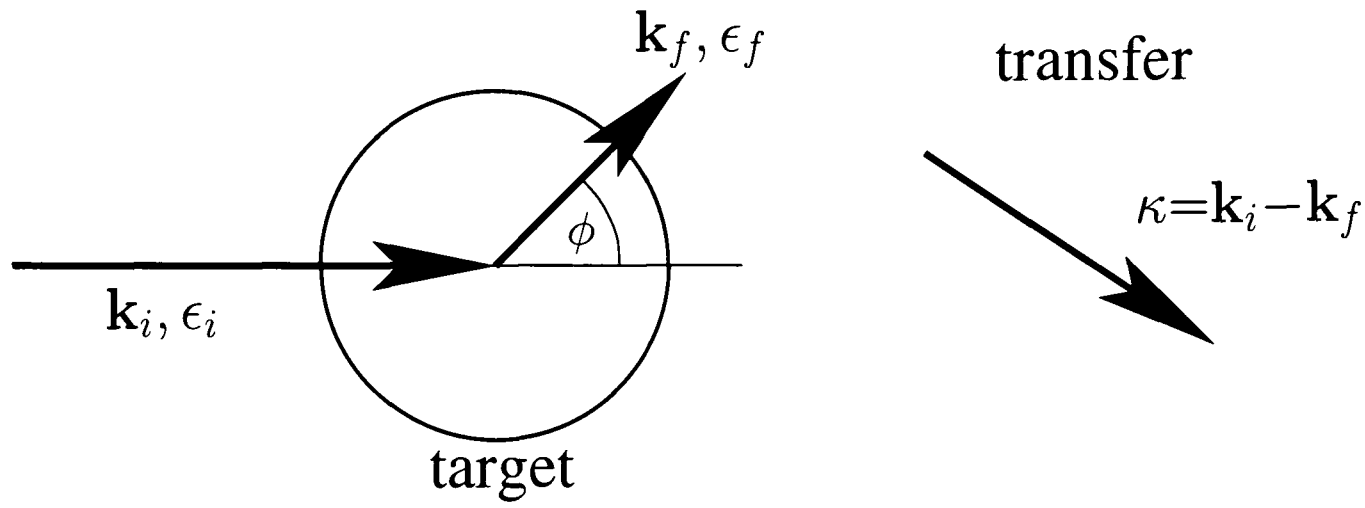

Figure 3.1: Schematic illustration of a neutron scattering event in terms of the variables used in the text. In this two-dimensional figure only one scattering angle (ϕ) is shown. The energy transfer, given by Eq. (3.2), is determined by the difference in the length of the vectors $\mathbf{k}_i$ and $\mathbf{k}_f$.

The geometry of these events is illustrated schematically in Fig. 3.1. Thus, the incoming neutron has momentum $\hbar\mathbf{k}_i$ and an associated energy $\epsilon_i = \hbar^2 k_i^2/2m_n$, where m_n is the neutron mass and k_i=$|\mathbf{k}_i|$. On interacting with the target system it is scattered through angles θ and ϕ into the solid angle $d\Omega = \sin\theta\, d\theta\, d\phi$ such that the outgoing neutron has momentum $\hbar\mathbf{k}_f$ and energy $\epsilon_f = \hbar^2 k_f^2/2m_n$. The scattering event can be characterized by the neutron to target momentum transfer

$$\hbar\boldsymbol{\kappa} = \hbar(\mathbf{k_i} - \mathbf{k_f}), \tag{3.1}$$

and the associated energy transfer

$$\hbar\omega = \epsilon_i - \epsilon_f = E_f - E_i, \tag{3.2}$$

where E_i ($\equiv\hbar\omega_i$) and E_f ($\equiv\hbar\omega_f$) are respectively the energies of the initial and final states of the target. Note that this last equation is just the statement that energy is conserved during the scattering event. These experiments are sensitive to structure and dynamics on length-scales of the same order of magnitude as the wavelengths of

the incoming neutrons. Therefore 'thermal' neutrons, i.e. those with $\epsilon_i \approx k_B T$, are often used since their wavelengths correspond to typical interparticle separations in condensed-phase molecular systems [76], e.g. the de Broglie wavelength of a neutron with energy $k_B T$ at 298 K is 1.8 Å.

3.2.1 The first Born approximation

The principal experimental observable is the partial differential cross-section,

$$\frac{d^2\sigma}{d\Omega\, d\omega}, \tag{3.3}$$

which is defined as the fraction of neutrons with incident energy ϵ_i scattered into solid angle $d\Omega$ with an energy transfer between ω and $\omega + d\omega$. This quantity was first related to a time correlation function by van Hove [75]. However, the rigorous derivation of the connection requires a certain amount of quantum scattering theory and since such material is of no relevance to the rest of this thesis an alternative development is presented that is loosely based upon that of Hansen and McDonald [80].

The basic quantities that determine the partial differential cross section are the state-to-state transition rates (probability per unit time) for the possible scattering events. If the incoming neutron state is $|\mathbf{k}_i\rangle$ and the initial target state is $|i\rangle$ then in a combined notation the initial state of the entire system is $|i, \mathbf{k}_i\rangle$. Since the perturbation of the target by the neutron is weak, Fermi's golden rule [81] can be used for the transition rate from $|i, \mathbf{k}_i\rangle$ to the final state $|f, \mathbf{k}_f\rangle$, i.e.

$$W_{if} = \frac{2\pi}{\hbar} \left| \left\langle f, \mathbf{k}_f \left| \hat{V} \right| i, \mathbf{k}_i \right\rangle \right|^2 \rho_f, \tag{3.4}$$

where $\hat{V}$ is the neutron-target interaction potential. This potential induces the scattering and couples the neutron to the structure and dynamics of the target system.

The symbol ρ_f denotes the density of final states for the entire system and can be decomposed as

$$\rho_f = \rho_{\mathbf{k}_f} \delta(\hbar\omega - \hbar(\omega_f - \omega_i)), \tag{3.5}$$

in which $\rho_{\mathbf{k}_f}$ is the density of final states of the neutron, and the delta function enforces the energy transfer condition (Eq. (3.2)) on the final states of the target.

In three dimensions the density of neutron states is [80]

$$\rho_{\mathbf{k}_f} = d\mathbf{k}_f/(2\pi)^3 = k_f^2\, dk_f\, d\Omega/(2\pi)^3 = (m_n/\hbar^2)\,\hbar\, k_f\, d\omega\, d\Omega/(2\pi)^3. \tag{3.6}$$

Inserting this into Eq. (3.4) and dividing by the incident flux of neutrons, $\hbar k_i/m_n$, gives a restricted partial differential cross-section for the energy transfer $\hbar\omega$, the momentum transfer ($\hbar\boldsymbol{\kappa}$) and a specific pair of initial and final target states:

$$\left(\frac{d^2\sigma}{d\Omega\, d\omega}\right)_{if} = \frac{k_f}{k_i}\left(\frac{m_n}{2\pi\hbar^2}\right)^2 \left|\left\langle f, \mathbf{k}_f \left| \hat{V} \right| i, \mathbf{k}_i \right\rangle\right|^2 \delta(\omega - (\omega_f - \omega_i)). \tag{3.7}$$

Note that the energy and momentum transfer conditions (Eq. (3.1) and Eq. (3.2)) uniquely determine the initial ($\mathbf{k}_i$) and final ($\mathbf{k}_f$) neutron momenta. However, in the process of measurement the experiment will observe all the thermally accessible initial target states and, furthermore, there may be multiple final target states consistent with the energy transfer condition. Thus, the partial differential cross-section is obtained as the average of $(d^2\sigma/d\Omega\, d\omega)_{if}$ over all target state pairs ($|i\rangle$,$|f\rangle$) weighted by the probability of observing the initial state in a canonical ensemble (obeying Boltzmann statistics), i.e. if $p_i = e^{-\beta E_i}/Z$ then

$$\frac{d^2\sigma}{d\Omega\, d\omega} = \sum_{if} p_i \left(\frac{d^2\sigma}{d\Omega\, d\omega}\right)_{if}, \tag{3.8}$$

or

$$\frac{d^2\sigma}{d\Omega\, d\omega} = \frac{1}{Z}\frac{k_f}{k_i}\left(\frac{m_n}{2\pi\hbar^2}\right)^2 \sum_{if} e^{-\beta E_i} \left|\left\langle f, \mathbf{k}_f \left| \hat{V} \right| i, \mathbf{k}_i \right\rangle\right|^2 \delta(\omega - (\omega_f - \omega_i)), \tag{3.9}$$

where E_i is the energy of the initial target state and Z is the canonical partition function.

Further development of the expression for the partial differential cross-section requires a definition of the interaction potential $\hat{V}$. The specific details of the neutron-nucleon interaction are not well-established, but it is known to be very short-ranged [76]. The interaction potential for a neutron scattering from an array of N nuclei is therefore written as a sum of delta functions

$$\hat{V} = \frac{2\pi\hbar^2}{m_n} \sum_{j=1}^{N} b_j\, \delta(\mathbf{q}_n - \hat{\mathbf{q}}_j), \tag{3.10}$$

where $\mathbf{q}_n$ is the neutron position and $\hat{\mathbf{q}}_j$ is the position operator of nucleus j. In this sum, b_j is the 'scattering length' parameter – it may be positive or negative, real or complex [76]. Inserting this interaction potential into the transition matrix-elements gives

$$\left\langle f, \mathbf{k}_f \left| \hat{V} \right| i, \mathbf{k}_i \right\rangle = \frac{2\pi\hbar^2}{m_n} \sum_{j=1}^{N} b_j \left\langle f \left| \left\langle \mathbf{k}_f \left| \delta(\mathbf{q}_n - \hat{\mathbf{q}}_j) \right| \mathbf{k}_i \right\rangle \right| i \right\rangle, \tag{3.11}$$

where the inner Dirac bracket represents

$$\left\langle \mathbf{k}_f \left| \delta(\mathbf{q}_n - \hat{\mathbf{q}}_j) \right| \mathbf{k}_i \right\rangle = \int d\mathbf{q}_n\, \psi^*_{\mathbf{k}_f} \delta(\mathbf{q}_n - \hat{\mathbf{q}}_j) \psi_{\mathbf{k}_i}. \tag{3.12}$$

In this expression $\psi_{\mathbf{k}_i}$ and $\psi_{\mathbf{k}_f}$ are the incoming and outgoing neutron wavefunctions. The incoming wavefunction is a plane wave

$$\psi_{\mathbf{k}_i} = e^{+i\mathbf{k}_i \cdot \mathbf{q}_n}, \tag{3.13}$$

and for scattering from a weak interaction potential it can be assumed that the outgoing neutron wavefunction has the same form, i.e,

$$\psi_{\mathbf{k}_f} = e^{+i\mathbf{k_f}\cdot\mathbf{q}_n}. \tag{3.14}$$

The adoption of this form for the scattered wavefunction is essentially an invocation of the 'first Born approximation' of quantum scattering theory [81, 82]. For a more detailed statement of this approximation see Ref. [80]. It should be noted that the 'weak interaction' condition used here is entirely consistent with the 'weak perturbation' justification for employing the golden rule expression in Eq. (3.4). With these wavefunctions the integral (Eq. (3.12)) becomes

$$\int d\mathbf{q}_n\, \psi^*_{\mathbf{k}_f} \delta(\mathbf{q}_n - \hat{\mathbf{q}}_j)\psi_{\mathbf{k}_i} = \int d\mathbf{q}_n\, e^{-i\mathbf{k_f}\cdot\mathbf{q}_n}\, \delta(\mathbf{q}_n - \hat{\mathbf{q}}_j)\, e^{+i\mathbf{k_i}\cdot\mathbf{q}_n} = e^{+i\boldsymbol{\kappa}\cdot\hat{\mathbf{q}}_j}. \tag{3.15}$$

Combining this result with Eq. (3.9) and Eq. (3.11) gives the partial differental cross-section as

$$\frac{d^2\sigma}{d\Omega\, d\omega} = \frac{1}{Z}\frac{k_f}{k_i}\sum_{if} e^{-\beta E_i} \left| \left\langle f \left| \sum_{j=1}^{N} b_j\, e^{+i\boldsymbol{\kappa}\cdot\hat{\mathbf{q}}_j} \right| i \right\rangle \right|^2 \delta(\omega - (\omega_f - \omega_i)). \tag{3.16}$$

At this point it is worth pausing to consider the physical content of this expression. It is clearly a canonically-weighted sum over the pairs of initial and final target states that are consistent with the energy transfer $\hbar\omega$. The summand contains a transition probability for the scattering process which connects the initial and final target states with an *instantaneous* momentum jump of $\hbar\boldsymbol{\kappa}$ [83]. Within the first Born approximation this additional momentum is the only change to the initial target state during the scattering event [76]. Conservation of momentum requires a concomitant change in the neutron states (Eq. (3.13) to Eq. (3.14)). A further note is that the spin state of the neutron has been ignored throughout this discussion.

3.2.2 The time correlation function

The derivation has reached a rather general expression for the partial differental cross-section (Eq. (3.16)). Further development of this equation depends on the nature of the atomic nuclei that compose the target. Since even the simplest scattering system will illustrate the relationship between $d^2\sigma/d\Omega\, d\omega$ and the (as yet undefined) time correlation function it is this which is considered first. Thus, if the target is composed of a single type of isotope with zero nuclear spin then the scattering lengths of all N nuclei are identical ($b_j = b$ for all j) and the matrix element in Eq. (3.16) becomes

$$\left\langle f \left| \sum_{j=1}^{N} b_j\, e^{+i\boldsymbol{\kappa}\cdot\hat{\mathbf{q}}_j} \right| i \right\rangle = b \left\langle f \left| \sum_{j=1}^{N} e^{+i\boldsymbol{\kappa}\cdot\hat{\mathbf{q}}_j} \right| i \right\rangle . \tag{3.17}$$

These matrix elements can be brought into a more succinct form by considering the target's particle (or number) density at a point $\mathbf{q}$

$$\hat{\rho}(\mathbf{q}) = \sum_{j=1}^{N} \delta(\mathbf{q} - \hat{\mathbf{q}}_j). \tag{3.18}$$

The Fourier components of this density

$$\hat{\rho}_{\boldsymbol{\kappa}} = \int d\mathbf{q}\, e^{-i\boldsymbol{\kappa}\cdot\mathbf{q}}\, \hat{\rho}(\mathbf{q}) = \sum_{j=1}^{N} e^{-i\boldsymbol{\kappa}\cdot\hat{\mathbf{q}}_j}, \tag{3.19}$$

will be recognised in the matrix elements above. The partial differential cross-section for scattering from this simple target system is therefore reduced to the more elegant form

$$\frac{d^2\sigma}{d\Omega\, d\omega} = \frac{b^2}{Z}\frac{k_f}{k_i} \sum_{if} e^{-\beta E_i} \left|\langle f \left|\hat{\rho}_{-\boldsymbol{\kappa}}\right| i\rangle\right|^2 \delta(\omega - (\omega_f - \omega_i)). \tag{3.20}$$

The time correlation function is then reached by inserting the Fourier representation

of the delta function into Eq. (3.20), i.e.

$$\delta(\omega - (\omega_f - \omega_i)) = \frac{1}{2\pi} \int_{-\infty}^{\infty} dt\, e^{-i(\omega-(\omega_f-\omega_i))t}, \tag{3.21}$$

to give (after some rearrangement)

$$\frac{d^2\sigma}{d\Omega\, d\omega} = \frac{b^2}{Z}\frac{k_f}{k_i}\frac{1}{2\pi} \int_{-\infty}^{\infty} dt\, e^{-i\omega t} \sum_{if} e^{-\beta E_i} \left|\langle f \left|\hat{\rho}_{-\boldsymbol{\kappa}}\right| i\rangle\right|^2 e^{-i(\omega_i-\omega_f)t}. \tag{3.22}$$

Focusing on the summand

$$\begin{aligned} e^{-\beta E_i} \left|\langle f \left|\hat{\rho}_{-\boldsymbol{\kappa}}\right| i\rangle\right|^2 e^{-i(\omega_i-\omega_f)t} &= e^{-\beta E_i} \langle i \left|\hat{\rho}_{\boldsymbol{\kappa}}\right| f\rangle \langle f \left|\hat{\rho}_{-\boldsymbol{\kappa}}\right| i\rangle\ e^{-i(\omega_i-\omega_f)t}, \\ &= e^{-\beta E_i} \langle i \left|\hat{\rho}_{\boldsymbol{\kappa}}\right| f\rangle \left\langle f \left| e^{+iE_f t/\hbar} \hat{\rho}_{-\boldsymbol{\kappa}} e^{-iE_i t/\hbar} \right| i\right\rangle, \\ &= \left\langle i \left| e^{-\beta\hat{H}} \hat{\rho}_{\boldsymbol{\kappa}} \right| f\right\rangle \left\langle f \left| e^{+i\hat{H}t/\hbar} \hat{\rho}_{-\boldsymbol{\kappa}} e^{-i\hat{H}t/\hbar} \right| i\right\rangle, \end{aligned} \tag{3.23}$$

where $\hbar\omega_i = E_i$ and $\hbar\omega_f = E_f$ were used for the second equality and the Schrödinger equation leads to the third. The final target states form a complete set

$$1 = \sum_f |f\rangle \langle f|, \tag{3.24}$$

which can be removed from the partial differential cross-section (Eq. (3.22)) to give

$$\frac{d^2\sigma}{d\Omega\, d\omega} = \frac{b^2}{Z}\frac{k_f}{k_i}\frac{1}{2\pi} \int_{-\infty}^{\infty} dt\, e^{-i\omega t} \sum_i \left\langle i \left| e^{-\beta\hat{H}} \hat{\rho}_{\boldsymbol{\kappa}} e^{+i\hat{H}t/\hbar} \hat{\rho}_{-\boldsymbol{\kappa}} e^{-i\hat{H}t/\hbar} \right| i\right\rangle. \tag{3.25}$$

Finally, since the sum over i is just a trace operation in the basis of initial target states the partial differential cross-section can be written as

$$\frac{d^2\sigma}{d\Omega\, d\omega} = b^2 \frac{k_f}{k_i}\frac{N}{2\pi} \int_{-\infty}^{\infty} dt\, e^{-i\omega t}\, F(\boldsymbol{\kappa}, t), \tag{3.26}$$

where $F(\boldsymbol{\kappa}, t)$ is the long-sought-after time correlation function

$$\begin{aligned} F(\boldsymbol{\kappa}, t) &= \frac{1}{NZ}\mathrm{tr}\left[e^{-\beta\hat{H}}\hat{\rho}_{\boldsymbol{\kappa}}\, e^{+i\hat{H}t/\hbar}\hat{\rho}_{-\boldsymbol{\kappa}}\, e^{-i\hat{H}t/\hbar}\right], \\ &= \frac{1}{NZ}\mathrm{tr}\left[e^{-\beta\hat{H}}\hat{\rho}_{\boldsymbol{\kappa}}\,\hat{\rho}_{-\boldsymbol{\kappa}}(t)\right], \end{aligned} \tag{3.27}$$

and $\hat{\rho}_{-\boldsymbol{\kappa}}(t)$ is the Heisenberg time-evolved density operator. This correlation function is known as the 'intermediate scattering function' and its Fourier transform, the 'dynamic structure factor', is $S(\boldsymbol{\kappa}, \omega)$

$$S(\boldsymbol{\kappa}, \omega) = \frac{1}{2\pi}\int_{-\infty}^{\infty} dt\, e^{-i\omega t}\, F(\boldsymbol{\kappa}, t), \tag{3.28}$$

and so

$$\frac{d^2\sigma}{d\Omega\, d\omega} = b^2\frac{k_f}{k_i}\, NS(\boldsymbol{\kappa}, \omega). \tag{3.29}$$

For the sake of completeness note that the more familiar 'static structure factor' $S(\boldsymbol{\kappa})$ is related to $S(\boldsymbol{\kappa}, \omega)$ by

$$S(\boldsymbol{\kappa}) = \int_{-\infty}^{\infty} d\omega\, S(\boldsymbol{\kappa}, \omega). \tag{3.30}$$

Neutron scattering measurements of $S(\boldsymbol{\kappa})$ are used to obtain the pair distribution functions of liquids ($g(\mathbf{r})$) since the former function can be converted to the latter with a spatial Fourier transform [80]. The ubiquity of the pair distribution function in the theory of liquids has meant that many of the standard neutron-scattering references base their theoretical discussion on $g(\mathbf{r})$ and its time-dependent generalisation, $G(\mathbf{r}, t)$, rather than on $S(\boldsymbol{\kappa}, \omega)$ or $F(\boldsymbol{\kappa}, t)$. However $G(\mathbf{r}, t)$ and $g(\mathbf{r})$ are of lesser importance in this thesis and are not discussed at length – see instead Refs. [27, 75, 80].

3.2.3 Coherent and incoherent scattering

The preceding analysis holds only for a particularly simple scattering system that is composed of a single type of isotope with zero nuclear spin. If the target includes multiple types of isotope and/or nuclei with nonzero nuclear spin then the scattering lengths (b_j) will not be uniform throughout the sample. In this case, the expressions for the partial differential cross-section must be developed to include the inhomogeneity.

To begin this development, the double sum of the 'first Born approximation' (Eq. (3.16)) is restated as:

$$\frac{1}{Z}\sum_{if} e^{-\beta E_i} \left\langle i \left| \sum_{j=1}^{N} b_j^* \, e^{-i\boldsymbol{\kappa}\cdot\hat{\mathbf{q}}_j} \right| f \right\rangle \left\langle f \left| \sum_{k=1}^{N} b_k \, e^{+i\boldsymbol{\kappa}\cdot\hat{\mathbf{q}}_k} \right| i \right\rangle \delta(\omega - (\omega_f - \omega_i)). \qquad (3.31)$$

In contrast to the previous simple case, a constant scattering length cannot be extracted from the sums over the nuclei. Instead consider the immediate substitution of the Fourier representation of the delta function. The steps from Eq. (3.22) to Eq. (3.26) now result in the partial differential cross-section being proportional to the temporal Fourier transform of

$$\frac{1}{Z}\sum_{j,k=1}^{N} \mathrm{tr}\left[e^{-\beta\hat{H}} \left(b_j^* \, e^{-i\boldsymbol{\kappa}\cdot\hat{\mathbf{q}}_j} \right) e^{+i\hat{H}t/\hbar} \left(b_k \, e^{+i\boldsymbol{\kappa}\cdot\hat{\mathbf{q}}_k} \right) e^{-i\hat{H}t/\hbar} \right]. \qquad (3.32)$$

If the Hamiltonian $\hat{H}$ is independent of the nuclear spin there will be neither correlation between the nuclear spins nor between the spins and the nuclear positions. This independence of the nuclear spin states from the cartesian degrees of freedom means that the trace can be written as the product of an average over the spin states and a trace over all nonspin degrees of freedom [76, 80]. The preceding expression is therefore written as

$$\frac{1}{Z}\sum_{j,k=1}^{N} (\overline{b_j^* b_k}) \, \mathrm{tr}\left[e^{-\beta\hat{H}} e^{-i\boldsymbol{\kappa}\cdot\hat{\mathbf{q}}_j} \, e^{+i\hat{H}t/\hbar} e^{+i\boldsymbol{\kappa}\cdot\hat{\mathbf{q}}_k} \, e^{-i\hat{H}t/\hbar} \right], \qquad (3.33)$$

where $(\overline{b_j^* b_k})$ is the average over the nuclear spins and their orientations. The 'distinct' $(j \neq k)$ terms in this double sum involve uncorrelated scattering lengths at different sites, i.e.,

$$\overline{b_j^* b_k} = |\overline{b_j^*}|\,|\overline{b_k}| = |\bar{b}|^2, \tag{3.34}$$

because the average scattering length will be the same at each site in an isotropic liquid. For the 'self' $(j=k)$ terms the spin average is

$$\overline{b_j^* b_k} = \overline{|b_k|^2} = \overline{|b|^2}. \tag{3.35}$$

A succinct statement of these considerations is

$$\overline{b_j^* b_k} = |\bar{b}|^2 + \delta_{j,k}(\overline{|b|^2} - |\bar{b}|^2), \tag{3.36}$$

which can be rewritten as

$$\overline{b_j^* b_k} = b_{\text{coh}}^2 + \delta_{j,k} b_{\text{inc}}^2, \tag{3.37}$$

where the pre-emptively labelled parameters are defined

$$b_{\text{coh}}^2 = |\bar{b}|^2 \quad ; \quad b_{\text{inc}}^2 = \overline{|b|^2} - |\bar{b}|^2. \tag{3.38}$$

Substitution of Eq. (3.37) into Eq. (3.33) gives

$$N b_{\text{coh}}^2 F(\boldsymbol{\kappa}, t) + N b_{\text{inc}}^2 F_s(\boldsymbol{\kappa}, t), \tag{3.39}$$

where the 'self' intermediate scattering function is

$$F_s(\boldsymbol{\kappa}, t) = \frac{1}{NZ} \sum_{j=1}^{N} \text{tr}\left[e^{-\beta \hat{H}} e^{-i\boldsymbol{\kappa}\cdot\hat{\mathbf{q}}_j}\, e^{+i\hat{H}t/\hbar}\, e^{+i\boldsymbol{\kappa}\cdot\hat{\mathbf{q}}_j}\, e^{-i\hat{H}t/\hbar} \right]. \tag{3.40}$$

The partial differential cross-section is then

$$\frac{d^2\sigma}{d\Omega\, d\omega} = N\frac{k_f}{k_i}\left(b_{\text{coh}}^2 S(\boldsymbol{\kappa},\omega) + b_{\text{inc}}^2 S_{\text{inc}}(\boldsymbol{\kappa},\omega)\right), \tag{3.41}$$

where, following Eq. (3.28), $S_{\text{inc}}(\boldsymbol{\kappa},\omega)$ is defined as the temporal Fourier transform of $F_s(\boldsymbol{\kappa},t)$. The b_{coh}^2 term, which contains the information on the structure and collective dynamics of the target system, is the 'coherent' scattering component. The b_{inc}^2 term, which only contains information on the motion of individual scatterers, is the 'incoherent' component.

The difference between coherent and incoherent scattering is hinted at by the equations for their respective scattering lengths (Eq. (3.38)). In a general target system the variation in nuclear spin and nuclear spin orientation from one nucleus to the next will give a scattering potential that varies throughout the sample. Coherent scattering involves identical scattering from each nucleus and is therefore related to the average of the scattering potential. This leads to the definition of b_{coh} as the average scattering length. The interference between the scattered waves originating from each nucleus probes the collective structure and dynamics of the condensed-phase target. Since the instantaneous deviations from the average scattering potential are distributed at random they lead to an incoherent scattering which involves no interference between scattered waves from different nuclei, and which therefore only probes the single-particle dynamics. The incoherent scattering length b_{inc} is thus defined as the root-mean-square deviation of the scattering length [76].

Most systems scatter neutrons with a combination of coherent and incoherent character. It is clear that the simple scattering system of the previous subsection has a constant scattering potential and will therefore display only coherent scattering. In contrast, a target of a composition such that half the nuclei scatter with length $+b$ and

half scatter with length -b will have an average scattering length of zero. However, the root-mean-square deviation of the scattering length will be nonzero and the target will therefore be a purely incoherent scatterer as long as each type of nucleus is randomly distributed [27]. To give real examples, ^{36}Ar (spin-0) is essentially coherent whereas the scattering from ^{1}H nuclei (spin-$\frac{1}{2}$) is predominantly incoherent.

What of the scattering from liquid para-hydrogen? At first sight, the scattering from an array of ^{1}H nuclei might be expected to be incoherent because their nuclear spins would be able to adopt different angles relative to the neutron and the scattering length will vary with this orientation. However, the internuclear distance in a hydrogen molecule (0.74 Å) is shorter than the typical wavelength of a thermal neutron (~2 Å) and the molecule therefore interacts with such neutrons as a compound spin-0 particle. While this would lead to coherent scattering, a complicating factor in the experimental data used in this chapter is that they were obtained using neutrons of sufficient incident energy to induce the J=0→1 rotational transition in the hydrogen molecule. Since this is clearly a single-particle process the observed scattering is incoherent. Further experimental details will be found in the relevant section (Section 3.5). To facilitate the following discussion and comparison with experiment the remainder of the chapter will be limited to incoherent scattering and the associated 'self' intermediate scattering functions and dynamic structure factors.

3.2.4 Properties of $F_s(\boldsymbol{\kappa}, t)$ and $S_{\text{inc}}(\boldsymbol{\kappa}, \omega)$

This theory section concludes by noting some important properties of the self intermediate scattering function and the incoherent dynamic structure factor.

The first property concerns a symmetry of the liquid para-hydrogen target. In particular, simple liquids are said to be isotropic in the sense that all directions in the fluid are, on average, equivalent. This means that the cross-sections for neutron scattering

from liquid para-hydrogen must be independent of the direction of the momentum transfer vector ($\hbar\boldsymbol{\kappa}$) and can therefore depend only on its magnitude ($\hbar\kappa$). Thus,

$$F_s(\boldsymbol{\kappa}, t) \rightarrow F_s(\kappa, t), \quad ; \quad S_{\text{inc}}(\boldsymbol{\kappa}, \omega) \rightarrow S_{\text{inc}}(\kappa, \omega), \tag{3.42}$$

and the isotropy also ensures that

$$F_s(-\kappa, t) = F_s(\kappa, t). \tag{3.43}$$

The second property is a symmetry inherent to $F_s(\kappa, t)$:

$$F_s(\kappa, -t) = \left(F_s(\kappa, t)\right)^* . \tag{3.44}$$

This can be shown using the isotropy of the liquid, i.e. $F_s(\kappa, -t) = F_s(-\kappa, -t)$, and

$$F_s(-\kappa, -t) = \frac{1}{NZ} \sum_{j=1}^{N} \text{tr} \left[e^{-\beta\hat{H}} e^{+i\boldsymbol{\kappa}\cdot\hat{\mathbf{q}}_j} \, e^{-i\hat{H}t/\hbar} \, e^{-i\boldsymbol{\kappa}\cdot\hat{\mathbf{q}}_j} \, e^{+i\hat{H}t/\hbar} \right] = \left(F_s(\kappa, t)\right)^* . \tag{3.45}$$

In turn this means that $S_{\text{inc}}(\kappa, \omega)$ can be written

$$S_{\text{inc}}(\kappa, \omega) = \frac{1}{\pi} \text{Re} \left[\int_0^\infty dt \, e^{-i\omega t} F_s(\kappa, t) \right] . \tag{3.46}$$

3.3 Calculating $F_s(\kappa, t)$

The previous section employed certain approximations to demonstrate that the neutron-scattering partial differential cross-section, as measured by experiment, can be related to the time correlation function of reciprocal-space particle density fluctuations ($F_s(\kappa, t)$). In many condensed-phase systems this time correlation function will have significant quantum-mechanical character, but an exact quantum-dynamical evalua-

tion of it is presently unfeasible for reasons given in the Introduction. This section will therefore describe two approaches for calculating the approximate quantum dynamics of $F_s(\kappa, t)$, both of which are based upon the RPMD method. The first approach (RPMD-F) is the direct application of the RPMD model to the Kubo transform of $F_s(\kappa, t)$. The second approach (RPMD-G) is required because RPMD-F will be found to fail for the high momentum transfers at which the experimental data were recorded. RPMD-G is a combination of the Gaussian approximation to $F_s(\kappa, t)$ and the direct RPMD treatment of the velocity autocorrelation function.

3.3.1 RPMD-F and multidimensional RPMD

The Kubo transform of $F_s(\kappa, t)$ is labelled $\tilde{F}_s(\kappa, t)$ and has the following exact definition

$$\tilde{F}_s(\kappa, t) = \frac{1}{\beta} \int_0^\beta d\lambda \, F_s^\lambda(\kappa, t), \tag{3.47}$$

where

$$F_s^\lambda(\kappa, t) = \frac{1}{NZ} \sum_{j=1}^{N} \mathrm{tr} \left[e^{-(\beta-\lambda)\hat{H}} e^{-i\boldsymbol{\kappa}\cdot\hat{\mathbf{q}}_j} \, e^{-\lambda\hat{H}} e^{+i\hat{H}t/\hbar} e^{+i\boldsymbol{\kappa}\cdot\hat{\mathbf{q}}_j} \, e^{-i\hat{H}t/\hbar} \right]. \tag{3.48}$$

For reasons of notational simplicity the density operators have been written as functions of $(\boldsymbol{\kappa} \cdot \hat{\mathbf{q}}_j)$ despite the isotropy noted earlier. Clearly $\boldsymbol{\kappa}$ can be chosen in any direction in the isotropic liquid – for example, if it is taken along the x-direction then

$$\boldsymbol{\kappa} \cdot \hat{\mathbf{q}}_j = \kappa \, \hat{x}_j, \tag{3.49}$$

where $\hat{x}_j$ is the position operator for the x-coordinate of the j^{th} nucleus. In a calculation one should in fact average $\tilde{F}_s(\kappa, t)$ over a number of different directions of $\boldsymbol{\kappa}$, as is done in Section 3.5.

In the $3N$ physical dimensions of an N-particle liquid system the RPMD approximation (Eq. (2.22)) to the Kubo-transformed self intermediate scattering function is

$$\tilde{F}_s(\kappa,t) \simeq \frac{1}{(2\pi\hbar)^{3Nn} Z_n} \int d\mathbf{p}(0) \int d\mathbf{q}(0)\, e^{-\beta_n H_n(\mathbf{p}(0),\mathbf{q}(0))} \frac{1}{N} \sum_{j=1}^{N} \rho_j^{-\boldsymbol{\kappa}}(0) \rho_j^{\boldsymbol{\kappa}}(t), \qquad (3.50)$$

where n is the number of ring-polymer beads, $\beta_n{=}\beta/n$, and $H_n(\mathbf{p},\mathbf{q})$ is the classical Hamiltonian for the system of N n-bead ring-polymers

$$H_n(\mathbf{p},\mathbf{q}) = \sum_{j=1}^{N} \sum_{k=1}^{n} \left[\frac{\mathbf{p}_{j,k}^2}{2m} + \frac{1}{2} m\omega_n^2 (\mathbf{q}_{j,k} - \mathbf{q}_{j,k+1})^2 \right] + \sum_{k=1}^{n} V(\mathbf{q}_{1,k}, \ldots, \mathbf{q}_{N,k}). \qquad (3.51)$$

Note that the particle mass m is the same for all degrees of freedom and that, as in the previous chapter, $\omega_n{=}1/(\beta_n\hbar)$ and $\mathbf{q}_{j,0}{=}\mathbf{q}_{j,n}$ for all j. The canonical partition function of the n-bead ring polymer system is

$$Z_n = \frac{1}{(2\pi\hbar)^{3Nn}} \int d\mathbf{p} \int d\mathbf{q}\, e^{-\beta_n H_n(\mathbf{p},\mathbf{q})}, \qquad (3.52)$$

and the particle density functions $\rho_j^{\boldsymbol{\kappa}}(t)$ are averaged over the n beads of the ring-polymer for the j^{th} particle, i.e.,

$$\rho_j^{\boldsymbol{\kappa}}(t) = \frac{1}{n} \sum_{k=1}^{n} e^{+i\boldsymbol{\kappa}\cdot\mathbf{q}_{j,k}(t)}. \qquad (3.53)$$

The Hamiltonian H_n in Eq. (3.51) leads to the equations of motion that are used to evolve the ring-polymer phase-space variables forward in time,

$$\begin{aligned} \dot{\mathbf{p}}_{j,k} &= -m\omega_n^2 \left[2\mathbf{q}_{j,k} - \mathbf{q}_{j,k+1} - \mathbf{q}_{j,k-1} \right] - \frac{\partial V(\mathbf{q}_{1,k}, \ldots, \mathbf{q}_{N,k})}{\partial \mathbf{q}_{j,k}}, \\ \dot{\mathbf{q}}_{j,k} &= \frac{\mathbf{p}_{j,k}}{m}. \end{aligned} \qquad (3.54)$$

These equations constitute a statement of the RPMD model for a system with multiple degrees of freedom. The increased complexity of such a system as compared to the one-dimensional models of the previous chapter has necessitated a change in notation. In the equations above:

(i) $\mathbf{p}$ and $\mathbf{q}$ (without indices) are respectively the momentum and position vectors for the entire ring-polymer system, i.e. they are vectors of length $3Nn$,

(ii) $\mathbf{p}_{j,k}$ and $\mathbf{q}_{j,k}$ are respectively the momentum and position vectors for the k^{th} bead of the j^{th} particle, and are vectors of length 3,

(iii) time is no longer a subscript to variables (or functions) but instead appears as, for example, $\mathbf{p}(t)$, $\mathbf{q}_{j,k}(t)$ or $\rho_j^{\kappa}(t)$. It is frequently suppressed to simplify the notation.

The symmetry of the RPMD-F approximation to $F_s(\kappa,t)$ (Eq. (3.50)) is governed by the fact that it correlates complex functions rather than the real functions considered in the previous chapter (Section 2.3). There, the RPMD model was found to share three important symmetries with the exact Kubo-transformed correlation function and to be a real and even function of time. At first it does not seem that such a statement can be made here because for $A_n^*(\mathbf{q})=B_n(\mathbf{q})$ it is only immediately obvious that the detailed balance (Eq. (2.51)) and time reversal (Eq. (2.56)) symmetries hold. However, due to the reversibility of classical mechanics the RPMD model is an even function of time for *all* position-dependent A_n and B_n and the RPMD-F approximation to $\tilde{F}_s(\kappa,t)$ can therefore be shown to be a real and even function of time. This subsection ends by noting that the standard correlation function $F_s(\kappa,t)$ can be recovered from $\tilde{F}_s(\kappa,t)$ by Fourier-transforming into the frequency domain and applying Eq. (1.15).

3.3.2 RPMD-G and the Gaussian approximation

The Gaussian approximation is derived in Appendix A following the work of Rahman, Singwi and Sjölander [77] – only a brief outline of that derivation is presented here. The first step is to note that the equivalence of the particles at equilibrium in an isotropic liquid means that the self intermediate scattering function (Eq. (3.40)) can be written in the exact form

$$F_s(\kappa,t) = e^{+i\omega_R t}\left\langle e^{+i\hat{H}'t/\hbar}\, e^{-i\hat{H}t/\hbar}\right\rangle = e^{+i\omega_R t}\left\langle \hat{A}(\kappa,t)\right\rangle, \tag{3.55}$$

where the second equality serves to define $\hat{A}(\kappa,t)$ and where the 'recoil frequency',

$$\omega_R = \frac{\hbar\kappa^2}{2m}, \tag{3.56}$$

is such that $\hbar\omega_R$ is the kinetic energy of a previously stationary nucleus after the scattering event, and $\langle\ldots\rangle$ denotes the canonical equilibrium average of Eq. (1.17). The momentum-shifted Hamiltonian is

$$\hat{H}' = \hat{H} + \frac{\hbar}{m}\hat{\mathbf{p}}\cdot\boldsymbol{\kappa}. \tag{3.57}$$

Now, an iterative procedure leads to an exact expression for the thermal average of the operator $\hat{A}(\kappa,t)$, i.e.,

$$\left\langle \hat{A}(\kappa,t)\right\rangle = \sum_{j=0}^{\infty}(-\kappa^2)^j \int_0^t dt_1 \cdots \int_0^{t_{2j-1}} dt_{2j}\ \langle \hat{v}(t_{2j})\cdots\hat{v}(t_1)\rangle\,. \tag{3.58}$$

However, Rahman, Singwi and Sjölander [77] also obtain an additional form for $\left\langle \hat{A}(\kappa,t)\right\rangle$

$$\left\langle \hat{A}(\kappa,t)\right\rangle = \exp\left[\sum_{j=1}^{\infty}(-\kappa^2)^j\gamma_j(t)\right], \tag{3.59}$$

where $\gamma_j(t)$ is a combination of $(k{\leq}j)$-point velocity correlation functions. The physical basis of the Gaussian approximation is that it neglects all contributions to the higher-order velocity correlation functions that appear in expression Eq. (3.58) (e.g. $\langle \hat{v}(t_4) \ldots \hat{v}(t_1) \rangle$) except those that arise from products of two-point correlation functions (e.g. $\langle \hat{v}(t_2)\hat{v}(t_1) \rangle$). In terms of Eq. (3.59) the Gaussian approximation is the assumption that $\gamma_j(t){=}0$ for all $j{>}1$, i.e.,

$$\left\langle \hat{A}(\kappa, t) \right\rangle = e^{-\kappa^2 \gamma_1(t)}, \tag{3.60}$$

and so

$$F_s^g(\kappa, t) = e^{+i\omega_R t}\, e^{-\kappa^2 \gamma_1(t)}. \tag{3.61}$$

Appendix A shows that $\gamma_1(t)$ can be written

$$\gamma_1(t) = \frac{1}{3} \int_0^t dt' \, (t - t') \, c^0_{\mathbf{vv}}(t'), \tag{3.62}$$

where $c^0_{\mathbf{vv}}(t)$ is the velocity autocorrelation function

$$c^0_{\mathbf{vv}}(t) = \frac{1}{Z} \sum_{j=1}^{N} \mathrm{tr} \left[e^{-\beta \hat{H}} \, \hat{\mathbf{v}}_j \cdot e^{+i\hat{H}t/\hbar} \, \hat{\mathbf{v}}_j e^{-i\hat{H}t/\hbar} \right]. \tag{3.63}$$

The RPMD model cannot be used as a direct approximation to the velocity autocorrelation function because it can only be applied to correlation functions that involve position-dependent operators. The $\mathbf{v}_j$ operators correlated in $c^0_{\mathbf{vv}}(t)$ clearly depend on the particle's momentum and not its position. However, consider the following time derivative of the position autocorrelation function

$$\dot{c}^0_{\mathbf{qq}}(t) = \frac{1}{Z} \mathrm{tr} \left[e^{-\beta \hat{H}} \left(-\frac{i}{\hbar} \left[\hat{H}, \hat{\mathbf{q}} \right] \right) e^{+i\hat{H}t/\hbar} \hat{\mathbf{q}} \, e^{-i\hat{H}t/\hbar} \right] = -c^0_{\mathbf{vq}}(t). \tag{3.64}$$

The first equality is obtained by a (commutation-allowed) reordering of the operators

in the trace and the second recognises the Heisenberg equation of motion for $\hat{\mathbf{q}}$. Taking another time derivative yields

$$\ddot{c}^0_{\mathbf{qq}}(t) = -c^0_{\mathbf{vv}}(t). \tag{3.65}$$

This relationship also holds between the Kubo-transformed analogues of the position and velocity autocorrelation functions. Thus, the RPMD approximation (Eq. (2.22)) is applied to $\tilde{c}_{\mathbf{qq}}(t)$ and differentiated twice with respect to time to give an approximate $\tilde{c}_{\mathbf{vv}}(t)$:

$$\tilde{c}_{\mathbf{vv}}(t) \simeq \frac{1}{(2\pi\hbar)^{3Nn} Z_n} \int d\mathbf{p}(0) \int d\mathbf{q}(0)\, e^{-\beta_n H_n(\mathbf{p}(0),\mathbf{q}(0))} \frac{1}{N} \sum_{j=1}^{N} \mathbf{v}_{j,n}(0) \cdot \mathbf{v}_{j,n}(t). \tag{3.66}$$

Many of the quantities in this expression were defined in the previous subsection. The usual ring-polymer equations of motion are implied and the sum over particles is only included to improve the statistics of the calculation. As always in the RPMD model, the correlated functions ($\mathbf{v}_{j,n}$) are averages over the beads of the ring polymer

$$\mathbf{v}_{j,n}(t) = \frac{1}{nm} \sum_{k=1}^{n} \mathbf{p}_{j,k}(t). \tag{3.67}$$

The RPMD-G approach to calculating $F_s^g(\kappa, t)$ involves taking the RPMD approximation to $\tilde{c}_{\mathbf{vv}}(t)$ (Eq. (3.66)) and inverting the Kubo-transform in the frequency domain using the relationship obtained in an earlier chapter (Eq. (1.15)). The approximate $c^0_{\mathbf{vv}}(t)$ is then substituted into Eq. (3.62) to obtain an RPMD approximation to $\gamma_1(t)$ and therefore, via the Gaussian approximation, to $F_s(\kappa, t)$.

Validity

In order to identify the times at which the Gaussian approximation is valid, consider the exact expression for the equilibrium average of $\hat{A}(\kappa,t)$

$$\left\langle \hat{A}(\kappa,t) \right\rangle = \sum_{j=0}^{\infty} (-\kappa^2)^j \int_0^t dt_1 \cdots \int_0^{t_{2j-1}} dt_{2j} \, \langle \hat{v}(t_{2j}) \cdots \hat{v}(t_1) \rangle \, . \tag{3.68}$$

Now, as $t \rightarrow 0$ the time-integrals collapse [77] and

$$\lim_{t\rightarrow 0} \left\langle \hat{A}(\kappa,t) \right\rangle = \sum_{j=0}^{\infty} (-\kappa^2)^j \left\langle \hat{v}^{2j} \right\rangle , \tag{3.69}$$

but for a system with a Gaussian velocity distribution

$$\left\langle \hat{v}^{2j} \right\rangle = \frac{(2j)!}{2^j j!} \left\langle \hat{v}^2 \right\rangle^j . \tag{3.70}$$

The velocity distribution in all classical and harmonic systems is Gaussian, and the non-Gaussian component in anharmonic quantum systems is of order $\hbar^4$ and can often be neglected [84]. In many systems, therefore, the short-time limit of $\left\langle \hat{A}(\kappa,t) \right\rangle$ is indeed given by (the short-time limit of) two-time velocity correlation functions. Since no higher-order velocity correlations contribute, the Gaussian approximation is then exact as $t \rightarrow 0$.

Next consider that each integral in Eq. (3.68) is dominated by those parts of the integrand which have the time variables clustered together. As an example, the four-time correlation function is nonzero only around $t_1 \simeq t_2 \simeq t_3 \simeq t_4$ or, for example, $t_1 \simeq t_2, t_3 \simeq t_4$. This is because all correlation must vanish as any one time is removed from the proximity of the others since the velocity at that time point will become independent of the remaining (clustered) velocities. As the time t increases there are many more ways of grouping the times into pairs than any configuration that involves larger clusters

(e.g. quadruples). Therefore, at long times it is again true that correlations between pairs of velocities dominates $F_s(\kappa, t)$ and so the Gaussian approximation becomes exact as $t \rightarrow \infty$. A more quantitative consideration of the long-time validity of the Gaussian approximation is given in Ref. [77]. In summary, the Gaussian approximation is exact at short and long times, but at intermediate times the nature of the interparticle interaction is important and the Gaussian approximation is not necessarily correct.

The time limits in which the Gaussian approximation is exact determine the range of momentum transfers for which it will be accurate. Thus, high momentum transfers, through the operators $e^{\pm i\kappa\hat{q}}$, set a short length-scale upon which the particle positions become rapidly decorrelated. This means that the correlation function $F_s(\kappa, t)$ decays quickly to zero. Therefore, to the extent that the velocity distribution is Gaussian, the Gaussian approximation is exact at high κ because only short-time information is important. At low κ the correlation function is long-lived and therefore intermediate times become important. Since the Gaussian approximation is not exact at these intermediate times, there is no guarantee that it will be accurate at low momentum transfers.

Time-reversal and 'detailed balance' symmetries

One reason to expect that the RPMD-G method will give an accurate description of incoherent neutron scattering spectra is the pair of time symmetries that the RPMD-G correlation function, $F_s^g(\kappa, t)$, shares with the exact correlation function, $F_s(\kappa, t)$.

The time-reversal symmetry of $F_s(\kappa, t)$ was established (Subsection 3.2.4) as

$$F_s(\kappa, -t) = (F_s(\kappa, t))^* . \tag{3.71}$$

Now consider the effect of the same time inversion ($t \rightarrow -t$) on the Gaussian approxi-

mation (Eq. (3.61)),

$$F_s^g(\kappa, -t) = e^{-i\omega_R t}\, e^{-\kappa^2 \gamma_1(-t)}. \tag{3.72}$$

Changing the integration variable in the $\gamma_1(t)$ function ($\tau' = -t'$) gives

$$\gamma_1(-t) = \frac{1}{3}\int_0^{-t} dt'\,(-t-t')\,c_{\mathbf{vv}}^0(t') = \frac{1}{3}\int_0^{t} d\tau'\,(t-\tau')\,c_{\mathbf{vv}}^0(-\tau'). \tag{3.73}$$

But it is well-known [27] that the exact velocity autocorrelation function (Eq. (3.63)) satisfies its own time-reversal symmetry,

$$c_{\mathbf{vv}}^0(-t) = \left(c_{\mathbf{vv}}^0(t)\right)^*, \tag{3.74}$$

and so

$$\gamma_1(-t) = \gamma_1^*(t), \tag{3.75}$$

or

$$F_s^g(\kappa, -t) = e^{-i\omega_R t}\, e^{-\kappa^2 \gamma_1^*(t)} = \left(F_s^g(\kappa, t)\right)^*, \tag{3.76}$$

in agreement with Eq. (3.71). Significantly, the RPMD approximation to $c_{\mathbf{vv}}^0(t)$ can also be shown to satisfy the time-reversal symmetry (Eq. (3.74)) by the following argument. The analysis of the previous chapter shows that the RPMD approximation to $\tilde{c}_{\mathbf{vv}}(t)$ is a real and even function of time, making its Fourier transform $\tilde{C}_{\mathbf{vv}}(\omega)$ a real and even function of ω. Using Eq. (1.15), the approximate $C_{\mathbf{vv}}^0(\omega)$ therefore satisfies

$$C_{\mathbf{vv}}^0(-\omega) = e^{-\beta\hbar\omega} C_{\mathbf{vv}}^0(\omega), \tag{3.77}$$

and because this $C_{\mathbf{vv}}^0(\omega)$ is also real, the RPMD approximation to $c_{\mathbf{vv}}^0(t)$ indeed possesses the required symmetry (Eq. (3.74)). Therefore, the time-reversal symmetry of the Gaussian approximation (Eq. (3.76)) holds even when the approximate RPMD

velocity autocorrelation function is used.

The other time symmetry that RPMD-G satisfies is most often expressed in the frequency domain

$$S_{\rm inc}(\kappa,-\omega) = e^{-\beta\hbar\omega}\, S_{\rm inc}(\kappa,\omega), \tag{3.78}$$

and called the 'detailed balance' symmetry. An equivalent time-domain expression is

$$(F_s(\kappa,t))^* = F_s(\kappa,t+i\hbar\beta). \tag{3.79}$$

To confirm this, note that it implies

$$S_{\rm inc}(\kappa,-\omega) = \frac{1}{2\pi}\int_{-\infty}^{\infty} dt\, e^{-i\omega t}\, F_s(\kappa,t+i\hbar\beta), \tag{3.80}$$

where the reality of $S_{\rm inc}(\kappa,\omega)$ (Eq. (3.46)) has also been used. Changing integration variables to $t' = t + i\hbar\beta$ gives

$$S_{\rm inc}(\kappa,-\omega) = e^{-\beta\hbar\omega}\,\frac{1}{2\pi}\int_{-\infty+i\hbar\beta}^{\infty+i\hbar\beta} dt'\, e^{-i\omega t'}\, F_s(\kappa,t'), \tag{3.81}$$

and since $F_s(\kappa,\pm\infty+iy)$=0 for $0\leq y\leq\hbar\beta$ a deformation of the integration contour leads to

$$S_{\rm inc}(\kappa,-\omega) = e^{-\beta\hbar\omega}\,\frac{1}{2\pi}\int_{-\infty}^{\infty} dt'\, e^{-i\omega t'}\, F_s(\kappa,t') = e^{-\beta\hbar\omega}\, S_{\rm inc}(\kappa,\omega), \tag{3.82}$$

proving the assertion above.

The question of whether the Gaussian approximation satisfies the 'detailed balance' symmetry in Eq. (3.78) can therefore be addressed through Eq. (3.79). Applying the

Gaussian approximation to each side of that equation gives

$$e^{-i\omega_R t}\, e^{-\kappa^2 \gamma_1^*(t)} = e^{+i\omega_R t}\, e^{-\hbar\omega_R \beta}\, e^{-\kappa^2 \gamma_1(t+i\hbar\beta)}. \tag{3.83}$$

Equating the exponential arguments, and using the definition of ω_R, gives

$$-i\frac{\hbar t}{2m} - \frac{1}{3}\int_0^t dt'\,(t-t')\,\left(c^0_{\mathbf{vv}}(t')\right)^* = +i\frac{\hbar t}{2m} - \frac{\hbar^2\beta}{2m} - \frac{1}{3}\int_0^{t+i\hbar\beta} dt'\,((t+i\hbar\beta)-t')\,c^0_{\mathbf{vv}}(t'), \tag{3.84}$$

after κ^2 has been cancelled from each term. A change of integration variable ($\tau = t' - i\hbar\beta$) allows the integral on the right-hand side to be separated

$$\begin{aligned}\frac{1}{3}\int_0^{t+i\hbar\beta} dt'\,((t+i\hbar\beta)-t')\,c^0_{\mathbf{vv}}(t') \;&=\; \frac{1}{3}\int_0^t d\tau\,(t-\tau)\,\left(c^0_{\mathbf{vv}}(\tau)\right)^* \\ &\quad + \frac{1}{3}\int_{-i\hbar\beta}^0 d\tau\,(t-\tau)\,c^0_{\mathbf{vv}}(\tau+i\hbar\beta),\end{aligned} \tag{3.85}$$

where the 'detailed balance' symmetry of the exact $c^0_{\mathbf{vv}}(\tau)$ for real τ (i.e. the analogue of Eq. (3.79)) has been used. Again, this property is possessed by the RPMD approximation. Substituting Eq. (3.85) into Eq. (3.84) and equating the time-dependent and time-independent parts on each side of the equality then gives two conditions that must hold separately

$$\frac{i\hbar}{m} = \frac{1}{3}\int_{-i\hbar\beta}^0 dt\, c^0_{\mathbf{vv}}(t+i\hbar\beta), \tag{3.86}$$

and

$$\frac{\hbar^2\beta}{2m} = \frac{1}{3}\int_{-i\hbar\beta}^0 dt\, t\, c^0_{\mathbf{vv}}(t+i\hbar\beta). \tag{3.87}$$

Using the notation introduced in Chapter 1 it can be established that

$$\begin{aligned} c^0_{\mathbf{vv}}(t+i\hbar\beta) &= \frac{1}{Z}\mathrm{tr}\left[e^{-\beta\hat{H}}\,\hat{\mathbf{v}}\cdot e^{+i\hat{H}(t+i\hbar\beta)/\hbar}\,\hat{\mathbf{v}}\,e^{-i\hat{H}(t+i\hbar\beta)/\hbar}\right], \\ &= \frac{1}{Z}\mathrm{tr}\left[e^{-(\beta-(\beta-it/\hbar))\hat{H}}\,\hat{\mathbf{v}}\,e^{-(\beta-it/\hbar)\hat{H}}\cdot\hat{\mathbf{v}}\right], \\ &= c^{\beta-\mathrm{it}/\hbar}_{\mathbf{vv}}(0), \end{aligned} \tag{3.88}$$

and that

$$\begin{aligned} c^{\beta-\alpha}_{\mathbf{vv}}(0) &= \frac{1}{Z}\mathrm{tr}\left[e^{-(\beta-(\beta-\alpha))\hat{H}}\,\hat{\mathbf{v}}\,e^{-(\beta-\alpha)\hat{H}}\cdot\hat{\mathbf{v}}\right], \\ &= \frac{1}{Z}\mathrm{tr}\left[e^{-\alpha\hat{H}}\,\hat{\mathbf{v}}\,e^{-(\beta-\alpha)\hat{H}}\cdot\hat{\mathbf{v}}\right], \\ &= c^{\alpha}_{\mathbf{vv}}(0). \end{aligned} \tag{3.89}$$

The first condition is therefore

$$\frac{i\hbar}{m} = \frac{1}{3}\int_{-i\hbar\beta}^{0} dt\, c^{\mathrm{it}/\hbar}_{\mathbf{vv}}(0), \tag{3.90}$$

and on substituing $t = i\hbar\lambda$ becomes

$$\frac{i\hbar}{m} = \frac{i\hbar}{3}\int_{-\beta}^{0} d\lambda\, c^{-\lambda}_{\mathbf{vv}}(0) = \frac{i\hbar}{3}\int_{0}^{\beta} d\lambda'\, c^{\lambda'}_{\mathbf{vv}}(0) = \frac{i\hbar\beta}{3}\tilde{c}_{\mathbf{vv}}(0), \tag{3.91}$$

after a second change of variables $\lambda = -\lambda'$ that reveals the time-zero Kubo-transformed velocity autocorrelation function. Since the RPMD equations, which are exact at t=0, can be used to show that $\tilde{c}_{\mathbf{vv}}(0) = 3/\beta m$, the first condition (Eq. (3.86)) is satified.

Performing the same changes of integration variable on the second condition leaves

$$\frac{\hbar^2\beta}{2m} = \frac{\hbar^2\beta}{3}\left(\frac{1}{\beta}\int_{0}^{\beta} d\lambda\,\lambda\, c^{\lambda}_{\mathbf{vv}}(0)\right). \tag{3.92}$$

The fact that

$$c_{\mathbf{vv}}^{\beta/2+\alpha}(0) = c_{\mathbf{vv}}^{\beta/2-\alpha}(0), \tag{3.93}$$

motivates yet another change of integration variables: $\lambda' = \lambda - \beta/2$ gives

$$\frac{1}{\beta}\int_0^{\beta} d\lambda\, \lambda\, c_{\mathbf{vv}}^{\lambda}(0) = \frac{1}{\beta}\int_{-\beta/2}^{\beta/2} d\lambda'\, \lambda'\, c_{\mathbf{vv}}^{\beta/2+\lambda'}(0) + \frac{\beta}{2}\tilde{c}_{\mathbf{vv}}(0), \tag{3.94}$$

after reversing the change of variables in the second term. The first term can be shown to be zero by splitting the integration at λ'=0 and using Eq. (3.93). The time-zero value of $\tilde{c}_{\mathbf{vv}}(0)$ then confirms that the second condition (Eq. (3.87)) is also satisfied

$$\frac{\hbar^2\beta}{2m} = \frac{\hbar^2\beta}{3}\left(\frac{1}{\beta}\int_0^{\beta} d\lambda\, \lambda\, c_{\mathbf{vv}}^{\lambda}(0)\right) = \frac{\hbar^2\beta}{3}\left(\frac{3}{2m}\right). \tag{3.95}$$

Thus, the Gaussian approximation satisfies 'detailed balance' (Eq. (3.78)) if the velocity autocorrelation function used in the $\gamma_1(t)$ integral does too. It is reasonably easy to show that the RPMD approximation to $c_{\mathbf{vv}}^{0}(t)$ possesses this property by using the real-and-even nature of the RPMD approximation to $\tilde{c}_{\mathbf{vv}}(t)$ to confirm the frequency-domain statement of 'detailed balance' (i.e. Eq. (3.77)). In summary, the fact that these two symmetries are satisfied by the RPMD-G correlation function suggests that it may provide a reasonable approximation to the exact incoherent intermediate scattering function.

3.4 Spectral moment analysis

This section will present exact results for the spectral moments of the incoherent dynamic structure factor, $S_{\mathrm{inc}}(\kappa,\omega)$, and its Kubo-transformed analogue, $\tilde{S}_{\mathrm{inc}}(\kappa,\omega)$. These results are valid at all momentum transfers ($\hbar\kappa$) and can therefore be used as a purely theoretical test of the effect of operator nonlinearity on the accuracy of

the RPMD (i.e. RPMD-F) model. The same tests can also be used to examine the accuracy of the Gaussian approximation (i.e. RPMD-G) across a broad range of κ values.

In this thesis the spectral moments of the incoherent dynamic structure factor $S_{\mathrm{inc}}(\kappa,\omega)$ are defined as being centred on the recoil frequency ω_R (Eq. (3.56)), i.e.,

$$\mu_k(\kappa) = \int_{-\infty}^{\infty} d\omega\, (\omega - \omega_R)^k S_{\mathrm{inc}}(\kappa,\omega), \tag{3.96}$$

although some authors have them centred on ω=0 [85]. Since $F_s(\kappa,t)$ is the inverse Fourier transform of $S_{\mathrm{inc}}(\kappa,\omega)$, i.e.,

$$F_s(\kappa,t) = \int_{-\infty}^{\infty} d\omega\, e^{+i\omega t} S_{\mathrm{inc}}(\kappa,\omega), \tag{3.97}$$

an equivalent definition of $\mu_k(\kappa)$ is

$$\mu_k(\kappa) = i^{-k} \left[\frac{d^k}{dt^k}\left(e^{-i\omega_R t} F_s(\kappa,t)\right)\right]_{t=0}. \tag{3.98}$$

This time-domain expression will be used to derive the first three (k=0, 1, 2) moments of the exact $S_{\mathrm{inc}}(\kappa,\omega)$ [77]. Thus, substituting the exact expression for $F_s(\kappa,t)$ given in Eq. (3.55) and using the exact time-integral expression for the canonical average of $\left\langle \hat{A}(\kappa,t)\right\rangle$ (Eq. (3.58)) gives

$$\mu_k(\kappa) = i^{-k} \left[\frac{d^k}{dt^k}\left(\sum_{j=0}^{\infty}(-\kappa^2)^j \int_0^t dt_1 \cdots \int_0^{t_{2j-1}} dt_{2j}\, \langle \hat{v}(t_{2j}) \cdots \hat{v}(t_1)\rangle\right)\right]_{t=0}. \tag{3.99}$$

For the zeroth (k=0) moment every term in the sum, except j=0, is zero because the integral over dt_1 collapses at t=0. The j=0 term gives

$$\mu_0(\kappa) = 1. \tag{3.100}$$

Now, because

$$\frac{\partial}{\partial x}\int_0^x dy\, f(y) = f(x), \tag{3.101}$$

if $f(y)$ has no explicit dependence on x, the first terms of $\mu_1(\kappa)$ (k=1) are

$$i\mu_1(\kappa) = -\kappa^2 \int_0^t dt_2\, \langle \hat{v}(t_2)\hat{v}(t)\rangle + \kappa^4 \int_0^t dt_2 \int_0^{t_2} dt_3 \int_0^{t_3} dt_4\, \langle \hat{v}(t_4)\hat{v}(t_3)\hat{v}(t_2)\hat{v}(t)\rangle + \cdots . \tag{3.102}$$

Since every term involves an integral from 0 to t that collapses at t=0,

$$\mu_1(\kappa) = 0. \tag{3.103}$$

For $\mu_2(\kappa)$ however, the leading term involves no such integral and

$$-\mu_2(\kappa) = -\kappa^2 \langle \hat{v}(t)\hat{v}(t)\rangle , \tag{3.104}$$

or

$$\mu_2(\kappa) = \frac{\kappa^2}{3} c^0_{\mathbf{vv}}(0) = \frac{2\kappa^2}{3m} \langle KE\rangle , \tag{3.105}$$

where m and $\langle KE\rangle$ are respectively the mass and the average kinetic energy of the scattering nucleus. The latter can be obtained exactly for the liquid para-hydrogen system via a standard PIMD calculation. Continuing the time-derivative analysis in this way provides access to the higher moments of $S_{\mathrm{inc}}(\kappa,\omega)$ [77], although they become more difficult to evaluate and are not needed for the purposes of this chapter.

At first sight, it does not appear to be possible to show that RPMD-F will get any of the $\mu_{k=0,1,2}(\kappa)$ moments correct (the principal difficulty being the analytic inversion of the Kubo transform [86]). The RPMD-F moments will instead be calculated numerically from the simulation results presented in the next section, and comparison with the exact moments derived here will then provide the required test of the accuracy of the

method.

More progress can be made with the moments of the RPMD-G approach. From the equation for the Gaussian approximation (Eq. (3.61)) it is clear that

$$F_s^g(\kappa, 0) = 1, \tag{3.106}$$

since $\gamma_1(0)$=0 (Eq. (3.62)). The Gaussian approximation therefore obtains the zeroth moment $\mu_0(\kappa)$ correctly. Furthermore,

$$\frac{d}{dt}\left(e^{-i\omega_R t} F_s^g(\kappa, t)\right) = -\kappa^2 \dot{\gamma}_1(t) e^{-\kappa^2 \gamma_1(t)}, \tag{3.107}$$

where

$$\dot{\gamma}_1(t) = \frac{1}{3}\int_0^t dt'\, c_{\mathbf{vv}}^0(t'). \tag{3.108}$$

Since $\dot{\gamma}_1(t)$ is zero at t=0, the first (k=1) moment of the Gaussian approximation is also exact. Now,

$$\frac{d^2}{dt^2}\left(e^{-i\omega_R t} F_s^g(\kappa, t)\right) = \left[-\kappa^2 \ddot{\gamma}_1(t) + \left(\kappa^2 \dot{\gamma}_1(t)\right)^2\right] e^{-\kappa^2 \gamma_1(t)}. \tag{3.109}$$

The results for $\gamma_1(0)$ and $\dot{\gamma}_1(0)$ combine with

$$\ddot{\gamma}_1(0) = \frac{1}{3} c_{\mathbf{vv}}^0(0), \tag{3.110}$$

to show that the Gaussian approximation gives the first three moments correctly if the exact velocity autocorrelation function is used in the $\gamma_1(t)$ integral. However, the RPMD-G approach uses the approximate RPMD velocity correlation function and is therefore only guaranteed to get $\mu_0(\kappa)$ and $\mu_1(\kappa)$ correct. The extent to which the RPMD-G $\mu_2(\kappa)$ agrees with the (numerically) exact result obtained by PIMD provides

a useful test of the accuracy of the RPMD approximation to $c^0_{\mathbf{vv}}(t)$.

The *Kubo-transformed* incoherent dynamic structure factor,

$$\tilde{S}_{\mathrm{inc}}(\kappa,\omega) = \frac{1}{2\pi}\int_{-\infty}^{\infty} dt\, e^{-i\omega t}\, \tilde{F}_s(\kappa,t), \tag{3.111}$$

gives rise to another set of spectral moments which are defined as

$$\tilde{\mu}_k(\kappa) = \int_{-\infty}^{\infty} d\omega\, \omega^k\, \tilde{S}_{\mathrm{inc}}(\kappa,\omega) = i^{-k}\left[\frac{d^k \tilde{F}_s(\kappa,t)}{dt^k}\right]_{t=0}, \tag{3.112}$$

where $\tilde{F}_s(\kappa,t)$ is the Kubo-transformed self intermediate scattering function (Eq. (3.47) and Eq. (3.48)). The exact $\tilde{\mu}_{k=0,1,2}(\kappa)$ moments can be used as additional tests of the accuracy of the two approximate RPMD schemes. Firstly, the reality (Eq. (3.46)) and 'detailed balance' symmetry (Eq. (3.78)) of $S_{\mathrm{inc}}(\kappa,\omega)$, together with the frequency-domain relationship

$$\tilde{S}_{\mathrm{inc}}(\kappa,\omega) = \frac{\beta\hbar\omega}{1-e^{-\beta\hbar\omega}} S_{\mathrm{inc}}(\kappa,\omega), \tag{3.113}$$

ensure that $\tilde{S}_{\mathrm{inc}}(\kappa,\omega)$ is a real and even function of ω. It is therefore immediately clear that all odd-k moments of $\tilde{S}_{\mathrm{inc}}(\kappa,\omega)$ are zero. Secondly, the first two even moments are [87]

$$\tilde{\mu}_0(\kappa) = \tilde{F}_s(\kappa,0) \equiv \chi_s(\kappa), \tag{3.114}$$

and

$$\tilde{\mu}_2(\kappa) = \frac{\kappa^2}{\beta m}, \tag{3.115}$$

where $\chi_s(\kappa)$ is the 'static susceptibility' function. The second moment increases quadratically with the magnitude of the momentum transfer and indicates that, if higher moments are neglected, the incoherent dynamic structure factor broadens as κ increases. This is consistent with a more rapid decay of $\tilde{F}_s(\kappa,t)$ as the particle positions quickly decorrelate on the short length-scales defined by large momentum

transfers. In fact, higher moments cannot always be neglected – in many liquids $\tilde{\mu}_4(\kappa)$ dips around κ=2 Å^{-1} [85], which corresponds to a length that is typical of liquid-phase interparticle separations. This is the 'narrowing' phenomenon identified by de Gennes, in which persistent structure at certain wavelengths causes slow decorrelation of the particle positions and long-lived neutron scattering correlation functions [85].

What of the Kubo-transformed spectral moments calculated by the approximate RPMD F method? Since the RPMD model is exact in the time-zero limit, RPMD-F is guaranteed to give the correct $\tilde{\mu}_0(\kappa)$. Furthermore, it has already been argued that the RPMD approximation to $\tilde{F}_s(\kappa,t)$ is a real and even function of time (Subsection 3.3.1). This property allows the approximate $\tilde{S}_{\mathrm{inc}}(\kappa,\omega)$ to be written

$$\tilde{S}_{\mathrm{inc}}(\kappa,\omega) = \frac{1}{\pi}\int_0^\infty dt\,\cos(\omega t)\tilde{F}_s(\kappa,t), \tag{3.116}$$

which is clearly a real and even function of ω. Therefore RPMD-F correctly predicts that all the odd-k moments, including $\tilde{\mu}_1(\kappa)$, are zero.

This leaves the RPMD-F result for $\tilde{\mu}_2(\kappa)$, which is related to the second time derivative of the RPMD approximation to $\tilde{F}_s(\kappa,t)$ by Eq. (3.112). The statistical equivalence of the particles in an isotropic liquid means that only one of them need be considered in the formal expression for the incoherent correlation function, thus taking j=1 in Eq. (3.50) gives

$$\tilde{F}_s(\kappa,t) \simeq \frac{1}{(2\pi\hbar)^{3Nn}Z_n}\int d\mathbf{p}(0)\int d\mathbf{q}(0)\, e^{-\beta_n H_n(\mathbf{p}(0),\mathbf{q}(0))}\rho_1^{-\boldsymbol{\kappa}}(0)\rho_1^{\boldsymbol{\kappa}}(t). \tag{3.117}$$

The Fourier-space density function now involves the positions $\mathbf{q}_{1,l}$ of the l=1, ..., n

ring-polymer beads representing the j=1 particle,

$$\rho_1^{\boldsymbol{\kappa}}(t) = \frac{1}{n}\sum_{l=1}^{n} e^{+i\boldsymbol{\kappa}\cdot\mathbf{q}_{1,l}(t)}. \tag{3.118}$$

Suppressing the redundant particle index, the first time derivative of this correlation function is

$$\frac{d\tilde{F}_s(\kappa,t)}{dt} \simeq \frac{1}{(2\pi\hbar)^{3Nn}Z_n}\int d\mathbf{p}(0)\int d\mathbf{q}(0)\, e^{-\beta_n H_n(\mathbf{p}(0),\mathbf{q}(0))}\rho^{-\boldsymbol{\kappa}}(0)\dot{\rho}^{\boldsymbol{\kappa}}(t), \tag{3.119}$$

but the conservation of phase-space volume [27], the time-reversibility of the ring-polymer dynamics (Eq. (2.54)), and the $\mathbf{p}$-inversion symmetry of the ring-polymer Hamiltonian can be used to convert this expression to

$$\frac{d\tilde{F}_s(\kappa,t)}{dt} \simeq \frac{-1}{(2\pi\hbar)^{3Nn}Z_n}\int d\mathbf{p}(0)\int d\mathbf{q}(0)\, e^{-\beta_n H_n(\mathbf{p}(0),\mathbf{q}(0))}\dot{\rho}^{-\boldsymbol{\kappa}}(0)\rho^{\boldsymbol{\kappa}}(t). \tag{3.120}$$

Taking the second time derivative and setting t=0 gives

$$\left.\frac{d^2\tilde{F}_s(\kappa,t)}{dt^2}\right|_{t=0} \simeq \frac{-1}{(2\pi\hbar)^{3Nn}Z_n}\int d\mathbf{p}\int d\mathbf{q}\, e^{-\beta_n H_n(\mathbf{p},\mathbf{q})}\dot{\rho}^{-\boldsymbol{\kappa}}\dot{\rho}^{\boldsymbol{\kappa}}, \tag{3.121}$$

and because

$$\dot{\rho}^{\boldsymbol{\kappa}} = \frac{i}{nm}\sum_{l=1}^{n}\boldsymbol{\kappa}\cdot\mathbf{p}_l\, e^{+i\boldsymbol{\kappa}\cdot\mathbf{q}_l}, \tag{3.122}$$

where $\mathbf{p}_l$ is the momentum conjugate to $\mathbf{q}_l$, the result is

$$\left.\frac{d^2\tilde{F}_s(\kappa,t)}{dt^2}\right|_{t=0} \simeq \frac{-1}{n^2m^2}\sum_{k,l=1}^{n}\frac{1}{(2\pi\hbar)^{3Nn}Z_n}\int d\mathbf{p}\int d\mathbf{q} e^{-\beta_n H_n(\mathbf{p},\mathbf{q})}\,(\boldsymbol{\kappa}\cdot\mathbf{p}_k)(\boldsymbol{\kappa}\cdot\mathbf{p}_l)\, e^{-i\boldsymbol{\kappa}\cdot(\mathbf{q}_k-\mathbf{q}_l)}. \tag{3.123}$$

However, any term in the double sum with $k\neq l$ involves an integrand that is an odd function of $\mathbf{p}_l$ (and also of $\mathbf{p}_k$) and the corresponding integral is therefore zero. Only

the diagonal terms are nonzero, i.e.,

$$\left.\frac{d^2\tilde{F}_s(\kappa,t)}{dt^2}\right|_{t=0} \simeq \frac{-1}{n^2m^2}\sum_{l=1}^{n}\frac{1}{(2\pi\hbar)^{3Nn}Z_n}\int d\mathbf{p}\int d\mathbf{q}\, e^{-\beta_n H_n(\mathbf{p},\mathbf{q})}\,(\boldsymbol{\kappa}\cdot\mathbf{p}_l)^2. \tag{3.124}$$

Each term in the sum can be considered separately and is

$$\frac{\int d\mathbf{p}\int d\mathbf{q}\, e^{-\beta_n H_n(\mathbf{p},\mathbf{q})}\,(\boldsymbol{\kappa}\cdot\mathbf{p}_l)^2}{\int d\mathbf{p}\int d\mathbf{q}\, e^{-\beta_n H_n(\mathbf{p},\mathbf{q})}} = \frac{\int d\mathbf{p}_l\, e^{-\beta_n(\mathbf{p}_l)^2/2m}\,(\boldsymbol{\kappa}\cdot\mathbf{p}_l)^2}{\int d\mathbf{p}_l\, e^{-\beta_n(\mathbf{p}_l)^2/2m}}, \tag{3.125}$$

since all the integrals except the one over $\mathbf{p}_l$ cancel with an equivalent in the ring-polymer partition function (see definition of Z_n in Eq. (3.52)). With the notation $\mathbf{p}_l = (p_x, p_y, p_z)^T$ such that $(\boldsymbol{\kappa}\cdot\mathbf{p}_l)^2 = (\kappa_x p_x + \kappa_y p_y + \kappa_z p_z)^2$, the right-hand side separates further

$$\frac{\int d\mathbf{p}_l\, e^{-\beta_n(\mathbf{p}_l)^2/2m}\,(\boldsymbol{\kappa}\cdot\mathbf{p}_l)^2}{\int d\mathbf{p}_l\, e^{-\beta_n(\mathbf{p}_l)^2/2m}} = \sum_{\zeta=x,y,z}\left[\kappa_\zeta^2\frac{\int dp_\zeta\, e^{-\beta_n p_\zeta^2/2m}\,p_\zeta^2}{\int dp_\zeta\, e^{-\beta_n p_\zeta^2/2m}}\right] \tag{3.126}$$

because any cross-terms (e.g. $\kappa_x\kappa_y p_x p_y$) are again odd functions of two of the momenta and therefore integrate to zero. The Gaussian integrals are easily evaluated, and leave

$$\sum_{\zeta=x,y,z}\left[\kappa_\zeta^2\frac{\int dp_\zeta\, e^{-\beta_n p_\zeta^2/2m}\,p_\zeta^2}{\int dp_\zeta\, e^{-\beta_n p_\zeta^2/2m}}\right] = \frac{m}{\beta_n}\kappa^2, \tag{3.127}$$

since $\kappa^2 = \kappa_x^2 + \kappa_y^2 + \kappa_z^2$. Finally, summing over all l=1, ..., n identical terms gives

$$\left.\frac{d^2\tilde{F}_s(\kappa,t)}{dt^2}\right|_{t=0} \simeq \frac{-1}{n^2m^2}\left(n\frac{m}{\beta_n}\kappa^2\right) = \frac{-\kappa^2}{m\beta}, \tag{3.128}$$

and so in the approximate RPMD-F method

$$\tilde{\mu}_2(\kappa) = -\left.\frac{d^2\tilde{F}_s(\kappa,t)}{dt^2}\right|_{t=0} = \frac{\kappa^2}{m\beta}, \tag{3.129}$$

in agreement with the exact result. The classical approximation to $\tilde{F}_s(\kappa,t)$ (obtained by setting n=1 in Eq. (3.50)) can be analysed in the same way, and is also found to give $\tilde{\mu}_2(\kappa)$ correctly. However, in contrast to the RPMD-F approach, the classical approximation fails for the zeroth moment $\tilde{\mu}_0$.

A remaining question is whether the RPMD-G method will be exact for any of the Kubo-transformed spectral moments $\tilde{\mu}_k(\kappa)$. Some progress can be made by recalling that the RPMD-G approach satisfies the 'detailed balance' symmetry of $S_{\rm inc}(\kappa,\omega)$ (Eq. (3.78)). In combination with Eq. (3.113) this proves that the RPMD-G approximation to $\tilde{S}_{\rm inc}(\kappa,\omega)$ is a real and even function of ω, and that it therefore correctly predicts that all the odd-k Kubo-transformed moments are zero. Furthermore, it has been shown that [86]

$$\left.\frac{dF_s(\kappa,t)}{dt}\right|_{t=0} = -i\frac{\beta\hbar}{2}\left.\frac{d^2\tilde{F}_s(\kappa,t)}{dt^2}\right|_{t=0}, \tag{3.130}$$

because $\tilde{F}_s(\kappa,t)$ is an even function of time. Since the RPMD-G approach can be shown to give the left-hand side correctly by arguments similar to those following Eq. (3.107) it must also be correct for the right-hand side and thus $\tilde{\mu}_2(\kappa)$. Note that although RPMD-F has been shown to be correct for $d^2\tilde{F}_s(\kappa,t)/dt^2$ and thus $dF_s(\kappa,t)/dt$, it is not exact for the recoil-centred $\mu_1(\kappa)$ because this also involves $F_s(\kappa,0)$ for which the method is incorrect. In order to clarify a potentially confusing discussion, Table 3.1 summarises which of the (six) moments can be shown to be given correctly by each of the approximation schemes. The accuracy with which the remaining moments are obtained will be investigated numerically in the next section.

Table 3.1: Spectral moments of the approximations to $S_{\text{inc}}(\kappa,\omega)$ and $\tilde{S}_{\text{inc}}(\kappa,\omega)$.

Moment	RPMD-F	RPMD-G
$\mu_0(\kappa)$	$\times$	$\surd$
$\mu_1(\kappa)$	$\times$	$\surd$
$\mu_2(\kappa)$	$\times$	$\times$
$\tilde{\mu}_0(\kappa)$	$\surd$	$\times$
$\tilde{\mu}_1(\kappa)$	$\surd$	$\surd$
$\tilde{\mu}_2(\kappa)$	$\surd$	$\surd$

3.5 Results

The first paragraph of this chapter established two main aims. On one hand, the effect of operator nonlinearity on the accuracy of the RPMD model was to be investigated within a realistic model of a multidimensional molecular system, the idea being to go beyond the simple one-dimensional tests of the previous chapter. On the other hand, the final *raison d'être* of methods such as RPMD is the rationalization and/or prediction of experimental results, and so an estimation of accuracy based upon comparison with experiment was also required. These aims are addressed in this section by combining the methodologies and moment tests described previously with a realistic model of [79], and recent experimental data for [22], the liquid para-hydrogen system.

3.5.1 Spectral moment tests

This subsection applies the spectral moment tests derived in Section 3.4 to the results of the RPMD-F method (described in Subsection 3.3.1) in order to examine the effect of operator nonlinearity on the RPMD model. The moment tests are also applied to the results of the RPMD-G approach (described in Subsection 3.3.2) in order to establish

the range of κ values for which this implementation of the Gaussian approximation is valid.

The six exact spectral moments ($\mu_{k=0,1,2}(\kappa)$ and $\tilde{\mu}_{k=0,1,2}(\kappa)$) are valid for the incoherent dynamic structure factors of any isotropic liquid. For the reasons given in the chapter introduction however, the present study focusses on inelastic neutron scattering from liquid para-hydrogen at a temperature of 14 K and a density of 23.5 nm^{-3}. This (T, ρ) state point is the same as that used in a previous RPMD study of the system-size dependence of the self-diffusion constant of liquid para-hydrogen [21]. While these conditions are not identical to the experimental state point, they are similar enough for the purposes of the present work since both T and ρ are within 2.5% of the experimental values [74].

The general details of the RPMD calculations follow those of the previous study [21]. Indeed, some of the approximate velocity autocorrelation functions that were calculated for the determination of self-diffusion constant have been re-used in this work. The Silvera-Goldman potential [79] was adopted for the interaction between each pair of para-hydrogen molecules. As mentioned previously, this potential has been shown to give a rather accurate description of the static equilibrium properties of the liquid [78]. Furthermore, at the low temperature of interest here, the anisotropic part of the potential can be neglected because almost all the molecules are in the spherically-symmetric $J=0$ rotational state. The potential interactions between each pair of ring-polymers was truncated at a centroid-to-centroid distance of 15 a_0 and the usual periodic boundary conditions were employed along with the minimum image convention in order to limit the magnitude of effects arising from the finite size of the simulation cell [1].

For these moment tests a system of only N=108 para-hydrogen molecules was used. This small system size would not be suitable for phenomena that are dependent on large length-scales (e.g. diffusion constants [21]). It is sufficient here because the

moment tests can be applied using exact PIMD calculations of the average kinetic energy $\langle KE \rangle$ and susceptibility function $\chi_s(\kappa)$ at N=108. The $\langle KE \rangle$ is obtained with the standard virial estimator [88] and $\chi_s(\kappa)$ as the $t \rightarrow 0$ limit of $\tilde{F}_s(\kappa, t)$. The standard RPMD algorithm described in Section 2.2 was followed and was found to require n=48 ring-polymer beads for convergence. An initial face-centred cubic lattice of para-hydrogen molecules was relaxed with a 100 ps equilibration phase, and a timestep of 0.5 fs was used throughout the calculations. The RPMD approximation to $\tilde{F}_s(\kappa, t)$ (RPMD-F) was calculated at the lowest 12 values of κ that are consistent with the dimension L of the cubic simulation cell (the 'Laue Condition' [89]):

$$\kappa = \frac{2\pi l}{L} \quad ; \quad l = 1, 2, \ldots . \tag{3.131}$$

The statistical error was reduced by averaging each $\tilde{F}_s(\kappa, t)$ over the six cartesian directions ($\pm x$,$\pm y$ and $\pm z$) for κ. The velocity autocorrelation functions were calculated as the mean of 100 time-averaged ring-polymer trajectories of length 4 ps. This procedure gave $c^0_{\mathbf{vv}}(t)$ out to 2 ps.

The incoherent dynamic structure factors of the RPMD-F and RPMD-G methods are plotted in Fig. 3.2 as a function of the energy transfer $\hbar\omega$ for the different values of the momentum transfer $\hbar\kappa$. The figure shows a growing discrepancy between the results of the two approximate schemes as the momentum transfer is increased. At the lowest κ the RPMD-F and RPMD-G dynamic structure factors are almost indistinguishable. The exact results for $S_{\mathrm{inc}}(\kappa, \omega)$ in this system cannot be calculated, but it is known that in the small κ (or 'diffusive') regime the dynamic structure factor takes the form of a Lorentzian centred on ω=0 and parameterised by the diffusion constant D [27], i.e.,

$$S_{\mathrm{inc}}(\kappa \rightarrow 0, \omega) = \frac{D\kappa^2/\pi}{\omega^2 + (D\kappa^2)^2}. \tag{3.132}$$

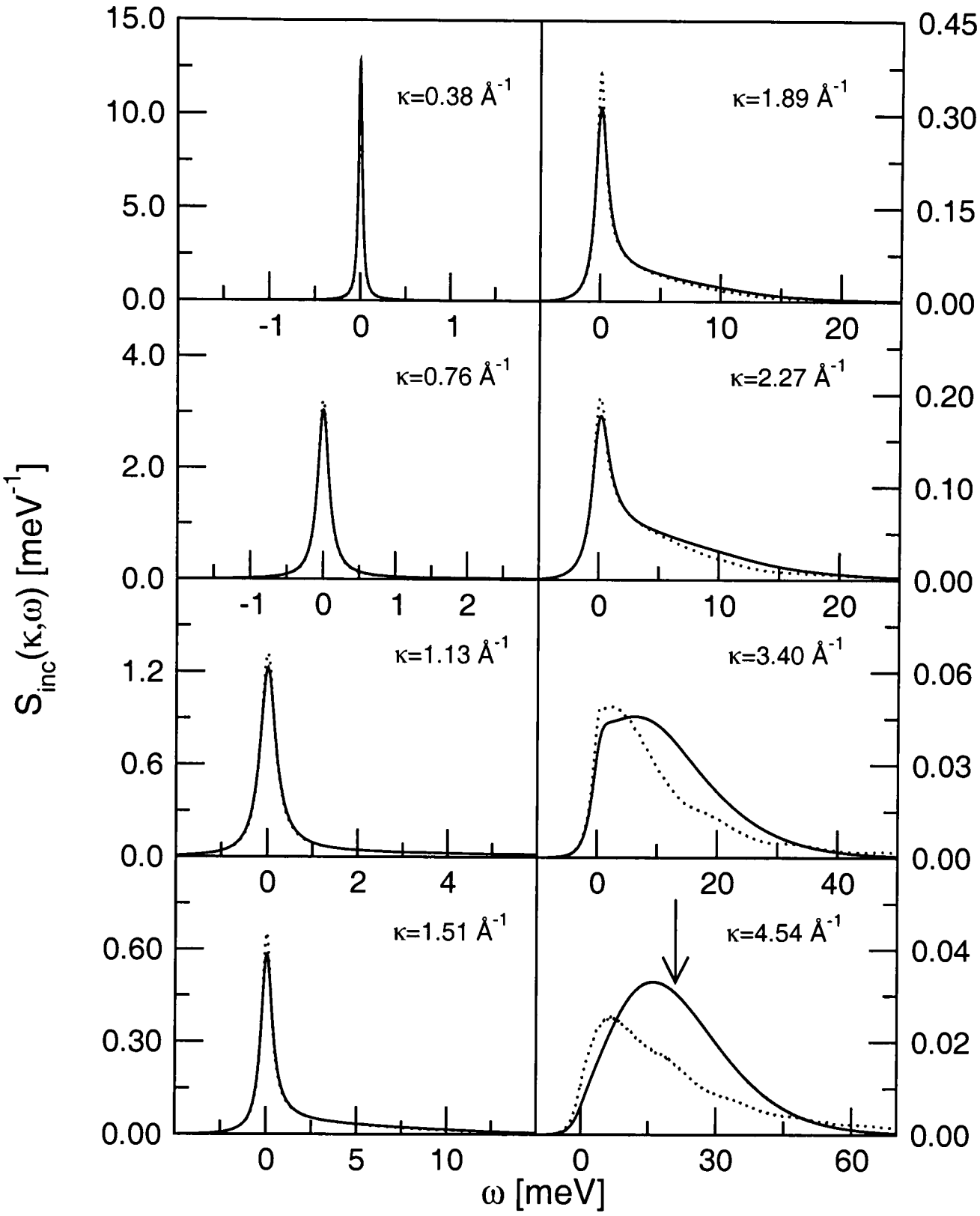

Figure 3.2: Incoherent dynamic structure factors as a function of energy transfer at a broad range of momentum transfers in the liquid para-hydrogen (T=14 K, ρ=23.5 nm^{-3}) system. Both the RPMD-F (dotted line) and the RPMD-G (solid line) approximations are shown. At the highest momentum transfer an arrow indicates the recoil frequency ω_R, defined in Eq. (3.56).

The approximate schemes seem to capture the Lorentzian nature of this limit rather well. At the highest momentum transfers there are significant differences between the RPMD-F and RPMD-G structure factors, perhaps the most striking being the positions of the maxima of the two approximations to $S_{\text{inc}}(\kappa,\omega)$. At κ=4.54 Å^{-1} the peak in the RPMD-F result occurs at a lower frequency than that of the RPMD-G approach. In the large κ (or 'impulsive') limit the dynamic structure factor of a system with a Gaussian velocity distribution is a Gaussian centred on the recoil frequency ω_R (Eq. (3.56)) [76],

$$S_{\text{inc}}(\kappa\rightarrow\infty,\omega)=\left(\frac{\beta_{\text{eff}}m}{2\pi\kappa^2}\right)^{1/2}e^{-\beta_{\text{eff}}m(\omega-\omega_R)^2/2\kappa^2}, \tag{3.133}$$

where $\beta_{\text{eff}}=3/(2\langle KE\rangle)$. The recoil frequency is indicated in the final panel of Fig. 3.2 and it can be seen that, of the two approximate schemes, the peak position of the RPMD-G approach is in better agreement with ω_R.

Whilst the dynamic structure factors in Fig. 3.2 reveal a difference between the two approximate schemes at high momentum transfers, the lack of exact results for $S_{\text{inc}}(\kappa,\omega)$ means that the figure does not directly show which is superior, nor if there is any change in the quality of the RPMD-F approximation as κ (and therefore the operator nonlinearity) increases. However, the previous section established exact results for the spectral moments ($\mu_{k=0,1,2}(\kappa)$) of $S_{\text{inc}}(\kappa,\omega)$ and in Fig. 3.3 these are plotted at all twelve values of κ along with the moments of the RPMD-F and RPMD-G approaches.

The RPMD-F results for all three spectral moments show a severe deterioration at high momentum transfers, and are only accurate below $\kappa\leq$1.5 Å^{-1}. Now, the RPMD-F approach is a direct application of the RPMD model to a Kubo-transformed correlation function ($\tilde{F}_s(\kappa,t)$). In addition, it has already been established that the operators

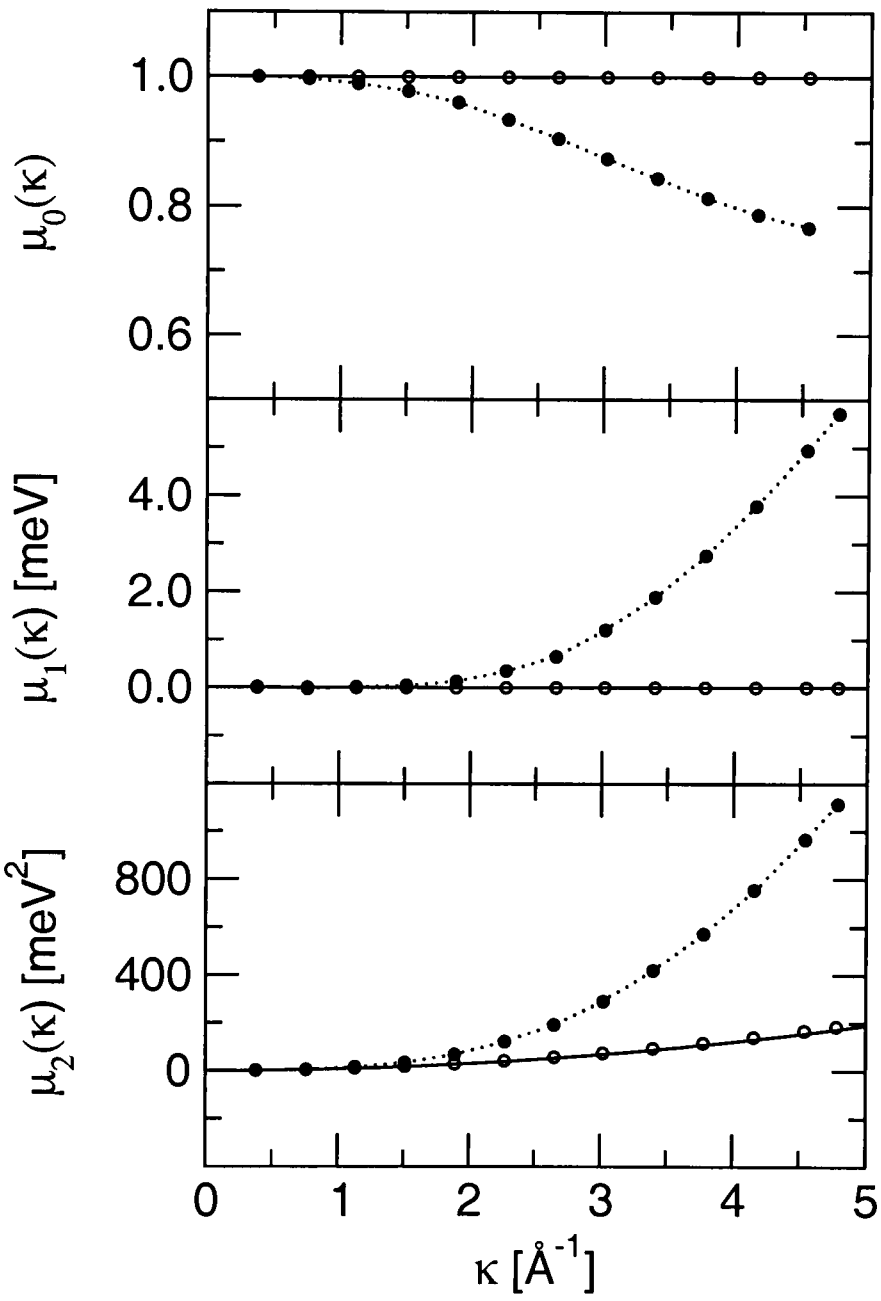

Figure 3.3: The first three moments $\mu_{k=0,1,2}(\kappa)$ of the incoherent dynamic structure factors in Fig. 3.2 as a function of the momentum transfer κ. The exact results are represented as a solid line, the RPMD-F results as filled circles connected by a dotted line, and the RPMD-G results as open circles.

correlated in this $\tilde{F}_s(\kappa, t)$ correlation function become more nonlinear as the momentum transfer $\hbar\kappa$ is increased. Thus, the failure of RPMD-F at high κ shows that the accuracy of the RPMD model does indeed decrease away from the linear operator limit in which (to the extent that the system potential is harmonic) it is exact. The importance of this conclusion is all the greater because it is based upon the results of calculations performed in a multidimensional model of a condensed-phase system. Furthermore, the specific system chosen (liquid para-hydrogen) exhibits significant quantum mechanical effects and is therefore exactly the sort of system for which RPMD is intended. This failure of the RPMD model contrasts with its success for the one-dimensional nonlinear operator problem (Fig. 2.3) of the previous chapter.

The spectral moments tests suggest that the RPMD-F approach will be not be able to generate dynamic structure factors that agree well with the experimental results since they are high κ measurements ($1.78 \leq \kappa[\text{Å}^{-1}] \leq 5.55$). However, all is not lost: the question of whether the RPMD-G approach also breaks down at high κ remains. Of the first set of spectral moments it is only $\mu_2(\kappa)$ that might throw any light on the issue because RPMD-G has been shown to be analytically exact for $\mu_0(\kappa)$ and $\mu_1(\kappa)$. It was previously established (Section 3.4) that both the exact and RPMD-G second moments are proportional to the average kinetic energy of a molecule in the liquid. The exact $\langle KE \rangle$, as calculated by a PIMD calculation for a periodically replicated box of 108 para-hydrogen molecules at T=14 K and ρ=23.5 nm^{-3}, was found to be 5.48 meV in previous work [21]. The same quantity derived from the time-zero value of the RPMD approximation to $c^0_{\mathbf{vv}}(t)$ is 5.83 meV. Thus the deviation of the RPMD-G $\mu_2(\kappa)$ from the exact result is ~6% at all κ, resulting in the considerable improvement on the RPMD-F results seen in the bottom panel of Fig. 3.3.

For confirmation of the superiority of the RPMD-G approach consider the Kubo-transformed spectral moments, $\tilde{\mu}_{k=0,1,2}(\kappa)$, for which RPMD-F is exact at all κ. The

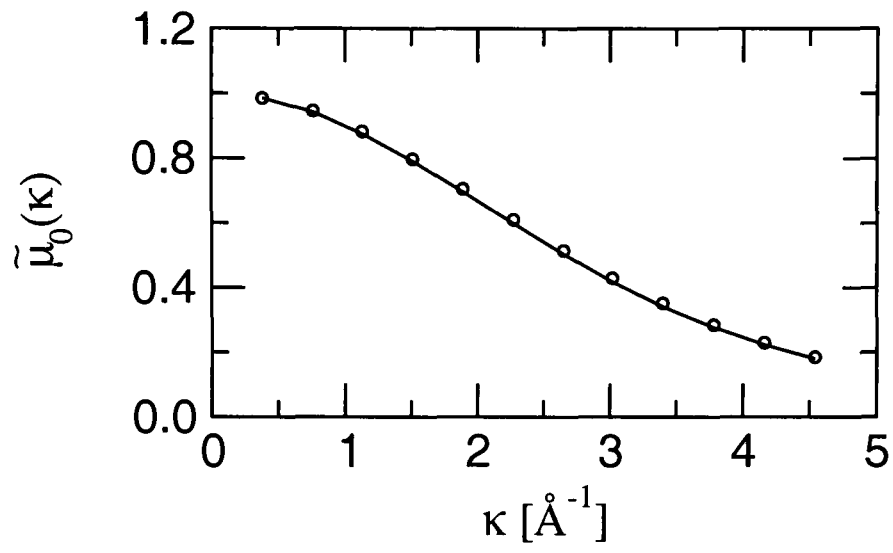

Figure 3.4: The first $\tilde{\mu}_0(\kappa)$ moment of the Kubo-transformed incoherent dynamic structure factor as a function of the momentum transfer κ. The exact result (which coincides with that of the RPMD-F method) is represented as a solid line and the RPMD-G result is indicated with open circles.

RPMD-G approximation to $\tilde{\mu}_0(\kappa)$ is plotted against the exact result in Fig. 3.4, but the two higher moments are not shown because RPMD-G has already been shown to be exact for $\tilde{\mu}_1(\kappa)$ and $\tilde{\mu}_2(\kappa)$ (see the table at the end of Section 3.4). The figure shows that the RPMD-G approximation is in excellent agreement with the exact result at all values of κ considered. Thus, it can be concluded that, in contrast to the RPMD-F approach, the RPMD-G method suffers no serious breakdown at high momentum transfers. It is this approximation scheme which will therefore be used to compute neutron scattering spectra for comparison with the experimental results.

As an endnote to this subsection, the same liquid para-hydrogen system has been studied with two CMD-based approaches [90] (see Section 1.4). One, analogous to RPMD-F, an approximation to $\tilde{F}_s(\kappa, t)$, and the other, analogous to RPMD-G, an implementation of the Gaussian approximation using the CMD approximation to the velocity autocorrelation function. Similar results for the incoherent dynamic structure factors were obtained and spectral moments, although not discussed in any detail, again suggested that the Gaussian approximation was the more accurate of the approaches. In light of this CMD study it is perhaps not surprising the RPMD-G method

is preferable to RPMD-F.

3.5.2 Experimental comparison

Having identified the RPMD-G method as a rather promising approach for calculating the incoherent dynamic structure factors of the liquid para-hydrogen system, the remainder of this section is concerned with using it to generate results than can be compared with the recent experimental work of Colognesi et al. [22].

Before presenting these comparisons some important experimental details must be mentioned. Firstly, the experimental set-up could not scan the energy transfer ($\hbar\omega$) at a constant momentum transfer ($\hbar\kappa$). Instead, the geometry of the experiment dictated that $S_{\mathrm{inc}}(\kappa,\omega)$ could only be measured along two lines in the 'kinematic' (κ,ω) plane. The scattered neutrons were detected at two fixed angles of 42.6° (forward scattering) and 137.7° (backward scattering) relative to the incident neutron pulse. At each angle only those neutrons of a particular (kinetic) energy were recorded: 3.35 meV in the forward direction and 3.32 meV in the backward direction. Because the final energy was fixed, the energy transfer could be controlled by varying the energy of the incident neutrons. However, since the scattering angle is also fixed, the energy transfer dictates the momentum transfer. The kinematic lines, denoted $\kappa_F(\omega)$ and $\kappa_B(\omega)$, can be inferred from the information above and the conservation of energy and linear momentum. The experimental paper contains a figure that depicts these kinematic lines [22].

Secondly, it has already been noted that the experiment measured the cross-section for neutron scattering with a concomitant rotational (and so nuclear spin) transition:

$$n + \mathrm{H}_2(J=0) \rightarrow n + \mathrm{H}_2(J=1). \tag{3.134}$$

The energy transfer therefore contains a component that excites the translational motion of scatterer and a component that produces the rotational transition. The energy relevant to the incoherent dynamic structure factor is the former, and so Colognesi et al. [22] subtracted the latter when reporting their results for $S_{\mathrm{inc}}(\kappa,\omega)$. This frequency shift has a value of $\hbar\omega_{10}$=14.53 meV, which is the J=0 to J=1 spacing of the hydrogen molecule. It must be stressed that the momentum transfers κ_F and κ_B are still determined by the total energy transfer. The quantities that have actually been calculated to compare with the experimental measurements are therefore $S_{\mathrm{inc}}(\kappa_F(\omega'),\omega)$ and $S_{\mathrm{inc}}(\kappa_B(\omega'),\omega)$ where ω'=ω+ω_{10}.

Thirdly, an interesting conclusion of the experimental study was that, taken together, the forward and backward scattering results were not consistent with the Gaussian approximation. In particular, Colognesi et al. [22] used the forward scattering data and the Gaussian approximation to fix the parameters in a (Levesque-Verlet [91]) model of the velocity autocorrelation function. This was then used to generate results along the backward scattering kinematic line. These were found to be in disagreement with the backward scattering experiments, and it was therefore concluded that the two independent sets of experimental data indicated some level of breakdown of the Gaussian approximation [22]. As such, these data should present a real challenge to the current RPMD-G calculations.

Now, for the spectral moments tests it was argued that a system composed of a rather small number of para-hydrogen molecules would suffice because comparison was being made with the exact results for that system size. However, the experimental results are effectively in the infinite system-size limit, and any agreement with the simulation is liable to be impaired by finite system-size effects. The problem is most acute in the low momentum transfer limit since the correlation functions involved are sensitive to dynamics on larger length-scales. Put another way, the incoherent dynamic structure

factor at low κ is determined by the diffusion constant D (Eq. (3.132)). This quantity has been previously shown to increase rather significantly as the number of para-hydrogen molecules in the simulation increases [21]. One would therefore expect the dynamic structure factors to be sensitive to system size in the low κ regime.

For this comparison with experiment, therefore, a larger system was required. Thus, the velocity autocorrelation function was calculated at two (fairly large) system sizes and the results were extrapolated to $N{=}\infty$ with a procedure that will now be described. The earlier RPMD study [21] confirmed that the self-diffusion coefficient of this liquid para-hydrogen system shows the following scaling with N [92, 93]

$$D(N) = D - dN^{-1/3}, \tag{3.135}$$

where $D(N)$ is the diffusion constant for a system of N molecules and d is independent of N. Since

$$D = \frac{1}{3}\int_0^\infty dt\, \tilde{c}_{\mathbf{vv}}(t), \tag{3.136}$$

the (Kubo-transformed) velocity correlation function must also scale with N

$$\tilde{c}_{\mathbf{vv}}(t;N) = \tilde{c}_{\mathbf{vv}}(t) - \tilde{c}(t)N^{-1/3}, \tag{3.137}$$

where

$$D(N) = \frac{1}{3}\int_0^\infty dt\, \tilde{c}_{\mathbf{vv}}(t;N), \tag{3.138}$$

and

$$d = \frac{1}{3}\int_0^\infty dt\, \tilde{c}(t). \tag{3.139}$$

By calculating velocity autocorrelation functions at different system sizes $\tilde{c}(t)$ can be

eliminated from Eq. (3.137). For example, for N_1=864 and N_2=500,

$$\tilde{c}_{\mathbf{vv}}(t) = 6\tilde{c}_{\mathbf{vv}}(t;864) - 5\tilde{c}_{\mathbf{vv}}(t;500). \tag{3.140}$$

This extrapolated Kubo-transformed velocity autocorrelation function was then substituted into the Gaussian approximation (Eq. (3.61)) to generate the RPMD-G incoherent dynamic structure factor along the two kinematic lines, $\kappa_F(\omega')$ and $\kappa_B(\omega')$. The comparison of these results with those of the experiment is now discussed.

The RPMD-G approximation to the incoherent dynamic structure factor along the forward-scattering kinematic line is shown in the upper panel of Fig. 3.5 along with the corresponding experimental measurement of Colognesi et al. [22]. The lower panel shows the RPMD-G and experimental results along the backward-scattering line. Following the procedure adopted by the experimentalists, a small linear term of $(4 \times 10^{-5}\ \mathrm{meV}^{-2})\times\omega$ has been added to the calculated $S_{\mathrm{inc}}(\kappa_B(\omega'),\omega)$ to mimic a frequency-dependent background contribution to the experimental data [22]. No such contribution has been added to the forward scattering results since the experimental measurements in the upper panel have already been corrected for the background term.

The agreement between the RPMD-G and experimental results is not perfect but it is nonetheless remarkably good. There are slightly larger discrepancies along the forward scattering line, and this is consistent with the Gaussian approximation being less reliable at the lower momentum transfers of $\kappa_F(\omega')$ (Subsection 3.3.2 and [77]). In addition, the simulation seems to be unable to exactly reproduce the ω=0 diffusive peaks observed by the experiment along both kinematic lines. The reason for this is not clear – it may be that the isotropic pair potential [79] is inadequate. Certainly, CMD studies that combined the Gaussian approximation with the same pair potential

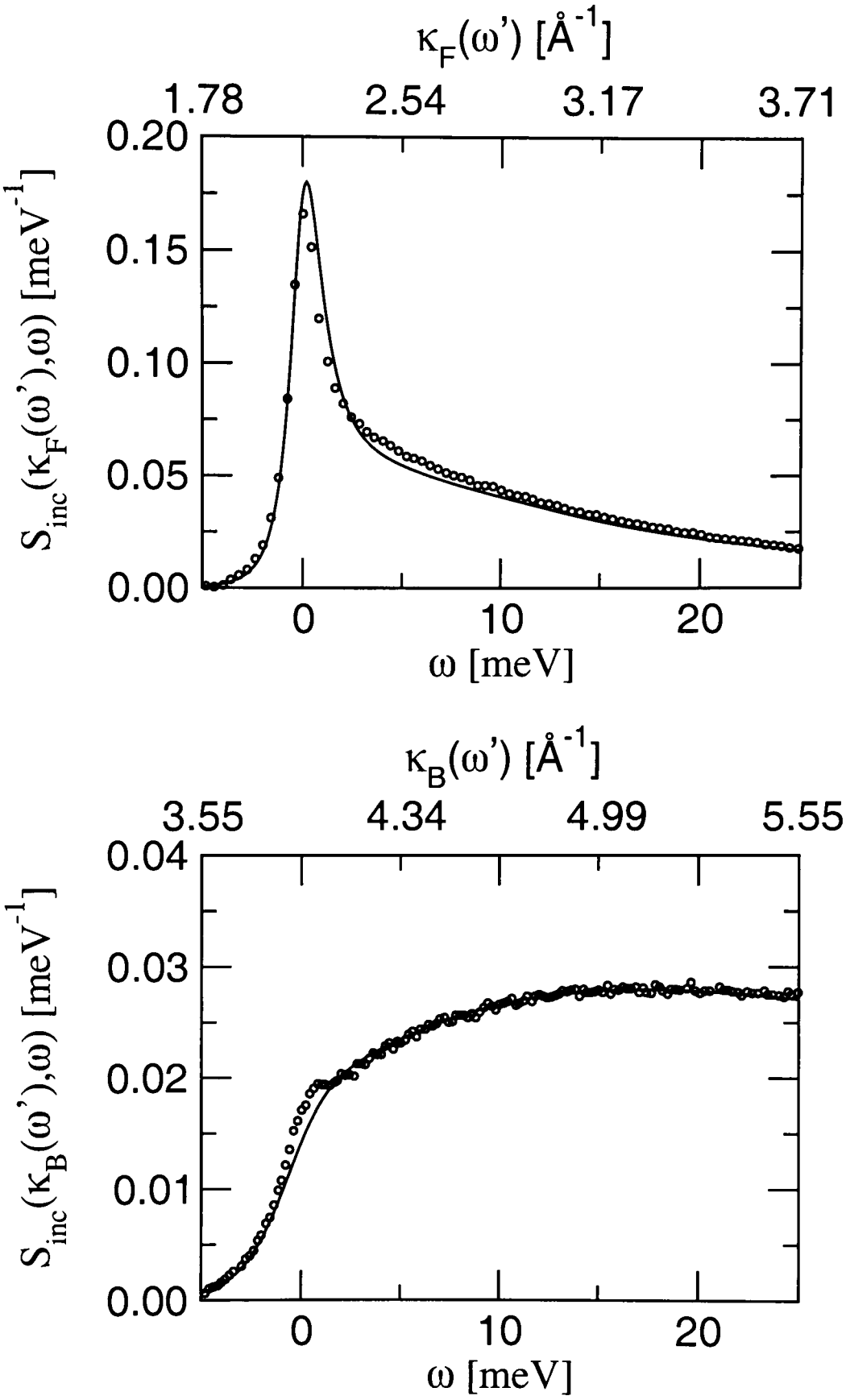

Figure 3.5: The experimental incoherent dynamic structure factor measured along the two kinetic lines ($\kappa_F(\omega')$ and $\kappa_B(\omega')$) and the same quantities calculated by the RPMD-G method. In each panel, both the momentum transfer and the energy transfer are labelled along the abscissa. As outlined in the text, $\omega' = \omega + \omega_{10}$, where $\hbar\omega_{10} = 14.53$ meV is the $J = 0$ to $J = 1$ rotational energy spacing of the hydrogen molecule.

to simulate the results of an earlier version of the current experiment also failed to observe any remnant of the diffusive peak along the backward scattering line [94].

To summarize, the agreement between the results of the RPMD-G approach developed in this chapter and those of the recent experimental work is good. The success of the RPMD-G approach in predicting the incoherent dynamic structure factor of this liquid para-hydrogen system is consistent with its performance in the spectral moments tests of the previous subsection.

3.6 Summary

This investigation of the inelastic neutron scattering from liquid para-hydrogen has firmly established that the quality of the RPMD approximation degrades as the operators involved in the correlation function become more nonlinear. An important consequence of this is that operator nonlinearity should be taken into consideration when the RPMD model is applied to the study of a condensed-phase quantum dynamical process.

Some insight into the nature of this breakdown of the RPMD approximation can be gained by considering neutron scattering from free-motion particles. For a free particle, the motion along each cartesian axis is independent of the others, and therefore the axis defined by the direction of $\boldsymbol{\kappa}$ is the only spatial dimension that needs to be considered. The RPMD-F approximation (Eq. (3.50)) to the self intermediate scattering function of a free particle is thus

$$\tilde{F}_s(\kappa,t) \simeq \frac{1}{(2\pi\hbar)^n Z_n} \int d\mathbf{p}(0) \int d\mathbf{q}(0)\, e^{-\beta_n H_n(\mathbf{p}(0),\mathbf{q}(0))} e^{-i\kappa q_1(0)} \rho^{\boldsymbol{\kappa}}(t), \tag{3.141}$$

if the equivalence of the n ring-polymer beads is exploited. The notation is that used throughout this chapter, and as has been done once before (Section 3.4), the redundant

particle index has been dropped. Thus, $q_1(0)$ is the position of the first ring-polymer bead at t=0 and $\mathbf{p}(0)$ and $\mathbf{q}(0)$ are vectors of length n. The ring-polymer partition function is defined as the single-particle/one-dimension analogue of Eq. (3.52), and $\rho^{\kappa}(t)$ is given by

$$\rho^{\kappa}(t) = \frac{1}{n}\sum_{k=1}^{n} e^{+i\kappa q_k(t)}. \tag{3.142}$$

The free motion ring-polymer Hamiltonian is

$$H_n(\mathbf{p},\mathbf{q}) = \sum_{k=1}^{n}\left[\frac{p_k^2}{2m} + \frac{1}{2}m\omega_n^2(q_k - q_{k+1})^2\right] = \frac{\mathbf{p}^{\mathrm{T}}\cdot\mathbf{p}}{2m} + \frac{1}{2}m\omega_n^2\,\mathbf{q}^{\mathrm{T}}\cdot\mathbf{A}\cdot\mathbf{q}, \tag{3.143}$$

and an analytic diagonalization of the real symmetric matrix $\mathbf{A} = \mathbf{C}\cdot\mathbf{a}\cdot\mathbf{C}^{\mathrm{T}}$ allows it to be written as

$$H_n(\mathbf{P},\mathbf{Q}) = \sum_{k=1}^{n}\left[\frac{P_k^2}{2m} + \frac{1}{2}m\Omega_k^2 Q_k^2\right], \tag{3.144}$$

where the 'normal-mode' coordinates are $\mathbf{Q} \equiv \mathbf{C}^{\mathrm{T}}\cdot\mathbf{q}$ and $\mathbf{P} \equiv \mathbf{C}^{\mathrm{T}}\cdot\mathbf{p}$ and $\Omega_k = 2\omega_n \sin(k\pi/n)$. The meaning of the notation $Q_k(t)$ should be obvious. This normal-mode transformation is discussed in some detail in Appendix B. Here, it means that the correlation function $\tilde{F}_s(\kappa,t)$ becomes

$$\tilde{F}_s(\kappa,t) \simeq \frac{1}{n}\sum_{k=1}^{n} I_k(\kappa,t), \tag{3.145}$$

where the orthogonality of $\mathbf{C}$ has been used to write

$$I_k(\kappa,t) = \frac{\int d\mathbf{P}(0)\int d\mathbf{Q}(0)\, e^{-\beta_n H_n(\mathbf{P}(0),\mathbf{Q}(0))}\exp[-i\kappa\sum_{l=1}^{n}(C_{1l}Q_l(0) - C_{kl}Q_l(t))]}{\int d\mathbf{P}(0)\int d\mathbf{Q}(0)\, e^{-\beta_n H_n(\mathbf{P}(0),\mathbf{Q}(0))}}. \tag{3.146}$$

In the normal-mode representation the ring-polymer Hamiltonian is just a collection of n uncoupled harmonic oscillators and the time-evolution of $Q_l(t)$ can therefore be

written in closed form as

$$Q_l(t) = Q_l(0)\cos(\Omega_l t) + \frac{P_l(0)}{m\Omega_l}\sin(\Omega_l t). \tag{3.147}$$

Substituting this into $I_k(\kappa, t)$ allows the $2n$-dimensional integral to be separated into $2n$ one-dimensional integrals, each of which can be done by completing the square in the exponential argument to leave a simple Gaussian integral. In the case of the zero-frequency mode (l=n) the position integral cancels with an equivalent term in the denominator, and because $C_{kn} = 1/\sqrt{n}$ the final result is

$$\tilde{F}_s(\kappa, t) \simeq e^{-\kappa^2 t^2/2m\beta}\frac{1}{n}\sum_{k=1}^{n}\exp\left[-\frac{\kappa^2}{2\beta_n m}\sum_{l=1}^{n-1}\phi_{kl}(t)\right] \tag{3.148}$$

where

$$\phi_{kl}(t) = \frac{1}{\Omega_l^2}\left(C_{kl}^2 + C_{1l}^2 - 2C_{kl}C_{1l}\cos(\Omega_l t)\right). \tag{3.149}$$

This free-motion RPMD correlation function was evaluated at a (fairly arbitrary) momentum transfer of κ=0.76 Å^{-1} and the corresponding dynamic structure factor ($S_{\rm inc}(\kappa, \omega)$) was obtained with a Fourier transform and the frequency-domain relationship in Eq. (1.15). For consistency with the previous calculations, the number of ring-polymer beads was taken as n=48, the temperature as T=14 K and the mass was that of the hydrogen molecule. The free-motion RPMD dynamic structure factor is plotted in Fig. 3.6 as $\omega^2 S_{\rm inc}(\kappa, \omega)$ so that the high-frequency components are amplified. In order to assess the accuracy of the RPMD expression (Eq. (3.148)), the figure also includes the result of an exact free-motion calculation at this momentum transfer [76].

The exact and RPMD results shown in Fig. 3.6 are almost identical around the zero of

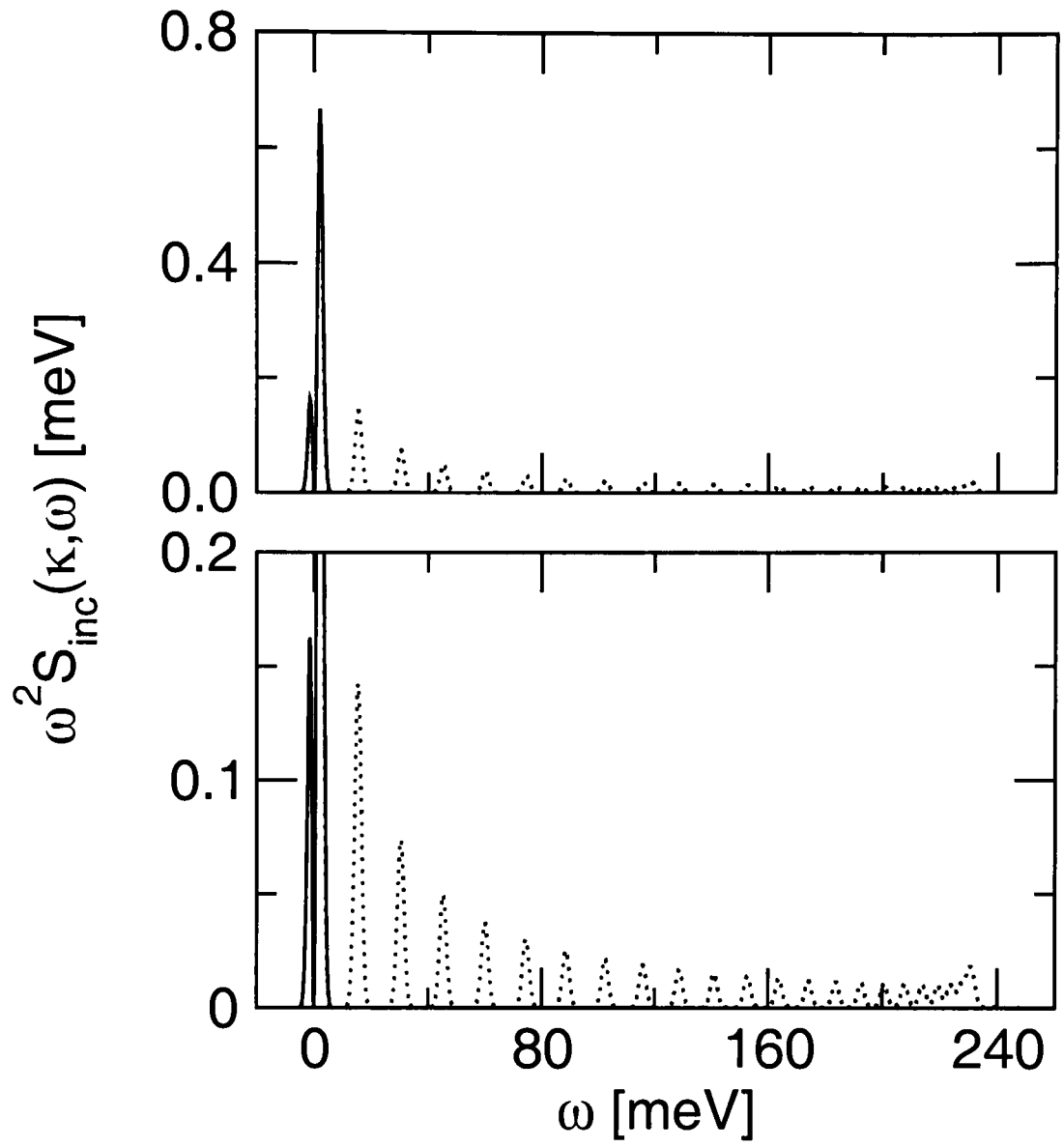

Figure 3.6: Incoherent dynamic structure factors for a free-motion particle with a mass equal to that of the hydrogen molecule at a temperature of 14 K. The upper panel shows the full zero-frequency peak, whereas in the lower panel the ordinate scale has been increased to show the spurious high-frequency peaks in the RPMD result. In both panels, the exact result [76] is represented as a solid line and the RPMD result (Eq. (3.148)) as a dotted line.

the energy transfer ($\omega \leq 10\,\mathrm{meV}$). It is immediately clear, however, that the RPMD dynamic structure factor displays a spurious progression of peaks at higher frequencies. On close inspection, it appears that there may be one such peak for each distinct ring-polymer normal-mode frequency (Ω_l). This implies that these spectral features are due to the oscillations in the kinetic spring system of the ring polymer. The amplitude of these oscillations is so low that they would not be observed in the correlation function that corresponds to $S_{\mathrm{inc}}(\kappa, \omega)$. Furthermore, they are only problematic at high κ where the relevant length-scale is short enough to expose the artifical internal structure of the ring polymer. The amplitude of the oscillations is then sufficient to significantly degrade the accuracy of the spectral moments of the dynamic structure factor, as illustrated in Fig. 3.3.

In conclusion, the data from a recent experiment on neutron scattering from liquid para-hydrogen were recorded at high momentum transfers for which the RPMD-F approach is inaccurate due to the problems with operator nonlinearity identified and analysed above. However, a simple solution to this problem is available in the form of the Gaussian approximation, to which the only dynamical input is the velocity autocorrelation function. The RPMD-G approach combines this Gaussian approximation with the RPMD evaluation of the velocity autocorrelation function and has been shown to differ from RPMD-F in that it suffers no degradation in accuracy at high momentum transfers. On the contrary, this approach was found to be remarkably effective for computing the incoherent dynamic structure factors of liquid para-hydrogen, giving excellent, almost quantitative, agreement with the experimental data.

Chapter 4

Chemical reaction rates

Accurate quantum-mechanical methods for studying the details of small-molecule chemical reactions in the gas-phase are well-established and have been highly successful [24]. However, it has not yet been possible to provide a general and exact quantum-mechanical approach that can be used to evaluate the reaction rates in more complex molecular systems (e.g. clusters, surfaces, solutions and biomolecules), despite the importance of such processes [23].

There are, of course, computationally feasible methods that provide a *classical* description of chemical dynamics [95–97], and for many condensed-phase reactive systems these approaches are perfectly adequate. However, one has only to look as far as the fundamental biological processes of photosynthesis [98] or enzymatic catalysis [99, 100] to find examples of reactions in complex systems for which quantum-mechanical effects are thought to play a crucial role. For reasons that are widely-known [12], the exact quantum-mechanical techniques that have been so successful for studying small-molecule gas-phase reactions are not directly applicable to reactions in larger systems. Therefore, because of the interest in studying such processes computationally [12, 23], there is a need for approximate quantum-mechanical approaches that are capable of calculating chemical reaction rates in condensed-phase systems.

This chapter will develop such a method by combining an exact correlation function formulation of the canonical rate coefficient [25, 101, 102] with the RPMD approximation of Chapter 2. For clarity, the discussion in this chapter restricts itself to one-dimensional bimolecular reactions – multi-dimensional reactive systems are considered in the next chapter. Much of this work appears in Refs. [103] and [104].

4.1 Correlation function formulation of $k(T)$

A one-dimensional model for a chemical reaction has the Hamiltonian,

$$\hat{H} = H(\hat{p}, \hat{q}) = \frac{\hat{p}^2}{2m} + V(\hat{q}), \tag{4.1}$$

where p and q are respectively the momentum and position along a 'reaction' coordinate and m is the relevant mass. For an activated bimolecular reaction, $V(q)$ is a barrier potential that tends to constant values as $q \to \pm\infty$. By adopting the asymptotic form of the scattering wavefunction to evaluate the reactive flux through a surface located in the asymptotic region of this potential, and by using the fact that the flux from a time-independent wavefunction through a closed surface is zero (*vide infra*), Miller derived the following equation for the canonical rate coefficent [25, 102]:

$$\begin{aligned} k(T) &= \lim_{t\to\infty} \frac{1}{Q_r(T)} \mathrm{tr}\left[e^{-\beta\hat{H}/2} \hat{F}\, e^{-\beta\hat{H}/2} e^{+i\hat{H}t/\hbar} \hat{h}\, e^{-i\hat{H}t/\hbar} \right], \\ &\equiv \frac{1}{Q_r(T)} \lim_{t\to\infty} c_{\mathrm{fs}}^{\beta/2}(t). \end{aligned} \tag{4.2}$$

Here $\beta{=}1/k_B T$ and $Q_r(T)$ is the reactant partition function per unit length (for a one-dimensional bimolecular reaction). The second line defines the 'symmetrically thermalized' flux-side correlation function ($c_{\mathrm{fs}}^{\beta/2}(t)$) in terms of the step function oper-

ator $\hat{h}$,

$$\hat{h} = h(\hat{q} - q^{\ddagger}), \tag{4.3}$$

and its time derivative, the flux operator $\hat{F}$,

$$\hat{F} = \frac{i}{\hbar}\left[\hat{H}, \hat{h}\right]. \tag{4.4}$$

The former operator projects onto the product side of the dividing surface $q = q^{\ddagger}$, i.e. for a position eigenstate $|q\rangle$,

$$\begin{aligned} \hat{h}|q\rangle &= 0, \quad q < q^{\ddagger}, \\ &= |q\rangle, \quad q \geq q^{\ddagger}. \end{aligned} \tag{4.5}$$

Since $dh(\hat{q})/dq = \delta(\hat{q})$ the flux operator is

$$\hat{F} = \frac{1}{2m}\left[\hat{p}\,\delta(\hat{q} - q^{\ddagger}) + \delta(\hat{q} - q^{\ddagger})\,\hat{p}\right]. \tag{4.6}$$

The rate coefficient expression (Eq. (4.2)) contains the compound operator

$$\hat{\mathcal{P}} = \lim_{t\to\infty} e^{+i\hat{H}t/\hbar}\,\hat{h}\,e^{-i\hat{H}t/\hbar}, \tag{4.7}$$

which projects onto all states which reside in the product region as $t \to \infty$. Thus, this formulation gives the canonical rate coefficient in terms of a thermally-weighted average correlation between the flux through a dividing surface at $t=0$ and the product-side population as $t \to \infty$.

The rate coefficient can also be related to the (symmetrically-thermalized) 'side-side'

correlation function

$$c_{\rm ss}^{\beta/2}(t) = {\rm tr}\left[e^{-\beta\hat{H}/2}\hat{h}\,e^{-\beta\hat{H}/2}e^{+i\hat{H}t/\hbar}\hat{h}\,e^{-i\hat{H}t/\hbar}\right]. \tag{4.8}$$

To see this, consider reordering the operators in the trace of this correlation function:

$$c_{\rm ss}^{\beta/2}(t) = {\rm tr}\left[e^{-\beta\hat{H}/2}e^{-i\hat{H}t/\hbar}\hat{h}\,e^{+i\hat{H}t/\hbar}e^{-\beta\hat{H}/2}\hat{h}\right], \tag{4.9}$$

so that

$$\begin{aligned}\frac{d}{dt}c_{\rm ss}^{\beta/2}(t) &= -{\rm tr}\left[e^{-\beta\hat{H}/2}e^{-i\hat{H}t/\hbar}\frac{i}{\hbar}\left[\hat{H},\hat{h}\right]\,e^{+i\hat{H}t/\hbar}e^{-\beta\hat{H}/2}\hat{h}\right], \\ &= -c_{\rm fs}^{\beta/2}(t),\end{aligned} \tag{4.10}$$

where the final equality involves reversing the operator reordering and using Eq. (4.4).

From Eq. (4.2)

$$k(T) = -\frac{1}{Q_r(T)}\lim_{t\to\infty}\frac{d}{dt}c_{\rm ss}^{\beta/2}(t). \tag{4.11}$$

The fact that the flux operator is the Heisenberg time derivative of the step function operator can be used again to obtain a third equivalent formulation of $k(T)$. Since $c_{\rm fs}^{\beta/2}(t)$ is an odd function of time, the trace in Eq. (4.2) is zero at t=0 [25] and therefore

$$\begin{aligned}k(T) &= \frac{1}{Q_r(T)}\left|{\rm tr}\left[e^{-\beta\hat{H}/2}\hat{F}\,e^{-\beta\hat{H}/2}e^{+i\hat{H}t/\hbar}\hat{h}\,e^{-i\hat{H}t/\hbar}\right]\right|_{t=0}^{t=\infty} \\ &= \frac{1}{Q_r(T)}\int_0^\infty dt\,c_{\rm ff}^{\beta/2}(t),\end{aligned} \tag{4.12}$$

where

$$\begin{aligned} c_{\mathrm{ff}}^{\beta/2}(t) &= \frac{d}{dt}\mathrm{tr}\left[e^{-\beta\hat{H}/2}\hat{F}\,e^{-\beta\hat{H}/2}e^{+i\hat{H}t/\hbar}\hat{h}\,e^{-i\hat{H}t/\hbar}\right] \\ &= \mathrm{tr}\left[e^{-\beta\hat{H}/2}\hat{F}\,e^{-\beta\hat{H}/2}e^{+i\hat{H}t/\hbar}\frac{i}{\hbar}\left[\hat{H},\hat{h}\right]\,e^{-i\hat{H}t/\hbar}\right] \\ &= \mathrm{tr}\left[e^{-\beta\hat{H}/2}\hat{F}\,e^{-\beta\hat{H}/2}e^{+i\hat{H}t/\hbar}\hat{F}\,e^{-i\hat{H}t/\hbar}\right]. \end{aligned} \tag{4.13}$$

There are many attractive features of these correlation function expressions for $k(T)$ (Eq. (4.2), Eq. (4.11) and Eq. (4.12)). Firstly, they are as valid in many-dimensional systems as for the one-dimensional case presented here [102]. Secondly, they provide a direct means of evaluating the reaction rate coefficient without first having to calculate all the state-to-state reaction probabilities [25]. Thirdly, at least for bimolecular reactions, the correlation functions involving the flux operator only require the evaluation of the dynamics in the region surrounding a well-chosen dividing-surface. Thus, only a relatively short time-evolution is required to obtain $k(T)$.

Another property of these exact expressions for $k(T)$ is that they are independent of the choice of dividing surface $q^{\ddagger}$, i.e. they do not depend on how one chooses to distinguish reactants from products. This feature is of course shared by any exact formulation of the rate coefficient, but it is absent from many approximate treatments. The independence can be established as follows: Eq. (4.12) is rewritten as,

$$k(T)Q_r(T) = \int_0^{\infty} dt\, c_{\mathrm{ff}}^{\beta/2}(t) = \frac{1}{2}\int_{-\infty}^{\infty} dt\, c_{\mathrm{ff}}^{\beta/2}(t), \tag{4.14}$$

because $c_{\mathrm{ff}}^{\beta/2}(t)$ is an even function of time. The time-evolution operators in this correlation function can then be expressed as

$$e^{\pm i\hat{H}t/\hbar} = \int_{-\infty}^{\infty} dE\, e^{\pm iEt/\hbar}\,\delta(\hat{H}-E), \tag{4.15}$$

so from Eq. (4.13) and Eq. (4.14) one has

$$k(T)Q_r(T) = \frac{(2\pi\hbar)}{2}\int_{-\infty}^{\infty}dE\int_{-\infty}^{\infty}dE' \times \mathrm{tr}\left[e^{-\beta\hat{H}/2}\hat{F}\,e^{-\beta\hat{H}/2}\,\delta(\hat{H}-E)\hat{F}\,\delta(\hat{H}-E')\right]\,\delta(E-E'). \tag{4.16}$$

after recognising the integral over the time-dependent terms as the Dirac delta function $\delta(E-E')$. This can be used to collapse one of the energy integrals to give

$$k(T)Q_r(T) = \frac{1}{(2\pi\hbar)}\int_{-\infty}^{\infty}dE\,e^{-\beta E}\,N(E), \tag{4.17}$$

where $N(E)$ is the microcanonical rate coefficient,

$$N(E) = \frac{(2\pi\hbar)^2}{2}\mathrm{tr}\left[\hat{F}\delta(\hat{H}-E)\hat{F}\delta(\hat{H}-E)\right], \tag{4.18}$$

which quantifies the reaction rate at a fixed energy E.

If $N(E)$ is independent of the choice of dividing surface then Eq. (4.17) would show that the same must be true of $k(T)$. To establish the independence of $N(E)$ the delta functions are expressed in terms of continuum energy eigenstates [104]

$$\delta(\hat{H}-E) = \frac{1}{(2\pi\hbar)}|\Psi_E\rangle\langle\Psi_E|, \tag{4.19}$$

so that a cyclic permutation of the operators in the trace of Eq. (4.18) leaves

$$N(E) = \frac{1}{2}\left|\left\langle\Psi_E\left|\hat{F}\right|\Psi_E\right\rangle\right|^2. \tag{4.20}$$

Using Eq. (4.6) for the flux operator gives

$$\left\langle\Psi_E\left|\hat{F}\right|\Psi_E\right\rangle = \frac{1}{2m}\left[\left\langle\Psi_E\left|\hat{p}\,\delta(\hat{q}-q^{\ddagger})\right|\Psi_E\right\rangle + \left\langle\Psi_E\left|\delta(\hat{q}-q^{\ddagger})\hat{p}\right|\Psi_E\right\rangle\right]. \tag{4.21}$$

With $\hat{p}{=}{-}i\hbar\, d/dq$ the second matrix element can be evaluated as

$$\begin{aligned}\left\langle \Psi_E \left| \delta(\hat{q}-q^\ddagger)\hat{p} \right| \Psi_E \right\rangle &= \int dq\, \Psi_E^*(q)\, \delta(q-q^\ddagger)\, \langle q \left| \hat{p} \right| \Psi_E \rangle\,, \\ &= -i\hbar \int dq\, \Psi_E^*(q)\, \delta(q-q^\ddagger)\, \langle q | \partial \Psi_E/\partial q \rangle \\ &= -i\hbar \Psi_E^*(q^\ddagger) \frac{d\Psi_E(q^\ddagger)}{dq^\ddagger}. \end{aligned} \tag{4.22}$$

Furthermore, because $\hat{p}$ is hermitian

$$\begin{aligned}\left\langle \Psi_E \left| \hat{p}\, \delta(\hat{q}-q^\ddagger) \right| \Psi_E \right\rangle &= \left\langle \hat{p}\Psi_E \left| \delta(\hat{q}-q^\ddagger) \right| \Psi_E \right\rangle \\ &= i\hbar \frac{d\Psi_E^*(q^\ddagger)}{dq^\ddagger} \Psi_E(q^\ddagger), \end{aligned} \tag{4.23}$$

and thus

$$\left\langle \Psi_E \left| \hat{F} \right| \Psi_E \right\rangle = -\frac{i\hbar}{2m} \left[\Psi_E^*(q^\ddagger) \frac{d\Psi_E(q^\ddagger)}{dq^\ddagger} - \frac{d\Psi_E^*(q^\ddagger)}{dq^\ddagger} \Psi_E(q^\ddagger) \right] \equiv j_E(q^\ddagger), \tag{4.24}$$

where $j_E(q^\ddagger)$ is the time-independent probability density flux through the dividing surface at $q^\ddagger$, and

$$N(E) = \frac{1}{2} |j_E(q^\ddagger)|^2. \tag{4.25}$$

In order to prove that $j_E(q^\ddagger)$, $N(E)$ (via Eq. (4.25)) and $k(T)$ (via Eq. (4.17)) are independent of $q^\ddagger$, the quantum-mechanical continuity equation

$$\frac{\partial}{\partial q^\ddagger} j_E(q^\ddagger) = -\frac{\partial}{\partial t} |\Psi_E(q^\ddagger)|^2 = 0, \tag{4.26}$$

must be established. Thus, differentiating $j_E(q^\ddagger)$ (Eq. (4.24)) with respect to $q^\ddagger$ and

cancelling the terms involving first derivatives leaves

$$\frac{\partial}{\partial q^{\ddagger}} j_E(q^{\ddagger}) = -\frac{i\hbar}{2m}\left[\Psi_E^*(q^{\ddagger})\frac{d^2\Psi_E(q^{\ddagger})}{(dq^{\ddagger})^2} - \frac{d^2\Psi_E^*(q^{\ddagger})}{(dq^{\ddagger})^2}\Psi_E(q^{\ddagger})\right]. \tag{4.27}$$

Differentiating $|\Psi_E(q^{\ddagger})|^2$ with respect to time and using the time-dependent Schrödinger equation gives the same result, proving the first equality in Eq. (4.26). Finally, because $|\Psi_E(q^{\ddagger})|^2$ is the probability density of an energy eigenstate, its time derivative is zero. Hence the second equality in Eq. (4.26) and the independence of the exact canonical rate coefficient from the choice of dividing surface.

So far, this section has established that the exact ($q^{\ddagger}$-independent) canonical rate coefficient can be expressed in terms of three different, but related, symmetrically thermalized correlation functions. In fact, because Eq. (4.2) can be written

$$k(T) = \frac{1}{Q_r(T)}\mathrm{tr}\left[e^{-\beta\hat{H}/2}\hat{F}\,e^{-\beta\hat{H}/2}\hat{\mathcal{P}}\right], \tag{4.28}$$

where $\hat{\mathcal{P}}$ is defined in Eq. (4.7), and because $\left[\hat{H},\hat{\mathcal{P}}\right]$=0,

$$\begin{aligned} k(T) &= \frac{1}{Q_r(T)}\mathrm{tr}\left[e^{-(\beta-\lambda)\hat{H}}\hat{F}\,e^{-\lambda\hat{H}}\hat{\mathcal{P}}\right], \\ &= \frac{1}{Q_r(T)}\lim_{t\to\infty} c_{\mathrm{fs}}^{\lambda}(t), \end{aligned} \tag{4.29}$$

i.e. the rate coefficient can be given in terms of the lambda flux-side correlation function $c_{\mathrm{fs}}^{\lambda}(t)$ (see Eq. (1.9)). The commutation of $\hat{\mathcal{P}}$ with $\hat{H}$ is necessary for a well-defined rate coefficient to exist, and is evident from the original definition of the former operator in terms of the eigenstates of the latter [102].

Integrating the last equation over the range $0 \leq \lambda \leq \beta$ introduces the Kubo-transformed

flux-side correlation function (see Eq. (1.14))

$$k(T) = \frac{1}{Q_r(T)} \lim_{t\to\infty} \tilde{c}_{\rm fs}(t), \tag{4.30}$$

where

$$\tilde{c}_{\rm fs}(t) = \frac{1}{\beta}\int_0^\beta d\lambda \, {\rm tr}\left[e^{-(\beta-\lambda)\hat{H}}\,\hat{F}\,e^{-\lambda\hat{H}}\,e^{+i\hat{H}t/\hbar}\hat{h}\,e^{-i\hat{H}t/\hbar}\right]. \tag{4.31}$$

The rate coefficient $k(T)$ can also be related to the Kubo-transformed side-side and flux-flux correlation functions by repeating the arguments that led from Eq. (4.8) to Eq. (4.11) and from Eq. (4.2) to Eq. (4.12). Thus,

$$k(T) = -\frac{1}{Q_r(T)} \lim_{t\to\infty} \frac{d}{dt}\tilde{c}_{\rm ss}(t), \tag{4.32}$$

$$k(T) = \frac{1}{Q_r(T)}\int_0^\infty dt\, \tilde{c}_{\rm ff}(t), \tag{4.33}$$

where the definitions of $\tilde{c}_{\rm ss}(t)$ and $\tilde{c}_{\rm ff}(t)$ follow by analogy to Eq. (4.31). Although the Kubo-transformed formulations of $k(T)$ are equivalent to those presented earlier (Eq. (4.2), Eq. (4.11) and Eq. (4.12)), it should be stressed that the correlation functions involved in the various expressions will, in general, differ. Historically, Yamamoto used a development based upon linear response theory to obtain the Kubo-transformed formulation of $k(T)$ (Eq. (4.31)) *before* Miller's work on the symmetrically thermalized version [25, 101].

With the theoretical framework in hand, the outline of the RPMD approach to calculating chemical reaction rates is now clear. The approximate method, introduced in Chapter 2, will be applied to the Kubo-transformed correlation functions that determine $k(T)$ via the expressions above. A number of potential problems are, however, immediately apparent. Firstly, whereas the step function operator $\hat{h}$ depends only on position, the flux operator $\hat{F}$ also depends on momentum. Since the RPMD model

can only be used for correlation functions involving position-dependent operators, one seems to be restricted to calculating the rate coefficient through $\tilde{c}_{\mathrm{ss}}(t)$. Unfortunately, calculations based upon side-side correlation functions are inefficient because a significant part of the computational effort is involved with evaluating dynamics in regions far from the reaction barrier. Such motion does not lead to a change in $\tilde{c}_{\mathrm{ss}}(t)$ and therefore makes no contribution to the rate coefficient. However, Section 4.3 describes a way in which a RPMD approximation to the Kubo-transformed flux-side correlation function can, in fact, be obtained.

Secondly, one might suspect that the accuracy of the RPMD approximation would be poor because the step function operator is a highly nonlinear function of $\hat{q}$. This suspicion follows from the previous chapter's analysis of the effect of operator nonlinearity on the performance of the new method. The third concern is that the first time derivative of $\tilde{c}_{\mathrm{fs}}(t)$, i.e. $\tilde{c}_{\mathrm{ff}}(t)$, is infinite at $t = 0$ [13]. This suggests that a very small time step might be required to converge the RPMD correlation functions. If the RPMD method were not restricted to Kubo-transformed correlation functions then this problem could be avoided by calculating the symmetrically thermalized $c_{\mathrm{fs}}^{\beta/2}(t)$. This, however, is not the case and these second and third concerns have no easy solution. Only by considering the results of $k(T)$ calculations based upon the RPMD method will it be seen that they are insignificant.

4.2 Existing approximate methods

An *exact* calculation of a reaction rate coefficient using the expressions of the previous section would require the evaluation of the quantum dynamics of the entire reactive system and is therefore impractical in many cases. However, the correlation function formalism of chemical reaction rates has proved to be a useful basis for many *approximate* quantum-mechanical rate theories. In order to put the development of an

RPMD-based reaction rate approach in context, this section presents a summary of these existing approximate methods.

In those cases for which an exact calculation is not feasible, perhaps the most obvious way to proceed is to replace the quantum-mechanical correlation function with its classical limit. This 'classical reactive flux' method [95–97] gives a sufficiently accurate description of many chemical reactions. It only requires the evaluation of classical trajectories upon the potential energy surface of the reactive system and furthermore, because of the validity of the Liouville equation and the reversibility of classical mechanics the results are also formally independent of the choice of dividing surface. Another virtue of the classical reactive flux method is that it provides the classical transition-state theory result 'for free' as its short-time limit [105, 106].

However, due to the interest in calculating chemical reaction rates for systems in which the classical approximation is inaccurate, many of the approaches introduced in Chapter 1 have been used to include approximate quantum-mechanical effects in the reaction correlation functions. Both the classical Wigner model (CWM) (see Section 1.3 and Refs. [14, 15, 57]) and the centroid molecular dynamics (CMD) method (see Section 1.4 and also Ref. [56]) have been applied to the evaluation of $k(T)$. A noteworthy complication in the latter case is that CMD is formally restricted to correlation functions involving linear operators [20] and so it cannot be applied to any of the (nonlinear) correlation functions that appear in the $k(T)$ expressions above. This problem was circumvented by Geva, Shi and Voth [56] who demonstrated that the step function operator ($\hat{h}$) in $\tilde{c}_{\mathrm{fs}}(t)$ (Eq. (4.31)) can be replaced with the linear position operator ($\hat{q}$) without changing the long-time limit of the correlation function. Their 'flux-position' correlation function, which *can* be approximated by CMD, therefore gives the same canonical rate coefficient as the expressions in the previous section.

A different type of approximate method entirely neglects the dynamics of the reac-

tion correlation functions and therefore provides a purely statistical description of the reaction rate. Classical transition-state theory (CTST), which has provided the enduring concepts with which chemical reactivity is rationalized, is the obvious example of such a method [105, 106]. As alluded to above, it can be obtained by substituting the short-time limit of the classical flux-side correlation into the classical limit of Eq. (4.2). The basic assumption of CTST is that trajectories which reach the dividing surface react, i.e. they pass through the surface and do not return through it ('no recrossing') [105, 106]. The CTST rate coefficient is

$$k_{\mathrm{CTST}}(T) = \left[\frac{1}{2}\left\langle|\dot{q}|\right\rangle_{cl}\right] \frac{Q^{\ddagger}_{\mathrm{cl}}(T)}{Q_{r,\mathrm{cl}}(T)}, \tag{4.34}$$

where $Q_{r,\mathrm{cl}}(T)$ and $Q^{\ddagger}_{\mathrm{cl}}(T)$ are respectively the classical reactant and dividing-surface partition functions. This transition-state theory picture is most valid at temperatures less than, or comparable to, the reaction activation energy [102]. However, in this regime an important contribution to the canonical rate coefficient can come from quantum-mechanical tunneling through the barrier top. The inability of classical mechanics to describe such processes and the perceived validity (and utility) of the basic transition-state theory picture has motivated many attempts to find a quantum version of transition-state theory (QTST).

One particularly simple and appealing QTST was derived by Voth, Chandler and Miller [107] following an idea due to Gillan [108, 109]. The one difference between their expression and Eq. (4.34) is that the classical probability ratio $Q^{\ddagger}_{\mathrm{cl}}/Q_{r,\mathrm{cl}}$ is replaced with one evaluated using the path-integral formulation of quantum statistical mechanics. Thus, the QTST expression is

$$k_{\mathrm{QTST}}(T) = \left[\frac{1}{2}\left\langle|\dot{q}|\right\rangle_{cl}\right] \frac{Q^{\ddagger}(T)}{Q_r(T)}, \tag{4.35}$$

where Q_r and $Q^{\ddagger}$ are now quantum-mechanical partition functions. Both Q_r and $Q^{\ddagger}$ can be evaluated with the path-integral techniques of Chapter 1, with the latter being defined as a sum over all cyclic paths which have their centroids located in the dividing surface. The connection of this QTST with the short-time limit of a quantum-mechanical flux-side correlation is explored later in this chapter. Other QTSTs include that of Pollak and Liao [110] (which is an extension of the Voth-Chandler-Miller QTST) and that of Hansen and Andersen [111].

This section ends by highlighting a promising method for calculating low temperature rate coefficients that, in common with every other approach summarized above, is an approximation to one of the quantum-mechanical reaction correlation functions. The recently-introduced quantum instanton (QI) model of Miller and co-workers is in the same spirit as a QTST since it is an approximation constructed from short-time information [112–118]. This is clear from the fact that the model can be derived using a second-order cumulant approximation to the symmetrically-thermalized flux-flux correlation function in Eq. (4.13) [112], i.e., since $c_{\rm ff}^{\beta/2}(t)$ is even,

$$\begin{aligned} c_{\rm ff}^{\beta/2}(t) &\simeq c_{\rm ff}^{\beta/2}(0) + \frac{t^2}{2}\ddot{c}_{\rm ff}^{\beta/2}(0) \\ &\simeq c_{\rm ff}^{\beta/2}(0) \exp\left[\frac{\ddot{c}_{\rm ff}^{\beta/2}(0)}{2c_{\rm ff}^{\beta/2}(0)}t^2\right]. \end{aligned} \tag{4.36}$$

Then, because the form of this cumulant approximation is a Gaussian ($\ddot{c}_{\rm ff}^{\beta/2}(0)$ is negative), the integral in Eq. (4.12) becomes

$$k_{\rm QI}(T)Q_r(T) = \frac{1}{2}c_{\rm ff}^{\beta/2}(0)\left(\frac{2\pi c_{\rm ff}^{\beta/2}(0)}{-\ddot{c}_{\rm ff}^{\beta/2}(0)}\right)^{1/2}. \tag{4.37}$$

Various versions of the basic QI concept have been applied to a one-dimensional model of the collinear H+H_2 reaction and have been found to give rate coefficients with *maximum* errors of 20-50% versus the exact result over a wide range of tem-

peratures [112, 113]. The QI model has also been applied to a series of reactions of increased complexity, including a variety of collinear atom-diatom reactions [115], the $H+CH_4$ hydrogen abstraction reaction [114] and a model for proton transfer in a polar solvent [117].

The principal deficiency of all rate theories that lack information on the dynamics of the reactive process (e.g. QTSTs, the QI model) is that dividing-surface recrossing effects are not properly described. The importance of these effects in reactions involving many degrees of freedom is yet to be firmly established. As far as classical dynamics is valid it has been argued that recrossing is negligible in such systems [115], but its absence from the quantum-dynamical picture is not as clear. The results of calculations presented in the next chapter throw some light on this issue. It is, however, certain that the neglect of recrossing means that these short-time rate coefficients can vary enormously depending on the choice of dividing surface. This is a considerable problem because the location of the optimum dividing surface can be very difficult to establish in reactive systems that involve many degrees of freedom [119].

4.3 A bead-pinned $\tilde{c}_{\mathrm{fs}}(t)$ (RPMD-B)

Having surveyed some of the existing approaches to calculating approximate rate coefficients for condensed-phase chemical reactions, the discussion now turns to the development of the first of two RPMD-based methods, both of which implement the correlation function formulation of $k(T)$ that was described in Section 4.1. Chapter 2 established that the RPMD approximation can only be directly applied to Kubo-transformed correlation functions which involve position-dependent operators. Therefore, of the numerous expressions for the canonical rate coefficient obtained in Section 4.1, only

$\tilde{c}_{\rm ss}(t)$ in Eq. (4.32) can be treated by the RPMD model. The approximation is

$$\tilde{c}_{\rm ss}(t) \simeq \frac{1}{(2\pi\hbar)^n} \int d\mathbf{p}_0 \int d\mathbf{q}_0 \, e^{-\beta_n H_n(\mathbf{p}_0,\mathbf{q}_0)} \, h_n(\mathbf{q}_0) h_n(\mathbf{q}_t), \tag{4.38}$$

where n is the number of ring-polymer beads and $\beta_n{=}\beta/n$. Although the notation in this expression might be familiar from previous chapters, the definitions of the various terms are repeated here in order to keep this discussion self-contained. So, $\mathbf{p}_t$ and $\mathbf{q}_t$ are vectors of the n momenta and positions of the ring-polymer beads at time t and, following Eq. (4.1) for the Hamiltonian of a one-dimensional reaction, $H_n(\mathbf{p},\mathbf{q})$ is

$$H_n(\mathbf{p},\mathbf{q}) = \sum_{k=1}^{n} \left(\frac{p_k^2}{2m} + \frac{1}{2} m\omega_n^2 (q_k - q_{k+1})^2 + V(q_k) \right), \tag{4.39}$$

where the time subscript has been suppressed and p_k and q_k are respectively the momentum and position of the $k^{\rm th}$ ring-polymer bead. As before, $\omega_n{=}1/\beta_n\hbar$, $q_{n+1}{=}q_1$ and m denotes the mass relevant to motion along the coordinate q.

The external potential $V(q)$ is the potential energy barrier for the reaction and the step function $h_n(\mathbf{q})$ is the following average over the beads of the ring-polymer,

$$h_n(\mathbf{q}) = \frac{1}{n} \sum_{k=1}^{n} h(q_k - q^{\ddagger}), \tag{4.40}$$

where $h(q_k - q^{\ddagger})$ is zero unless $q_k \geq q^{\ddagger}$, in which case it is equal to one. Lastly, the positions of the ring-polymer beads at time t are determined by the ring-polymer equations of motion

$$\begin{aligned} \dot{q}_k &= +\frac{\partial H_n}{\partial p_k} = \frac{p_k}{m}, \\ \dot{p}_k &= -\frac{\partial H_n}{\partial q_k} = -m\omega_n^2 \left[2q_k - q_{k+1} - q_{k-1}\right] - \frac{dV(q_k)}{dq_k}. \end{aligned} \tag{4.41}$$

As it stands, Eq. (4.38) does not represent a viable approach to calculating the thermal rate coefficient. The reason is that the $h_n(\mathbf{q}_0)$ in the integrand means that the integral is determined by ring-polymer trajectories that have at least one bead on the product side of the dividing surface at time zero. Most members of this set of trajectories exist far from the reaction barrier, and therefore barrier crossings, which determine the rate of change of $\tilde{c}_{\rm ss}(t)$ and hence $k(T)$ (Eq. (4.32)), are extremely rare. Any simulation based on these equations would therefore expend the vast majority of its effort tracking trajectories which are not contributing to the value of the rate coefficient.

However, since the flux operator is the time derivative of the step function operator, $\tilde{c}_{\rm ss}(t)$ is related to $\tilde{c}_{\rm fs}(t)$ by

$$\frac{d}{dt}\tilde{c}_{\rm ss}(t) = -\tilde{c}_{\rm fs}(t), \tag{4.42}$$

which is just the Kubo-transformed analogue of Eq. (4.10). Differentiation of Eq. (4.38) with respect to time therefore yields a RPMD approximation to the Kubo-transformed flux-side correlation function. Thus,

$$\tilde{c}_{\rm fs}(t) \simeq \frac{-1}{(2\pi\hbar)^n}\int d\mathbf{p}_0 \int d\mathbf{q}_0\, e^{-\beta_n H_n(\mathbf{p}_0,\mathbf{q}_0)}\, h_n(\mathbf{q}_0)\dot{h}_n(\mathbf{q}_t), \tag{4.43}$$

and because of the ring-polymer symmetry in Eq. (2.51), the time-reversibility of the ring-polymer dynamics, i.e.,

$$\mathbf{q}_{-t}(\mathbf{p}_0,\mathbf{q}_0) = \mathbf{q}_t(-\mathbf{p}_0,\mathbf{q}_0), \tag{4.44}$$

and the $\mathbf{p}$-inversion symmetry of the ring-polymer Hamiltonian (Eq. (4.39)), this can be rearranged to

$$\tilde{c}_{\rm fs}(t) \simeq \frac{1}{(2\pi\hbar)^n}\int d\mathbf{p}_0 \int d\mathbf{q}_0\, e^{-\beta_n H_n(\mathbf{p}_0,\mathbf{q}_0)}\, \dot{h}_n(\mathbf{q}_0)h_n(\mathbf{q}_t). \tag{4.45}$$

Now, in one dimension,

$$\dot{h}_n(\mathbf{q}) = \frac{1}{n}\sum_{k=1}^{n}\frac{dh(q_k - q^\ddagger)}{dq_k}\frac{dq_k}{dt} = \frac{1}{n}\sum_{k=1}^{n}\delta_k(\mathbf{q})\,v_k(\mathbf{p}), \tag{4.46}$$

where

$$\delta_k(\mathbf{q}) = \delta(q_k - q^\ddagger) \tag{4.47}$$

$$\text{and} \qquad v_k(\mathbf{p}) = p_k/m. \tag{4.48}$$

However, each ring-polymer bead is formally equivalent (consider Eq. (4.39)) and so each of the n terms in $\dot{h}_n$ gives the same correlation function. Choosing $k = 1$ for simplicity, we obtain

$$\tilde{c}_{\mathrm{fs}}(t) \simeq \frac{1}{(2\pi\hbar)^n}\int d\mathbf{p}_0 \int d\mathbf{q}_0\, e^{-\beta_n H_n(\mathbf{p}_0,\mathbf{q}_0)}\,\delta_1(\mathbf{q}_0)\,v_1(\mathbf{p}_0)\,h_n(\mathbf{q}_t). \tag{4.49}$$

This RPMD approximation to $\tilde{c}_{\mathrm{fs}}(t)$ has a simple interpretation that is sketched in Fig. 4.1. At time zero the first bead is pinned to the dividing surface and contributes a factor of p_1/m to the integrand. This initial velocity factor is then correlated with the fraction of the ring-polymer located on the product side of the dividing surface at a later time t, as quantified by $h_n(\mathbf{q}_t)$. The long-time limit of this expression determines the RPMD approximation to the canonical rate coefficient. Although it is only the first bead that is pinned to the dividing surface, the remaining beads must lie nearby because of the kinetic spring terms in the ring-polymer Hamiltonian (Eq. (4.39)). As a consequence, if the dividing surface is chosen to coincide with the top of the potential energy barrier (a sensible choice) then reactive ring-polymer trajectories will be sampled far more frequently than would be the case for the hypothetical $\tilde{c}_{\mathrm{ss}}(t)$ calculation outlined above. This makes the $\tilde{c}_{\mathrm{fs}}(t)$-based RPMD approach, which will

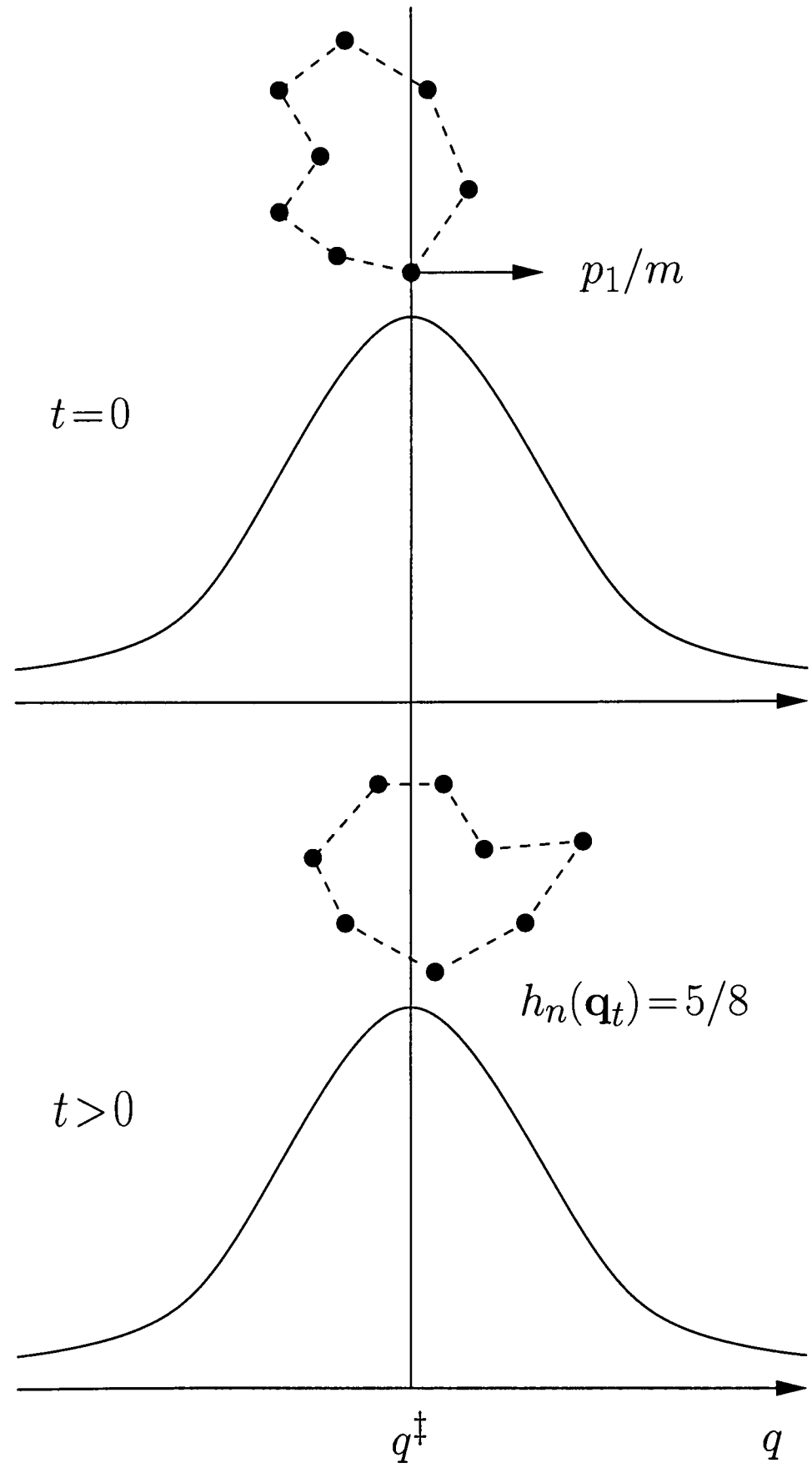

Figure 4.1: A sketch illustrating the RPMD-B expression for the canonical rate coefficient. Top: at $t=0$ a single bead is pinned to the dividing surface and contributes a velocity term to the correlation function (Eq. (4.49)). Bottom: after the ring-polymer dynamics (Eq. (4.41)) have been evolved the ring-polymer contributes the ring-averaged step function $h_n(\mathbf{q}_t)$ (Eq. (4.40)) to the correlation function at time t. The long-time limit of this correlation function gives the canonical rate coefficient in accordance with Eq. (4.30).

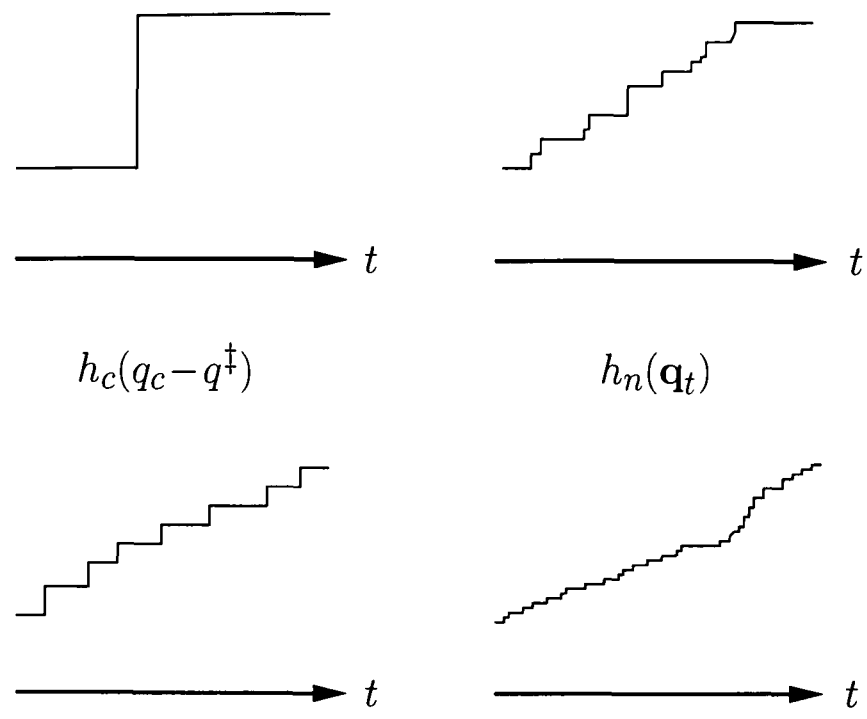

Figure 4.2: A schematic illustration of the equivalent $t \to \infty$ gradients of the two RPMD approximations to the Kubo-transformed side-side correlation function (Eq. (4.38) and Eq. (4.51)). Top row: for a single trajectory crossing the dividing surface the time evolution of the two step functions ($h_n(\mathbf{q}_t)$ in Eq. (4.40) and $h_c(\mathbf{q}_t)$ in Eq. (4.52)) is different. Bottom row: when averaged over a large number M such trajectories the evolution of the functions is similar. As $M \to \infty$ the time derivatives of the step functions, and hence of the correlation functions, are identical.

be called RPMD-B in this thesis, much more efficient.

Finally for this section, note that the RPMD-B expression (Eq. (4.49)) reduces to the purely classical flux-side correlation function,

$$c_{\mathrm{fs}}^{\mathrm{cl}}(t) \simeq \frac{1}{2\pi\hbar} \int dp_0 \int dq_0 \, e^{-\beta H(p_0,q_0)} \, \delta(q_0 - q^\ddagger) \, \frac{p_0}{m} h(q_t), \tag{4.50}$$

at $n = 1$. The RPMD-B method is therefore as efficient as the classical reactive flux method for reactions in which classical mechanics is sufficient.

4.4 A centroid-pinned $\tilde{c}_{\mathrm{fs}}(t)$ (RPMD-C)

The second RPMD-based approach to calculating canonical rate coefficients starts with an alternative RPMD expression for the side-side correlation function (com-

pare Eq. (4.38)):

$$\tilde{c}_{\mathrm{ss}}(t) \simeq \frac{1}{(2\pi\hbar)^n} \int d\mathbf{p}_0 \int d\mathbf{q}_0 \, e^{-\beta_n H_n(\mathbf{p}_0,\mathbf{q}_0)} \, h_c(\mathbf{q}_0) h_c(\mathbf{q}_t), \tag{4.51}$$

where the step functions are now

$$h_c(\mathbf{q}) = h(q_c - q^\ddagger), \tag{4.52}$$

and q_c is the position centroid of the ring-polymer necklace (Eq. (2.30)). Instead of correlating the average step function of the n ring-polymer beads (h_n of Eq. (4.38)), this expression correlates the step functions of the ring-polymer centroids (h_c above). The equivalence of these two formulations can be seen with the aid of Fig. 4.2. For any single trajectory crossing the dividing surface the time-evolution of h_n is clearly different to that of h_c. However, after an initial period equal to the time taken for the trajectories sampled on the reaction barrier to move off it, the change in each correlation function is due to the same subset of barrier-crossing trajectories, i.e. those which originate off the barrier. When averaged over this set of trajectories, the functions h_n and h_c will have the same time derivative and therefore give the same rate [120].

The equivalence of the two approximate side-side correlation functions (Eq. (4.38) and Eq. (4.51)) extends to their inefficiency as means to calculate $k(T)$. However, following the previous section, the time derivative of this second RPMD approximation to $\tilde{c}_{\mathrm{ss}}(t)$ can be taken to give an approximate $\tilde{c}_{\mathrm{fs}}(t)$:

$$\tilde{c}_{\mathrm{fs}}(t) \simeq \frac{1}{(2\pi\hbar)^n} \int d\mathbf{p}_0 \int d\mathbf{q}_0 \, e^{-\beta_n H_n(\mathbf{p}_0,\mathbf{q}_0)} \, \delta_c(\mathbf{q}_0) \, v_c(\mathbf{p}_0) \, h_c(\mathbf{q}_t). \tag{4.53}$$

The new centroid-dependent terms are

$$\delta_c(\mathbf{q}) = \delta(q_c - q^\ddagger), \tag{4.54}$$

and

$$v_c(\mathbf{p}) = p_c/m, \tag{4.55}$$

where p_c is the momentum centroid of the ring-polymer,

$$p_c = \frac{1}{n}\sum_{k=1}^{n} p_k. \tag{4.56}$$

The physical interpretation of this RPMD-C approximation is sketched in Fig. 4.3 (compare Fig. 4.1). It is now the position centroid (q_c) and not the position of a single bead which is pinned to the dividing surface at time zero. Likewise, the $t=0$ velocity factor is that of the centroid rather than a single bead (the standard deviation of the single-bead momentum distribution is a factor of $\sqrt{n}$ larger than that of the centroid). This velocity factor is then correlated with the product-side centroid step function at a later time t (quantified by $h_c(\mathbf{q}_t)$) and the long-time limit of the resulting correlation function (Eq. (4.51)) gives the same rate coefficient as the RPMD-B approximation. Although the expressions for the two approaches take the same form and give the same rate coefficient, the slight differences in the definitions of the terms involved in each will be seen to have a substantial effect on their efficiency.

4.5 Analytical results for a parabolic barrier

Before examining the efficacy of these RPMD methods through numerical calculations, some hope that they might be useful comes from considering their (analytical) results for the parabolic barrier problem, i.e.,

$$V(q) = -\frac{1}{2}m\omega_b^2 q^2, \tag{4.57}$$

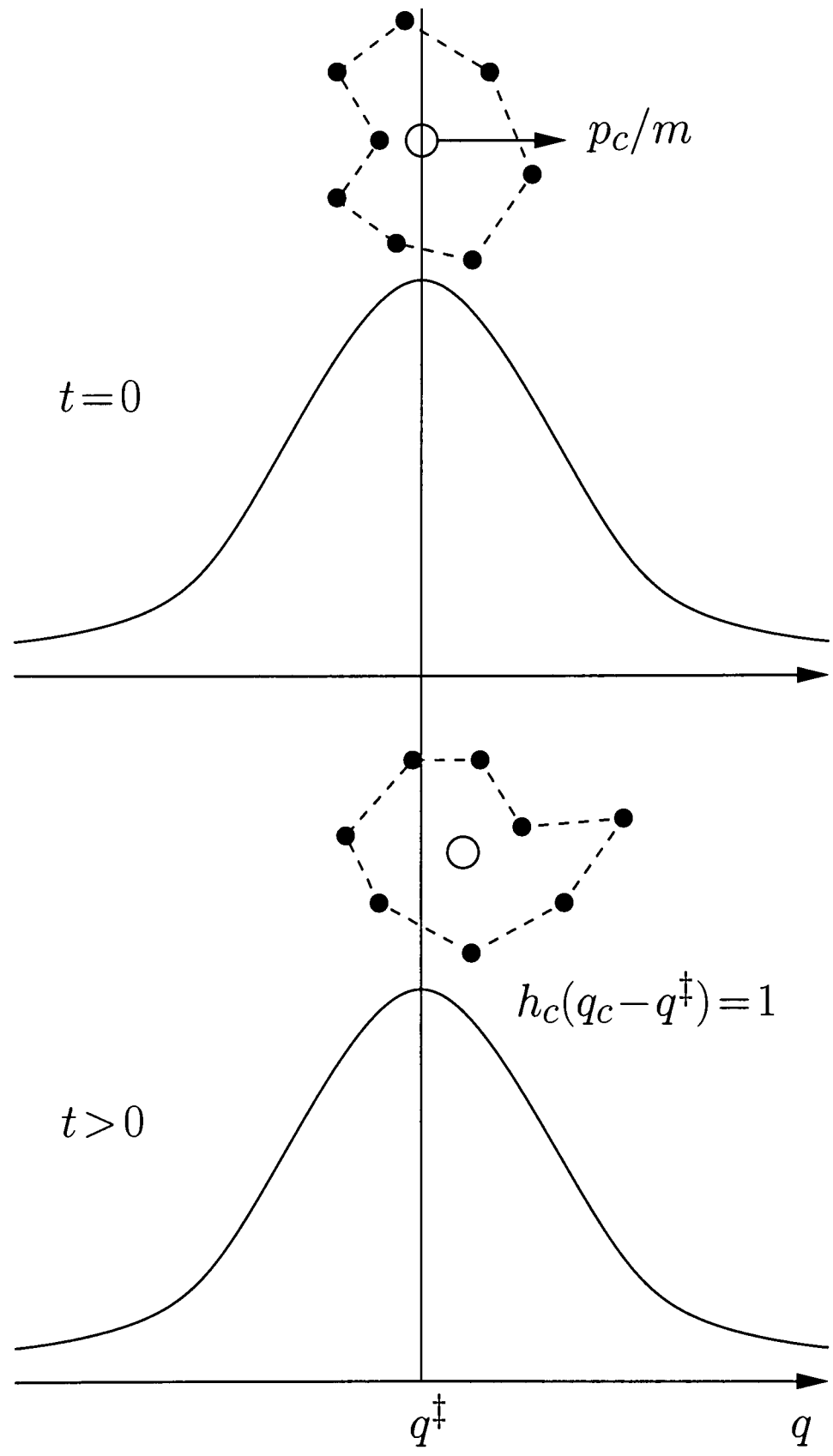

Figure 4.3: A sketch illustrating the RPMD-C expression for the canonical rate coefficient. Top: at $t=0$ the centroid is pinned to the dividing surface and contributes a velocity term to the correlation function (Eq. (4.53)). Bottom: after the ring-polymer dynamics (Eq. (4.41)) have been evolved the ring polymer contributes the centroid step function $h_c(q_c - q^\ddagger)$ (Eq. (4.52)) to the correlation function at time t. The long-time limit of this correlation function gives the canonical rate coefficient in accordance with Eq. (4.30).

where $i\omega_b$ is the imaginary barrier frequency. With this potential energy function the ring-polymer Hamiltonian (Eq. (4.39)) is a purely quadratic function of the $\{p_j\}$ and $\{q_j\}$ coordinates:

$$H_n(\mathbf{p},\mathbf{q}) = \sum_{k=1}^{n}\left(\frac{p_k^2}{2m} + \frac{1}{2}m\omega_n^2(q_k - q_{k+1})^2 - \frac{1}{2}m\omega_b^2 q_k^2\right). \tag{4.58}$$

Furthermore, the entire ring-polymer potential energy function (ϕ_n of Eq. (1.29)) and all except its second derivatives vanish at $\mathbf{q}$=$\mathbf{0}$. Therefore, a normal-mode transformation can be found that diagonalizes $H_n(\mathbf{p},\mathbf{q})$ and allows it to be rewritten exactly as a sum of n *uncoupled* harmonic oscillators:

$$H_n(\mathbf{p},\mathbf{q}) \rightarrow H_n(\mathbf{P},\mathbf{Q}) = \sum_{k=1}^{n}\left(\frac{P_k^2}{2m} + \frac{1}{2}m\Omega_k^2 Q_k^2\right). \tag{4.59}$$

This normal-mode transformation is described in some detail in Appendix B, where the precise definitions of $\mathbf{P}$, $\mathbf{Q}$ and the $\{\Omega_k\}$ are given. This appendix also establishes that the position of n^{th} normal mode (Q_n) is related to the position centroid (q_c) by

$$Q_n = \sqrt{n}\, q_c. \tag{4.60}$$

Thus, the k=n term in the normal-mode Hamiltonian (Eq. (4.59)) describes a centroid mode which (on this parabolic barrier) is completely decoupled from the high-frequency oscillations of the ring polymer.

The motion of the decoupled centroid determines the RPMD-C approximation to the correlation function (Eq. (4.53)), which can be written in terms of the ring-polymer normal modes as

$$\tilde{c}_{\text{fs}}(t) \simeq \frac{1}{(2\pi\hbar)^n}\int d\mathbf{P}_0 \int d\mathbf{Q}_0\, e^{-\beta_n H_n(\mathbf{P}_0,\mathbf{Q}_0)}\, \delta_c(\mathbf{Q}_0)\, v_c(\mathbf{P}_0)\, h_c(\mathbf{Q}_t). \tag{4.61}$$

using the orthogonality of the normal-mode transformation. For the obvious dividing surface (i.e. $q^{\ddagger}$=0), the integrand of this expression can be rewritten as

$$\delta_c(\mathbf{Q}_0)\, v_c(\mathbf{P}_0)\, h_c(\mathbf{Q}_t) = \delta(Q_n(0))\, \frac{P_n(0)}{m}\, h(P_n(0)). \tag{4.62}$$

Here, $P_n(0)$ is the momentum conjugate to Q_n at t=0 and $h(P_n)$ is zero for P_n<0 and one otherwise. The change in the step function ($h_c(\mathbf{Q}_t) \rightarrow h(P_n(0))$) is permitted because the decoupling means that no centroid trajectory which originates at the top of the parabolic barrier will ever recross it. Substituting Eq. (4.62) into Eq. (4.61) leaves a collection of $2n$ Gaussian integrals, which can be evaluated to give

$$\tilde{c}_{\rm fs}(t) \simeq \frac{1}{(2\pi\hbar)^n}\, \frac{1}{\beta_n} \left(\frac{2\pi m}{\beta_n}\right)^{(n-1)/2} \prod_{k=1}^{n-1} \left[\frac{2\pi}{m\beta_n \Omega_k^2}\right]^{1/2}. \tag{4.63}$$

The first factor is the normalization retained from Eq. (4.61), the second arises from the P_n momentum integral, and the third is the result of the remaining $(n-1)$ momenta integrals. The final term comes from the $(n-1)$ position integrals that remain after the $\delta(Q_n(0))$ has been employed. This collection simplifies to

$$\tilde{c}_{\rm fs}(t) \simeq \frac{1}{\beta_n h} \prod_{k=1}^{n-1} \left[\frac{1}{4\sin^2(k\pi/n) - (\omega_b/\omega_n)^2}\right]^{1/2}, \tag{4.64}$$

which in the limit $n \rightarrow \infty$ is [103]

$$\tilde{c}_{\rm fs}(t) \simeq \frac{1}{\beta h}\, \frac{\beta\hbar\omega_b/2}{\sin(\beta\hbar\omega_b/2)}. \tag{4.65}$$

This is equal to the exact quantum-mechanical result and therefore RPMD-C gives the correct rate coefficient for any parabolic barrier. The equivalence of the two RPMD approaches dictates that RPMD-B is also exact, as proved independently in the Appendix of Ref. [103].

This parabolic barrier result suggests that the nonlinearity of the flux and step function operators might not be as big a problem for the RPMD approximation as one might expect from the discussion of the previous chapter. This optimism is tempered by the realization that Eq. (4.62) implies that the parabolic barrier result is a short-time result that doesn't require dynamical information (for $q^{\ddagger} = 0$). Clearly then, the RPMD-B/C approaches are exact for the parabolic barrier problem because no dynamical approximation need be invoked – in the $t \to 0$ limit RPMD is exact regardless of the degree of operator nonlinearity.

4.6 Dividing-surface sampling

In order to complete the description of the RPMD-B/C methods, this section outlines efficient procedures for sampling ring-polymer trajectories with either a single bead (RPMD-B) or the centroid (RPMD-C) pinned to the dividing surface. Both methods employ importance-sampling techniques [121] that utilise Gaussian terms which are revealed in the RPMD-B/C correlation functions after certain orthogonal transformations are applied to the ring-polymer position coordinates. The section addresses only these practical matters and it may therefore be skipped if the results of the new methods are of more immediate interest.

Take the RPMD-B method first – Eq. (4.49) can be rewritten as

$$\tilde{c}_{\mathrm{fs}}(t) \simeq \frac{N_p N_q}{(2\pi\hbar)^n} \int d\mathbf{p}_0 \int d\mathbf{q}_0 \, P_p(\mathbf{p}_0) \, P_q(\mathbf{q}_0) \, \exp\left[-\beta_n \sum_{k=1}^{n} V(q_k(0))\right] \, v_1(\mathbf{p}_0) \, h_n(\mathbf{q}_t), \tag{4.66}$$

where $P_p(\mathbf{p}_0)$ and $P_q(\mathbf{q}_0)$ are respectively those parts of the integrand that will be used to sample $\mathbf{p}_0$ and $\mathbf{q}_0$, and N_p and N_q are normalization constants. The function $P_p(\mathbf{p})$

is already in the form of a normalized Gaussian sampling distribution:

$$P_p(\mathbf{p}) = \frac{1}{N_p} \exp\left[-\beta_n \sum_{k=1}^{n} \frac{p_k^2}{2m}\right], \tag{4.67}$$

and therefore

$$N_p = \int d\mathbf{p} \exp\left[-\beta_n \sum_{k=1}^{n} \frac{p_k^2}{2m}\right] = \left(\frac{2\pi m}{\beta_n}\right)^{n/2}. \tag{4.68}$$

Numerical routines are used to draw the initial momenta ($\mathbf{p}_0$) from these Gaussian distributions [121].

The sampling of the initial positions is biased using the kinetic spring system, i.e.,

$$P_q(\mathbf{q}) = \frac{1}{N_q} \exp\left[-\beta_n \sum_{k=1}^{n} \frac{1}{2} m\omega_n^2 (q_k - q_{k+1})^2\right] \delta_1(\mathbf{q}), \tag{4.69}$$

where $\delta_1(\mathbf{q})$ is defined in Eq. (4.47) and

$$N_q = \int d\mathbf{q} \exp\left[-\beta_n \sum_{k=1}^{n} \frac{1}{2} m\omega_n^2 (q_k - q_{k+1})^2\right] \delta_1(\mathbf{q}). \tag{4.70}$$

In order to use this $P_q(\mathbf{q})$ for the same kind of Gaussian-based importance sampling that is used to sample the momenta it is necessary to bring it into the same form as $P_p(\mathbf{p})$, i.e. a collection of *uncoupled* Gaussian functions. This is done by changing the coordinate system used to describe the positions of the ring-polymer beads. It turns out that a discrete sine transform of the $k = 2, \ldots, n$ position coordinates has the required effect whilst being consistent with the $\delta_1(\mathbf{q})$ constraint [103]. The transformation is accomplished by pre-multiplying the ring-polymer position vector $\mathbf{q}$ with the transpose of the sine transform matrix $\mathbf{S}$. The matrix $\mathbf{S}$ and the standard deviations of the resulting uncoupled Gaussian functions can be found through a line of reasoning similar to that presented in Appendix B. This transformation is also used to evaluate the normalization constant N_q – the integration over the uncoupled

Gaussians combines with Eq. (4.68) to give

$$\frac{N_p N_q}{(2\pi\hbar)^n} = (m/2\pi\beta\hbar^2)^{1/2} = 1/\Lambda(T), \tag{4.71}$$

where $\Lambda(T)$ is the thermal de Broglie wavelength. This $\Lambda(T)$ is proportional to the average de Broglie wavelength of particles at canonical equilibrium at temperature T.

A sketch of the RPMD-B position sampling algorithm for $q^\ddagger = 0$ is then as follows: (i) the positions of the $k = 2, \ldots, n$ modes are sampled from the Gaussians described above, (ii) the (cartesian) position of the first bead is set equal to zero, and (iii) the sine transform is inverted by pre-multiplying the sampled position vector by $\mathbf{S}$. This procedure yields a cartesian position for every ring-polymer bead. If $q^\ddagger \neq 0$ an extra (final) step is the translation of the entire ring polymer to the dividing surface, i.e. $q_k \rightarrow q_k + q^\ddagger$ for all k. When combined with the momentum sampling described above this algorithm produces an initial phase-space point for the ring-polymer trajectory. The $t = 0$ terms in the RPMD-B correlation function (Eq. (4.66)) can be evaluated immediately, and the ring-polymer dynamics can be evolved to obtain the time-dependent term.

Now consider the RPMD-C method – Eq. (4.53) can be rewritten as

$$\tilde{c}_{\rm fs}(t) \simeq \frac{N_p N_q}{(2\pi\hbar)^n} \int d\mathbf{p}_0 \int d\mathbf{q}_0 \, P_p(\mathbf{p}_0) \, P'_q(\mathbf{q}_0) \, \exp\left[-\beta_n \sum_{k=1}^{n} V(q_k(0))\right] \, v_c(\mathbf{p}_0) \, h_c(\mathbf{q}_t). \tag{4.72}$$

The sampling for the momenta is identical to that involved in the RPMD-B approach. The positions, however, are now sampled from

$$P'_q(\mathbf{q}) = \frac{1}{N_q} \exp\left[-\beta_n \sum_{k=1}^{n} \frac{1}{2} m\omega_n^2 (q_k - q_{k+1})^2\right] \delta_c(\mathbf{q}) \,, \tag{4.73}$$

where $\delta_c(\mathbf{q})$ is defined in Eq. (4.54) and

$$N_q = \int d\mathbf{q} \exp\left[-\beta_n \sum_{k=1}^{n} \frac{1}{2} m\omega_n^2 (q_k - q_{k+1})^2\right] \delta_c(\mathbf{q}). \tag{4.74}$$

The coordinate transformation that turns this sampling function into a collection of uncoupled Gaussians is a discrete Fourier transform. In fact, it is just the ring-polymer normal-mode transformation that has been mentioned before (Section 3.6 and Section 4.5) and which is described in Appendix B. Thus, the transformed positions are now just the ring-polymer normal-mode coordinates. Furthermore, since the centroid is proportional to the zero-frequency normal mode, the $\delta_c(\mathbf{q})$ can be imposed directly upon these transformed positions. The matrix that accomplishes this transformation, and the standard deviations of the resulting Gaussian sampling functions, are established in Appendix B. The first $(n-1)$ normal-mode positions are sampled from Gaussian distributions with means of zero, but to effect the centroid-pinning the distribution of the n^{th} mode has a mean of $\sqrt{n}q^{\ddagger}$ and zero standard deviation.

The position sampling algorithm is now: (i) sample the positions of the $k=1,\ldots,n$ normal modes from the Gaussians described above (note that this fixes the centroid to the dividing surface), and (ii) invert the normal-mode (Fourier) transform by pre-multiplying the sampled position vector by the discrete Fourier transform matrix $\mathbf{C}$. The dividing-surface sampling is completed by sampling the initial momenta. Those terms in the RPMD-C correlation function which are not evaluated at $t=0$ must then be obtained by evolving the ring-polymer equations of motion.

4.7 A symmetric Eckart barrier

The symmetric Eckart barrier

$$V(q) = \frac{V_0}{\cosh^2(q/a)}, \tag{4.75}$$

when parameterized to mimic the collinear $H+H_2$ reaction, i.e.,

$$V_0 = 0.425\,\mathrm{eV}, \tag{4.76}$$

$$a = 0.734\,\mathrm{a_0}, \tag{4.77}$$

$$m = 1061\,m_e, \tag{4.78}$$

is a standard model for gas-phase bimolecular reactions. The availability of the exact quantum-mechanical rate coefficients of this model has motivated a number of studies based upon approximate quantum-dynamical techniques [112, 113, 122]. Here, it forms the basis of a numerical study which will seek to assess the accuracy and relative efficiency of the RPMD-B/C methods. The temperature range that will be considered ($2000 \geq T[\mathrm{K}] \geq 200$) stretches from the high-temperature classical limit to the low-temperature regime in which quantum-mechanical tunneling through the barrier is dominant and where the quantum reaction rate coefficients are orders of magnitude higher than the classical ones. This model therefore presents a comprehensive test of the new methods and also facilitates critical comparison with the results of alternative approximate methods (see Section 4.2).

First, some details of the RPMD-B/C calculations. The reaction partition function is required when either of these approximations to $\tilde{c}_{\mathrm{fs}}(t)$ is substituted into Eq. (4.30)

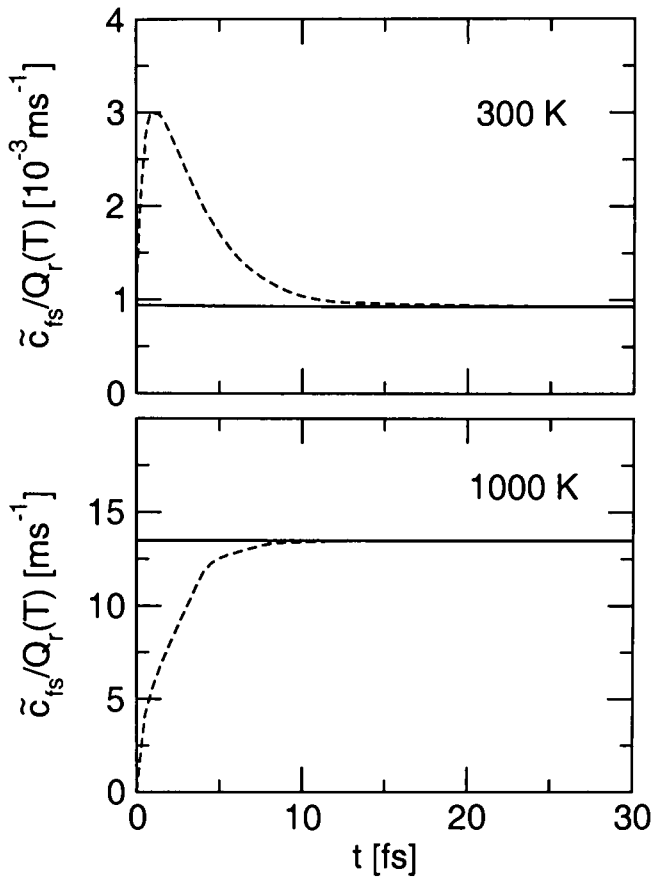

Figure 4.4: Approximate Kubo-transformed flux-side correlation functions as calculated by the RPMD-B (dotted line) and RPMD-C (solid line) methods for the symmetric Eckart barrier at 300 and 1000 K.

and for free translational motion in one dimension it is

$$Q_r(T) = \left(m/2\pi\beta\hbar^2\right)^{1/2} = 1/\Lambda(T), \tag{4.79}$$

which has units of reciprocal length. For both RPMD-B and RPMD-C the number of ring-polymer beads required for convergence at the lowest temperature (200 K) was 128, and a time step of 0.5 fs was found to converge the ring-polymer dynamics. The dividing surface has been located at $q^{\ddagger}$=0 (the barrier top) in all calculations reported in this section, although Section 4.9 will formally establish the invariance of the results to this choice.

In order to demonstrate that the two RPMD flux-side correlation functions are equivalent in the long-time limit, Fig. 4.4 shows $\tilde{c}_{\rm fs}(t)/Q_r(T)$ versus time for both methods at a low (300 K) and a high (1000 K) temperature. By Eq. (4.30), the approximate

canonical rate coefficient is equal to the value of these plots at the point where they become independent of time (the 'plateau' value). Their equivalence at long times is clear from the figure, as is the apparently instantaneous attainment of the plateau value by the RPMD-C correlation functions. The latter observation implies that trajectories sampled in the RPMD-C approach need to be followed for only a very short time. By contrast, the RPMD-B method takes about 10 fs to reach the long-time limit at both temperatures. Thus, this approach requires more time evolution and is significantly less efficient than RPMD-C for the symmetric Eckart barrier.

The origin of this difference in efficiency is that pinning the centroid is a stronger constraint on the initial positions of the ring-polymer beads than pinning a single bead. This means that the RPMD-C approach samples ring-polymers with beads more evenly distributed around, and in greater proximity to, the top of the barrier. As a result there is less dividing-surface recrossing by the centroid in RPMD-C than by the single bead in RPMD-B. Thus, the RPMD-C correlation function reaches the long-time limit more quickly (see Fig. 4.4). These considerations will apply equally well to all models for activated chemical reactions, and therefore the shorter time-evolution required by RPMD-C is expected to be quite general.

Another consequence of the tighter RPMD-C constraint on the initial positions of the ring-polymer beads is illustrated in Fig. 4.5, which plots histograms of the factors

$$f_1(\mathbf{p},\mathbf{q}) = \frac{p_1}{m} e^{-\beta_n \sum_{k=1}^{n} V(q_k)}, \tag{4.80}$$

and

$$f_c(\mathbf{p},\mathbf{q}) = \frac{p_c}{m} e^{-\beta_n \sum_{k=1}^{n} V(q_k)}, \tag{4.81}$$

which are respectively present (evaluated at $t = 0$) in the RPMD-B and RPMD-C integrands. For each method, the histogram is constructed from the f factors of the

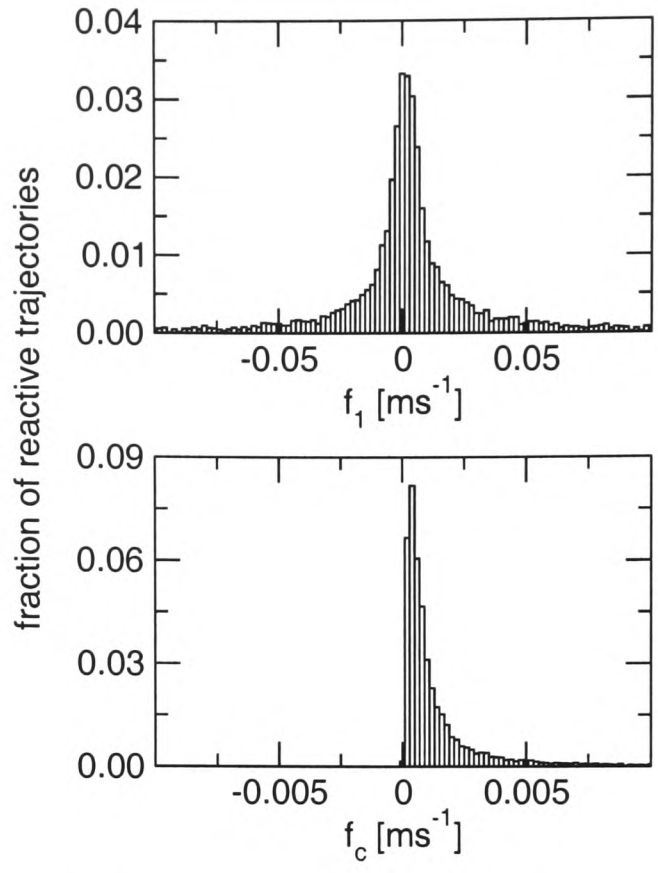

Figure 4.5: Histograms of the RPMD-B $f_1(\mathbf{p},\mathbf{q})$ factor (Eq. (4.80)) and the RPMD-C $f_c(\mathbf{p},\mathbf{q})$ factor (Eq. (4.81)) for the symmetric Eckart barrier at 300 K.

trajectories that localize on the product side of the barrier as $t\rightarrow\infty$. Since the exponential factors are positive, the negative sides of the histograms arise from trajectories with beads/centroids that are initially located at the dividing surface and heading towards the reactant region. The fact that they end up on the product side requires them to recross the dividing surface. Conversely, the positive sides of the histograms are due to trajectories with beads/centroids initially heading towards the product side and which, therefore, do not (necessarily) recross the dividing surface. The canonical rate coefficient arises from an incomplete cancellation between the positive and negative sides of each histogram.

Perhaps the first point to note is the contrast between the negative sides of the histograms. The top panel of Fig. 4.5 shows that there must be a very substantial cancellation between the $f_1<0$ and $f_1>0$ trajectories when the rate is calculated by the RPMD-B method. This implies that the initial direction of motion of the pinned bead

is a poor indicator of which side of the barrier the ring-polymer will end up on. By contrast, the bottom panel shows that in the RPMD-C method the initial direction of the pinned centroid is strongly correlated with the final location of the ring-polymer. This is an illustration of the comparative scarcity of recrossing trajectories in the RPMD-C approach that was mentioned above.

A direct consequence of the stronger correlation between the factors in the integrand of the RPMD-C approximation is that it requires far fewer trajectories to converge than the RPMD-B method. In the latter case, the delicately-balanced cancellation required in the top panel of Fig. 4.5 must be enforced with a larger number of trajectories because there is a larger variation in the contribution that each makes to the correlation function. The symmetric Eckart model illustrates this point – whereas the RPMD-C calculations gave converged rate coefficients with 10^5 ring-polymer trajectories, the RPMD-B approach needed 10^7. So, in addition to requiring the ring-polymer trajectories to be evolved for a shorter time than the RPMD-B method, the sampling required to evaluate the RPMD-C integral is more efficient. For these reasons the RPMD-B method will be now be abandoned and all further work in this chapter concerns the RPMD-C approach of Section 4.4.

Having demonstrated the relative efficiency of the RPMD-C method, it remains to establish its accuracy and to compare it with other approximate approaches. Therefore Fig. 4.6 is an Arrhenius plot of the exact, RPMD-C and classical transition-state theory (CTST) rate coefficients of the symmetric Eckart barrier at temperatures ranging from 200 K to 2000 K. The CTST results are the 'exact' classical results because there is no recrossing of a dividing surface located at the top of a one-dimensional bimolecular reaction barrier in classical mechanics. The figure also shows the percentage error in the RPMD-C rate coefficient as a function of $1/T$. It is clear that the new method becomes exact in the high-temperature (classical) limit. More interestingly,

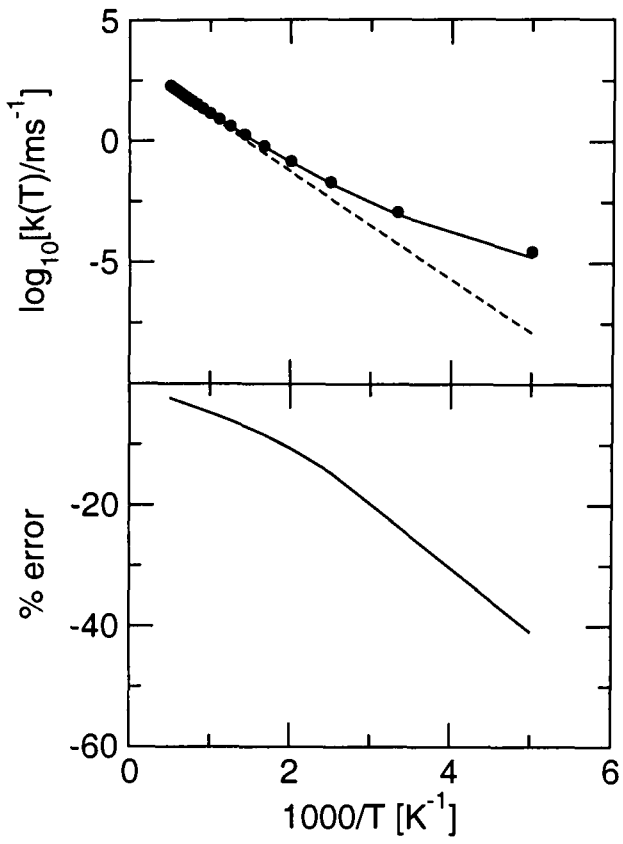

Figure 4.6: Top: an Arrhenius plot of the canonical rate coefficient for the symmetric Eckart barrier. The exact quantum-mechanical (filled circles), RPMD-C (solid line) and classical (dashed line) results are shown. Bottom: the percentage error in the RPMD-C result as a function of $1000/T$.

it performs rather well even at the lowest temperatures where quantum-mechanical tunneling effects make the dominant contribution to $k(T)$. At 200 K the quantum-mechanical rate coefficient is three orders of magnitude higher than the classical one but the RPMD-C result is still within 50% of the exact result. Overall, the quality of these results encourages the application of the new method to more challenging and more complex models of chemical reactions.

The accuracy of RPMD-C for this symmetric Eckart barrier is comparable to that of the classical Wigner model (CWM) (Section 4.2 and Ref. [122]). For this one-dimensional system the Wigner-transform of the flux operator can be evaluated numerically without approximation and the CWM can therefore reach down to the low temperatures considered here. However, this approach to the CWM evaluation of rate coefficients is only feasible for low-dimensional systems, whereas in principle there is

nothing preventing the RPMD-C methodology from being applied to far larger reactive systems. The accuracy of the RPMD-C method is also comparable to that of the simpler versions of the QI theory [112, 113], although more advanced QI techniques do somewhat better at the lowest of the temperatures considered here.

4.8 The short-time limit

The rapid attainment of the plateau value in Fig. 4.4 and the asymmetry in the bottom panel of Fig. 4.5 show that dividing-surface recrossing is of little importance in the RPMD-C treatment of the symmetric Eckart model. The dynamics of the ring-polymer trajectories therefore play a small role in determining the value of the RPMD-C rate coefficient in this particular system. It is now demonstrated that neglecting the dynamics of the new method completely (e.g. taking the short-time limit) leads to the quantum transition-state theory introduced in Section 4.2.

Consider the RPMD-C correlation function (Eq. (4.53)) in the short-time limit. At such times, the dynamics of the ring-polymer have not started to be influenced by the forces exerted by the barrier potential. The initial momentum of the ($q^{\ddagger}$-pinned) ring-polymer centroid is therefore the only factor governing which side of the dividing surface it occupies as $t \to 0$. As a result, one may write

$$\lim_{t\to 0} h_c(\mathbf{q}_t) = h(p_c(0)), \tag{4.82}$$

which is a step function that is zero unless the initial centroid momentum (Eq. (4.56)) is positive. Substituting this result into Eq. (4.53) allows a separation of the position and momentum integrals in the RPMD-C correlation function,

$$\tilde{c}_{\mathrm{fs}}(t \to 0_+) = \lim_{n\to\infty} \frac{1}{(2\pi\hbar)^n} I_p^{(n)} I_q^{(n)}, \tag{4.83}$$

where

$$I_p^{(n)} = \int d\mathbf{p}\, \frac{p_c}{m}\, h(p_c) \exp\left[-\beta_n \sum_{k=1}^{n} p_k^2/2m\right], \tag{4.84}$$

and

$$I_q^{(n)} = \int d\mathbf{q}\, \delta(q_c - q^\ddagger) \exp\left[-\beta_n \sum_{k=1}^{n} \left(\frac{1}{2} m\omega_n^2 (q_k - q_{k+1})^2 + V(q_k)\right)\right]. \tag{4.85}$$

The momentum integral (Eq. (4.84)) can be done using the ring-polymer normal-mode transformation discussed in Appendix B since this naturally introduces p_c as an integration variable and therefore allows the step function $h(p_c)$ to be taken into account. The resulting Gaussian integration gives

$$I_p^{(n)} = \frac{1}{2} \langle |\dot{q}| \rangle_{\mathrm{cl}} \left(\frac{2\pi m}{\beta_n}\right)^{n/2}, \tag{4.86}$$

where the first factor is the classical reactive flux through the dividing surface

$$\frac{1}{2} \langle |\dot{q}| \rangle_{\mathrm{cl}} = \left(\frac{1}{2\pi m \beta}\right)^{1/2}. \tag{4.87}$$

A path-integral discretization of the centroid-constrained partition function [108, 109]

$$Q(q^\ddagger) = \mathrm{tr}\left[e^{-\beta \hat{H}}\, \delta(\hat{q} - q^\ddagger)\right], \tag{4.88}$$

shows that

$$Q(q^\ddagger) = \lim_{n\to\infty} \left(\frac{m}{2\pi\beta_n \hbar^2}\right)^{n/2} I_q^{(n)}. \tag{4.89}$$

Therefore,

$$\tilde{c}_{\mathrm{fs}}(t \to 0_+) = \frac{1}{2} \langle |\dot{q}| \rangle_{\mathrm{cl}}\, Q(q^\ddagger), \tag{4.90}$$

or

$$\frac{1}{Q_r(T)}\,\tilde{c}_{\rm fs}(t\rightarrow 0_+) = \frac{1}{2}\,\langle|\dot{q}|\rangle_{\rm cl}\,\frac{Q(q^\ddagger)}{Q_r(T)} \equiv k_{\rm QTST}. \tag{4.91}$$

The short-time limit of the RPMD-C method is therefore identical to the Voth-Chandler-Miller quantum transition-state theory (QTST) [107]. This result, which holds quite generally, means that RPMD-C provides a dynamic correction to the QTST rate coefficient in the same way that the classical reactive flux method gives the dynamic correction to that of classical transition-state theory. In those reactions for which recrossing trajectories are rare, the RPMD-C correlation function will rapidly converge on the QTST result and will therefore provide an efficient means to calculate an approximate $k(T)$.

4.9 The long-time limit

From Eq. (4.91) it is evident that the *short-time* (QTST) approximation to the rate coefficient varies with the chosen location of the dividing surface ($q^\ddagger$). However, it was shown in Section 4.1 that the exact quantum-mechanical $k(T)$ is independent of $q^\ddagger$. It is therefore appropriate to establish the dependence of the RPMD-C rate coefficient on the choice of dividing surface. The equivalent classical considerations are illustrative and begin this section.

Using arguments analogous to those presented in the previous section, it can be shown that the short-time limit of $c_{\rm fs}^{\rm cl}(t)$ (Eq. (4.50)) leads to the classical transition-state theory (CTST) rate coefficient,

$$k_{\rm CTST}(T) = \left[\frac{1}{2}\,\langle|\dot{q}|\rangle_{cl}\right]\frac{Q_{\rm cl}^\ddagger(T)}{Q_{r,{\rm cl}}(T)} = \left[\frac{1}{2}\,\langle|\dot{q}|\rangle_{cl}\right]e^{-\beta V(q^\ddagger)}, \tag{4.92}$$

where the second equality holds for a one-dimensional reactive system. From the final term in this expression it is clear that the value of $k_{\rm CTST}(T)$ depends on where one

chooses to locate the dividing surface $q^{\ddagger}$. In a CTST calculation this choice of $q^{\ddagger}$ is generally optimized such that the rate coefficient $k_{\mathrm{CTST}}(T)$ is minimised [106, 123].

However, the 'exact' classical $k_{\mathrm{cl}}(T)$ is obtained not from the short-time limit of $c_{\mathrm{fs}}^{\mathrm{cl}}(t)$ but from its long-time plateau value. To establish that the latter is independent of the choice of dividing surface note that the classical canonical phase-space distribution is an even function of p_0, the initial momentum. Thus, the forward ($p_0 > 0$) and backward ($p_0 < 0$, remember that $q_t(-p_0, q_0) = q_{-t}(p_0, q_0)$) parts of each classical trajectory are sampled with equal weight. For a recrossing trajectory, the forward and backward parts end up on the same side of the dividing surface as $t \to \infty$ and therefore make contributions to $c_{\mathrm{fs}}^{\mathrm{cl}}(t)$ of equal magnitude but opposite sign (see the integrand of Eq. (4.50)). These contributions cancel, and as a result, recrossing trajectories have no direct influence on the value of the exact classical rate coefficient. This leaves a set of reactive trajectories which will have crossed any dividing surface as $t \to \infty$ and which make all the nonzero contributions to $k_{\mathrm{cl}}(T)$. A consequence of this is that the exact classical rate coefficient is independent of the choice of dividing surface.

The considerations in the previous paragraphs show that the classical reactive flux method can be regarded as a dynamic correction to classical transition-state theory. In just the same way, the ring-polymer dynamics in the RPMD-C method correct the $q^{\ddagger}$-dependence of the short-time QTST rate coefficient. This is easiest to see from the RPMD-C approximation to the side-side correlation function (Eq. (4.51)). Differentiating this approximate $\tilde{c}_{\mathrm{ss}}(t)$ once with respect to $q^{\ddagger}$ gives

$$\frac{\partial \tilde{c}_{\mathrm{ss}}(t)}{\partial q^{\ddagger}} = \frac{-1}{(2\pi\hbar)^n} \int d\mathbf{p}_0 \int d\mathbf{q}_0 \, e^{-\beta_n H_n(\mathbf{p}_0, \mathbf{q}_0)} \left[\delta_c(\mathbf{q}_0) h_c(\mathbf{q}_t) + h_c(\mathbf{q}_0) \delta_c(\mathbf{q}_t)\right], \qquad (4.93)$$

where $h_c(\mathbf{q})$ and $\delta_c(\mathbf{q})$ are defined in Eq. (4.52) and Eq. (4.54) respectively. Since the ring-polymer dynamics are classical dynamics (albeit in an extended phase space) they

conserve the ring-polymer Hamiltonian and the Liouville equation holds. As a direct consequence, the ring-polymer phase-space density and volume are conserved, i.e.,

$$e^{-\beta_n H_n(\mathbf{p}_t,\mathbf{q}_t)} = e^{-\beta_n H_n(\mathbf{p}_0,\mathbf{q}_0)}, \tag{4.94}$$

and

$$d\mathbf{p}_t\, d\mathbf{q}_t = d\mathbf{p}_0\, d\mathbf{q}_0. \tag{4.95}$$

Following a shift in the time origin, these two properties allow the second term in the integrand of Eq. (4.93) to be written as

$$\frac{-1}{(2\pi\hbar)^n} \int d\mathbf{p}_0 \int d\mathbf{q}_0\, e^{-\beta_n H_n(\mathbf{p}_0,\mathbf{q}_0)}\, h_c(\mathbf{q}_{-t})\delta_c(\mathbf{q}_0). \tag{4.96}$$

However, the time-reversibility of the ring-polymer dynamics (Eq. (4.44)) and the $\mathbf{p}$-inversion symmetry of the ring-polymer Hamiltonian,

$$H_n(-\mathbf{p},\mathbf{q}) = H_n(\mathbf{p},\mathbf{q}), \tag{4.97}$$

can be used show that this second term is identical to the first. Therefore,

$$\frac{\partial \tilde{c}_{\rm ss}(t)}{\partial q^\ddagger} = \frac{-2}{(2\pi\hbar)^n} \int d\mathbf{p}_0 \int d\mathbf{q}_0\, e^{-\beta_n H_n(\mathbf{p}_0,\mathbf{q}_0)}\, \delta_c(\mathbf{q}_0) h_c(\mathbf{q}_t), \tag{4.98}$$

and since $\tilde{c}_{\rm fs}(t)$ is just minus the time derivative of $\tilde{c}_{\rm ss}(t)$,

$$\frac{\partial \tilde{c}_{\rm fs}(t)}{\partial q^\ddagger} = \frac{2}{(2\pi\hbar)^n} \int d\mathbf{p}_0 \int d\mathbf{q}_0\, e^{-\beta_n H_n(\mathbf{p}_0,\mathbf{q}_0)}\, \delta_c(\mathbf{q}_0)\, \delta_c(\mathbf{q}_t) v_c(\mathbf{p}_t), \tag{4.99}$$

where the centroid velocity factor $v_c(\mathbf{p})$ is defined in Eq. (4.55). From the integrand of this expression it is clear that $\partial \tilde{c}_{\rm fs}(t)/\partial q^\ddagger = 0$ unless there are ring-polymer trajectories that have centroids which (a) start at the dividing surface at $t = 0$, (b) return to

the dividing surface at time t, and (c) have a nonzero centroid velocity at time t. Whilst there can certainly be trajectories that fulfil all three requirements at a general time t, conditions (b) and (c) are incompatible in the long-time limit – any trajectory that sits at $q^\ddagger$ as $t \to \infty$ must be stationary and cannot have a velocity component directed away from the dividing surface. In the limit $t \to \infty$, therefore, one must have $\partial \tilde{c}_{\mathrm{fs}}(t)/\partial q^\ddagger = 0$ for all possible choices of $q^\ddagger$. The long-time limit of the RPMD-C approximation to $\tilde{c}_{\mathrm{fs}}(t)$ and the RPMD-C rate coefficient (via Eq. (4.30)) are thus formally independent of the choice of the dividing surface. Although presented here for the one-dimensional case, similar arguments hold for activated chemical reactions with any number of degrees of freedom.

In Fig. 4.7, the symmetric Eckart barrier is used to demonstrate the dependence of the RPMD-C and QTST rate coefficients on the choice of dividing surface. The top panel shows five such surfaces superimposed upon the symmetric Eckart potential – one at the top of the barrier, two at the points where it has half its maximum value and another two twice as far out again. The middle panel plots the RPMD-C correlation function against time for each dividing surface at a temperature of 300 K. Note that, by symmetry, there are only three distinct correlation functions, and that they converge on the same long-time limit and thus give the same RPMD-C approximation to $k(T)$ regardless of $q^\ddagger$. From their short-time behaviour, it is also evident that there is more recrossing from the dividing surfaces further from the barrier top. Choosing such surfaces therefore results in calculations that require longer time evolution and more trajectories for convergence (see Section 4.7).

The bottom panel shows the variation of the RPMD-C and QTST rate coefficients with $q^\ddagger$ at 300 K. Clearly, the QTST rate coefficient varies tremendously depending on where the dividing surface is placed – over this range of $q^\ddagger$ it takes values that span nearly six orders of magnitude. The QTST method is most accurate when the dividing

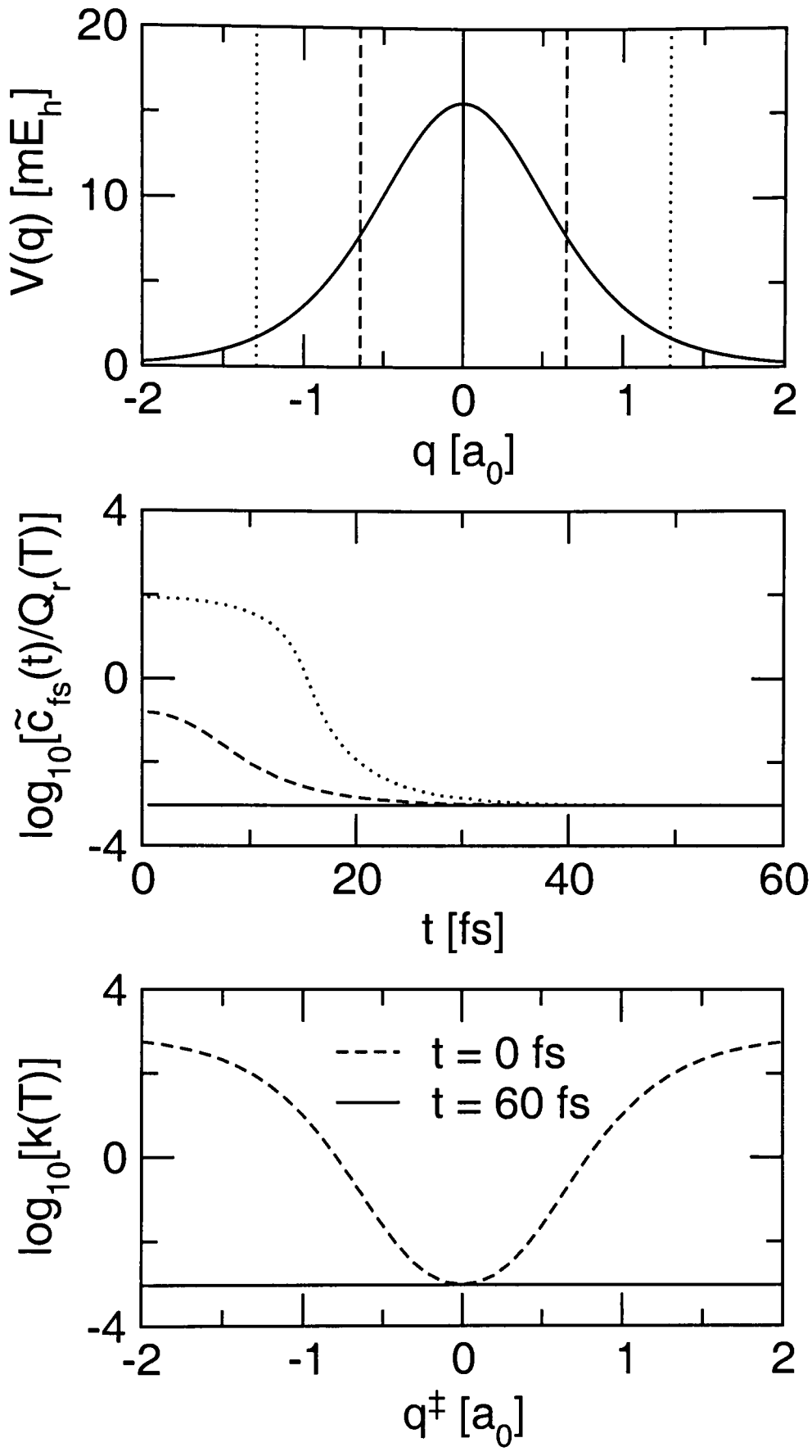

Figure 4.7: Top: five different dividing surfaces superimposed upon the symmetric Eckart barrier potential. Middle: the RPMD-C flux-side correlation functions for each dividing surface at 300 K. There are only three distinct results by symmetry. Bottom: the QTST ($t \to 0$) and RPMD-C ($t \to \infty$) rate coefficients as functions of the location of the dividing surface, also at 300 K.

surface is located at the top of the barrier, in which case it gives the same result as RPMD-C (within graphical accuracy). This is because there is negligible recrossing of this dividing surface by the RPMD-C trajectories. In contrast to the sensitivity of the QTST approach, the result of the RPMD-C calculation is visibly independent of the location of the dividing surface.

As revealed by the analysis above (Eq. (4.93) to Eq. (4.99)), this invariance of the RPMD-C rate coefficient relies on the validity of the Liouville equation for the ring-polymer phase space. This guarantees the conservation of the phase-space volume as well as the conservation of the phase-space density [27]. As in a classical reactive flux calculation [95–97], the symmetry of the ring-polymer Hamiltonian then ensures that the contributions from forward and backward parts of recrossing ring-polymer trajectories cancel out exactly in the long-time limit and have no direct influence on the RPMD-C rate coefficient. Of course, if one chooses a dividing surface that generates a preponderance of recrossing ring-polymer trajectories then the method becomes inefficient precisely because such trajectories don't directly contribute to the approximate $k(T)$. Nevertheless, the independence of the RPMD-C results from the choice of dividing surface may turn out to be a very useful feature when it comes to performing rate calculations for complex reactions since locating the optimal QTST dividing surface in large reactive systems is often a difficult task [119].

4.10 An asymmetric Eckart barrier

In the previous section it was found that the RPMD-C rate coefficients for the symmetric Eckart barrier were graphically identical to, and therefore no more accurate than, the results of an optimized QTST calculation [107]. However, it was also shown that the RPMD-C approach would obtain the same results wherever the dividing surface was placed, whereas the QTST rate coefficients were found to be highly sensitive

to this choice. For the symmetric Eckart barrier this difference does not translate into a practical advantage for the RPMD-C method because the optimal QTST dividing surface is determined by symmetry, and therefore does not have to be located by a laborious search procedure [119]. This section considers a related one-dimensional barrier potential with somewhat different characteristics.

The *asymmetric* Eckart barrier is defined by the potential [110]:

$$V(q) = \frac{A}{1+e^{-2q/a}} + \frac{B}{\cosh^2(q/a)}, \tag{4.100}$$

where, in units such that $\hbar = k_B = m = 1$, the parameters are: $A = -18/\pi$, $B = 13.5/\pi$ and $a = 8/\sqrt{3\pi}$. Note that the first term in this potential desymmetrizes the second (a symmetric Eckart barrier) so that $V(q \to -\infty) = 0$ and $V(q \to \infty) = A$.

In contrast to the situation encountered in previous sections, the optimal QTST dividing surface for this problem cannot be determined by symmetry and must be located numerically. Due to the finite size of the ring polymers in the discretized QTST expression (Eq. (4.91), Eq. (4.89) and Eq. (4.85)), locating the optimal QTST dividing surface is not even as simple as finding the top of the potential barrier. Thus, in this system the fact that the rate coefficient of the RPMD-C method is independent of the choice of dividing surface might confer upon it a practical advantage, i.e. it may require less computation than an optimized QTST calculation. Whether it does or not will depend on the balance between the effort involved in the $q^\ddagger$-optimization (QTST) and that needed to evaluate the ring-polymer dynamics (RPMD-C). Additional motivation for studying this problem comes from the fact that even the optimal dividing surface has been found to give QTST results that are of relatively poor accuracy at low temperatures [124]. One can therefore hope that the dynamics in the RPMD-C method might provide rate coefficients that are in better agreement with the exact

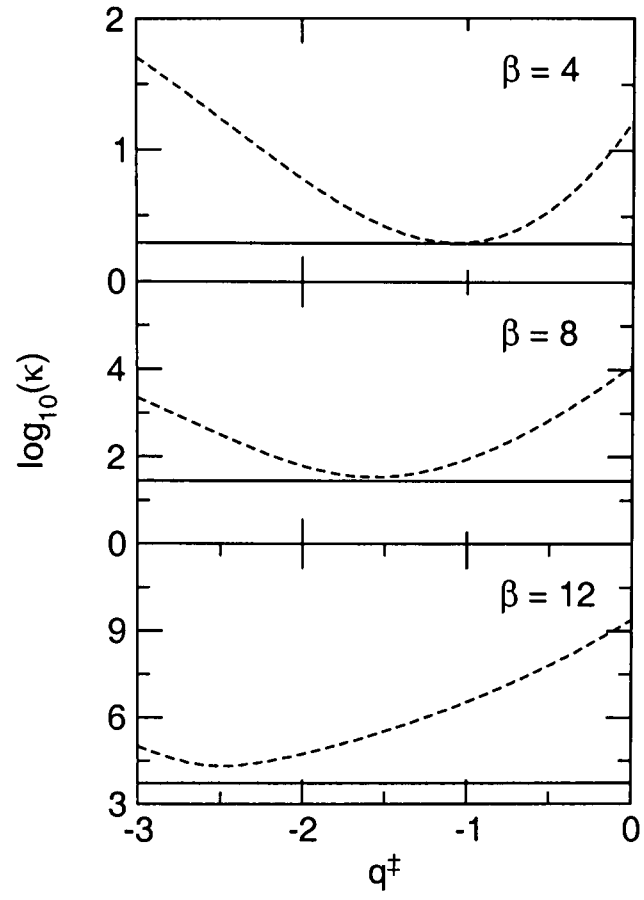

Figure 4.8: Transmission coefficients (Eq. (4.101)) for the asymmetric Eckart barrier as calculated by the RPMD-C (solid line) and QTST (dotted line) methods at three different temperatures. The results are plotted as functions of the location of the dividing surface.

results.

In order to establish that the QTST results for the asymmetric Eckart barrier do indeed depend upon where the dividing surface is placed, Fig. 4.8 plots the dimensionless transmission coefficients,

$$\kappa = \frac{k(T)}{k_{\rm cl}(T)}, \tag{4.101}$$

that result from QTST (and RPMD-C) calculations performed for $-3 \leq q^{\ddagger} \leq 0$. For this one-dimensional barrier system the exact classical rate coefficient ($k_{\rm cl}(T)$) is given exactly by classical transition-state theory (Eq. (4.34)). At each of the three temperatures considered it is clear that the QTST results vary by orders of magnitude within this range of $q^{\ddagger}$, with greater variation at lower temperature. The RPMD-C results are again seen to be independent of the choice of dividing surface.

Whilst the sensitivity of the QTST results to the choice of $q^{\ddagger}$ echoes that observed for the *symmetric* Eckart barrier, there are two new phenomena apparent in the results for the asymmetric system. Firstly, the optimum QTST dividing surface, i.e. the value of $q^{\ddagger}$ that minimises the QTST transmission coefficient, is found to vary with temperature. For classical transition-state theory (CTST) the optimum dividing surface is the top of the potential barrier ($q^{\ddagger}_{\mathrm{CTST}} = -(a/2)\ln(2)$) for all T, since there is never any dividing-surface recrossing amongst classical trajectories launched from this point.

In the high-temperature limit the ring polymer contracts to a point particle and so QTST becomes equivalent to CTST and shares the same optimal dividing surface. However, as the temperature is lowered the ring polymer expands due to a weakening of the kinetic springs. Since the centroid-pinned ring polymer has its beads dispersed on either side of the dividing surface, its centroid is subject to forces arising from both sides of the potential – this is clear from:

$$\dot{p}_c = \frac{1}{n}\sum_{j=1}^{n}\dot{p}_j = -\frac{1}{n}\sum_{k=1}^{n}\frac{dV(q_k)}{dq_k}. \tag{4.102}$$

Moving away from the top of the barrier, the forces increase more rapidly and are generally greater on the product side because the parameter A is negative. Thus, if the QTST dividing surface is just kept at $q^{\ddagger}_{\mathrm{CTST}}$ as the temperature is decreased, the centroid of the expanding ring polymer will experience an increased initial force towards the product side. Greater recrossing will be a direct consequence of this, i.e. more centroids with negative initial momentum will end up at positive q in the long-time limit. As a result of this effect, the optimum QTST dividing surface is found further towards the reactant region at lower temperatures. This point is illustrated in Fig. 4.9.

The second new phenomenon observed in Fig. 4.8 is that even at the optimum dividing

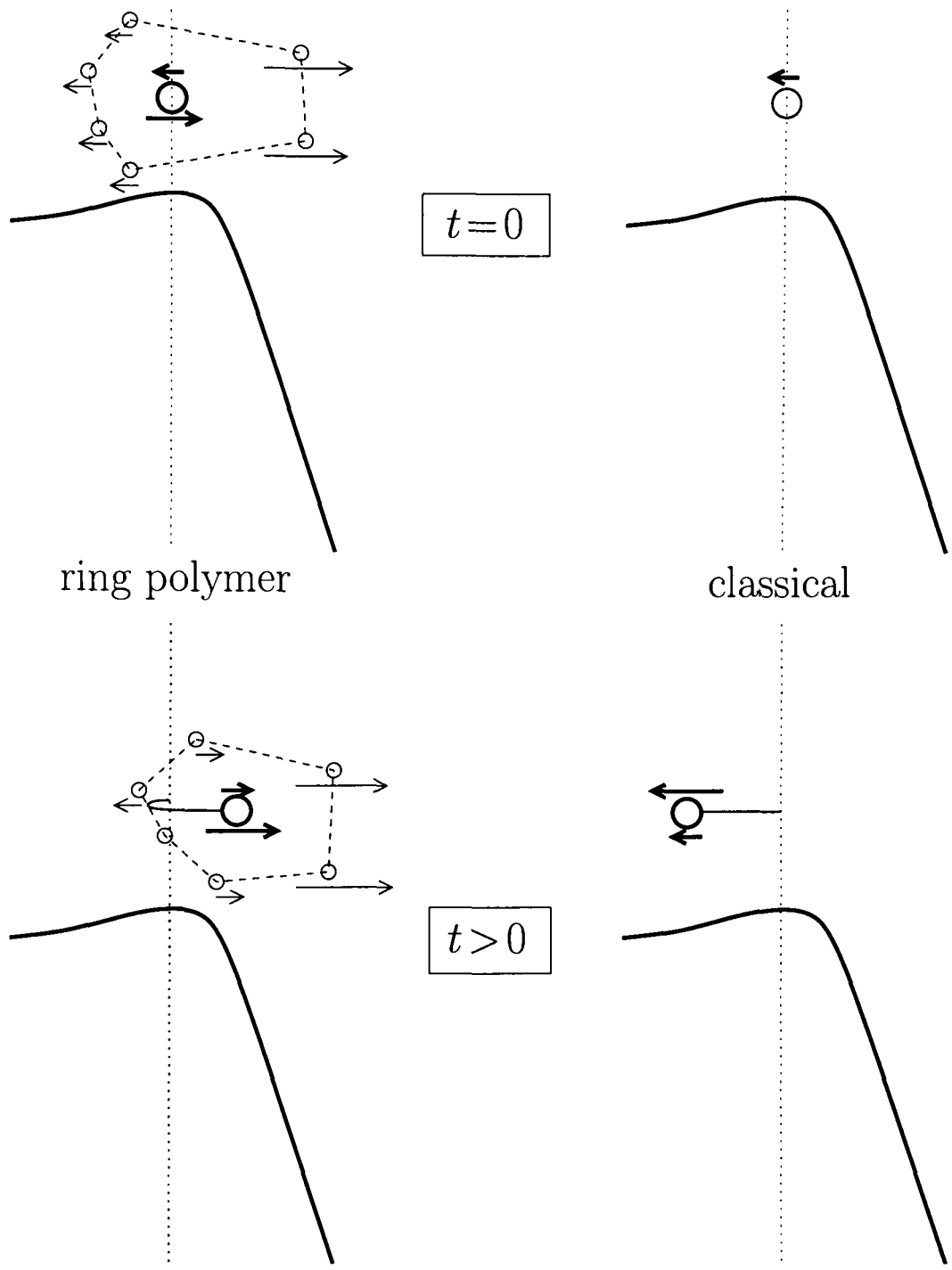

Figure 4.9: Schematic illustration of the recrossing induced by the spatial dispersion of the ring polymer versus the absence of recrossing effects in a purely classical description. An arrow below an object indicates the force exerted upon it by the potential (excludes kinetic spring forces). An arrow above an object indicates its momentum. Vertical dotted lines indicate the optimal CTST dividing surface. Top: the ring-polymer centroid (left, in bold) and the classical particle (right) are pinned to the top of the barrier at $t = 0$ and have the same initial momentum towards reactants. Whereas there is no force on the classical particle there is a force pulling the centroid towards products. Bottom: as a result of the different initial forces the ring-polymer centroid has recrossed the dividing surface whereas the classical particle hasn't.

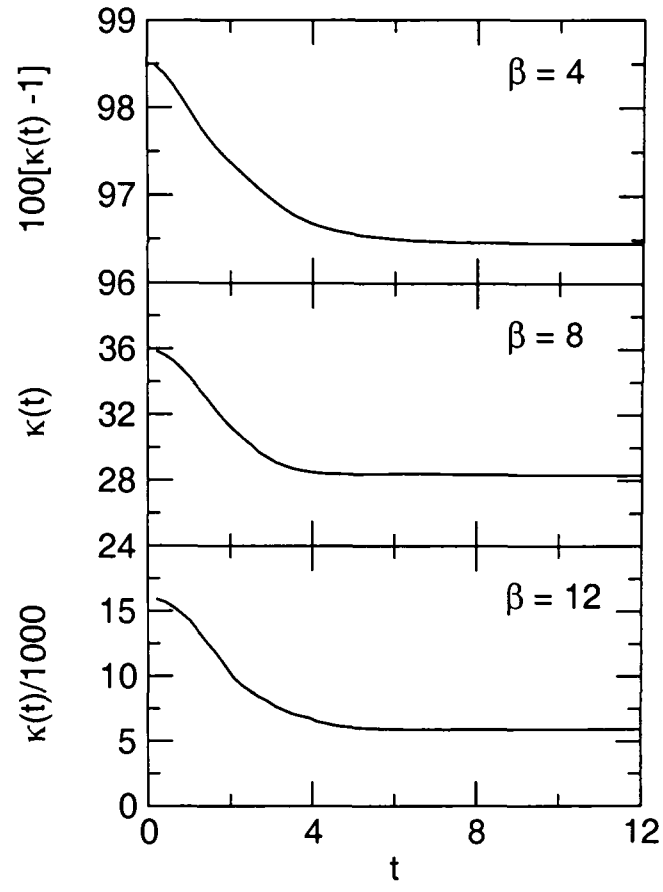

Figure 4.10: Time-dependent RPMD-C transmission coefficents (Eq. (4.103)) for the asymmetric Eckart barrier at the three temperatures considered in Fig. 4.8.

surface the QTST results are higher than those of the RPMD-C method. At the lowest temperature a significant gap is visible between the minimum of the QTST curve and the RPMD-C line (n.b. the ordinate is logarithmic in κ). The origins of this effect are clear in Fig. 4.10, which plots the RPMD-C time-dependent transmission coefficients,

$$\kappa(t) = \frac{\tilde{c}_{\mathrm{fs}}(t)}{Q_r(T)\, k_{\mathrm{cl}}(T)}, \tag{4.103}$$

for the optimal QTST dividing surface at each of the three temperatures. The significance of this quantity is that in the short-time limit it gives the optimum QTST transmission coefficient and in the long-time limit it gives the RPMD-C result. At each temperature, the decay of $\kappa(t)$ indicates that recrossing is occuring from the optimal QTST dividing surface. This is the cause of the disagreement between the RPMD-C and optimal QTST results in Fig. 4.8. Note that the different ordinate scales of the panels in Fig. 4.10 disguise the greater extent of the recrossing at lower temperatures,

Table 4.1: Transmission coefficients (Eq. (4.101)) for the asymmetric Eckart barrier.

β	QTST[a]	CV[b]	PL[c]	RPMD-C	QM
2	1.2	1.2	1.2	1.2	1.2
4	2.0	2.2	2.0	2.0	2.0
6	5.6	6.4	5.6	5.3	5.3
8	36	31	44	28	26
10	540	340	1100	310	250
12	16000	7600	28000	5900	4100

[a]QTST of Voth, Chandler and Miller (Eq. (4.91))
[b]QTST of Cao and Voth [124, 125]
[c]QTST of Pollak and Liao [110]

which results in the larger discrepancies in the lower panels of Fig. 4.8.

Finally, an assessment of the accuracy of these RPMD-C calculations can be made using Table 4.1, which shows the RPMD-C transmission coefficients alongside the exact quantum-mechanical κ. Also shown are the results of the primitive QTST which has been involved throughout this discussion [107] and those of two other quantum transition-state theories [110, 124, 125]. Both the RPMD-C and primitive QTST transmission coefficients required $n = 256$ ring-polymer beads for convergence, and the QTST result was obtained using the optimum dividing surface at each temperature.

A couple of points can made about the accuracy of the RPMD-C results for this asymmetric Eckart barrier. Firstly, it is similar to that which was observed for the symmetric Eckart barrier. This is significant because other approximate techniques have been found to give less accurate rate coefficients for the asymmetric problem [124]. Secondly, the recrossing identified in previous paragraphs has the effect of making the RPMD-C transmission coefficients more accurate than those of the primitive QTST

of Voth, Chandler and Miller QTST [107]. This improvement of the RPMD-C results over those of the primitive QTST approach is seen to increase at lower temperatures. Thirdly, note a contrast with the symmetric Eckart barrier: there, the optimal QTST dividing surface effectively eliminated recrossing effects so that the QTST was made as accurate as RPMD-C and here it merely minimises recrossing so that the RPMD-C results are superior. Of the other QTSTs, that of Cao and Voth is closest in accuracy to the RPMD-C method. Overall, the agreement between the RPMD-C and exact results is encouraging and motivates the application of the new method to reactive systems of greater complexity.

4.11 Summary

This chapter has presented two RPMD-based approaches to calculating approximate canonical rate coefficients for chemical reactions. It has been shown that one of these methods (RPMD-C) is significantly more efficient than the other (RPMD-B) because a smaller proportion of the ring-polymer trajectories that it samples recross the dividing surface. In addition, the RPMD-C method has been shown to have a number of desirable properties – it gives the exact quantum-mechanical rate coefficient for a parabolic reaction barrier, it tends to a well-defined quantum transition-state theory in the short-time limit and in the long-time ($k(T)$-determining) limit the results are independent of the choice of dividing surface.

The RPMD-C method has been applied to one symmetric and one asymmetric Eckart barrier. Over the broad ranges of temperature considered the RPMD-C rate coefficients were always found to be within 50% of the exact quantum-mechanical values, and were often much more accurate than that. Even at the lowest temperatures (where the maximum errors occur) the accuracy of the new method is satisfying since the corresponding classical rate coefficients are out by more than three orders of magnitude.

In short, the accuracy of the RPMD-C approach for these one-dimensional models of bimolecular chemical reactions seems to be as good as, if not better than, that of numerous alternative approximate methods.

The attractive short- and long-time limits of the new method, and the practical advantages that they might imply, are independent of the complexity of the chemical reaction under investigation. However, it remains to be seen whether the accuracy that is apparent for one-dimensional reactions will persist for calculations involving larger reactive systems. This question is tackled in the next chapter. It is an important one because, as discussed in the opening paragraphs of this chapter, it is not (generally) possible to calculate the exact quantum-mechanical rate coefficients of complex reactive systems and therefore approximate methods like RPMD-C become a necessity.

This chapter closes with some comments on an interesting observation. The recrossing seen in Fig. 4.10 is a non-classical effect since, as discussed previously, no classical trajectory recrosses the optimum CTST dividing surface for a one-dimensional bimolecular reaction barrier. The 'non-classical' recrossing is due to the finite size of the ring-polymer and the fact that it is subject to forces derived from a number of different points on the potential barrier (Eq. (4.102)). Thus, there can be a retarding force on the centroid motion that is of the opposite sign to that which would be exerted on a purely classical particle at the same position (this can be inferred from Fig. 4.9). These forces, which promote recrossing dynamics, will always be present unless the barrier potential is parabolic, in which case the force on the centroid is just a linear function of the centroid position. As a result, ring-polymer trajectories always accelerate away from a dividing surface placed at the top of a parabolic barrier and do not recross.

It can thus be concluded that the non-classical recrossing phenomenon is induced by anharmonicity in the potential at the dividing surface. From the current application

it appears that potential asymmetry (clearly a form of anharmonicity) is particularly important in this respect. It also appears that the relative extent of the non-classical recrossing in the RPMD-C correlation function decreases as the temperature is increased. In contrast, classical recrossing effects would be expected to increase at higher temperatures. An interesting question is whether or not this non-classical recrossing will be important in large reactive systems, since its classical counterpart is thought not to be [115].

Chapter 5

Condensed-phase chemical reaction rates

In the preceding chapter the RPMD-C method was applied to a couple of one-dimensional model reactions and the resulting rate coefficients were shown to be in excellent agreement with exact quantum-mechanical calculations over wide ranges of temperature. Despite this success, the fact that the exact results are readily available for such systems limits the value of the approximate RPMD-C evaluation of their rate coefficients.

In contrast, the computational effort required to calculate an accurate quantum-mechanical rate coefficient for a large reactive system is almost always prohibitive, and so some kind of approximate technique has to be used. Some such methods have been discussed in Section 4.2 of the previous chapter. However, the RPMD-C approach has a number of desirable properties – it reduces to a well-defined quantum transition-state theory in the short-time limit and in the long-time limit the RPMD-C rate coefficient is independent of the choice of dividing surface. Thus, it would be a particularly attractive approach if it could be demonstrated that the accuracy shown for the one-dimensional models extends to more complex (condensed-phase) reactive systems.

This chapter will therefore develop a multidimensional generalization of the RPMD-C method and will examine its accuracy for a reaction which involves many degrees of freedom. For the latter purpose the 'system-bath' model will be employed. This describes the effect of a typical condensed-phase environment on a proton-transfer reaction using a bilinear coupling between a one-dimensional reactive subsystem and a representative bath of harmonic oscillators [9]. The rate processes in this model have been studied with a large number of techniques but the most important here is the (system-specific) real-time path-integral approach of Topaler and Makri [26]. The exact quantum-mechanical rate coefficients that result from their work present a unique opportunity to evaluate the accuracy of approximate rate theories in the context of a multidimensional model of a condensed-phase chemical reaction. Furthermore, the fact that many groups have exploited this possibility means that the system-bath model is very useful for drawing comparison between different approximate methods [14, 26, 56, 126–130]. Much of this work has appeared in Ref. [103].

5.1 The system-bath model

The classical Hamiltonian for the model is:

$$H(\mathbf{p},\mathbf{q}) = \frac{p_1^2}{2m} + V_1(q_1) + \sum_{j=2}^{f}\left[\frac{p_j^2}{2m} + \frac{1}{2}m\omega_j^2\left(q_j - \frac{c_j q_1}{m\omega_j^2}\right)^2\right], \tag{5.1}$$

in which q_1 is the position coordinate of the reactive subsystem and the $\{q_j\}$ (for $j=2,\ldots,f$) are the positions of $(f-1)$ bath modes. For all degrees of freedom, p_j is the momentum conjugate to q_j and the relevant mass is m. The f momentum and f position coordinates are collected in the vectors $\mathbf{p}$ and $\mathbf{q}$ respectively.

The reactive subsystem is chosen to be a (symmetric) double well with the potential

energy function

$$V_1(q) = -\frac{1}{2}m\omega_b^2 q^2 + \frac{m^2\omega_b^4}{16V_0^\ddagger}q^4, \tag{5.2}$$

where $i\omega_b$ is the imaginary harmonic frequency of the barrier between the wells and $V_0^\ddagger$ is its height. In order to model a condensed-phase proton transfer the parameters are taken to be $\omega_b = 500$ cm^{-1}, $V_0^\ddagger = 2085$ cm^{-1} and $m = m_{\rm p} \simeq 1836\ m_{\rm e}$. Note that when this potential is inserted into Eq. (5.1) the difference between the potential at the transition state (the barrier top) and the reactant minimum (the well bottom) is $V_0^\ddagger$ regardless of the values of the coupling coefficients $\{c_j\}$ [26]. This property will greatly simplify the interpretation of the change in the rate coefficient as the system-bath coupling strength is varied.

The effect of the environment on the reactive subsystem is entirely governed by the spectral density of the bath, which is here taken to be of Ohmic form [131]

$$J_{\rm C}(\omega) = \eta\omega e^{-\omega/\omega_{\rm c}}, \tag{5.3}$$

where the parameter η is the system-bath coupling strength and the exponential cut-off frequency is set to $\omega_{\rm c} = 500$ cm^{-1}. Before this continuous spectral density can be used in a numerical calculation it must be discretized to a finite set of bath frequencies, i.e. [131],

$$J_{\rm D}(\omega) = \frac{\pi}{2}\sum_{j=2}^{f}\frac{c_j^2}{m\omega_j}\delta(\omega - \omega_j), \tag{5.4}$$

each of which is then associated with a single harmonic oscillator degree of freedom. Now, there are many ways of choosing the $\{\omega_j\}$ and $\{c_j\}$ in this equation so that the Ohmic spectral density in Eq. (5.3) is reproduced and, furthermore, the properties of the system-bath model are independent of how this is done [26]. However, different discretization schemes require different numbers of oscillator frequencies to provide a converged description of the bath. It is clearly desirable to have to use as few bath

degrees of freedom as possible and so these calculations adopt the discretization:

$$\omega_j = -\omega_c \ln\left(\frac{j-3/2}{f-1}\right), \tag{5.5}$$

and

$$c_j = \omega_j \left[\frac{2\eta m \omega_c}{(f-1)\pi}\right]^{1/2}, \tag{5.6}$$

for $j=2,\ldots,f$, which has been shown to be highly efficient in Ref. [103].

This discretization scheme can be obtained by recognising that the area under $J_{\mathrm{D}}(\omega)$ should equal that under $J_{\mathrm{C}}(\omega)$, and that this can be enforced by discretizing $J_{\mathrm{C}}(\omega)$ and then requiring that $J_{\mathrm{D}}(\omega)$ gives the same spectral density at each discrete frequency. To begin an explicit derivation of Eq. (5.5) and Eq. (5.6) note that

$$\int_0^\infty d\omega\, J_{\mathrm{D}}(\omega) = \frac{\pi}{2}\sum_{j=2}^{f}\frac{c_j^2}{m\omega_j}, \tag{5.7}$$

by virtue of the Dirac delta functions in Eq. (5.4). Then

$$\int_0^\infty d\omega\, J_{\mathrm{C}}(\omega) = \eta\int_0^\infty d\omega\,\omega\, e^{-\omega/\omega_c} = -\eta\,\omega_c^2\int_0^1 dx\ln(x), \tag{5.8}$$

after the change of integration variables $x=e^{-\omega/\omega_c}$. Applying a $(f-1)$-point midpoint quadrature to this last integral gives

$$\int_0^\infty d\omega\, J_{\mathrm{C}}(\omega) = \eta\,\omega_c\,\Delta x\sum_{j=2}^{f}(-\omega_c\ln(x_j)), \tag{5.9}$$

where $x_j = (j-3/2)\Delta x$ and $\Delta x = 1/(f-1)$. Inverting the change of integration variables identifies the summand as the discrete frequency ω_j in Eq. (5.5), and equating the right-hand sides of Eq. (5.7) and Eq. (5.9) then gives Eq. (5.6) for the coupling coefficients. In Ref. [103] it is shown that $f=10$ is sufficient to converge the classical

rate coefficient over a wide range of coupling strengths (η) at temperatures of 200 and 300 K.

Finally for this section, note that Zwanzig [132] has shown that the dynamics of the Hamiltonian in Eq. (5.1) are equivalent to those of a generalized Langevin equation

$$m\frac{d^2q_1(t)}{dt^2} + m\int_{-\infty}^{t} dt'\,\gamma(t-t')\dot{q}_1(t') + \frac{\partial V_1(q_1)}{\partial q_1} = \xi(t), \tag{5.10}$$

i.e., they are equivalent to the one-dimensional motion of the particle along the double-well coordinate subject to both frictional damping ($\gamma(t-t')$) and fluctuating forces ($\xi(t)$) [26]. Indeed, many of the approximate treatments of this problem take Eq. (5.10) as their starting point. For a summary of the approximate analytical theories for the system-bath model see Ref. [26]. Alternative numerical approaches will be discussed later in the chapter.

5.2 Multidimensional RPMD-C

The f-dimensional generalization of the RPMD-C approximation to the Kubo-transformed side-side correlation function in Section 4.4 is

$$\tilde{c}_{\mathrm{ss}}(t) \simeq \frac{1}{(2\pi\hbar)^{nf}}\int d\mathbf{p}_0 \int d\mathbf{q}_0\, e^{-\beta_n H_n(\mathbf{p}_0,\mathbf{q}_0)}\, h_c[s(\mathbf{q}_0)]h_c[s(\mathbf{q}_t)]. \tag{5.11}$$

In this expression $\mathbf{p}_0$ and $\mathbf{q}_0$ are vectors of length nf that contain the initial momentum and position coordinates of the multidimensional ring polymer. For a more general system than that described in Eq. (5.1), i.e. for a system with a classical Hamiltonian of the form:

$$H = \sum_{j=1}^{f}\frac{p_j^2}{2m_j} + V(q_1,\ldots,q_f), \tag{5.12}$$

the ring-polymer Hamiltonian is

$$H_n(\mathbf{p},\mathbf{q}) = \sum_{j=1}^{f}\sum_{k=1}^{n}\left[\frac{(p_{j,k})^2}{2m_j} + \frac{1}{2}m_j\omega_n^2(q_{j,k}-q_{j,k+1})^2\right] + \sum_{k=1}^{n} V(q_{1,k},\ldots,q_{f,k}), \quad (5.13)$$

where, as always, $\omega_n = 1/\beta_n\hbar$ and $\beta_n = 1/nk_BT$. The scalar variables $p_{j,k}$ and $q_{j,k}$ are the momentum and position coordinates of the k^{th} ring-polymer bead in the j^{th} degree of freedom. The position of the centroid along the j^{th} degree of freedom is labelled $q_{j,c}$ and defined as

$$q_{j,c} = \frac{1}{n}\sum_{k=1}^{n} q_{j,k}. \quad (5.14)$$

In general, $s(\mathbf{q}) = s(q_{1,c},\ldots,q_{f,c})$ is a function of all f centroid position variables which gives the location of the multidimensional ring-polymer centroid along the (yet to be defined) reaction coordinate. It is negative when the centroid is on the reactant side of the $(f-1)$-dimensional dividing surface and positive when it is on the product side. The dividing surface therefore occurs at $s(\mathbf{q})=0$ and so the step function

$$h_c[s(\mathbf{q})] = h[s(q_{1,c},\ldots,q_{f,c})], \quad (5.15)$$

discriminates between reactants and products such that it is zero for the former and one for the latter.

The statistical efficiency of a calculation based upon Eq. (5.11) would be dismal for the reasons identified during the discussion of its one-dimensional analogue (Section 4.4). Therefore, one must proceed as before and take the time derivative of Eq. (5.11) to yield the following approximation to $\tilde{c}_{\text{fs}}(t)$:

$$\tilde{c}_{\text{fs}}(t) \simeq \frac{1}{(2\pi\hbar)^{nf}}\int d\mathbf{p}_0 \int d\mathbf{q}_0\, e^{-\beta_n H_n(\mathbf{p}_0,\mathbf{q}_0)}\, \delta_c[s(\mathbf{q}_0)]\, v_c(\mathbf{p}_0,\mathbf{q}_0)\, h_c[s(\mathbf{q}_t)]. \quad (5.16)$$

In this expression $\delta_c[s(\mathbf{q})]$ is a Dirac delta function at the dividing surface $(s(\mathbf{q})=0)$,

the centroid velocity term is

$$v_c(\mathbf{p},\mathbf{q}) = \sum_{j=1}^{f} \frac{\partial s(q_{1,c},\ldots,q_{f,c})}{\partial q_{j,c}} \frac{p_{j,c}}{m_j}, \tag{5.17}$$

and the momentum centroid is

$$p_{j,c} = \frac{1}{n}\sum_{k=1}^{n} p_{j,k}. \tag{5.18}$$

The physical interpretation of these multidimensional RPMD-C equations is similar to the one-dimensional case and Fig. 4.3 applies if the abscissa is now understood to be the reaction coordinate of the f-dimensional system. As before, the approximate flux-side correlation function is constructed from ring-polymer trajectories which have their centroids pinned to the dividing surface at $t=0$. Each of these trajectories contributes a term which correlates the initial centroid velocity $v_c(\mathbf{p}_0,\mathbf{q}_0)$ with the centroid step function $h_c[s(\mathbf{q}_t)]$ evaluated at a later time t. The required time-evolution is obtained using the classical equations of motion that arise from the ring-polymer Hamiltonian in Eq. (5.13). The long-time limit of the resulting correlation function then determines the canonical rate coefficient via Eq. (4.30). Note that Eq. (5.16) correctly reduces to the one-dimensional RPMD-C expression (Eq. (4.53)) for $f = 1$ and to a purely classical (but multidimensional) flux-side correlation function as $n \to 1$.

So far, this section has formulated the RPMD-C method for a general multidimensional system but it now turns to the specific treatment of the system-bath model described in the previous section. An important step is the selection of the reaction coordinate to be used in the evaluation of Eq. (5.16). In this work it is taken to be the single unstable normal mode at the transition state ($\mathbf{q} = \mathbf{0}$) of the classical system-bath

potential

$$V(q_1,\ldots,q_f) = V_1(q_1) + \sum_{j=2}^{f} \frac{1}{2} m\omega_j^2 \left(q_j - \frac{c_j q_j}{m\omega_j^2} \right)^2 . \tag{5.19}$$

This choice of reaction coordinate implies that the dividing surface is composed of the remaining $f-1$ transition-state normal modes. In this discussion care must be taken to avoid confusion between the normal modes of the transition state of the system-bath potential and the normal modes of kinetic spring system of the ring polymer – the latter have appeared earlier in this thesis (e.g. Section 4.4) and will also become involved below.

In order to implement this choice of reaction coordinate the RPMD-C correlation function (Eq. (5.16)) must be transformed so that it is written in terms of the transition-state normal modes. In general, a normal-mode transformation is obtained by diagonalizing the second-derivative matrix (i.e. the Hessian) of a potential energy function at a stationary point (such that the first-derivative vector vanishes). For the transition-state normal modes of the system-bath potential a statement of the diagonalization is

$$\sum_{j=1}^{f}\sum_{j'=1}^{f} D_{j,l} \left(\frac{\partial^2 V}{\partial q_j \partial q_{j'}} \right)_{\mathbf{q}=\mathbf{0}} D_{j',l'} = m\tilde{\omega}_l^2 \delta_{l,l'}, \tag{5.20}$$

where the derivative is the (j,j') element of the Hessian matrix of V (Eq. (5.19)), $D_{j,l}$ is an element of the (orthogonal) matrix $\mathbf{D}$ that effects the diagonalization, and $\tilde{\omega}_l$ is the frequency associated with the l^{th} normal mode. This diagonalization is performed numerically. If the transition-state normal modes in Eq. (5.20) are arranged in order of increasing normal-mode frequency then the current choice of reaction coordinate is $\tilde{q}_1 = \sum_{j=1}^{f} D_{j,1} q_j$.

Now, since the columns of $\mathbf{D}$ are the transition-state normal-mode vectors in the basis of the original system-bath coordinates, the momenta and positions for each (f-dimensional) ring-polymer bead can be transformed to the normal-mode representation

via

$$\tilde{p}_{j,k} = \sum_{l=1}^{f} D_{l,j}\, p_{l,k}, \tag{5.21}$$

and

$$\tilde{q}_{j,k} = \sum_{l=1}^{f} D_{l,j}\, q_{l,k}. \tag{5.22}$$

The position of the centroid along the reaction coordinate ($s(\mathbf{q})$) is then

$$s(\mathbf{q}) = \tilde{q}_{1,c}, \tag{5.23}$$

where $\tilde{q}_{1,c}$ is the centroid coordinate along the unstable transition-state normal mode. This is obtained as

$$\tilde{q}_{1,c} = \sum_{l=1}^{f} D_{l,1}\, q_{l,c}, \tag{5.24}$$

where the $\{q_{l,c}\}$ are the original centroid coordinates defined in Eq. (5.14).

The RPMD-C correlation function can now be written in terms of the transition-state normal modes and the chosen reaction coordinate (Eq. (5.23)). Firstly, the orthogonality of $\mathbf{D}$ is used to obtain the following transition-state normal-mode representation of the ring-polymer Hamiltonian:

$$H_n(\tilde{\mathbf{p}}, \tilde{\mathbf{q}}) = \sum_{j=1}^{f} \sum_{k=1}^{n} \left[\frac{(\tilde{p}_{j,k})^2}{2m} + \frac{1}{2} m\omega_n^2 (\tilde{q}_{j,k} - \tilde{q}_{j,k+1})^2 \right] + \sum_{k=1}^{n} \tilde{V}(\tilde{q}_{1,k}, \ldots, \tilde{q}_{f,k}), \tag{5.25}$$

where $\tilde{V}(\tilde{q}_{1,k}, \ldots, \tilde{q}_{f,k}) \equiv V(q_{1,k}, \ldots, q_{f,k})$ of Eq. (5.19), and $\tilde{\mathbf{p}}$ and $\tilde{\mathbf{q}}$ are respectively vectors of the nf (transition-state) normal-mode momenta and positions.

Secondly, the remaining terms in the correlation function simplify: the dividing-surface delta function is

$$\delta_c[s(\mathbf{q})] = \delta_c[\tilde{q}_{1,c}] \equiv \delta_c(\tilde{\mathbf{q}}), \tag{5.26}$$

the centroid velocity term in Eq. (5.17) is,

$$v_c(\mathbf{p},\mathbf{q}) = \sum_{j=1}^{f} \frac{\partial \tilde{q}_{1,c}}{\partial q_{j,c}} \frac{p_{j,c}}{m} = \frac{\tilde{p}_{1,c}}{m} \equiv v_c(\tilde{\mathbf{p}}), \tag{5.27}$$

because of Eq. (5.23) and $\partial \tilde{q}_{1,c}/\partial q_{j,c} = D_{j,1}$, and the step function is

$$h_c[s(\mathbf{q})] = h_c[\tilde{q}_{1,c}] \equiv h_c(\tilde{\mathbf{q}}). \tag{5.28}$$

Lastly, since $\mathbf{D}$ is orthogonal,

$$\int d\mathbf{p}_0 \int d\mathbf{q}_0 \rightarrow \int d\tilde{\mathbf{p}}_0 \int d\tilde{\mathbf{q}}_0, \tag{5.29}$$

and so the transition-state normal-mode representation of the RPMD-C flux-side correlation function for the multidimensional system-bath model is

$$\tilde{c}_{\mathrm{fs}}(t) \simeq \frac{1}{(2\pi\hbar)^{nf}} \int d\tilde{\mathbf{p}}_0 \int d\tilde{\mathbf{q}}_0 \, e^{-\beta_n H_n(\tilde{\mathbf{p}}_0,\tilde{\mathbf{q}}_0)} \, \delta_c(\tilde{\mathbf{q}}_0) \, v_c(\tilde{\mathbf{p}}_0) \, h_c(\tilde{\mathbf{q}}_t). \tag{5.30}$$

Although the dividing surface $\tilde{q}_{1,c} = 0$ is not unique, the arguments which established that the RPMD-C rate coefficient is independent of the choice of dividing surface in one-dimensional systems (Section 4.9) remain valid for this multidimensional generalization.

5.3 Multidimensional dividing-surface sampling

This section describes a scheme for sampling the $t = 0$ phase-space coordinates of the ring-polymer trajectories such that their centroids are initially pinned to the $(f-1)$-dimensional dividing surface. Just as in one dimension (Section 4.6), this will be done by identifying Gaussian sampling distributions within the integrand of the correlation

function (Eq. (5.30)).

The efficiency of a sampling scheme is generally increased by including more of the correlation function integrand in the sampling distribution since this tends to reduce the variance of the rest of the integrand and hence of the contributions to the integral [121]. The transition-state normal-modes are particularly useful in this respect because they can be used to include in the sampling distribution an obvious harmonic approximation to the normal-mode representation of the potential in Eq. (5.19), i.e.,

$$\tilde{V}(\tilde{q}_1, \ldots, \tilde{q}_f) \simeq \sum_{j=2}^{f} \frac{1}{2} m \tilde{\omega}_j^2 (\tilde{q}_j)^2. \tag{5.31}$$

In this approximate potential $\tilde{\omega}_j$ is the frequency associated with the j^{th} normal-mode and the absence of a dependence on the reaction coordinate $\tilde{q}_1$ should be noted. An exact restatement of the RPMD-C correlation function is then

$$\tilde{c}_{\text{fs}}(t) \simeq \frac{N_p N_q}{(2\pi\hbar)^{nf}} \int d\tilde{\mathbf{p}}_0 \int d\tilde{\mathbf{q}}_0 \; P_p(\tilde{\mathbf{p}}_0) P_q(\tilde{\mathbf{q}}_0) \, e^{-\beta_n \Delta V(\tilde{\mathbf{q}}_0)} \, v_c(\tilde{\mathbf{p}}_0) \, h_c(\tilde{\mathbf{q}}_t), \tag{5.32}$$

where the function $\Delta V(\tilde{\mathbf{q}})$ is the difference between the exact and approximate potentials,

$$\Delta V(\tilde{\mathbf{q}}) = \sum_{k=1}^{n} \tilde{V}(\tilde{q}_{1,k}, \ldots, \tilde{q}_{f,k}) - \sum_{j=2}^{f} \sum_{k=1}^{n} \frac{1}{2} m \tilde{\omega}_j^2 (\tilde{q}_{j,k})^2. \tag{5.33}$$

The sampling distributions are

$$P_p(\tilde{\mathbf{p}}) = \frac{1}{N_p} \exp\left[-\beta_n \sum_{j=1}^{f} \sum_{k=1}^{n} \frac{(\tilde{p}_{j,k})^2}{2m} \right], \tag{5.34}$$

with

$$N_p = \int d\tilde{\mathbf{p}} \exp\left[-\beta_n \sum_{j=1}^{f} \sum_{k=1}^{n} \frac{(\tilde{p}_{j,k})^2}{2m} \right] = \left(\frac{2\pi m}{\beta_n} \right)^{nf/2}, \tag{5.35}$$

and

$$P_q(\tilde{\mathbf{q}}) = \frac{1}{N_q} P_1(\tilde{q}_{1,1}, \ldots, \tilde{q}_{1,n}) \prod_{j=2}^{f} P_j(\tilde{q}_{j,1}, \ldots, \tilde{q}_{j,n}), \tag{5.36}$$

with

$$N_q = \int d\tilde{\mathbf{q}}\, P_1(\tilde{q}_{1,1}, \ldots, \tilde{q}_{1,n}) \prod_{j=2}^{f} P_j(\tilde{q}_{j,1}, \ldots, \tilde{q}_{j,n}). \tag{5.37}$$

The (unnormalized) sampling distribution for the first normal mode (i.e. the reaction coordinate) is

$$P_1(\tilde{q}_{1,1}, \ldots, \tilde{q}_{1,n}) = \exp\left[-\beta_n \sum_{k=1}^{n} \frac{1}{2} m\omega_n^2 (\tilde{q}_{1,k} - \tilde{q}_{1,k+1})^2\right] \delta_c(\tilde{\mathbf{q}}), \tag{5.38}$$

and for the remaining normal-modes one has

$$P_j(\tilde{q}_{j,1}, \ldots, \tilde{q}_{j,n}) = \exp\left[-\beta_n \sum_{k=1}^{n} \left(\frac{1}{2} m\omega_n^2 (\tilde{q}_{j,k} - \tilde{q}_{j,k+1})^2 + \frac{1}{2} m\tilde{\omega}_j^2 (\tilde{q}_{j,k})^2\right)\right]. \tag{5.39}$$

The sampling of ring-polymer positions along the reaction coordinate is identical to that employed for the one-dimensional RPMD-C calculations of the previous chapter (see Section 4.6). In short, $P_1(\tilde{q}_{1,1}, \ldots, \tilde{q}_{1,n})$ uses the kinetic spring system to bias the sampling of the ring-polymer beads such that they lie near the centroid, which is itself constrained to the dividing surface by the $\delta_c(\tilde{\mathbf{q}})$. Since the centroid is (proportional to) one of the *ring-polymer* normal mode coordinates, applying the ring-polymer normal-mode transformation (Appendix B) to $P_1(\tilde{q}_{1,1}, \ldots, \tilde{q}_{1,n})$ converts it to the required product of uncoupled Gaussian sampling functions *and* allows the $\delta_c(\tilde{\mathbf{q}})$ to be implemented. This sampling distribution uses no information on the shape of the potential energy barrier along the reaction coordinate since doing so leads to problems at low temperatures. The nature of these problems is the same as those encountered when a harmonic approximation to the potential along the reaction coordinate is used to evaluate the Wigner transform in the classical Wigner model (Section 4.2) [14].

For the $(f-1)$ transition-state normal modes that make up the dividing surface there is no delta function to constrain the centroid. A sampling distribution based solely on the kinetic spring system would therefore sample the centroid position uniformly between $-\infty$ and $+\infty$, which would be awkward and inefficient. However, since the approximate potential (Eq. (5.31)) is bound in each of these $(f-1)$ directions, including it in the sampling distribution (see Eq. (5.39)) keeps the centroid in the physically relevant region near the transition-state saddle point at $\mathbf{q}=\mathbf{0}$. The coordinate transformation required to convert the $P_j(\tilde{q}_{j,1},\ldots,\tilde{q}_{j,n})$ sampling function into a collection of uncoupled Gaussians (recall Section 4.6) is again the ring-polymer normal-mode transformation of Appendix B. This same transformation diagonalizes the augmented kinetic spring system because the approximate potential is a quadratic function of the $\{\tilde{q}_{j,k}\}$ and because the ring-polymer normal-mode transformation is orthogonal. The only effect of including the approximate potential in the sampling function is a perturbation of the ring-polymer normal-mode frequencies. If Ω_k^2 is an unperturbed ring-polymer normal-mode frequency then the perturbed frequency along the j^{th} transition-state normal mode is $\Omega_k^2+\tilde{w}_j^2$ where $\tilde{\omega}_j$ is the frequency associated with the j^{th} transition-state normal mode. See Appendix B.

In summary, the multidimensional dividing-surface sampling algorithm is as follows: (i) numerical routines [121] are used to sample all nf momentum coordinates from the Gaussian distribution in Eq. (5.34), (ii) along the reaction coordinate the position of the centroid is set to zero (the dividing surface) and all higher ring-polymer normal modes are sampled from Gaussian distributions with standard deviations that depend on the unperturbed ring-polymer normal-mode frequencies (Appendix B), (iii) for the remaining transition-state normal modes all n ring-polymer normal-mode coordinates are sampled from Gaussian functions that depend on the perturbed ring-polymer frequencies, and finally (iv) the ring-polymer normal-mode and the transition-state

normal-mode transformations are inverted (see Section 5.2). For example, the latter inversion is accomplished by

$$q_{j,k} = \sum_{l=1}^{f} D_{j,l}\, \tilde{q}_{l,k}. \tag{5.40}$$

Overall, the scheme samples a set of ring-polymer momenta and positions in the original coordinate system with the centroid pinned to the dividing surface.

The ring-polymer normal-mode transformation can also be used to evaluate the normalization constant N_q because it transforms the integrand of Eq. (5.37) into a product of Gaussian functions (and a $\delta_c(\tilde{q}_{1,c})$). The result of this integration can be combined with Eq. (5.35) to give

$$\frac{N_p N_q}{(2\pi\hbar)^{nf}} = \frac{1}{\Lambda(T)} \prod_{j=2}^{f} Q_n(\beta\hbar\tilde{\omega}_j), \tag{5.41}$$

where $1/\Lambda(T) = (m/2\pi\beta\hbar^2)^{1/2}$ (the reciprocal thermal wavelength) is the partition function per unit volume for motion along the reaction coordinate and

$$Q_n(\beta\hbar\omega) = \prod_{k=1}^{n} \left[4\sin^2(k\pi/n) + (\beta\hbar\omega/n)^2\right]^{-1/2}, \tag{5.42}$$

is the canonical partition function for an n-bead ring polymer in a harmonic potential of frequency ω. Note that $Q_n(\beta\hbar\omega)$ tends to the exact quantum-mechanical partition function for the harmonic oscillator as $n \rightarrow \infty$ $(1/[2\sinh(\beta\hbar\omega/2)])$ and to the classical partition function at $n=1$ $(1/\beta\hbar\omega)$.

5.4 Calculations

The multidimensional RPMD-C methodology (Sections 5.2 and 5.3) will now be applied to the system-bath model (Section 5.1). To facilitate comparison with previous

studies, the results are reported as the dimensionless 'transmission' coefficients

$$\kappa = \frac{k(T)}{k_{\rm CTST}(T)}, \tag{5.43}$$

rather than as the bare rate coefficients. In this expression $k_{\rm CTST}(T)$ is the classical transition-state theory (CTST) rate coefficient for the one-dimensional double-well in the absence of the bath degrees of freedom. From Eq. (4.34) and Eq. (4.87),

$$k_{\rm CTST}(T) = \left(\frac{1}{2\pi m\beta}\right)^{1/2} \frac{Q^{\ddagger}_{\rm cl}(T)}{Q_{r,{\rm cl}}(T)}, \tag{5.44}$$

where $Q^{\ddagger}_{\rm cl}(T)$ and $Q_{r,{\rm cl}}(T)$ are respectively the classical dividing-surface and reactant partition functions. In one dimension the former is

$$Q^{\ddagger}_{\rm cl}(T) = \frac{1}{2\pi\hbar}\int dp_1\, e^{-\beta p_1^2/2m}\int dq_1\, e^{-\beta V_1(q_1)}\delta(q_1) = \left(\frac{m}{2\pi\hbar^2\beta}\right)^{1/2}, \tag{5.45}$$

since the double-well potential $V_1(q)$ is zero at $q=0$, and, within a harmonic approximation to the reactant minimum of the one-dimensional double-well potential, the latter is

$$Q_{r,{\rm cl}}(T) \simeq \frac{e^{\beta V_0^{\ddagger}}}{\beta\hbar\omega_0}, \tag{5.46}$$

where $\omega_0 = \sqrt{2}\,\omega_b$ is the harmonic frequency of uncoupled reactant well. Thus,

$$k_{\rm CTST}(T) \simeq \frac{\omega_0}{2\pi} e^{-\beta V_0^{\ddagger}}. \tag{5.47}$$

The $k(T)$ numerator in Eq. (5.43) involves the quantum-mechanical reactant partition function. This is calculated in the same spirit as Eq. (5.46) by adopting the harmonic normal-mode approximation to the reactant minimum of the full system-bath potential [14]. From Eq. (5.42) it is immediately clear that the n-bead ring-polymer

partition function for this system of f uncoupled harmonic oscillators is

$$Q_r(T) \simeq e^{\beta V_0^{\ddagger}} \prod_{j=1}^{f} Q_n(\beta\hbar\omega_j^0), \tag{5.48}$$

where ω_j^0 is the frequency associated with the j^{th} reactant normal mode and the exponential prefactor accounts for the choice of energy origin.

These calculations use the n-bead approximation to $Q_r(T)$ despite the fact that (within the harmonic normal-mode approximation) the exact quantum-mechanical reactant partition function is also available analytically and would therefore require no more effort to implement. The approximate $Q_r(T)$ is favoured because it is consistent with the n-bead RPMD-C approximation to $\tilde{c}_{\text{fs}}(t)$ and, furthermore, because the use of the exact $Q_r(T)$ would give the RPMD-C expression for $k(T)$ the incorrect classical limit. A further comment is that it would be entirely feasible to relax the harmonic normal-mode approximation and calculate the exact quantum-mechanical $Q_r(T)$ on the true potential using a path-integral molecular dynamics or path-integral Monte Carlo method. This was not done in previous applications of approximate dynamical techniques to the system-bath rate coefficient [133] and for consistency, therefore, it is not done here. The true potential energy function must contain an anharmonic component that gives rise to the reaction barrier. It seems likely that this anharmonicity will cause the true potential energy surface to be lower than the harmonic approximation in the thermally important regions of the reactant well. This would result in the exact reactant partition function being larger than the approximate one used here and would make the rate coefficient lower.

This section closes by detailing the parameter values that were found to converge the RPMD-C calculations at the three temperatures considered. At 300 K a total of $1{\times}10^3$ *pairs* of initial (centroid-pinned) ring-polymer variables, $(\mathbf{p}_0, \mathbf{q}_0)$ and $(-\mathbf{p}_0, \mathbf{q}_0)$, were

sampled, whilst at 200 K twice as many were needed. An example of the relative efficiency of the RPMD-C method is that earlier calculations using the RPMD-B approach required 2×10^5 pairs of ring-polymer trajectories for convergence at these temperatures [103]. Averaging over the contributions arising from $(\mathbf{p}_0, \mathbf{q}_0)$ and $(-\mathbf{p}_0, \mathbf{q}_0)$ is statistically valid because the ring-polymer Hamiltonian is quadratic in $\mathbf{p}_0$ and, in addition, it has the effect of ensuring that $\tilde{c}_{\mathrm{fs}}(0) = 0$. At 100 K the increased spatial delocalization of the ring polymers meant that 1×10^5 trajectory pairs were required to converge the sampling of the initial phase-space distributions. It did not prove feasible to converge the RPMD-B calculation at this temperature. The number of ring-polymer beads required at the three temperatures was 16 at 300 K, 32 at 200 K and 128 at 100 K.

Following sampling (Section 5.3), the trajectories were evolved forward in time according to the equations of motion derived from the ring-polymer Hamiltonian. For this purpose an integration scheme based upon alternating external force and free-motion ring-polymer steps was constructed. The former steps account for the effect of forces derived from the system-bath potential and the latter account for the forces derived from the kinetic spring system; these steps can be evaluated analytically within the ring-polymer normal-mode representation (Appendix B). The time step for this propagation was set at 5% of the period of the highest frequency present in the bath – for nine bath oscillators sampled using the scheme derived in Section 5.1 this was $dt \simeq 1.15$ fs. In all calculations, the long-time limit in Eq. (4.30) was obtained by integrating the trajectories forward in time until $\tilde{c}_{\mathrm{fs}}(t)$ reached a plateau value. At the lowest temperature and the lowest system-bath coupling strength this took about 150 fs. In this bound (i.e. unimolecular) reaction system any trajectory which crosses the barrier once must continue to do so indefinitely. It is only the presence of the bath degrees of freedom that causes the ring-polymer trajectories to localize either side of

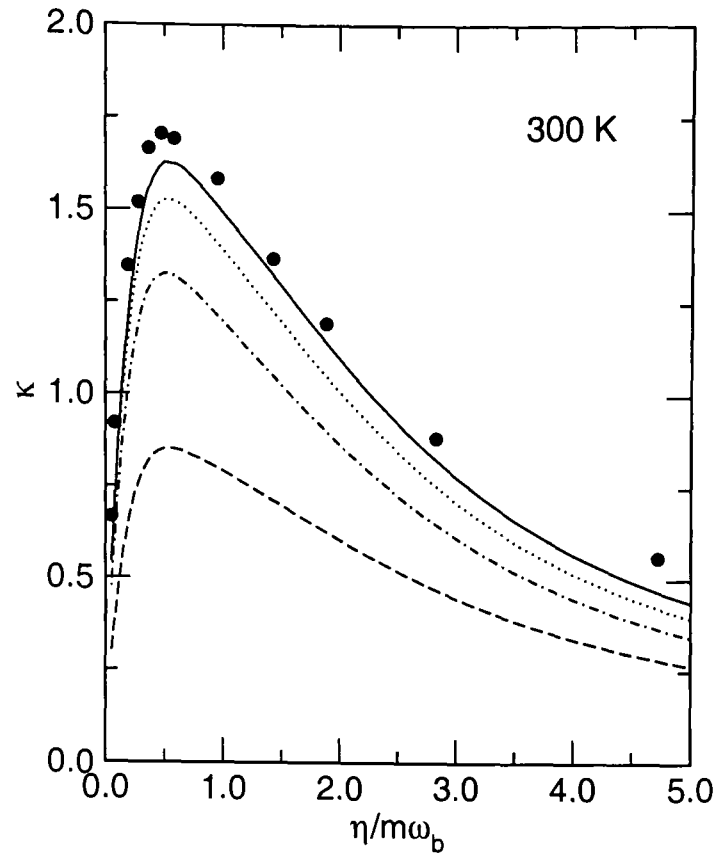

Figure 5.1: The transmission coefficient of the system-bath model as a function of the reduced coupling strength at 300 K. The exact quantum-mechanical results of Topaler and Makri [26] are shown as filled circles. A sequence of RPMD-C results obtained using $n = 1, 2, 4$ and 16 ring-polymer beads is plotted with long-dashed, dot-dashed, dotted and solid lines respectively. The first of these lines is the classical result and the last is the converged RPMD-C result.

the barrier for long enough for the plateau value to appear.

5.5 High temperature results (300 K and 200 K)

The RPMD-C transmission coefficients for the system-bath model are plotted against the (reduced) system-bath coupling strength at 300 K in Fig. 5.1 and at 200 K in Fig. 5.2. Both figures show a sequence of RPMD-C results that were obtained using an increasing number of ring-polymer beads (n) and each also displays the exact quantum-mechanical transmission coefficients of Topaler and Makri [26]. Note that the RPMD-C results increase monotonically with n and that they appear to provide a lower bound on the exact quantum-mechanical values.

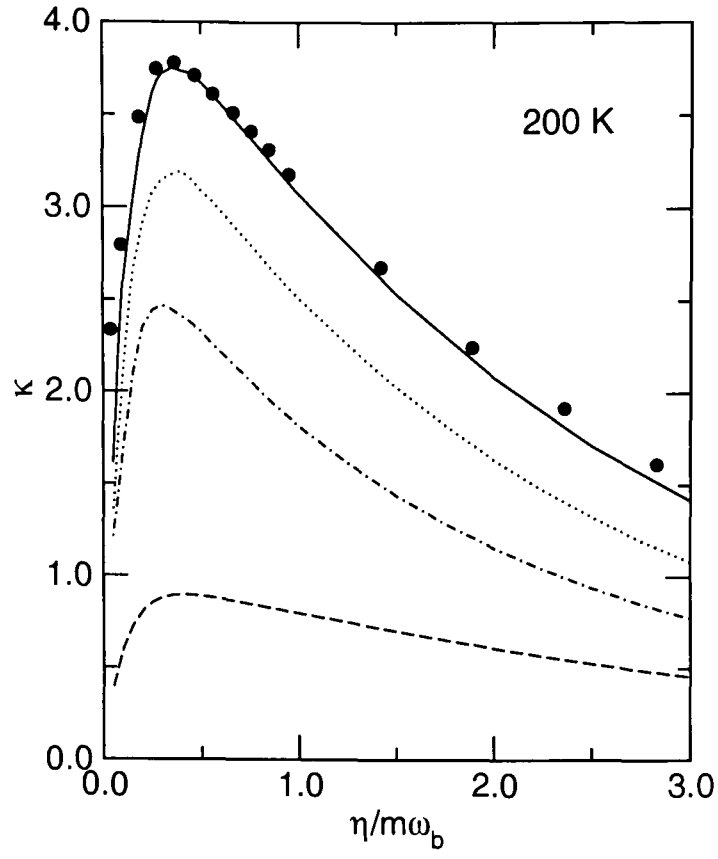

Figure 5.2: The transmission coefficient of the system-bath model as a function of the reduced coupling strength at 200 K. Symbols as for Fig. 5.1 but with $n=32$ beads in the converged RPMD-C result (solid line).

The $n=1$ results are the exact classical transmission coefficients for the full system-bath model and are always less than one. At low coupling strength this is because the exact $k_{\rm cl}(T)$ includes dividing-surface recrossing effects that are absent from the $k_{\rm CTST}(T)$ denominator of κ. At high coupling strength the recrossing is negligible but the coupling to the environment decreases the population ratio $Q^{\ddagger}_{\rm cl}/Q_{r,\rm cl}$ (*vide infra*) and therefore causes the exact classical rate coefficient to be lower than $k_{\rm CTST}(T)$ for the uncoupled double well.

At both temperatures the converged RPMD-C results are far more accurate than the classical transmission coefficients. Excellent agreement with the exact results is achieved and, in addition, the 'turnover' behaviour of the transmission coefficient is well-captured [126]. This turnover is entirely due to changes in $k(T)$ as the coupling strength varies because the $k_{\rm CTST}(T)$ denominator in κ (Eq. (5.43)) is evaluated for the uncoupled double well and is therefore independent of $\eta/m\omega_b$. The turnover is the

product of two opposing trends in $k(T)$ as a function of $\eta/m\omega_b$.

At the higher coupling strengths, the transmission coefficient is seen to decrease as $\eta/m\omega_b$ increases. Since this decrease is observed in quantum transition-state theory (QTST) calculations [26] it is not a dynamical effect. Furthermore, it is not simply due to an increasing reaction barrier height because the system-bath potential is constructed such that this quantity is constant. This high-η trend is instead the result of a 'tightening' of the transition-state potential which is apparent as an increase in the harmonic frequencies of $(f-1)$ normal modes in the dividing surface. This causes a decrease in the dividing-surface partition function ($Q^{\ddagger}$) which implies that fluctuations which place the reactant system at the top of the barrier, and hence reactive processes, are less likely to occur.

At the lower values of $\eta/m\omega_b$, as the system-bath coupling strength is decreased, the onset of dividing-surface recrossing causes a sharp fall in the transmission coefficient. This recrossing starts to occur because the energy associated with motion along the reaction coordinate is inefficiently dissipated into the environmental modes if the coupling is weak. In the classical picture, a reactive trajectory which has crossed the dividing surface is increasingly likely to come straight back across (and not localize in the reactant/product well) as the coupling strength is decreased. This recrossing is a purely dynamical phenomenon and the turnover is therefore absent from transition-state theory descriptions of the transmission coefficient.

The differences between the dynamics on either side of the turnover are clear in Fig. 5.3, which plots the RPMD-C time-dependent transmission coefficient,

$$\kappa(t) = \frac{\tilde{c}_{\mathrm{fs}}(t)}{Q_r(T)\, k_{\mathrm{CTST}}(T)}, \tag{5.49}$$

as calculated at typical high and low coupling strengths. The relevance of this figure

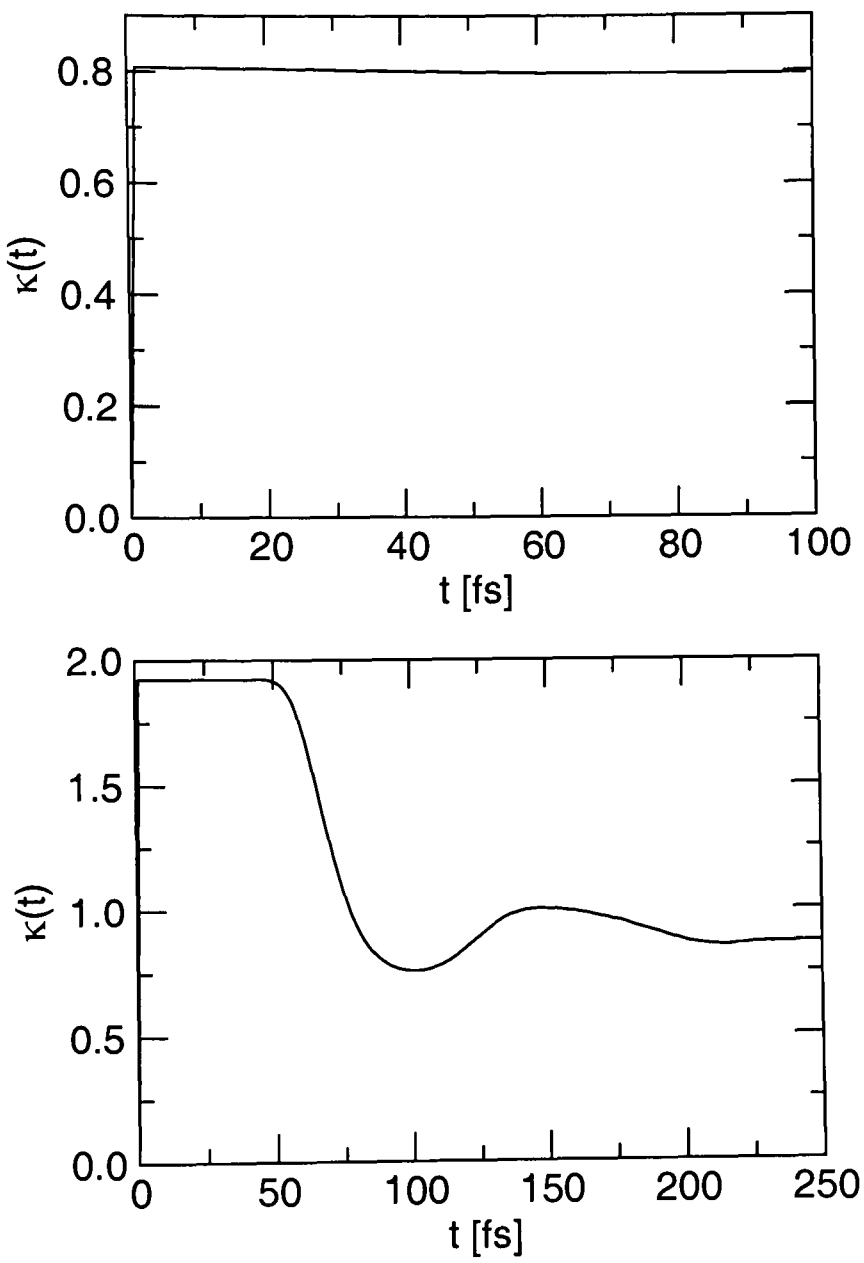

Figure 5.3: The time-dependent transmission coefficient (Eq. (5.49)) as calculated by the RPMD-C approach at 300 K. Top: high system-bath coupling strength, $\eta/m\omega_b = 3.0$. Bottom: low system-bath coupling strength, $\eta/m\omega_b = 0.10$.

is that the plateau value of $\kappa(t)$ is the time-independent κ of Eq. (5.43). At high coupling strength (above turnover) $\kappa(t)$ reaches the limiting value almost instantly. In contrast, the low coupling strength (below turnover) transmission coefficient undergoes at least three 'steps' (in alternating directions) after the initial increase. These step structures confirm the occurrence of the dividing-surface recrossing events that were previously invoked as the cause of the turnover effect. They also suggest that long-time dynamics have a significant role in determining the rate coefficient in the low coupling strength regime. The expected deterioration of the RPMD approximation at longer times (Chapter 2) would then suggest that the RPMD-C transmission coefficients would be less accurate at low $\eta/m\omega_b$, but the turnover figures (Figs. 5.1 and 5.2) are not conclusive in this respect.

Both the centroid molecular dynamics (CMD) method [56] and the classical Wigner model (CWM) [14] have been applied to the system-bath model at these two temperatures. The efficiency of the CMD calculation was greatly enhanced by analytically averaging over the bath degrees of freedom so that the dimensionality of the problem is reduced to one. The force on the centroid then depends only on its location along the double-well coordinate and this can be pre-calculated and tabulated before any trajectories are evolved. Such an approach directly exploits the harmonic nature of the bath oscillators and the bilinear system-bath coupling and is therefore not applicable to more complex/realistic systems.

Practical points aside, the RPMD-C turnover plots in Figs. 5.1 and 5.2 can be directly compared to figures that show the equivalent CMD and CWM results in Refs. [56] and [14]. The overall conclusion from such a comparison is that the three methods give results of almost equal accuracy for this problem. This is not unreasonable because the methods adopt similar strategies for evaluating the approximate quantum dynamics of complex molecular systems, i.e. an accurate treatment of the quantum

statistical mechanics of the Boltzmann operator is combined with an approximate classical dynamics for the real-time evolution. It is the approximate dynamics that allow these methods to capture the turnover behaviour of the transmission coefficient. An advantage of the RPMD-C method is that it requires neither the evaluation of a multi-dimensional Wigner transform (as does the CWM) nor the computationally expensive calculation of the force exerted on the centroid by the effective centroid potential (as does CMD – see Section 1.4) [20].

In addition to providing the exact quantum-mechanical transmission coefficients, Ref. [26] also presents the results of the QTST approach of Voth, Chandler and Miller [107] (which is referred to there as the 'centroid' method). As expected from the earlier discussion, these QTST results are accurate at the higher coupling strengths, but the lack of any dynamical information precludes the presence of recrossing effects and the turnover behaviour is therefore absent. Reference [26] also displays and comments upon the predictions of numerous relevant analytical theories in light of the exact results.

5.6 Low temperature results (100 K)

The previous section has demonstrated that the accuracy shown by the RPMD-C method for one-dimensional reactions is not necessarily lost when it is applied to more complex models of (condensed-phase) chemical reactions. Whilst satisfying, the relatively small values of the transmission coefficients shown in Figs. 5.1 and 5.2 indicate that the reactive processes in the system-bath model are fairly classical at these temperatures. The RPMD-C approximation is exact in the classical limit, and therefore the high-temperature transmission coefficients of the previous section do not present a particularly challenging test.

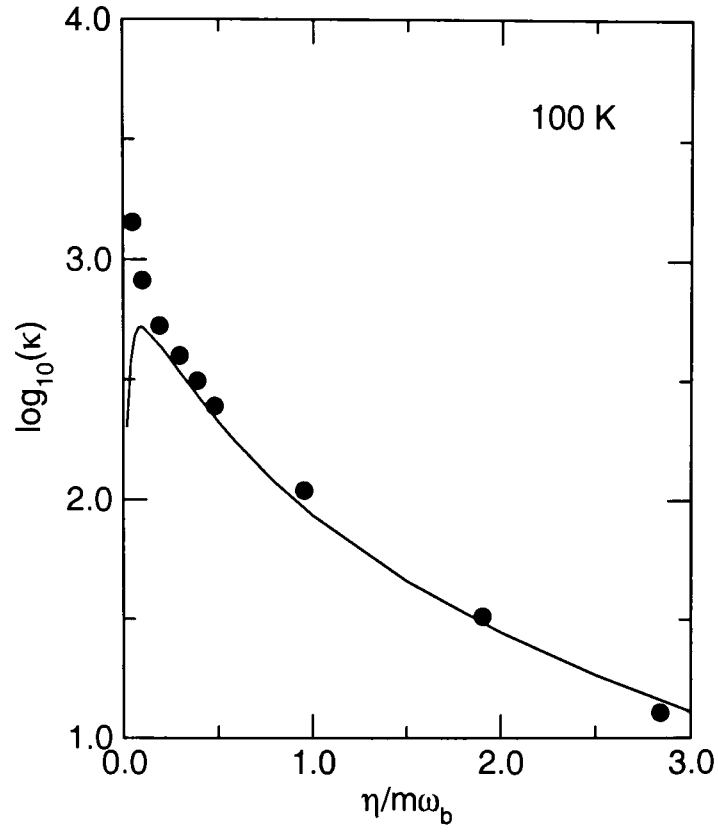

Figure 5.4: The transmission coefficient of the system-bath model as a function of the reduced coupling strength at a temperature of 100 K. The filled circles show the exact quantum-mechanical results of Topaler and Makri [26]. The solid line plots the (converged) RPMD-C results that were obtained with $n=128$ ring-polymer beads.

To complement the high temperature study this section presents the results of RPMD-C calculations for the system-bath model at a temperature of 100 K. The transmission coefficients are now much larger than before (i.e. there is a much greater quantum-mechanical enhancement of the rate) and so Fig. 5.4 plots the base-10 logarithm of κ as a function of the reduced system-bath coupling strength. At higher values of $\eta/m\omega_b$ the accuracy of the RPMD-C results is good, however it is clear that the approximate method predicts turnover at too high a coupling strength. (No turnover in the exact quantum-mechanical results is visible in Fig. 5.4 because it occurs at very low coupling strengths in this temperature regime [26].)

The incorrect position of the RPMD-C turnover and the associated underestimation of the low coupling-strength transmission coefficients are consistent with there being too much dividing-surface recrossing in the RPMD description of the dynamics in this

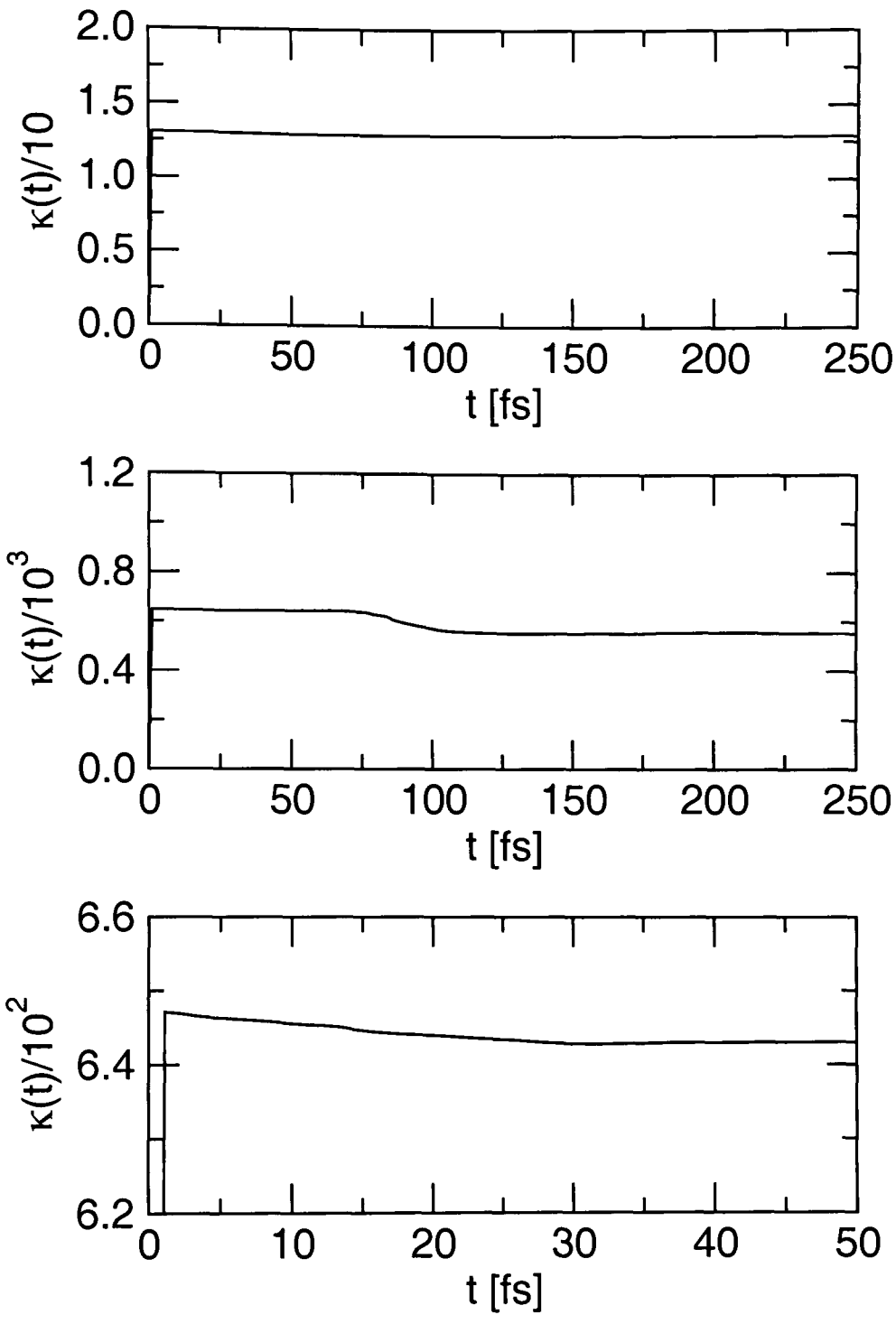

Figure 5.5: The time-dependent transmission coefficient (Eq. (5.49)) as calculated by the RPMD-C method for the system-bath model at 100 K. Top: high system-bath coupling strength ($\eta/m\omega_b = 3.0$). Middle: low system-bath coupling strength ($\eta/m\omega_b = 0.1$). Bottom: the initial decay at low system-bath coupling strength on an expanded ordinate scale ($\eta/m\omega_b = 0.1$).

parameter regime. This hypothesis can be tested by making a comparison between Fig. 5.5, which plots some RPMD-C time-dependent transmission coefficients at 100 K, and similar figures showing exact quantum-mechanical $\kappa(t)$ in Fig. 8 of Ref. [26]. Note that $\omega_0 t = 20$ in that reference corresponds to $t \simeq 150$ fs here. Also note that the comparison is necessarily qualitative since the figure here shows Kubo-transformed quantities whereas those in Ref. [26] involve the symmetrically thermalized correlation function. Nevertheless, it is clear that there are stark differences at low coupling strengths. The exact quantum-mechanical results show a sequence of *upwards* step structures whereas the RPMD-C $\kappa(t)$ undergoes a single *downwards* step of the sort that was observed at higher temperatures (in both the exact quantum-mechanical and RPMD-C calculations).

The upwards step structures in the quantum-mechanical results extend to fairly long times and have been ascribed to interference effects arising from coherent quantum dynamics in the weakly-coupled regime [26]. Since RPMD-C is based upon the classical dynamics of the ring-polymer phase-space such long-time interference effects are absent. As $\eta \rightarrow 0$ the relevant dynamics are those of an uncoupled one-dimensional double-well potential and the present failure of the RPMD approximation is therefore of a similar nature to that found at the higher temperature in the one-dimensional quartic oscillator problem in Fig. 2.2. At higher coupling strength the motion of the bath destroys the coherent dynamics along the reaction coordinate and the RPMD-C method is thus capable of an accurate description of the reactive processes. It is interesting to note that the upward step structure results in a quantum-dynamical enhancement of the rate coefficient which takes the exact κ above even that of the QTST approach (see Fig. 10 of Ref. [26]). This is in contrast to the situation in classical mechanics, where the classical transition-state theory rate coefficient is guaranteed to be greater than (or equal to) the exact classical result because classical recrossing

dynamics in the latter can only decrease the reaction rate.

It is often asserted than dividing-surface recrossing effects will be negligible for condensed phase chemical reactions [115], and this section therefore closes with a discussion about the observation of such effects in these results for the condensed-phase system-bath model. The issue is important since an absence of recrossing dynamics would enable quantum transition-state theories to provide an accurate description of condensed-phase rate coefficients and would simultaneously imply a certain redundancy of the approximate quantum-dynamical approaches to $k(T)$ (e.g. CWM, CMD and RPMD-C).

In the RPMD-C results presented above, the strength of the coupling between the reaction coordinate and the condensed-phase environment is important in determining whether or not dividing-surface recrossing effects are significant. At high system-bath coupling strengths there is no recrossing regardless of which temperatures are considered. At low system-bath coupling strengths there is extensive recrossing at the higher temperatures but it is of lower magnitude at the lower temperature – compare the RPMD-C transmission coefficients in the lower panels of Fig. 5.3 and Fig. 5.5.

It has already been established, however, that the RPMD-C results are not accurate in the low-η/low-T case, and that the true quantum dynamics in this regime exhibit a rather pronounced quantum-mechanical recrossing [26]. A different sort of quantum-mechanical recrossing was previously observed in the RPMD-C results for the asymmetric Eckart barrier (referred to as 'non-classical' recrossing in Section 4.10). It is characterized by a continuous decay of $\kappa(t)$ that begins at $t = 0$ and continues only for short times. This behaviour is in contrast with the intermediate-time step structures of 'classical' recrossing. The bottom panel of Fig. 5.5 shows that a similar effect *is* present in the ring-polymer dynamics of the system-bath model but it is far less extensive, and therefore important, than the classical recrossing.

The question of whether dividing-surface recrossing effects are important in condensed-phase chemical reactions is therefore a question about which range of coupling strengths $\eta/m\omega_b$ is physically relevant. The fact that dividing-surface recrossing is believed to have been observed experimentally [134] suggests that some reactions occur at low coupling strength and will require a dynamical theoretical treatment. It seems just as likely that other reactions will be strongly coupled to the environment and could therefore be accurately treated by QTSTs. Even if the optimal QTST dividing surface leads to negligible recrossing, it may not be easy to find in many complex systems. In such cases, the invariance of the RPMD-C rate coefficient to the choice of dividing surface would make the method an attractive option.

5.7 Summary

This chapter has presented the multidimensional generalization of the RPMD-C method and has applied it to the system-bath model for a proton-transfer reaction in solution. The accuracy of the approximate RPMD-C rate coefficient for this condensed-phase model has been shown to very good in all except the low coupling strength/low temperature regime in which coherent quantum-dynamical effects make an important contribution to the exact rate coefficient.

The system-bath model provides an indispensable test of approximate methods for calculating condensed-phase reaction rate coefficients because the exact quantum-mechanical results are available from the real-time path integral calculations of Topaler and Makri [26]. However, these exact calculations directly exploit the harmonicity of the bath oscillators and the bilinear system-bath coupling. There are many important and interesting condensed-phase reactions to which such an approach cannot be applied, and so there is a need for the development of accurate but efficient approximate schemes for evaluating the dynamics of complex reactive systems. The results in this

chapter suggest that the RPMD-C method is highly promising in this respect.

Chapter 6

Summary and Conclusions

This thesis has presented the Ring Polymer Molecular Dynamics (RPMD) approximation to the Kubo-transformed time correlation function and has shown how it may be used as the basis of an approximate quantum-mechanical method for calculating the dynamical properties of condensed-phase molecular systems. Such methods are needed because the exact quantum dynamics of all except the simplest models of condensed-phase systems cannot be evaluated by any existing technique. The RPMD approach has been used to calculate the following quantities:

(i) the position ($\hat{q}$), and position-cubed ($\hat{q}^3$), Kubo-transformed autocorrelation functions of a series of one-dimensional models involving harmonic, mildly anharmonic, and strongly anharmonic potential energy functions at low and high temperatures (Chapter 2),

(ii) the incoherent dynamic structure factors of a realistic multidimensional model of liquid para-hydrogen at a temperature of 14 K and a density of 23.5 nm^{-3} (Chapter 3),

(iii) the canonical rate coefficients of two one-dimensional models of bimolecular chemical reactions across wide ranges of temperature that include highly quantum

mechanical deep-tunneling regimes (Chapter 4),

(iv) the canonical rate coefficients of a many-dimensional model of a solution-phase proton transfer reaction (the system-bath model [26]) at a wide range of system-bath coupling strengths and temperatures of 100, 200, and 300 K (Chapter 5).

The performance of the RPMD approximation for each of these applications has been discussed at the end of the appropriate chapter and this thesis simply closes with a distillation of these earlier conclusions.

Accuracy

With a few exceptions discussed below, the approximate RPMD results reported in this thesis are in good agreement with exact quantum-mechanical results (Chapters 2, 4, and 5) and/or with experiment (Chapter 3). This encourages the use of the new method in future investigations of the quantum-dynamical properties of condensed-phase molecular systems.

Comparisons can be drawn between the accuracy of the RPMD method and that of a number of alternative approximate approaches. Firstly, whenever a comparison was possible, it was found that the results of the RPMD method were more accurate than those of the equivalent classical calculation (e.g. Section 2.4 and Section 5.5). Thus, it seems that the accurate treatment of the Boltzmann operator enables the RPMD method to provide a better approximation to the exact Kubo-transformed correlation function than is obtained using the classical approach (see closing comments of Section 1.1 and Ref. [29]).

Secondly, the accuracy of the RPMD results was found to be similar to that of two alternative approaches to calculating approximate quantum-dynamical properties of

condensed-phase systems, i.e. the Classical Wigner Model (CWM [14]) and the Centroid Molecular Dynamics (CMD [20]) method. This equivalence is not surprising because all three methods combine an exact treatment of the quantum Boltzmann operator with a classical dynamics for the real-time evolution. However, for reasons outlined in Chapter 1, it is reasonable to think that for most condensed-phase applications the RPMD approach will be more efficient than either of these alternative techniques.

Thirdly, when calculating rate coefficients (Chapters 4 and 5), it was found that the RPMD-C approach was almost always more accurate than the quantum transition-state theory (QTST) [107] that it tends to in the short-time limit. The new method was also found to be more accurate than a number of other QTSTs for the asymmetric Eckart barrier problem. This is because, in contrast to the statistical QTST methods, the RPMD-C approach is a dynamical rate theory and it is therefore able to describe dividing-surface recrossing effects. The one instance in which the approximate RPMD dynamics led to a rate coefficient which was less accurate than the QTST result was at very low coupling-strengths in the low-temperature (100 K) system-bath model, where the exact rate coefficient is dominated by exotic interference effects in the quantum dynamics (see Section 5.6).

Difficulties

Future applications of the RPMD method will perhaps find the most useful contribution of this thesis to be the identification of two situations in which the RPMD approximation breaks down.

The first of these situations occurs if there are significant quantum interference effects in the real-time dynamics that determine the Kubo-transformed correlation function of interest. Such effects, which are clearly system- and temperature-dependent, were

found in the exact quantum-mechanical results for the position autocorrelation function of the quartic oscillator (Section 2.4) and for the low-temperature (100 K) system-bath model at very low coupling-strengths (Section 5.6). Coherent dynamical effects such as this will not be captured in the RPMD model, nor in any other approximate correlation function that is based upon a classical description of the real-time dynamics (e.g. CWM or CMD).

However, the thermal averaging over the initial states of the large number of degrees of freedom in a condensed-phase system tends to preclude the presence of any long-time coherent dynamical effects in their quantum correlation functions. Thus, the exact treatment of the Boltzmann operator that *is* included in the RPMD approach should lead to a reasonable estimate of the quantum dynamical properties of a large number of condensed-phase molecular systems.

The second situation in which the RPMD model is inaccurate was identified by the systematic investigation of the neutron-scattering correlation functions in Chapter 3. It was firmly established that the RPMD approximation becomes less accurate as the nonlinearity of the operators involved in the correlation function is increased. This inaccuracy was ascribed to the artificial components of the RPMD correlation function that arise from the motion of the high-frequency normal modes of the ring-polymer kinetic spring system (see Appendix B and Ref. [135]). As the nonlinearity of the correlated operators is increased, the oscillation of the normal modes leads to spurious components of greater magnitude and causes a degradation in the accuracy of the RPMD model (Section 3.6). In short, highly nonlinear functions of the position operator change rapidly over short length-scales and therefore expose the artifical internal structure of the ring polymer.

Appendix A

Derivation of the Gaussian approximation

For completeness, this appendix presents a derivation of the Gaussian approximation due to Rahman, Singwi and Sjölander [77]. The first task is the simplification of the exact expression for $F_s(\kappa, t)$. Thus, Eq. (3.40) can be written as

$$F_s(\kappa, t) = \frac{1}{N} \sum_{j=1}^{N} \left\langle e^{-i\boldsymbol{\kappa}\cdot\hat{\mathbf{q}}_j}\, e^{+i\hat{H}t/\hbar}\, e^{+i\boldsymbol{\kappa}\cdot\hat{\mathbf{q}}_j}\, e^{-i\hat{H}t/\hbar} \right\rangle , \tag{A.1}$$

where $\langle \ldots \rangle$ denotes the canonical equilibrium average of Eq. (1.17). At equilibrium in an isotropic liquid each particle is statistically equivalent and only a single term in the sum need be retained, i.e.,

$$F_s(\kappa, t) = \left\langle e^{-i\boldsymbol{\kappa}\cdot\hat{\mathbf{q}}}\, e^{+i\hat{H}t/\hbar}\, e^{+i\boldsymbol{\kappa}\cdot\hat{\mathbf{q}}}\, e^{-i\hat{H}t/\hbar} \right\rangle , \tag{A.2}$$

where $\hat{\mathbf{q}}$ now refers to the position of one specific particle. Note, however, that the time-evolution operators and the canonical equilibrium average still involve the entire

system. It can be shown that [77]

$$e^{-i\boldsymbol{\kappa}\cdot\hat{\mathbf{q}}}\, e^{+iH(\hat{\mathbf{p}},\hat{\mathbf{q}})\,t/\hbar}\, e^{+i\boldsymbol{\kappa}\cdot\hat{\mathbf{q}}} = e^{+iH(\hat{\mathbf{p}}+\hbar\boldsymbol{\kappa},\hat{q})\,t/\hbar}, \tag{A.3}$$

and since $H{=}\hat{p}^2/2m{+}V(\hat{q})$, where m is the particle mass,

$$H(\hat{\mathbf{p}}+\hbar\boldsymbol{\kappa},\hat{\mathbf{q}}) = \left(\frac{\hat{\mathbf{p}}^2}{2m} + \frac{\hbar\hat{\mathbf{p}}\cdot\boldsymbol{\kappa}}{m} + V(\hat{\mathbf{q}})\right) + \frac{\hbar^2\kappa^2}{2m} = H'(\hat{\mathbf{p}},\hat{\mathbf{q}}) + \frac{\hbar^2\kappa^2}{2m}, \tag{A.4}$$

which serves to define $\hat{H}'$. Combining these last two results allows the self intermediate scattering function to be written

$$F_s(\kappa,t) = e^{+i\omega_R t}\left\langle e^{+i\hat{H}'t/\hbar}\, e^{-i\hat{H}t/\hbar}\right\rangle = e^{+i\omega_R t}\left\langle \hat{A}(\kappa,t)\right\rangle, \tag{A.5}$$

where the 'recoil frequency',

$$\omega_R = \frac{\hbar\kappa^2}{2m}, \tag{A.6}$$

is such that $\hbar\omega_R$ is the impulsive increase in kinetic energy of a previously stationary scattering particle, and

$$\hat{A}(\kappa,t) = e^{+i\hat{H}'t/\hbar}\, e^{-i\hat{H}t/\hbar}. \tag{A.7}$$

The next step is the development of a time expansion for $\hat{A}(\kappa,t)$. An equation of motion for this operator is given by Ref. [77] as

$$\frac{\partial\hat{A}(\kappa,t)}{\partial t} = i\kappa\hat{A}(\kappa,t)\hat{v}, \tag{A.8}$$

where $\hat{v}$ is the operator that gives the scatterer's velocity in the direction defined by $\boldsymbol{\kappa}$. Integrating from 0 to t,

$$\int_0^t dt_1\,\frac{\partial\hat{A}(\kappa,t_1)}{\partial t_1} = \hat{A}(\kappa,t) - 1 = i\kappa\int_0^t dt_1\,\hat{A}(\kappa,t_1)\hat{v}(t_1), \tag{A.9}$$

gives an equation for $\hat{A}(\kappa,t)$ that can be solved iteratively, i.e.,

$$\begin{aligned}\hat{A}(\kappa,t) &= 1+i\kappa\int_0^t dt_1\,\hat{A}(\kappa,t_1)\hat{v}(t_1)\\ &= 1+i\kappa\int_0^t dt_1\,\hat{v}(t_1)-\kappa^2\int_0^t dt_1\int_0^{t_1} dt_2\,\hat{A}(\kappa,t_2)\hat{v}(t_2)\hat{v}(t_1). \qquad \text{(A.10)}\end{aligned}$$

After j such substitutions of $\hat{A}(\kappa,t)$ the final integral in the series involves $\hat{A}(\kappa,t_{j+1})$. However, as $j\to\infty$, $t_j\to 0$ and so $\hat{A}(\kappa,t_{j+1})\to\hat{A}(\kappa,0)=1$ and the series converges to

$$\hat{A}(\kappa,t)=\sum_{j=0}^{\infty}(i\kappa)^j\int_0^t dt_1\int_0^{t_1} dt_2\cdots\int_0^{t_{j-1}} dt_j\,\hat{v}(t_j)\cdots\hat{v}(t_2)\hat{v}(t_1). \qquad \text{(A.11)}$$

The equilibrium average of $\hat{A}(\kappa,t)$ is then

$$\left\langle\hat{A}(\kappa,t)\right\rangle=\sum_{j=0}^{\infty}(i\kappa)^j\int_0^t dt_1\cdots\int_0^{t_{j-1}} dt_j\,\left\langle\hat{v}(t_j)\cdots\hat{v}(t_1)\right\rangle, \qquad \text{(A.12)}$$

but the terms involving odd powers of the velocity are zero because $e^{-\beta\hat{H}}$ is even in $\hat{v}$ [77] and so

$$\left\langle\hat{A}(\kappa,t)\right\rangle=\sum_{j=0}^{\infty}(-\kappa^2)^j\int_0^t dt_1\cdots\int_0^{t_{2j-1}} dt_{2j}\,\left\langle\hat{v}(t_{2j})\cdots\hat{v}(t_1)\right\rangle. \qquad \text{(A.13)}$$

At this point the original derivation of the Gaussian approximation [77] becomes rather involved. An alternative development is therefore given here – it is shown in Ref. [77] that the canonical equilibrium average of $\hat{A}(\kappa,t)$ can be written as

$$\left\langle\hat{A}(\kappa,t)\right\rangle=\exp\left[\sum_{j=1}^{\infty}(-\kappa^2)^j\gamma_j(t)\right]. \qquad \text{(A.14)}$$

Now, the expansion of this form in terms of κ^2 is

$$\left\langle \hat{A}(\kappa,t)\right\rangle = \left\langle \hat{A}(0,t)\right\rangle + \left|\frac{\partial\left\langle \hat{A}(\kappa,t)\right\rangle}{\partial\kappa^2}\right|_{\kappa^2=0}\kappa^2 + \frac{1}{2}\left|\frac{\partial^2\left\langle \hat{A}(\kappa,t)\right\rangle}{\partial\kappa^4}\right|_{\kappa^2=0}\kappa^4 + \ldots, \quad \text{(A.15)}$$

and at κ^2=0 the first few derivatives are

$$\begin{aligned}
\left\langle \hat{A}(0,t)\right\rangle &= 1 \\
\left|\frac{\partial\left\langle \hat{A}(\kappa,t)\right\rangle}{\partial\kappa^2}\right|_{\kappa^2=0} &= -\gamma_1(t) \\
\left|\frac{\partial^2\left\langle \hat{A}(\kappa,t)\right\rangle}{\partial\kappa^4}\right|_{\kappa^2=0} &= 2\gamma_2(t) + (\gamma_1(t))^2. \qquad \text{(A.16)}
\end{aligned}$$

Equating the coefficient of each power of κ^2 in Eq. (A.15) with that in Eq. (A.13) identifies

$$\begin{aligned}
\gamma_1(t) &= \int_0^t dt_1 \int_0^{t_1} t_2\ \langle\hat{v}(t_2)\hat{v}(t_1)\rangle \\
\gamma_2(t) &= \int_0^t dt_1 \int_0^{t_1} t_2 \int_0^{t_2} dt_3 \int_0^{t_3} dt_4\ \langle\hat{v}(t_4)\ldots\hat{v}(t_1)\rangle - \frac{1}{2}(\gamma_1(t))^2. \qquad \text{(A.17)}
\end{aligned}$$

The Gaussian approximation neglects all contributions to higher-order velocity correlation functions (e.g. $\langle\hat{v}(t_4)\ldots\hat{v}(t_1)\rangle$) apart from those arising from products of two-point correlation functions (e.g. $\langle\hat{v}(t_2)\hat{v}(t_1)\rangle$) [77]. This is equivalent to assuming that $\gamma_j(t)$=0 for all j greater than one, and gives

$$\left\langle \hat{A}(\kappa,t)\right\rangle = e^{-\kappa^2\gamma_1(t)}. \qquad \text{(A.18)}$$

The Gaussian approximation to $F_s(\kappa, t)$ is therefore

$$F_s^g(\kappa, t) = e^{+i\omega_R t}\, e^{-\kappa^2 \gamma_1(t)}. \tag{A.19}$$

The final task is the manipulation of $\gamma_1(t)$ to a form that involves the velocity autocorrelation function. Because a time correlation function is a property of a system at equilibrium, the time origin of the thermal average in the previous expression for $\gamma_1(t)$ can be shifted

$$\gamma_1(t) = \int_0^t dt_1 \int_0^{t_1} t_2 \, \langle \hat{v}(0)\hat{v}(t_1 - t_2)\rangle \, . \tag{A.20}$$

Since the three spatial dimensions are identical in an isotropic system their average can be taken to give

$$\gamma_1(t) = \frac{1}{3}\int_0^t dt_1 \int_0^{t_1} t_2 \, \langle \hat{\mathbf{v}}(0)\cdot\hat{\mathbf{v}}(t_1 - t_2)\rangle = \frac{1}{3}\int_0^t dt_1 \int_0^{t_1} t_2 \, c^0_{\mathbf{vv}}(t_1 - t_2). \tag{A.21}$$

The following change of integration variables

$$t_1' = t_1 - t_2 \quad ; \quad t_2' = t_2, \tag{A.22}$$

has a unit jacobian and so

$$\gamma_1(t) = \frac{1}{3}\int_0^t dt_1' \int_0^{t-t_1'} dt_2' \, c^0_{\mathbf{vv}}(t_1') = \frac{1}{3}\int_0^t dt_1' \, (t - t_1') \, c^0_{\mathbf{vv}}(t_1'), \tag{A.23}$$

which is the form given in Eq. (3.62).

Appendix B

Ring-polymer normal-mode transformation

The ring-polymer normal-mode transformation is used throughout this thesis to transform the position (and momentum) variables of the ring polymer to a new coordinate system in which the ring-polymer kinetic spring potential,

$$V_n(\mathbf{q}) = \sum_{k=1}^{n} \frac{1}{2} m\omega_n^2 (q_k - q_{k+1})^2, \tag{B.1}$$

has the form of n uncoupled harmonic oscillators. The potential $V_n(\mathbf{q})$ has been written here for a one-dimensional system with mass m and, as in the main body of this thesis, $\omega_n = 1/\beta_n\hbar$ where $\beta_n = 1/k_B T$, and $q_{n+1} = q_1$.

B.1 Derivation

First note that expanding the summand in Eq. (B.1) gives

$$V_n(\mathbf{q}) = \sum_{k=1}^{n} \frac{1}{2} m\omega_n^2 (q_k^2 + q_{k+1}^2 - q_k q_{k+1} - q_{k+1} q_k), \tag{B.2}$$

or

$$V_n(\mathbf{q}) = \sum_{k=1}^{n} \frac{1}{2} m\omega_n^2 (2q_k^2 - q_k q_{k+1} - q_k q_{k-1}), \tag{B.3}$$

after rearranging terms in the summation. In vector notation this is

$$V_n(\mathbf{q}) = \frac{1}{2} m\omega_n^2 \, \mathbf{q}^T \cdot \mathbf{A} \cdot \mathbf{q}, \tag{B.4}$$

where the matrix $\mathbf{A}$ has the form

$$\mathbf{A} = \begin{bmatrix} 2 & -1 & & & & -1 \\ -1 & 2 & -1 & & & \\ & -1 & \ddots & \ddots & & \\ & & \ddots & & & -1 \\ -1 & & & & -1 & 2 \end{bmatrix}. \tag{B.5}$$

Now, Eq. (B.4) shows that the different $\{q_k\}$ coordinates are coupled by the off-diagonal elements of the matrix $\mathbf{A}$. The uncoupling of the coordinates is therefore achieved by diagonalizing $\mathbf{A}$, i.e. by solving:

$$\mathbf{A} = \mathbf{C} \cdot \mathbf{a} \cdot \mathbf{C}^T, \tag{B.6}$$

for the matrices $\mathbf{a}$ and $\mathbf{C}$ where $\mathbf{a}$ is diagonal and (since $\mathbf{A}$ is symmetric) $\mathbf{C}$ is orthogonal, i.e.,

$$\mathbf{C}^T \cdot \mathbf{C} = \mathbf{I}. \tag{B.7}$$

The specific form of $\mathbf{A}$ (Eq. (B.5)) can be used to write the following scalar equivalent of Eq. (B.6): for $k, l = 1, \ldots, n$

$$-c_{k-1,l} + 2c_{k,l} - c_{k+1,l} = c_{k,l} a_l, \tag{B.8}$$

where $c_{k,l}$ is the element of the matrix $\mathbf{C}$ at row k and column l, and a_l is the l^{th} element along the diagonal of $\mathbf{a}$. The appropriate boundary conditions are

$$c_{n+1,l} = c_{1,l} \qquad \text{and} \qquad c_{0,l} = c_{n,l}, \tag{B.9}$$

which impose the necessary cyclic structure on the ring-polymer positions.

Matrix elements of the form

$$c_{k,l} = N\cos(2\pi kl/n), \tag{B.10}$$

where N is a normalization constant, can be shown to satisfy the boundary conditions in Eq. (B.9). When substituted into Eq. (B.8) they give

$$0 = -\cos(2\pi(k-1)l/n) + (2-a_l)\cos(2\pi kl/n) - \cos(2\pi(k+1)l/n), \tag{B.11}$$

after the normalization constants have been factored out. Using

$$\cos(x \pm y) = \cos(x)\cos(y) \mp \sin(x)\sin(y), \tag{B.12}$$

and extracting common factors yields

$$0 = -\cos(2\pi l/n) + (2-a_l) - \cos(2\pi l/n), \tag{B.13}$$

or

$$a_l = 2 - 2\cos(2\pi l/n) = 4\sin^2(l\pi/n), \tag{B.14}$$

for all $k, l = 1, \ldots, n$. Thus, a vector constructed from the elements in Eq. (B.10) as

$$\mathbf{c}_l = (c_{1,l}, c_{2,l}, \ldots, c_{n,l})^T, \tag{B.15}$$

is an eigenvector of the matrix $\mathbf{A}$ with an associated eigenvalue a_l given by Eq. (B.14). These eigenvectors $\mathbf{c}_l$ form the columns of the matrix $\mathbf{C}$.

However, the diagonalization of $\mathbf{A}$ (Eq. (B.6)) is not complete because Eq. (B.15) combined with Eq. (B.10) specifies only $(n/2+1)$ distinct eigenvectors. The reason for this is that $\cos(2\pi kl/n)$ is symmetric about $l=n/2$ and so as it stands,

$$\mathbf{c}_{n/2-l'} = \mathbf{c}_{n/2+l'}, \tag{B.16}$$

for $l' = 1, \ldots, (n/2-1)$. This is not satisfactory because the $\mathbf{c}_l$ eigenvectors that compose $\mathbf{C}$ are clearly not mutually orthogonal if Eq. (B.16) holds. The remaining $(n/2-1)$ distinct eigenvectors are obtained by redefining

$$c_{k,l} = N\sin(2\pi kl/n), \tag{B.17}$$

for $l = (n/2+1), \ldots, (n-1)$. These sine eigenvectors satisfy the cyclic boundary conditions in Eq. (B.9) and by substituting them into Eq. (B.8) it is found that they are associated with the same eigenvalues as the eigenvectors they have replaced. They complete the current diagonalization of $\mathbf{A}$ because they are orthogonal to each other and to the cosine eigenvectors defined above [43].

In summary, the eigenvalues of $\mathbf{A}$ (the diagonal elements of $\mathbf{a}$) are

$$a_l = 4\sin^2(l\pi/n), \tag{B.18}$$

for $l = 1, \ldots, n$. This implies that eigenvalue $a_{n/2-l'}$ is degenerate with $a_{n/2+l'}$ for

$l' = 1, \ldots, (n/2 - 1)$. The corresponding eigenvectors (the columns of $\mathbf{C}$) are

$$\begin{aligned} c_{k,l} &= N\cos(2\pi kl/n) \quad \text{for} \quad l = 1, \ldots, n/2 \ \text{ and } \ n, \\ c_{k,l} &= N\sin(2\pi kl/n) \quad \text{for} \quad l = n/2+1, \ldots, n-1. \end{aligned} \tag{B.19}$$

The normalization constants are

$$\begin{aligned} N &= \sqrt{1/n} \quad \text{for } \ l = n/2 \ \text{ or } \ n \quad \text{(distinct eigenvalues)}, \\ N &= \sqrt{2/n} \quad \text{for all other } l \quad \text{(degenerate eigenvalues)}. \end{aligned} \tag{B.20}$$

The chosen diagonalization of $\mathbf{A}$ can now be inserted into Eq. (B.4) to give

$$V_n(\mathbf{Q}) = \frac{1}{2} m\omega_n^2 \, \mathbf{Q}^T \cdot \mathbf{a} \cdot \mathbf{Q}, \tag{B.21}$$

where the transformation to the ring-polymer normal-mode coordinates is defined by

$$\mathbf{Q} \equiv \mathbf{C}^T \cdot \mathbf{q}. \tag{B.22}$$

Using the fact that the matrix $\mathbf{a}$ is diagonal, Eq. (B.21) becomes

$$V_n(\mathbf{Q}) = \frac{1}{2} m\omega_n^2 \sum_{l=1}^{n} a_l Q_l^2 = \sum_{l=1}^{n} \frac{1}{2} m\Omega_l^2 Q_l^2, \tag{B.23}$$

which is the potential for a collection of n uncoupled harmonic oscillators with ring-polymer normal-mode frequencies equal to

$$\Omega_l = \omega_n \sqrt{a_l} = 2\omega_n \sin(l\pi/n). \tag{B.24}$$

From Eq. (B.18) note that $a_n = 0$ and so the $l = n$ term in Eq. (B.23) defines a

potential for a zero-frequency harmonic oscillator. From Eq. (B.19) and Eq. (B.20) it is seen the eigenvector for this n^{th} normal-mode has elements $c_{k,n}=1/\sqrt{n}$ for all k and therefore Eq. (B.22) gives

$$Q_n = \frac{1}{\sqrt{n}} \sum_{k=1}^{n} q_k = \sqrt{n}\, q_c, \tag{B.25}$$

where the ring-polymer centroid position q_c is

$$q_c = \frac{1}{n} \sum_{k=1}^{n} q_k. \tag{B.26}$$

Part of the utility of the ring-polymer normal-mode transformation is therefore that it naturally introduces the centroid variable and can thus be used to simplify numerous expressions in this thesis.

B.2 Dividing-surface sampling

In Chapters 4 and 5, the ring-polymer normal-mode transformation is used to convert the RPMD-C position sampling distributions into products of uncoupled Gaussian functions. The transformation is described in a little more detail here.

For a one-dimensional reactive system the position sampling distribution is

$$P_q(\mathbf{q}) = \frac{1}{N_q}\, e^{-\beta_n V_n(\mathbf{q})} \delta_c(\mathbf{q}), \tag{B.27}$$

where N_q is the normalization constant

$$N_q = \int d\mathbf{q}\, e^{-\beta_n V_n(\mathbf{q})} \delta_c(\mathbf{q}), \tag{B.28}$$

and $\delta_c(\mathbf{q}) = \delta(q_c - q^\ddagger)$ is a delta function confining the centroid q_c to $q^\ddagger$, the chosen

dividing surface. Two steps are required to write $P_q(\mathbf{q})$ as a function of the ring-polymer normal mode coordinates $\mathbf{Q}$. Firstly, $V_n(\mathbf{q})$ is replaced by $V_n(\mathbf{Q})$ (Eq. (B.21)) without approximation. Secondly, since

$$\delta(ax) = \frac{1}{a}\delta(x), \tag{B.29}$$

from Eq. (B.25) one has

$$\delta_c(\mathbf{q}) = \delta(q_c - q^\ddagger) = \delta(\frac{Q_n}{\sqrt{n}} - q^\ddagger) = \sqrt{n}\,\delta(Q_n - \sqrt{n}q^\ddagger). \tag{B.30}$$

Thus,

$$P_q(\mathbf{Q}) = \frac{\sqrt{n}}{N_q}\exp\left[-\beta_n \sum_{k=1}^{n} \frac{1}{2} m\Omega_k^2 Q_k^2\right]\ \delta(Q_n - \sqrt{n}\,q^\ddagger). \tag{B.31}$$

This sampling distribution is clearly the sought-after product of uncoupled Gaussian functions. It dictates that the first $k=1,\ldots,n-1$ ring-polymer normal-mode positions are sampled from Gaussian distributions with means of zero and standard deviations of

$$\sigma_k = 1/\sqrt{\beta_n m\Omega_k^2}, \tag{B.32}$$

where Ω_k is the k^{th} ring-polymer normal-mode frequency in Eq. (B.24). To effect the centroid-pinning the n^{th} normal-mode position is sampled from a Gaussian with a mean of $\sqrt{n}\,q^\ddagger$ and zero standard deviation. The inverse of Eq. (B.22),

$$\mathbf{q} = \mathbf{C}\cdot\mathbf{Q}, \tag{B.33}$$

then returns the sampled ring-polymer positions in the original coordinate system.

The steps that are needed to transform $P_q(\mathbf{q})$ can also be used to write the normal-

ization prefactor in Eq. (B.31) as

$$N_q = \sqrt{n} \int d\mathbf{Q} \exp\left[-\beta_n \sum_{k=1}^{n} \frac{1}{2} m\Omega_k^2 Q_k^2\right] \delta(Q_n - \sqrt{n}\, q^{\ddagger}), \tag{B.34}$$

because the orthogonality of $\mathbf{C}$ (Eq. (B.7)) means that

$$\int d\mathbf{q} = \int |\det(\mathbf{C})|\, d\mathbf{Q} = \int d\mathbf{Q}. \tag{B.35}$$

Taking account of the delta function for the zero-frequency normal-mode leaves $n-1$ Gaussian integrals in Eq. (B.34), which yield

$$N_q = \sqrt{n} \left(\frac{2\pi}{\beta_n m}\right)^{\frac{n-1}{2}} \prod_{k=1}^{n-1} \left(\frac{1}{\Omega_k^2}\right)^{1/2}. \tag{B.36}$$

When combined with the normalization constant that arises from the momentum distribution (N_p in Eq. (4.68)) this result allows the prefactor of the RPMD-C correlation function (Eq. (4.72)) to be written

$$\frac{N_p N_q}{(2\pi\hbar)^n} = (m/2\pi\beta\hbar^2)^{1/2} = 1/\Lambda(T), \tag{B.37}$$

where $\Lambda(T)$ is the thermal de Broglie wavelength.

Finally, when a harmonic potential of $V(q) = m\omega^2 q^2/2$ is added to each bead of the ring-polymer kinetic-spring system (Section 5.3) one has

$$V_n(\mathbf{q}) = \sum_{k=1}^{n} \left[\frac{1}{2} m\omega_n^2 (q_k - q_{k+1})^2 + \frac{1}{2} m\omega^2 q_k^2\right], \tag{B.38}$$

instead of Eq. (B.1). In vector form,

$$V_n(\mathbf{q}) = \frac{1}{2} m\omega_n^2\, \mathbf{q}^T \cdot \mathbf{A} \cdot \mathbf{q} + \frac{1}{2} m\omega^2\, \mathbf{q}^T \cdot \mathbf{q}, \tag{B.39}$$

or in terms of the ring-polymer normal modes

$$V_n(\mathbf{Q}) = \frac{1}{2} m\omega_n^2 \, \mathbf{Q}^T \cdot \mathbf{a} \cdot \mathbf{Q} + \frac{1}{2} m\omega^2 \, \mathbf{Q}^T \cdot \mathbf{Q}, \tag{B.40}$$

using Eq. (B.6), Eq. (B.33), and the orthogonality of $\mathbf{C}$ (Eq. (B.7)). This is just

$$V_n(\mathbf{Q}) = \frac{1}{2} m \, \mathbf{Q}^T \cdot \left(\omega_n^2 \, \mathbf{a} + \omega^2 \, \mathbf{I}\right) \cdot \mathbf{Q}, \tag{B.41}$$

where $\mathbf{I}$ is the (diagonal) unit matrix. Comparison to Eq. (B.21) shows that the only effect of the harmonic potential on the ring-polymer normal-mode transformation is a shift of the normal-mode frequencies, i.e.,

$$\Omega_l = \omega_n \sqrt{a_l} \quad \rightarrow \quad \Omega_l = \omega_n \sqrt{a_l + \left(\frac{\omega}{\omega_n}\right)^2}. \tag{B.42}$$

This results in a shift in the standard deviations of the Gaussian sampling distributions when a harmonic potential is used to bias the sampling of the ring-polymer positions (Section 5.3).

References

[1] M. P. Allen and D. J. Tildesley, *Computer Simulation of Liquids*, Oxford Science Publications, (1987).

[2] D. Frenkel and B. Smit, *Understanding Molecular Simulation - From Algorithms to Applications*, Academic Press, San Diego, (1996).

[3] K. Binder (ed.), *Monte Carlo Methods in Statistical Physics*, Springer-Verlag, (1979).

[4] R. P. Feynman and A. R. Hibbs, *Quantum Mechanics and Path Integrals*, McGraw-Hill, New York, (1965).

[5] R. P. Feynman, *Statistical Mechanics*, Addison-Wesley, New York, (1972).

[6] H. Kleinert, *Path Integrals*, World Scientific, Singapore, (1995).

[7] R. Zwanzig, *Annu. Rev. Phys. Chem.*, **16**, 67 (1965).

[8] D. Chandler, *Introduction to Modern Statistical Mechanics*, Oxford University Press, (1987).

[9] A. O. Caldeira and A. J. Leggett, *Ann. Phys. (N.Y.)*, **149**, 374 (1983).

[10] D. E. Makarov and N. Makri, *Chem. Phys. Lett.*, **221**, 482 (1994).

[11] N. Makri, *J. Math. Phys.*, **36**, 2430 (1995).

[12] N. Makri, *Annu. Rev. Phys. Chem.*, **50**, 167 (1999).

[13] W. H. Miller, *J. Phys. Chem. A*, **102**, 793 (1998).

[14] H. Wang, X. Sun, and W. H. Miller, *J. Chem. Phys.*, **108**, 9726 (1998).

[15] R. Hernandez and G. A. Voth, *Chem. Phys.*, **233**, 243 (1998).

[16] J. Poulsen, G. Nyman, and P. J. Rossky, *J. Chem. Phys.*, **119**, 12179 (2003).

[17] J. Cao and G. A. Voth, *J. Chem. Phys.*, **100**, 5106 (1994).

[18] J. Cao and G. A. Voth, *J. Chem. Phys.*, **101**, 6168 (1994).

[19] S. Jang and G. A. Voth, *J. Chem. Phys.*, **111**, 2357 (1999).

[20] S. Jang and G. A. Voth, *J. Chem. Phys.*, **111**, 2371 (1999).

[21] T. F. Miller III and D. E. Manolopoulos, *J. Chem. Phys.*, **122**, 184503 (2005).

[22] D. Colognesi, M. Celli, M. Neumann, and M. Zoppi, *Phys. Rev. E*, **70**, 061202 (2004).

[23] W. H. Miller, *Proc. Natl. Acad. Sci. USA*, **102**, 6660 (2005).

[24] S. C. Althorpe and D. C. Clary, *Annu. Rev. Phys. Chem.*, **54**, 493 (2003).

[25] W. H. Miller, S. D. Schwartz, and J. W. Tromp, *J. Chem. Phys.*, **79**, 4889 (1983).

[26] M. Topaler and N. Makri, *J. Chem. Phys.*, **101**, 7500 (1994).

[27] D. A. McQuarrie, *Statistical Mechanics*, University Science Books, Sausalito, (2000).

[28] G. Ciccotti, D. Frenkel, and I. R. McDonald, *Simulation of Liquids and Solids*, North-Holland, Amsterdam, (1987).

[29] R. Ramírez, T. López-Ciudad, P. Kumar, and D. Marx, *J. Chem. Phys.*, **121**, 3973 (2004).

[30] H. Kim and P. J. Rossky, *J. Phys. Chem. B*, **106**, 8240 (2002).

[31] R. Kubo, *J. Phys. Soc. Jpn.*, **12**, 570 (1957).

[32] I. R. Craig and D. E. Manolopoulos, *J. Chem. Phys.*, **121**, 3368 (2004).

[33] D. Marx and M. H. Müser, *J. Phys.: Condens. Matter*, **11**, R117 (1999).

[34] M. Parrinello and A. Rahman, *J. Chem. Phys.*, **80**, 860 (1984).

[35] R. A. Kuharski and P. J. Rossky, *J. Chem. Phys.*, **82**, 5164 (1985).

[36] L. Schulman, *Techniques and Applications of Path Integration*, John Wiley & Sons, New York, (1981).

[37] P. A. M. Dirac, *The Principles of Quantum Mechanics*, Clarendon Press, (1981).

[38] D. Chandler and P. G. Wolynes, *J. Chem. Phys.*, **74**, 4078 (1981).

[39] M. Tuckerman, in *Quantum Simulations of Complex Many-Body Systems: from Theory to Applications*, eds. J. Grotendorst, D. Marx and A. Muramatsu, NIC Series Vol. 10, John von Neumann Institute for Computing, Forschungzentrum Jülich, (2002).

[40] R. Egger and C. H. Mak, in *Quantum Simulations of Complex Many-Body Systems: from Theory to Applications*, eds. J. Grotendorst, D. Marx and A. Muramatsu, NIC Series Vol. 10, John von Neumann Institute for Computing, Forschungzentrum Jülich, (2002).

[41] W. H. Miller, *J. Phys. Chem. A*, **105**, 2942 (2001).

[42] M. Thoss and H. Wang, *Annu. Rev. Phys. Chem.*, **55**, 299 (2004).

[43] G. B. Arfken and H. J. Weber, *Mathematical Methods for Physicists*, Academic Press, London, (2001).

[44] K. G. Kay, *Annu. Rev. Phys. Chem.*, **56**, 255 (2005).

[45] J. H. van Vleck, *Proc. Natl. Acad. Sci. USA*, **14**, 178 (1928).

[46] M. C. Gutzwiller, *Chaos in Classical and Quantum Mechanics*, Springer, New York, (1990).

[47] W. H. Miller, *J. Chem. Phys.*, **53**, 3578 (1970).

[48] V. S. Filinov, *Nucl. Phys. B*, **271**, 717 (1986).

[49] J. D. Doll, D. L. Freeman, and T. L. Beck, *Adv. Chem. Phys.*, **78**, 61 (1994).

[50] H. Wang, D. E. Manolopoulos, and W. H. Miller, *J. Chem. Phys.*, **115**, 6317 (2001).

[51] N. Makri, *Chem. Phys. Lett.*, **291**, 101 (1999).

[52] Q. Shi and E. Geva, *J. Chem. Phys.*, **118**, 8173 (2003).

[53] E. Wigner, *Phys. Rev.*, **40**, 749 (1932).

[54] R. C. Brown and E. J. Heller, *J. Chem. Phys.*, **75**, 186 (1981).

[55] X. Sun, H. Wang, and W. H. Miller, *J. Chem. Phys.*, **109**, 4190 (1998).

[56] E. Geva, Q. Shi, and G. A. Voth, *J. Chem. Phys.*, **115**, 9209 (2001).

[57] X. Sun, H. Wang, and W. H. Miller, *J. Chem. Phys.*, **109**, 7064 (1998).

[58] R. P. Feynman and H. Kleinert, *Phys. Rev. A*, **34**, 5080 (1986).

[59] E. Pollock and D. M. Ceperley, *Phys. Rev. B*, **30**, 2555 (1984).

[60] M. Sprik, M. L. Klein, and D. Chandler, *J. Chem. Phys.*, **83**, 3942 (1985).

[61] D. F. Coker, D. Thirumalai, and B. J. Berne, *J. Chem. Phys.*, **86**, 5689 (1987).

[62] D. Ceperley, *Rev. Mod. Phys.*, **67**, 279 (1995).

[63] S. Nosé, *J. Chem. Phys.*, **81**, 511 (1984).

[64] W. G. Hoover, *Phys. Rev. A*, **31**, 1695 (1985).

[65] G. J. Martyna, M. L. Klein, and M. Tuckerman, *J. Chem. Phys.*, **97**, 2635 (1992).

[66] M. Tuckerman, Y. Liu, G. Ciccotti, and G. J. Martyna, *J. Chem. Phys.*, **115**, 1678 (2001).

[67] H. C. Andersen, *J. Chem. Phys.*, **72**, 2384 (1980).

[68] R. W. Hall and B. J. Berne, *J. Chem. Phys.*, **81**, 3641 (1984).

[69] B. J. Berne and D. Thirumalai, *Annu. Rev. Phys. Chem.*, **37**, 401 (1986).

[70] M. Tuckerman, D. Marx, M.L. Klein, and M. Parrinello, *J. Chem. Phys.*, **104**, 5579 (1996).

[71] M. Tuckerman, G. J. Martyna, and B. J. Berne, *J. Chem. Phys.*, **97**, 1990 (1992).

[72] M. L. Boas, *Mathematical Methods in the Physical Sciences*, John Wiley and Sons, (1983).

[73] E. Jezek and N. Makri, *J. Phys. Chem. A*, **105**, 2851 (2001).

[74] I. R. Craig and D. E. Manolopoulos, *Chemical Physics*, **322**, 236 (2006).

[75] L. van Hove, *Phys. Rev.*, **95**, 249 (1954).

[76] S. W. Lovesey, *Theory of Neutron Scattering from Condensed Matter*, Clarendon Press, Oxford, (1984).

[77] A. Rahman, K. S. Singwi, and A Sjölander, *Phys. Rev.*, **126**, 986 (1962).

[78] D. Scharf, G. J. Martyna, and M. L. Klein, *Low Temp. Phys.*, **19**, 364 (1993).

[79] I. F. Silvera and V. V. Goldman, *J. Chem. Phys.*, **69**, 4209 (1978).

[80] J.-P. Hansen and I. R. McDonald, *Theory of Simple Liquids*, Academic Press, London, (1990).

[81] P. W. Atkins and R. S. Friedman, *Molecular Quantum Mechanics*, Oxford University Press, (1997).

[82] J. Z. H. Zhang, *Theory and Application of Quantum Molecular Dynamics*, World Scientific, Singapore, (1999).

[83] E. J. Heller, J. R. Reimers, and G. Drolshagen, *Phys. Rev. A*, **36**, 2613 (1987).

[84] V. F. Sears, *Phys. Rev. A*, **7**, 340 (1973).

[85] P. G. de Gennes, *Physica*, **25**, 825 (1959).

[86] B. J. Braams, T. F. Miller III, and D. E. Manolopoulos, *Chem. Phys. Lett.*, **418**, 175 (2005).

[87] R. Kubo, M. Toda, and N. Hashitsume, *Statistical Physics II: Nonequilibrium Statistic Mechanics*, Springer, New York, (1985).

[88] M. F. Herman, E. J. Bruskin, and B. J. Berne, *J. Chem. Phys.*, **76**, 5150 (1982).

[89] C. Kittel, *Introduction to Solid State Physics*, Wiley, New York, (1996).

[90] T. D. Hone and G. A. Voth, *J. Chem. Phys.*, **121**, 6412 (2004).

[91] D. Levesque and L. Verlet, *Phys. Rev. A*, **2**, 2514 (1970).

[92] B. Dünweg and K. Kremer, *J. Chem. Phys.*, **99**, 6983 (1993).

[93] I.-C. Yeh and G. Hummer, *J. Phys. Chem. B*, **108**, 15873 (2004).

[94] M. Celli, D. Colognesi, and M. Zoppi, *Phys. Rev. E*, **66**, 021202 (2002).

[95] J. C. Keck, *J. Chem. Phys.*, **32**, 1035 (1960).

[96] C. H. Bennett, in *Algorithms for Chemical Computation*, ed. R. E. Christoffersen, ACS Symposium Series, ACS (Washington D.C.), (1977).

[97] D. Chandler, *J. Chem. Phys.*, **68**, 2959 (1978).

[98] N. Makri, E. Sim, D. E. Makarov, and M. Topaler, *Proc. Natl. Acad. Sci.*, **93**, 3926 (1996).

[99] J. Gao and D. G. Truhlar, *Annu. Rev. Phys. Chem.*, **53**, 467 (2002).

[100] M. Garcia-Viloca, J. Gao, M. Karplus, and D. Truhlar, *Science*, **303**, 186 (2004).

[101] T. Yamamoto, *J. Chem. Phys.*, **33**, 281 (1960).

[102] W. H. Miller, *J. Chem. Phys.*, **61**, 1823 (1974).

[103] I. R. Craig and D. E. Manolopoulos, *J. Chem. Phys.*, **122**, 084106 (2005).

[104] I. R. Craig and D. E. Manolopoulos, *J. Chem. Phys.*, **123**, 034102 (2005).

[105] H. J. Eyring, *Chem. Phys.*, **3**, 107 (1934).

[106] E. Wigner, *Chem. Phys.*, **5**, 720 (1937).

[107] G. A. Voth, D. Chandler, and W. H. Miller, *J. Chem. Phys.*, **91**, 7749 (1989).

[108] M. J. Gillan, *J. Phys. C*, **20**, 3621 (1987).

[109] M. J. Gillan, *Phys. Rev. Lett.*, **58**, 563 (1987).

[110] E. Pollak and J.-L. Liao, *J. Chem. Phys.*, **108**, 2733 (1998).

[111] N. F. Hansen and H. C. Andersen, *J. Phys. Chem.*, **100**, 1137 (1996).

[112] W. H. Miller, Y. Zhao, M. Ceotto, and S. Yang, *J. Chem. Phys.*, **119**, 1329 (2003).

[113] C. Venkataraman and W. H. Miller, *J. Phys. Chem. A*, **108**, 3035 (2004).

[114] Y. Zhao, T. Yamamoto, and W. H. Miller, *J. Chem. Phys.*, **120**, 3100 (2004).

[115] M. Ceotto and W. H. Miller, *J. Chem. Phys.*, **120**, 6356 (2004).

[116] M. Ceotto, S. Yang, and W. H. Miller, *J. Chem. Phys.*, **122**, 044109 (2005).

[117] T. Yamamoto and W. H. Miller, *J. Chem. Phys.*, **122**, 044106 (2005).

[118] J. Vanicek, W. H. Miller, J. F. Castillo, and J. Aoiz, *J. Chem. Phys.*, **123**, 054108 (2005).

[119] A. Heyden, A. T. Bell, and F. J. Keil, *J. Chem. Phys.*, **123**, 224101 (2005).

[120] This argument assumes that the dividing surface is located at the top of the reaction barrier, but analogous conclusions hold even if it is not.

[121] W. H. Press, S. A. Teukolsky, W. T. Vetterling, and B. P. Flannery, *Numerical Recipes in Fortran 77: The Art of Scientific Computing*, Cambridge University Press, (1992).

[122] T. Yamamoto, H. Wang, and W. H. Miller, *J. Chem. Phys.*, **116**, 7335 (2002).

[123] E. Wigner, *Trans. Faraday Soc.*, **34**, 29 (1938).

[124] S. Jang and G. A. Voth, *J. Chem. Phys.*, **112**, 8747 (2000).

[125] J. Cao and G. A. Voth, *J. Chem. Phys.*, **105**, 6856 (1996).

[126] H. A. Kramers, *Physica*, **7**, 284 (1940).

[127] R. F. Grote and J.T. Hynes, *J. Chem. Phys.*, **73**, 2715 (1980).

[128] P. G. Wolynes, *Phys. Rev. Lett.*, **47**, 968 (1981).

[129] E. Pollak, *J. Chem. Phys.*, **85**, 865 (1986).

[130] E. Pollak, H. Grabert, and P. Hänggi, *J. Chem. Phys.*, **91**, 4073 (1989).

[131] A. J. Leggett, S. Chakravarty, A. T. Dorsey, M. P. Fisher, A. Garg, and W. Zwerger, *Rev. Mod. Phys.*, **59**, 1 (1987).

[132] R. Zwanzig, *J. Stat. Phys.*, **9**, 215 (1973).

[133] H. Wang (private communication).

[134] D. L. Hasha, T. Eguchi, and J. Jonas, *J. Am. Chem. Soc.*, **104**, 2290 (1982).

[135] A. Horikoshi and K. Kinugawa, *J. Chem. Phys.*, **122**, 174104 (2005).